Dynamical mean-field theory of strongly correlated fermion systems and the limit of infinite dimensions

Antoine Georges

Laboratoire de Physique Théorique de l'Ecole Normale Supérieure, 24, rue Lhomond, 75231 Paris Cedex 05, France

Gabriel Kotliar

Serin Physics Laboratory, Rutgers University, Piscataway, New Jersey 08854

Werner Krauth and Marcelo J. Rozenberg

Laboratoire de Physique Statistique de l'Ecole Normale Supérieure, 24, rue Lhomond, 75231 Paris Cedex 05, France

We review the dynamical mean-field theory of strongly correlated electron systems which is based on a mapping of lattice models onto quantum impurity models subject to a self-consistency condition. This mapping is exact for models of correlated electrons in the limit of large lattice coordination (or infinite spatial dimensions). It extends the standard mean-field construction from classical statistical mechanics to quantum problems. We discuss the physical ideas underlying this theory and its mathematical derivation. Various analytic and numerical techniques that have been developed recently in order to analyze and solve the dynamical mean-field equations are reviewed and compared to each other. The method can be used for the determination of phase diagrams (by comparing the stability of various types of long-range order), and the calculation of thermodynamic properties, one-particle Green's functions, and response functions. We review in detail the recent progress in understanding the Hubbard model and the Mott metal-insulator transition within this approach, including some comparison to experiments on three-dimensional transition-metal oxides. We present an overview of the rapidly developing field of applications of this method to other systems. The present limitations of the approach, and possible extensions of the formalism are finally discussed. Computer programs for the numerical implementation of this method are also provided with this article.

CONTENTS

I. Introduction 14
II. The Local Impurity Self-Consistent Approximation: An Overview 17
A. Dynamical mean-field equations 17
B. Physical content and connection with impurity models 19
C. The limit of infinite dimensions 20
III. Derivations of the Dynamical Mean-Field Equations 21
A. The cavity method 21
B. Local nature of perturbation theory in infinite dimensions 23
C. Derivation based on an expansion around the atomic limit 25
D. Effective medium interpretation 26
IV. Response Functions and Transport 27
A. General formalism 27
B. Frequency-dependent conductivity, thermopower and Hall effect 30
V. Phases with Long-Range Order 31
A. Ferromagnetic long-range order 31
B. Antiferromagnetic long-range order 31
C. Superconductivity and pairing 32
VI. Methods of Solution 33
A. Numerical solutions 34
1. Quantum Monte Carlo method 34
a. Introduction: A heuristic derivation 22
b. The Hirsch-Fye algorithm: Rigorous derivation 23
c. Implementation of the Hirsch-Fye algorithm 24
d. The LISA-QMC algorithm and a practical example 26
e. Relationship with other QMC algorithms 26
2. Exact diagonalization method 40
3. Comparison of exact diagonalization and Monte Carlo methods 43
4. Spectral densities and real frequency quantities: Comparison of various methods 44
5. Numerical calculation of susceptibilities and vertex functions 46
B. Analytic methods 48
1. Exact methods at low energy 48
2. The iterated perturbation theory approximation 50
3. Slave boson methods and the noncrossing approximation 51
4. Equations of motion decoupling schemes 53
C. The projective self-consistent technique 54
VII. The Hubbard Model and the Mott Transition 59
A. Early approaches to the Mott transition 59
B. Models and self-consistent equations 61
C. Existence of a Mott transition at half-filling 62
1. Metallic phase 62
2. Insulating phase 64
D. Phase diagram and thermodynamics 65
1. Paramagnetic phases 65
2. Thermodynamics 67
3. Antiferromagnetic phases 69
E. The zero-temperature metal-insulator transition 70
F. On the $T=0$ instability of the insulating solution 71
G. Response functions close to the Mott-Hubbard transition 72

 © 1996 The American Physical Society

1. Magnetic susceptibilities 72
2. Charge response and compressibility 74
3. Response to a finite magnetic field and metamagnetism 74
H. The Hubbard model away from half-filling: Doping the Mott insulator 75
1. Qualitative arguments 75
2. Single-particle properties 76
3. Thermodynamics 77
4. Transport properties and response functions 78
5. Phase diagram 79
I. Comparison with experiments 81
1. Phase diagrams 81
2. Photoemission spectra 82
3. Optical conductivity 83
4. Doped titanates 85
VIII. Application of the LISA to Various Models 86
A. Periodic Anderson model and the Kondo lattice 87
1. The periodic Anderson model 87
2. Half-filled case: Kondo insulators 88
3. The multichannel Kondo lattice 92
4. Metallic quantum spin glasses 92
B. The Falicov-Kimball model 93
C. Multiband models: combining LISA and LDA 95
D. The extended Hubbard model and excitonic effects 97
E. Electron-phonon coupling and the Holstein model 99
F. Colossal magnetoresistance and doped manganates 102
G. Systems with quenched disorder 104
1. Models of disorder 104
2. Interplay of disorder and SDW or CDW ordering 105
3. Formation of local moments and the Mott transition in disordered systems 105
IX. Beyond $d=\infty$: Including Spatial Fluctuations 107
A. Motivations 107
B. The Bethe-Peierls approximation 108
C. Self-consistent cluster approximations 109
D. Functional integral formulation and loop expansion 111
X. Conclusion 113
Acknowledgments 113
Appendix A: Fermiology in $d=\infty$ 113
1. Density of states of some $d=\infty$ lattices 113
2. Momentum dependence of response functions 115
3. Fermions on the Bethe lattice 116
Appendix B: Details of the Monte Carlo algorithm 117
1. Some derivations 117
2. Numerical implementation of the QMC and Gray code enumeration 118
3. Numerical implementation of the self-consistency condition 119
Appendix C: Details of the exact diagonalization algorithm 119
Appendix D: Access to FORTRAN programs 120
References 121

I. INTRODUCTION

The discovery of the heavy fermion compounds and of the high-temperature superconductors has revived interest in strongly correlated electron systems. These are systems in which the strength of the electron-electron interactions is comparable to or larger than the kinetic energy. The investigation of this class of systems goes back to the early 1960s. The main motivations at the time came from experiments on transition metal oxides, from the Mott metal-insulator transition, and from the problem of itinerant ferromagnetism.

Theoretical progress in the field has been impeded however by the extreme difficulty of dealing with even the simplest model Hamiltonians appropriate for these systems, such as the Hubbard model and the Kondo lattice model. Only in the one-dimensional case do we have a variety of theoretical tools at our disposal to study these models in a systematic manner. For two- and three-dimensional models, one is often unable to assess confidently whether a given physical phenomenon is indeed captured by the idealized Hamiltonian under consideration or whether a theoretical prediction reflects a true feature of this Hamiltonian, rather than an artifact of the approximation used in its solution. These difficulties originate in the nonperturbative nature of the problem, and reflect the presence of several competing physical mechanisms for even the simplest models. The interplay of localization and lattice coherence, of quantum and spatial fluctuations, and of various competing types of long-range order are important examples.

Numerous approximation schemes have been employed to circumvent these difficulties, but many theorists in the field have learned to consider with caution those approximations (such as arbitrary resummations of some class of diagrams) that are not based on some *controlled limit*, by which we mean that some extreme limit of the model is considered (often after some generalization) wherein the problem simplifies and can be solved in a controlled manner. The reason to favor these approaches is not that of out-of-place mathematical rigor, but rather that it is often easier to identify which of the physical aspects of the problem will be privileged by a specific limit, and thus to choose that specific limit best adapted to the physical phenomenon under consideration. In favorable cases, the physical ingredients that have been left out can be reintroduced by expanding around this starting point. Of course the dramatic increase in computational power has also stimulated a direct numerical solution of these models using exact diagonalization and quantum Monte Carlo methods, as recently reviewed by Dagotto (1994). However, the exact diagonalization technique is limited by the exponential growth of the computations with system size, while the quantum Monte Carlo method is restricted to rather high temperatures by the minus-sign problem. Despite the interest of these numerical studies, these limitations have often prevented the extraction of reliable low-energy information. Until these limitations are overcome, analytic tools remain essential for the study of the strong correlation problem.

This article reviews a new approach to the problem of strong correlations that has been developed over recent years and has led to some progress in our understanding of these systems. The essential idea is to replace a *lattice* model by a *single-site* quantum impurity problem embedded in an effective medium determined *self-*

consistently. The impurity model offers an intuitive picture of the local dynamics of a quantum many-body system. Also, a large number of techniques developed over a thirty-year period of intensive study of impurity models are available. The self-consistency condition captures the translation invariance and coherence effects of the lattice. We refer to this approach as the *local impurity self-consistent approximation* (LISA) in this article.

The LISA is the natural generalization of quantum many-body problems of the Weiss mean-field theory familiar from classical statistical mechanics. The term "mean-field theory" should be taken with caution however: the present approach *does not* assume that *all* fluctuations are frozen (this would lead to the Hartree-Fock approximation). Rather, it freezes spatial fluctuations but takes full account of *local* quantum fluctuations (i.e., of temporal fluctuations between the possible quantum states at a given lattice site). Hence the LISA method is best characterized as a "dynamical mean-field theory." The main difference with the classical case is that the on-site quantum problem remains a many-body problem (which nevertheless can be addressed with a variety of techniques).

As in classical statistical mechanics, this dynamical mean-field theory becomes *exact* in the limit of large spatial dimensions $d \to \infty$, or more appropriately in the limit of large lattice coordination (note that the coordination z is already quite large for several three-dimensional lattices: $z=6$ for a cubic lattice, $z=12$ for a face-centered-cubic lattice). This ensures the internal consistency of the approach and establishes $1/z$ as a control parameter. Indeed, it is the pioneering work of Metzner and Vollhardt (1989) on the limit of large dimensions for strongly correlated fermion models that triggered the developments leading to the LISA method in the form reviewed here. However, this approach may be viewed in a broader context, as a starting point for the investigation of many *finite-dimensional* strongly correlated systems, in the same sense that the Weiss mean-field theory is the starting point of most investigations in the classical statistical mechanics of three-dimensional systems. In particular, the method can be used as an approximation to more realistic models of actual materials, taking into account several orbitals, and specific lattice structure and density of states, as obtained, e.g., from local density approximation (LDA) calculations (cf. Sec. VIII.C). Calculations along these lines are only beginning to appear.

This article is a self-contained introduction to the LISA approach, which has only partly the character of a review. It contains (a) a discussion of the general theoretical formalism and several derivations of the dynamical mean-field equations, (b) a description of the algorithms which are useful for their solution, (c) source codes of computer programs implementing these algorithms, (d) a thorough discussion of analytic techniques developed to analyze the dynamical mean-field equations, and (e) several examples of physical problems to which the LISA approach has been successfully applied. Our hope is that making this package widely available will allow many workers to contribute in applying these techniques to the countless number of open problems in the field of strongly correlated electrons. With this idea in mind, we have indicated some possible directions for further research and pointed out the aspects of the formalism which need further improvement.

Several authors contributed in recent years to the emergence of the LISA approach in its present form, starting with the pioneering work of Metzner and Vollhardt (1989). These authors pointed out the scaling of the hopping amplitude that leads to a nontrivial limit of infinite spatial dimensions for lattice models of correlated fermions. More importantly, they recognized the potential usefulness of this limit by demonstrating the local nature of perturbation theory in $d=\infty$. Müller-Hartmann (1989a, 1989b, 1989c) also proved the locality of many-body Green's function perturbation theory and used it in order to derive self-consistent equations for the self-energy in terms of the (generally unknown) Luttinger-Ward functional, which he evaluated to various orders in weak-coupling perturbation theory. Following this work, self-consistent functional equations were derived and solved for the Falicov-Kimball model by Brandt and Mielsch (1989, 1990, 1991; see also, Janiš, 1991). These authors also pointed out how these equations could be formally extended to the Hubbard model. A mean-field interpretation of these equations was given for the Falicov-Kimball model by van Dongen and Vollhardt (1990). This interpretation is quite different from the LISA ideas however. Functional equations for the Green's function and the self-energy of the Hubbard model in infinite dimensions were derived by Janiš (1991) following the dynamical coherent potential approximation analogy, but, in this formulation, these functional equations did not lend themselves to explicit calculations.

Further progress was made possible by the realization (Ohkawa 1991a, 1991b; Georges and Kotliar, 1992) that the functional equations can be interpreted as an Anderson impurity model subject to a self-consistent bath: this is the main content of the LISA approach [see also the subsequent work of Jarrell (1992)]. In the work of Georges and Kotliar (1992), a precise correspondence with the classical mean-field theory, and the proper identification of the quantum analog of the Weiss effective field, was carried out. This allowed an immediate extension of the LISA method to phases with broken symmetry and to a large number of models of strongly correlated electrons (Georges, Kotliar, and Si, 1992). Using general properties on the single-impurity Anderson model in conjunction with the self-consistency condition, Georges and Kotliar (1992) also established that the metallic phase of the $d=\infty$ Hubbard model is a Fermi liquid for arbitrary doping and interaction strength. An important lesson of that work is that reliable techniques for treating the Anderson impurity model can be used to study correlated electrons in large dimensions. For example, the perturbative approach of Yosida and Yamada (1970, 1975) can be turned into an efficient "iterated perturbation theory" scheme in the LISA context

(Georges and Kotliar, 1992). Another example is the noncrossing approximation method first applied in the LISA context by Jarrell and Pruschke (1993a, 1993b) and Pruschke, Cox, and Jarrell (1993a, 1993b).

Many numerical methods have been recently implemented for the solution of the dynamical mean-field equations. The quantum Monte Carlo algorithm of Hirsch and Fye (1986) was first applied to this problem independently by Jarrell (1992), Rozenberg, Zhang, and Kotliar (1992), and Georges and Krauth (1992). Two different exact diagonalization algorithms were later introduced by Caffarel and Krauth (1994) and by Si *et al.* (1994). The Wilson numerical renormalization group approach to the single-impurity problem has been recently applied to the $d=\infty$ Hubbard model by Sakai and Kuramoto (1994) and Shimizu and Sakai (1995), and a projective renormalization method using in an essential way the self-consistency condition has been recently introduced by Moeller *et al.* (1995). One of the major applications of these methods and of the LISA approach has been the study of the Mott transition in the half-filled Hubbard model (Rozenberg, Zhang, and Kotliar, 1992; Georges and Krauth, 1992, 1993; Pruschke, Cox, and Jarrell, 1993a, 1993b; Zhang, Rozenberg, and Kotliar, 1993; Caffarel and Krauth, 1994; Laloux, Georges, and Krauth, 1994; Rozenberg, Kotliar, and Zhang, 1994; Rozenberg, Moeller and Kotliar, 1994; Moeller *et al.*, 1995). The important lesson learned from these studies is that no single technique stands out as the most appropriate, but a thorough understanding of the many-body phenomena associated with this problem required a combination of various numerical methods and of analytical approximations.

Having reviewed the recent history of the LISA approach, it is interesting to mention that early related ideas can be traced back in the literature, starting with the papers of Hubbard (1964, 1979) and Wang, Evenson, and Schrieffer (1969). Impurity models (without a self-consistent embedding) have been used to model the photoemission spectra of correlated solids for a long time (Zaanen and Sawatzky, 1987, 1990; Fujimori, Minami, and Sugano, 1984). The LISA method also has some relationship with the dynamical coherent potential approximation method for random alloys: indeed, a functional integral approach reduces the quantum many-body problem to averaging a free-particle problem over external fields with random variations in space and time (for recent work along those lines, see Turov and Grebenikov, 1988; Kakehashi, 1992). In this context, Schwartz and Siggia (1972) first recognized the importance of the inverse coordination number as the small parameter justifying the coherent potential approximation. In fact, the LISA equations first appeared in the literature as early as 1987, in the context of the periodic Anderson model, in an interesting but little known paper of Kuramoto and Watanabe (1987) that also emphasized the limit of large lattice coordination. Finally, the assumption of local vertices has sometimes been used as a simplifying hypothesis in many-body perturbation theory calculations (see, e.g., Treglia, Ducastelle, and Spanjaard, 1980).

The LISA dynamical mean-field approach can be compared and contrasted to other frequently used approximation schemes for lattice models of correlated fermions. In the Hartree-Fock approximation, the starting point is a mean-field theory in which *all* fluctuations, both spatial and temporal, are frozen. Fluctuations can then be treated by making random phase approximation expansions around the static and uniform saddle point. Local quantum fluctuations, however, are often nonperturbative in character (being associated, like in the Kondo problem, with tunneling events between degenerate minima), so that such expansions do not capture them correctly. The purpose of the dynamical mean-field approach is to privilege these fluctuations, by treating them from the beginning in a nonperturbative manner. Another type of approximation is based on the controlled limit of extending the spin symmetry from SU(2) to SU(N) (or some other group) and considering the large N limit (see, e.g., Newns and Read, 1987; Kotliar, 1993a, 1994 for reviews). These approaches make use of some auxiliary degrees of freedom (e.g., slave bosons) to describe the enlarged Hilbert space. The saddle point which holds at $N=\infty$ generally replaces the problem with a gas of renormalized quasiparticles. High-energy incoherent excitations are completely absent at the saddle-point level, and must be reintroduced by expanding in $1/N$. In contrast, the LISA dynamical mean-field theory treats the local aspects of both quasiparticles and incoherent high-energy excitations on the same footing. This is crucial for calculating thermodynamic properties or when considering systems having no characteristic low-energy scale. The limit of large lattice coordination is also a natural playground where one can test the different numerical techniques used in the treatment of the many-body problem in finite dimensions, without dealing with the additional complications of lattices of finite size (the thermodynamic limit is built in from the beginning in this approach).

The general organization of this article is as follows (see the Table of Contents). Section II gives a general overview of the method (without any formal justification), and introduces the reader to the dynamical mean-field equations, to the mapping onto a self-consistent impurity model, and to the connection with the limit of infinite dimensions. Sections III to V set up the theoretical framework: various useful derivations are presented in Sec. III, the calculation of response functions is considered in Sec. IV, and the extension of the formalism to phases with long-range order is described in Sec. V. Section VI reviews the various techniques available to solve the self-consistent impurity problem, including a detailed discussion and comparison of various numerical methods. This section has a deliberately technical character: the goal here is to provide sufficient information so that the reader can use these methods independently. To this aim, FORTRAN programs are provided with this article (accessible via the internet, see Appendix D).

The numerous possible applications of the dynamical mean-field approach to physical systems are only beginning to be explored, and the field is currently very active. We have chosen to discuss in detail only one of these applications. This is the purpose of Sec. VII, which reviews the recent progress made on the Hubbard model and the Mott metal-insulator transition. The LISA method has solved many open questions related to this phenomenon, which had proven intractable by previous techniques. Recently, concrete applications to the physics of transition-metal oxides have also appeared. Comparison to some experiments can be found in this section. In Sec. VIII, several other strongly correlated models are considered and a much less exhaustive approach is adopted. In each case, the associated impurity model and the self-consistency equations are given in order to illustrate the wide scope of the method, and a short summary of recent results obtained for these models is made. The purpose of this section is simply to provide a guide to the literature and to stimulate further work.

The dynamical mean-field method discussed in this paper can be applied as an approximation scheme directly to three-dimensional lattice problems (this is also true of the usual mean-field theory of classical spin systems). We have provided several derivations of the mean-field equations which, besides showing that they become exact in infinite dimensions, are aimed to give them an intuitive content. This approach is advocated throughout this article, and particularly in Sec. VIII.C. For this reason, this article is restricted to those aspects of the $d=\infty$ limit that are closely related to the idea of a dynamical mean-field approach and omitted (or briefly mentioned) other applications of this limit, such as the studies of variational wave functions in the $d\rightarrow\infty$ limit. Excellent expositions of these omitted topics already exist, and we refer the reader to the review articles of Vollhardt (1991, 1993, 1994). Earlier reviews of some of the topics treated in the present paper can be found in Kotliar (1993b), Freericks and Jarrell (1994b), and Pruschke, Jarrell, and Freericks (1995).

Finally, Sec. IX stresses the limitations of the mean-field approach in its present form and explores possible extensions of the formalism to systems where the dynamical effects of intersite interactions, the influence of long-wavelength collective modes, or certain forms of short-range order are important. This is currently one of the main theoretical challenges in the field, and the main role of Sec. IX is to outline what we perceive to be fruitful directions for further research.

II. THE LOCAL IMPURITY SELF-CONSISTENT APPROXIMATION: AN OVERVIEW

This section is devoted to a survey of the LISA method. We shall first describe the dynamical mean-field equations but, for the sake of clarity, will postpone detailed derivations to Sec. III. In order to stress the analogy with the familiar Weiss mean-field theory of classical statistical mechanics, we shall review in parallel the classical case and its quantum generalization. The connection with quantum impurity models will be explained in Sec. II.B. In Sec. II.C, the limit of infinite spatial dimensions of lattice fermion models will be presented. The dynamical mean-field equations become exact in this limit.

A. Dynamical mean-field equations

The goal of a mean-field theory is to approximate a lattice problem with many degrees of freedom by a *single-site effective problem* with less degrees of freedom. The underlying physical idea is that the dynamics at a given site can be thought of as the interaction of the degrees of freedom at this site with an external bath created by all other degrees of freedom on other sites.

The simplest illustration of this idea is the Ising model with ferromagnetic couplings $J_{ij}>0$ between nearest-neighbor sites of a lattice with coordination z:

$$H=-\sum_{\langle ij\rangle} J_{ij}S_iS_j-h\sum_i S_i\,. \tag{1}$$

The Weiss mean-field theory views each given site (say, o) as governed by an effective Hamiltonian:

$$H_{\rm eff}=-h_{\rm eff}S_o\,. \tag{2}$$

All interactions with the other degrees of freedom are lumped into the effective field $h_{\rm eff}$:

$$h_{\rm eff}=h+\sum_i J_{oi}m_i=h+zJm, \tag{3}$$

where $m_i=\langle S_i\rangle$ is the magnetization at site i, and translation invariance has been assumed ($J_{ij}=J$ for nearest-neighbor sites, $m_i=m$). Hence $h_{\rm eff}$ has been related to a local quantity which can in turn be computed from the single-site effective model $H_{\rm eff}$. For the simple case at hand, this reads $m=\tanh(\beta h_{\rm eff})$, which can be combined with (3) to yield the well-known mean-field equation for the magnetization:

$$m=\tanh(\beta h+z\beta Jm). \tag{4}$$

These mean-field equations are, in general, an approximation of the true solution of the Ising model. They become *exact* however in the limit where the *coordination of the lattice becomes large*. It is quite intuitive indeed that the neighbors of a given site can be treated globally as an external bath when their number becomes large, and that the spatial fluctuations of the local field become negligible. As is clear from Eq. (3), the coupling J must be scaled as $J=J^*/z$ to yield a sensible limit $z\rightarrow\infty$ (this scaling is such that both the entropy and internal energy per site remain finite, so as to maintain a finite T_c).

These ideas can be directly extended to quantum many-body systems. This will be illustrated here on the example of the Hubbard model:

$$H=-\sum_{\langle ij\rangle,\sigma} t_{ij}(c_{i\sigma}^{+}c_{j\sigma}+c_{j\sigma}^{+}c_{i\sigma})+U\sum_i n_{i\uparrow}n_{i\downarrow}\,. \tag{5}$$

It will be assumed in this section, for simplicity, that no symmetry breaking occurs, i.e., that one deals with the translation-invariant paramagnetic phase. Phases with long-range order will be dealt with in Sec. V.

Again, the mean-field description associates with this Hamiltonian a single-site effective dynamics, which is conveniently described in terms of an imaginary-time action for the fermionic degrees of freedom $(c_{o\sigma}, c^{+}_{o\sigma})$ at that site:

$$S_{\rm eff} = -\int_0^\beta d\tau \int_0^\beta d\tau' \sum_\sigma c^{+}_{o\sigma}(\tau)\mathcal{G}_0^{-1}(\tau-\tau')c_{o\sigma}(\tau') + U\int_0^\beta d\tau\, n_{o\uparrow}(\tau)n_{o\downarrow}(\tau). \quad (6)$$

$\mathcal{G}_0(\tau-\tau')$ plays the role of the Weiss effective field above. Its physical content is that of an effective amplitude for a fermion to be created on the isolated site at time τ (coming from the "external bath") and being destroyed at time τ' (going back to the bath). The main difference with the classical case is that this generalized "Weiss function" is a *function of time* instead of a single number. This, of course, is required to take into account *local quantum fluctuations*. Indeed, the mean-field theory presented here freezes spatial fluctuations but takes full account of local temporal fluctuations (hence the name "dynamical"). $\mathcal{G}_0$ plays the role of a bare Green's function for the local effective action $S_{\rm eff}$, but it should not be confused with the noninteracting local Green's function of the original lattice model.

A closed set of mean-field equations is obtained by supplementing Eq. (6) with the expression relating $\mathcal{G}_0$ to local quantities computable from $S_{\rm eff}$ itself, in complete analogy with Eq. (3) above. As will be shown below, this self-consistency condition reads

$$\mathcal{G}_0(i\omega_n)^{-1} = i\omega_n + \mu + G(i\omega_n)^{-1} - R[G(i\omega_n)]. \quad (7)$$

In this expression, $G(i\omega_n)$ denotes the on-site interacting Green's function calculated from the effective action $S_{\rm eff}$:

$$G(\tau-\tau') \equiv -\langle Tc(\tau)c^{+}(\tau')\rangle_{S_{\rm eff}}, \quad (8)$$

$$G(i\omega_n) = \int_0^\beta d\tau\, G(\tau)e^{i\omega_n\tau}, \quad \omega_n \equiv \frac{(2n+1)\pi}{\beta} \quad (9)$$

and $R(G)$ is the reciprocal function of the Hilbert transform of the density of states corresponding to the lattice at hand. Explicitly, given the noninteracting density of states $D(\epsilon)$,

$$D(\epsilon) = \sum_{\mathbf{k}} \delta(\epsilon-\epsilon_{\mathbf{k}}), \quad \epsilon_{\mathbf{k}} \equiv \sum_{ij} t_{ij}e^{i\mathbf{k}\cdot(\mathbf{R}_i-\mathbf{R}_j)}, \quad (10)$$

the Hilbert transform $\tilde{D}(\zeta)$ and its reciprocal function R are defined by

$$\tilde{D}(\zeta) \equiv \int_{-\infty}^{+\infty} d\epsilon\, \frac{D(\epsilon)}{\zeta-\epsilon}, \quad R[\tilde{D}(\zeta)] = \zeta. \quad (11)$$

Since G can in principle be computed as a functional of $\mathcal{G}_0$ using the impurity action $S_{\rm eff}$, Eqs. (6)–(8) form a closed system of functional equations for the on-site Green's function G and the Weiss function $\mathcal{G}_0$. These are the basic equations of the LISA method. In practice, the main difficulty lies in the solution of $S_{\rm eff}$. These equations can hardly be attributed to a single author, as detailed in the Introduction. They appeared first in an early work of Kuramoto and Watanabe (1987) for the periodic Anderson model. Following the paper of Metzner and Vollhardt (1989) that emphasized the interest of the $d\to\infty$ limit, these equations were obtained by several authors. Brandt and Mielsch (1989) derived and solved them for the Falicov-Kimball model; the case of the Hubbard model was considered by Janiš (1991), Ohkawa (1991a, 1991b), Georges and Kotliar (1992), and Jarrell (1992). The presentation followed here is closest to those of Georges and Kotliar (1992) and Georges, Kotliar, and Si (1992).

It is instructive to check these equations in two simple limits:

(i) In the *noninteracting limit* $U=0$, solving (6) yields $G(i\omega_n)=\mathcal{G}_0(i\omega_n)$ and hence, from (7), $G(i\omega_n) = \tilde{D}(i\omega_n+\mu)$ reduces to the free on-site Green's function.

(ii) In the *atomic limit* $t_{ij}=0$, one only has a collection of disconnected sites and $D(\epsilon)$ becomes a δ function, with $\tilde{D}(\zeta)=1/\zeta$. Then (7) implies $\mathcal{G}_0(i\omega_n)^{-1} = i\omega_n+\mu$ and the effective action $S_{\rm eff}$ becomes essentially local in time and describes a four-state Hamiltonian yielding $G(i\omega_n)_{\rm at} = (1-n/2)/(i\omega_n+\mu) + n/2(i\omega_n+\mu-U)$, with $n/2 = (e^{\beta\mu}+e^{\beta(2\mu-U)})/(1+2e^{\beta\mu}+e^{\beta(2\mu-U)})$.

Solving the coupled equations above not only yields *local quantities* but also allows us to reconstruct all the **k**-dependent correlation functions of the original lattice Hubbard model. For example, the Fourier transform of the one particle Green's function $G_{ij}(\tau-\tau') \equiv -\langle Tc_{i,\sigma}(\tau)c^{+}_{j,\sigma}(\tau')\rangle$ can be shown to read

$$G(\mathbf{k},i\omega_n) = \frac{1}{i\omega_n+\mu-\epsilon_{\mathbf{k}}-\Sigma(i\omega_n)}, \quad (12)$$

where the self-energy can be computed from the solution of the effective on-site problem as

$$\Sigma(i\omega_n) = \mathcal{G}_0^{-1}(i\omega_n) - G^{-1}(i\omega_n). \quad (13)$$

It is therefore **k**-independent in this approach i.e., purely local in space: $\Sigma_{ij}(i\omega_n)=\delta_{ij}\Sigma(i\omega_n)$ (Metzner and Vollhardt, 1989, Müller-Hartmann, 1989a, 1989b, 1989c). From this expression one sees that the "self-consistency condition," Eq. (7), relating G and $\mathcal{G}_0$, ensures that the on-site (local) component of the Green's function, given by $G_{ii}(i\omega_n)=\Sigma_{\mathbf{k}}G(\mathbf{k},i\omega_n)$, coincides with the Green's function $G(i\omega_n)$ calculated from the effective action $S_{\rm eff}$. Indeed, summing Eq. (12) over **k** yields $\tilde{D}(i\omega_n+\mu-\Sigma(i\omega_n))$. Identifying this expression with $G(i\omega_n)$ and using Eq. (13) leads to Eq. (7).

Thermodynamic quantities for the Hubbard model can all be simply related to their single-site model counterparts: the relevant expressions for the free energy and internal energy are given by Eqs. (46) and (47) in Sec. III.B. Two-particle Green's functions, dynamical response functions, and transport properties for the lattice

model can also be related to vertex functions of the on-site action $S_{\rm eff}$; this will be reviewed in Sec. IV.

B. Physical content and connection with impurity models

The structure of the dynamical mean-field theory is that of a functional equation for the local Green's function $G(i\omega_n)$ and the "Weiss function" $\mathcal{G}_0(i\omega_n)$. In contrast to mean-field theory for classical systems, the on-site effective action $S_{\rm eff}$ remains a many-body problem. This is because the present approach freezes *spatial fluctuations* but fully retains local quantum fluctuations. As a function of imaginary time, each site undergoes transitions between the four possible quantum states $|0\rangle$, $|\uparrow\rangle$, $|\downarrow\rangle$, $|\uparrow,\downarrow\rangle$ by exchanging electrons with the rest of the lattice described as an external bath. The dynamics of these processes is encoded in the Weiss function $\mathcal{G}_0(\tau-\tau')$.

For these reasons, no Hamiltonian form involving *only* the on-site degrees of freedom $(c_{o\sigma},c^+_{o\sigma})$ can be found for the effective on-site model: once the bath has been eliminated, $S_{\rm eff}$ necessarily includes retardation effects. In order to gain physical intuition and to make some practical calculations with $S_{\rm eff}$, it is useful to have such a Hamiltonian formulation. This is possible upon reintroducing auxiliary degrees of freedom describing the "bath." For example, one can view $(c_{o\sigma},c^+_{o\sigma})$ as an "impurity orbital" and the bath as a "conduction band" described by operators $(a_{l\sigma},a^+_{l\sigma})$ and consider the Hamiltonian

$$H_{\rm AM}=\sum_{l\sigma}\tilde{\epsilon}_l a^+_{l\sigma}a_{l\sigma}+\sum_{l\sigma}V_l(a^+_{l\sigma}c_{o\sigma}+c^+_{o\sigma}a_{l\sigma})$$
$$-\mu\sum_{\sigma}c^+_{o\sigma}c_{o\sigma}+Un_{o\uparrow}n_{o\downarrow}, \tag{14}$$

where the subscript AM denotes the Anderson model. This Hamiltonian is quadratic in $a^+_{l\sigma},a_{l\sigma}$; integrating these out gives rise to an action of the form (6), with

$$\mathcal{G}_0^{-1}(i\omega_n)^{\rm AM}=i\omega_n+\mu-\int_{-\infty}^{+\infty}d\omega\,\frac{\Delta(\omega)}{i\omega_n-\omega},$$
$$\Delta(\omega)\equiv\sum_{l\sigma}V_l^2\,\delta(\omega-\tilde{\epsilon}_l). \tag{15}$$

Hence Eq. (14) can be viewed as a Hamiltonian representation of $S_{\rm eff}$ provided $\Delta(\omega)$ (i.e., the parameters $V_l,\tilde{\epsilon}_l$) is chosen such as to reproduce the actual solution $\mathcal{G}_0$ of the mean-field equations. The spectral representation Eq. (15) is general enough to permit this in all cases. Note that the $\tilde{\epsilon}_l$'s are *effective* parameters that should not be confused with the single-particle energies $\epsilon_{\mathbf{k}}$ of the original lattice model. The Hamiltonian (14) is the familiar Anderson model of a magnetic impurity coupled to a conduction bath (Anderson, 1961). Note however that the shape of the conduction bath density of states $\Delta(\omega)$ is *not* known *a priori* in the present context but must be found by solving the self-consistent problem. The isolated site o plays the role of the impurity orbital, and the conduction bath is built out of all other sites.

There is of course a degree of arbitrariness in the Hamiltonian representation of the local action $S_{\rm eff}$. Instead of viewing it as an Anderson model, we can consider the Wolff model (Wolff, 1961), in which the interaction term acts only at a single-site of a conduction-electron lattice representing the bath

$$H_{\rm WM}=\sum_{l\sigma}\tilde{\epsilon}_l a^+_{l\sigma}a_{l\sigma}+Un_{o\uparrow}n_{o\downarrow}. \tag{16}$$

If we adopt this point of view the Weiss function is given by

$$\mathcal{G}_0^{\rm WM}=\int_{-\infty}^{+\infty}d\omega\,\frac{\Delta(\omega)}{i\omega_n-\omega},\quad \Delta(\omega)\equiv\sum_l\delta(\omega-\tilde{\epsilon}_l), \tag{17}$$

and it merely corresponds to a different spectral representation of $\mathcal{G}_0$.

Hence, the LISA approach to the Hubbard model maps the lattice problem onto that of an Anderson impurity embedded in a self-consistent medium (Ohkawa 1991a, 1991b; Georges and Kotliar, 1992; Georges, Kotliar, and Si, 1992; Jarrell, 1992). The solution of the mean-field equations involves the determination of $\mathcal{G}_0$ such that, when inserted into the Anderson model, the resulting impurity Green's function obeys the self-consistency condition (7).

The reduction of a lattice problem to a single-site problem with *effective* parameters is a common feature to both the classical and quantum mean-field constructions. The two constructions parallel each other quite precisely, as summarized in the "dictionary" displayed in Table I. The main difference is that the Weiss field is a number in the classical case, and a function in the quantum case. Physically, this reflects the existence of *many* energy scales in strongly correlated fermion models. (We note in passing that this also occurs in the mean-field theory of some classical problems with many energy scales, such as spin glasses.) This points to the limitations of other "mean-field" approaches, such as the Hartree-Fock approximation or slave bosons methods, where one attempts to parametrize the whole mean-field function by a single *number* (or a few of them). This in effect amounts to freezing local quantum fluctuations by replacing the problem with a purely classical one, and can only be reasonable when a single low-energy scale is important. This is the case, for instance, for a Fermi-liquid phase. However, even in such cases, parametrizing the Weiss field by a single number can only be satisfactory at low energy, and misses the high-energy incoherent features associated with the other energy scales in the problem. When no characteristic low-energy scale is present, a single number parametrization fails completely: this is the case, for example, when correlation functions have power-law decays as a function of frequency (as in x-ray edge problems). This occurs, e.g., in the Falicov-Kimball model (Sec. VIII.B).

TABLE I. Correspondence between the mean-field theory of a classical system and the (dynamical) mean-field theory of a quantum system.

Quantum case	Classical case	
$-\Sigma_{\langle ij\rangle\sigma} t_{ij} c^+_{i\sigma} c_{j\sigma} + U\Sigma_i n_{i\uparrow} n_{i\downarrow}$	$H = -\Sigma_{\langle ij\rangle} J_{ij} S_i S_j - h\Sigma_i S_i$	Hamiltonian
$t_{ij} \sim (1/\sqrt{d})^{\lvert i-j\rvert}$	$J_{ij} \sim (1/d)^{\lvert i-j\rvert}$ (ferromagnet)	Scaling
$G_{ij}(i\omega_n) = -\langle c^+_i(i\omega_n) c_j(i\omega_n)\rangle$	$\langle S_i S_j\rangle$	Correlation function
$G_{ii}(i\omega_n) = -\langle c^+_i(i\omega_n) c_i(i\omega_n)\rangle$	$m_i = \langle S_i\rangle$	Local observable
$-\int\int c^+_\sigma(\tau)\mathcal{G}_0^{-1}(\tau-\tau')c_\sigma(\tau') + \int U n_\uparrow n_\downarrow$	$H_{\rm eff} = -h_{\rm eff} S_0$	Single-site Hamiltonian
$H_{\rm eff} = \Sigma_{l\sigma}\tilde{\epsilon}_l a^+_{l\sigma} a_{l\sigma} + \Sigma_{l\sigma} V_l (a^+_{l\sigma} c_\sigma + \text{H.c.}) - \mu\Sigma_\sigma c^+_\sigma c_\sigma + U n_\uparrow n_\downarrow$		
$\mathcal{G}_0(i\omega_n)$	$h_{\rm eff}$	Weiss field/function
$\mathcal{G}_0^{-1}(i\omega_n) = \omega_n + \mu + G(i\omega_n)^{-1} - R[G(i\omega_n)]$	$h_{\rm eff} = z$ J m+h	Relation between Weiss field and local observable

Finally, besides its intuitive appeal, the mapping onto impurity models has proven to be useful for practical calculations. These models have been studied intensively in the last 30 years by a variety of analytical and numerical techniques, and this knowledge can be put to good use in order to understand strongly correlated lattice models in large dimensions. The crucial step is to use *reliable* tools to solve $S_{\rm eff}$. Recent progress in the field came from an effort in exploiting the connection with impurity models in a qualitative and quantitative manner.

C. The limit of infinite dimensions

The above mean-field equations become exact in the limit of infinite coordination on various lattices. In this section, we discuss several such examples and in each case we give the relation (7) between the local Green's function and the Weiss function $\mathcal{G}_0$ in explicit form. Notice that, in the paramagnetic phase, the lattice enters the mean-field equations only through the noninteracting density of states $D(\epsilon)$. Since many different lattices give rise to the same density of states in the limit of large coordination, one can construct models with the same single-particle properties (i.e., the same Green's function) in the paramagnetic phases but very different properties regarding magnetic responses and transitions to phases with long-range order (Müller-Hartmann, 1989a). We refer to Sec. IV and Appendix A for a more detailed explanation of this point, and to Sec. VII.D for explicit examples.

The first case to be discussed is the d-dimensional cubic lattice with nearest-neighbor hopping (with coordination $z=2d$). In order that the kinetic and interaction energies remain of the same order of magnitude in the $d\to\infty$ limit, the hopping amplitude must be scaled appropriately (Metzner and Vollhardt, 1989). The correct scaling is easily found from the Fourier transform $\epsilon_{\mathbf{k}}$ of t_{ij}, which for a generic vector $\mathbf{k}$ involves $\Sigma_{n=1}^{d}\cos(k_n)$, a sum of d numbers with essentially random signs. Hence t_{ij} must be scaled as

$$t_{ij} = \frac{t}{\sqrt{2d}}. \tag{18}$$

More precisely, this ensures that the density of states has a well-defined $d\to\infty$ limiting form, which reads (from the central-limit theorem)

$$D(\epsilon) = \frac{1}{t\sqrt{2\pi}} \exp\left(-\frac{\epsilon^2}{2t^2}\right). \tag{19}$$

This expression, and various useful properties of tight-binding electrons on a $d\to\infty$ cubic lattice, is derived in Appendix A. The Hilbert transform of (19) reads (for $t=1/\sqrt{2}$):

$$\tilde{D}(\zeta) = -is\sqrt{\pi}\,\exp(-\zeta^2)\,\text{erfc}(-is\zeta), \tag{20}$$

where $s=\text{sgn}[\text{Im}(\zeta)]$ and erfc denotes the complementary complex error function. There is no simple explicit form for the reciprocal function $R(G)$ in this case and hence (7) must be used as an implicit relation between $\mathcal{G}_0$ and G. The Gaussian density of states (19) is also obtained for the $d\to\infty$ cubic lattice with longer-range hopping along the *coordinate axis*. As discussed by Müller-Hartmann (1989a) and reviewed in Appendix A, next-nearest-neighbor hopping along the *diagonals* does change the density of states and provides an interesting $d=\infty$ model in which magnetic order is frustrated.

A second important example is the Bethe lattice (Cayley tree) with coordination $z\to\infty$ and nearest-neighbor hopping $t_{ij}=t/\sqrt{z}$. A semicircular density of states is obtained in this case (see, e.g., Economou, 1983):

$$D(\epsilon) = \frac{1}{2\pi t^2}\sqrt{4t^2-\epsilon^2}, \quad |\epsilon| < 2t. \tag{21}$$

The Hilbert transform and its reciprocal function take very simple forms

$$\tilde{D}(\zeta) = (\zeta - s\sqrt{\zeta^2-4t^2})/2t^2, \quad R(G) = t^2 G + 1/G \tag{22}$$

so that the self-consistency relation between the Weiss function and the local Green's function takes in this case the explicit form

$$\mathcal{G}_0^{-1}(i\omega_n)=i\omega_n+\mu-t^2G(i\omega_n). \tag{23}$$

The same density of states is also realized for a random Hubbard model on a fully connected lattice (all N sites pairwise connected) where the hoppings are independent random variables with variance $\overline{t_{ij}^2}=t^2/N$ (see Sec. VII).

Finally, the Lorentzian density of states

$$D(\epsilon)=\frac{t}{\pi(\epsilon^2+t^2)} \tag{24}$$

can be realized with a t_{ij} matrix involving long-range hopping (Georges, Kotliar, and Si, 1992). One possibility is to take $\epsilon_{\mathbf{k}}=t/d\Sigma_{i=1}^{d}\tan(k_i)\mathrm{sgn}(k_i)$ for the Fourier transform of t_{ij} on a d-dimensional lattice, with either $d=1$ or $d=\infty$. Because of the power-law tails of the density of states, this model needs a regularization to be properly defined. If one introduces a cutoff in the tails, which is like the bottom of a Fermi sea, then a $1/d$ expansion becomes well defined. Some quantities like the total energy are infinite if one removes the cutoff. Other low-energy quantities, like the difference between the energy at finite temperatures and at zero temperature, the specific heat, and the magnetic susceptibility have a finite limit when the cutoff is removed. The Hilbert transform of (24) reads $\tilde{D}(\zeta)=1/\{\zeta+it\ \mathrm{sgn}[\mathrm{Im}(\zeta)]\}$. Using this in (7), one sees that a drastic simplification arises in this model: the Weiss function no longer depends on G, and reads explicitly

$$\mathcal{G}_0(i\omega_n)^{-1}=i\omega_n+\mu+it\ \mathrm{sgn}\omega_n. \tag{25}$$

Hence the mean-field equations are no longer coupled, and the problem reduces to solving S_{eff} with (25). It turns out that (25) is precisely the form for which S_{eff} becomes solvable by Bethe ansatz, and thus many properties of this $d\to\infty$ lattice model with long-range hopping and a Lorentzian density of states can be solved for analytically (Georges, Kotliar, and Si, 1992). Some of its physical properties are nongeneric however (such as the absence of a Mott transition).

Other lattices can be considered, such as the $d=\infty$ generalization of the two-dimensional honeycomb and three-dimensional diamond lattices considered by Santoro *et al.* (1993), and are briefly reviewed in Appendix A. This lattice is bipartite but has no perfect nesting.

III. DERIVATIONS OF THE DYNAMICAL MEAN-FIELD EQUATIONS

In this section, we provide several derivations of the mean-field equations introduced above. In most instances, the simplest way to guess the correct equations for a given model with on-site interactions is to postulate that the self-energy can be computed from a single-site effective action involving (i) the original interactions and (ii) an arbitrary retarded quadratic term. The self-consistency equation is then obtained by writing that the interacting Green's function of this single-site action coincides with the site-diagonal Green's function of the lattice model, with identical self-energies. The derivations presented below prove the validity of this construction in the limit of large dimensions.

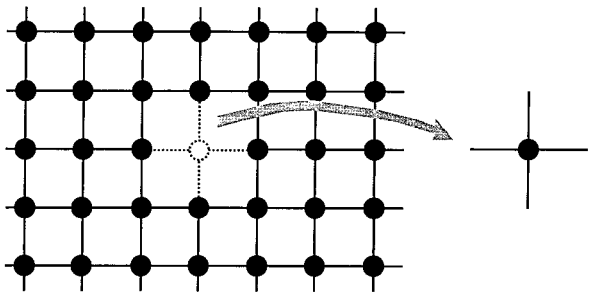

FIG. 1. Cavity created in the full lattice by removing a single site and its adjacent bonds.

A. The cavity method

The first derivation that we shall present is borrowed from classical statistical mechanics, where it is known under the name of "cavity method." It is not the first one that has historically been used in the present context, but it is both simply and easily generalized to several models. The underlying idea is to focus on a given site of the lattice, say $i=0$, and to explicitly integrate out the degrees of freedom on all other lattice sites in order to define an effective dynamics for the selected site.

Let us first illustrate this on the Ising model. The effective Hamiltonian H_{eff} for site o is defined from the partial trace over all other spins:

$$\sum_{S_i,i\neq o} e^{-\beta H}\equiv e^{-\beta H_{\mathrm{eff}}[S_o]}. \tag{26}$$

The Hamiltonian H in Eq. (1) can be split into three terms: $H=-h_oS_o-\Sigma_iJ_{io}S_oS_i+H^{(o)}$. $H^{(o)}$ is the Ising Hamiltonian for the lattice in which site o has been removed together with all the bonds connecting o to other sites, i.e., a "cavity" surrounding o has been created (Fig. 1). The first term acts at site o only, while the second term connects o to other sites. In this term, $J_{io}S_o\equiv\eta_i$ plays the role of a field acting on site i. Hence summing over the S_i's produces the generating functional of the connected correlation functions of the cavity Hamiltonian $H^{(o)}$ and a formal expression for H_{eff} can be obtained as

$$H_{\mathrm{eff}}=\mathrm{const}+\sum_{n=1}^{\infty}\sum_{i_1\cdots i_n}\frac{1}{n!}\,\eta_{i_1}\cdots\eta_{i_n}\langle S_{i_1}\cdots S_{i_n}\rangle_c^{(o)} \tag{27}$$

For a ferromagnetic system, with $J_{ij}>0$ scaled as $1/d^{|i-j|}$ ($|i-j|$ is the Manhattan distance between i and j), only the first ($n=1$) term survives in this expression in the $d\to\infty$ limit. Hence H_{eff} reduces to $H_{\mathrm{eff}}=-h_{\mathrm{eff}}S_o$, where the effective field reads

$$h_{\mathrm{eff}}=h+\sum_i J_{oi}\langle S_i\rangle^{(o)}. \tag{28}$$

$\langle S_i\rangle^{(o)}$ is the magnetization at site i once site o has been removed. The limit of large coordination brings in a fur-

ther simplification to this expression: because each site has of the order of d neighbors, removing a single site produces an effect of order $1/d$ in local quantities, which can be neglected. Hence the magnetization $\langle S_i\rangle^{(o)}$ calculated for the cavity Hamiltonian equals the magnetization $\langle S_i\rangle$ for the full Hamiltonian. Furthermore, translation invariance implies $\langle S_i\rangle=\langle S_o\rangle\equiv m$, so that $h_{\rm eff}=h+zJm$. On the other hand, the single-site effective Hamiltonian $H_{\rm eff}$ is easily solved to yield $m=\tanh\beta h_{\rm eff}$. Hence, a closed set of mean-field equations is found.

Let us mention that the relation between the magnetizations with and without the cavity is more involved for Ising models with nonuniform signs of J_{ij}. For spin-glass models with $J_{ij}=+1,-1$ at random, one is forced to scale the couplings as $1/\sqrt{d}$ so that a correction term must be retained in the difference $\langle S_i\rangle-\langle S_i\rangle^{(o)}$ (Thouless, Anderson, and Palmer, 1977; see also Mezard, Parisi, and Virasoro, 1987). This correction term, first discovered by Onsager (1936) in his studies on dielectrics, accounts for local-field effects created by the removal of one site ("reaction terms").

This derivation extends in a straightforward manner to quantum many-body models. It is convenient to write the partition function of the Hubbard model (5) as a functional integral over Grassmann variables:

$$Z=\int\prod_i Dc_{i\sigma}^{+}Dc_{i\sigma}e^{-S}, \tag{29}$$

$$S=\int_o^\beta d\tau\Bigg(\sum_{i\sigma}c_{i\sigma}^{+}\partial_\tau c_{i\sigma}-\sum_{ij,\sigma}t_{ij}c_{i\sigma}^{+}c_{j\sigma}-\mu\sum_{i\sigma}c_{i\sigma}^{+}c_{i\sigma}+U\sum_i n_{i\uparrow}n_{i\downarrow}\Bigg). \tag{30}$$

We follow closely the Ising analogy: all fermions are traced out except for site o in order to obtain an effective action:

$$\frac{1}{Z_{\rm eff}}e^{-S_{\rm eff}[c_{o\sigma}^{+},c_{o\sigma}]}\equiv\frac{1}{Z}\int\prod_{i\neq o,\sigma}Dc_{i\sigma}^{+}Dc_{i\sigma}e^{-S}. \tag{31}$$

Note that the knowledge of $S_{\rm eff}$ allows us to calculate *all the local* correlation functions of the original Hubbard model, since we can couple sources to degrees of freedom at site o. This observation is valid in any number of dimensions. In order to obtain a formal expression for $S_{\rm eff}$, the original action is again split into three parts: $S=S^{(o)}+S_o+\Delta S$, where $S^{(o)}$ is the lattice action in the presence of the "cavity," and

$$S_o=\int_0^\beta d\tau\Bigg(\sum_\sigma c_{o\sigma}^{+}(\partial_\tau-\mu)c_{o\sigma}+Un_{o\uparrow}n_{o\downarrow}\Bigg), \tag{32}$$

$$\Delta S=-\int_0^\beta d\tau\sum_{i\sigma}t_{io}(c_{i\sigma}^{+}c_{o\sigma}+c_{o\sigma}^{+}c_{i\sigma}). \tag{33}$$

Again, $\eta_i\equiv t_{io}c_{o\sigma}$ plays the role of a source coupled to $c_{i\sigma}^{+}$, and the integration over fermions for $i\neq o$ brings in the generating functional of the connected Green's functions $G^{(o)}$ of the cavity Hamiltonian:

$$S_{\rm eff}=\sum_{n=1}^{\infty}\sum_{i_1\cdots j_n}\int\eta_{i_1}^{+}(\tau_{i_1})\cdots\eta_{i_n}^{+}(\tau_{i_n})\eta_{j_1}(\tau_{j_1})\times\cdots\eta_{j_n}(\tau_{j_n})G^{(o)}_{i_1\cdots j_n}(\tau_{i_1}\cdots\tau_{i_n},\tau_{j_1}\cdots\tau_{j_n})+S_o+\text{const.} \tag{34}$$

As before, the large d limit (with a scaling $1/\sqrt{d}^{|i-j|}$ of the hopping t_{ij}) brings in a crucial simplification: the nth order term is of order $(1/d)^{n-2}$ so that only $n=2$ survives the $d\to\infty$ limit. This is easily seen by considering the first few terms. The scaling of t_{ij} ensures that $G_{ij}^{(o)}\sim(1/\sqrt{d})^{|i-j|}$ and so the first term is of order 1. The second-order term involves a connected four-point function $G_{ijkl}^{(o)}$ which falls off as $(1/\sqrt{d})^{|i-j|}(1/\sqrt{d})^{|i-k|}(1/\sqrt{d})^{|i-l|}$. When i,j,k,l are all different, there are four sums which give d^4 and four factors of t giving $1/d^2$. The net result is, since $|i-j|$, $|i-l|$, and $|i-k|$ are at least 2, of order $1/d$. Similarly, the terms where $i=j$ (distinct from k and l with $k\neq l$) contain three sums, which give d^3, four factors of t giving $1/d^2$, and a factor $1/d^2$ from $G^{(o)}$ since $|i-l|$ and $|k-i|$ are at least two. The result is again of order $1/d$. The effective action therefore reduces to Eq. (6) as $d\to\infty$, with

$$\mathcal{G}_0^{-1}(i\omega_n)=i\omega_n+\mu-\sum_{ij}t_{oi}t_{oj}G_{ij}^{(o)}(i\omega_n). \tag{35}$$

Expression (35) is important because it relates the Weiss function $\mathcal{G}_0$ to the Green's function $G_{ij}^{(o)}$ of a Hubbard model *with one site removed*. In order to obtain a closed set of equations, one still needs to relate the latter to the Green's function of the original lattice. Again, the $d\to\infty$ limit makes this possible here, but this relation takes, in general, a slightly more complicated form than for the classical Ising case discussed above. On the Bethe lattice, however, it remains very simple. In this case, the summation in (35) can be restricted to $i=j$ (since neighbors of o are completely disconnected on this lattice once the cavity has been introduced), and again, in the limit of infinite connectivity, removing one site does not change the Green's function so that $G_{ii}^{(o)}=G_{ii}$. Using translation invariance, one finally obtains Eq. (23) for the Weiss function on this lattice: $\mathcal{G}_0^{-1}=i\omega_n+\mu-t^2G(i\omega_n)$.

For a general lattice, the relation between the cavity and full Green's functions reads

$$G_{ij}^{(o)}=G_{ij}-\frac{G_{io}G_{oj}}{G_{oo}}. \tag{36}$$

This equation is most easily proven by using the expansion of Green's functions in the hopping matrix elements t_{kl}, which is described in Sec. III.C. First, we note that the additional paths contributing to G_{ij} and not to $G_{ij}^{(o)}$ are those which connect sites i and j through site o. Then, one observes that, in the $d=\infty$ limit, only those paths that go *once* through site o need to be considered. This is true provided we allow an arbitrary dressing of each site in a path by the irreducible cumulant M_1 defined in Sec. III.C. Because of this property, the contri-

bution of these additional paths is obviously proportional to $G_{io}G_{oj}$, but this quantity has to be divided by G_{oo} in order to count *only once* the contribution of paths leaving and returning to the intermediate site o. Interestingly, Eq. (36), which is essential to the whole formalism, already appears in early works of Hubbard himself: this is Eq. (36) of the so-called "Hubbard III" paper (Hubbard, 1964).

Inserting (36) into (35) we have to compute $\Sigma_{ij}t_{io}t_{jo}G_{ij}-(\Sigma_i t_{io}G_{io})^2/G_{oo}$. To proceed, let us use Fourier transforms and insert the form (12) of the lattice Green's function, assuming a local self-energy (this has to be justified independently by power counting in $1/d$). The above expression reads

$$\int_{-\infty}^{+\infty} d\epsilon D(\epsilon)\,\frac{\epsilon^2}{\zeta-\epsilon} - \left(\int_{-\infty}^{+\infty} d\epsilon D(\epsilon)\,\frac{\epsilon}{\zeta-\epsilon}\right)^2 \Bigg/ \int_{-\infty}^{+\infty} d\epsilon D(\epsilon)\,\frac{1}{\zeta-\epsilon}$$

with $\zeta \equiv i\omega_n+\mu-\Sigma(i\omega_n)$. This can be simplified further using the following relations:

$$\int_{-\infty}^{+\infty} \frac{D(\epsilon)\epsilon^2}{\zeta-\epsilon} = \zeta\int_{-\infty}^{+\infty} \frac{D(\epsilon)\epsilon}{\zeta-\epsilon},$$

$$\int_{-\infty}^{+\infty} \frac{D(\epsilon)}{\zeta-\epsilon}\,\epsilon = -1+\zeta\int_{-\infty}^{+\infty} \frac{D(\epsilon)}{\zeta-\epsilon}. \tag{37}$$

We have used $t_{oo}=\Sigma_{\mathbf{k}}t_{\mathbf{k}}=\int D(\epsilon)\epsilon=0$. Finally, inserting (36) into (35) yields

$$\mathcal{G}_0^{-1}=\Sigma+1/\tilde{D}(i\omega_n+\mu-\Sigma), \tag{38}$$

which coincides with (7) and (13).

B. Local nature of perturbation theory in infinite dimensions

From a historical perspective, the notion that in infinite dimensions the local Green's function obeys a closed set of functional equations was derived by various authors from considerations on perturbation theory in the interaction strength U.

Indeed, remarkable simplifications in the many-body diagrammatics occur in this limit, as first noticed by Metzner and Vollhardt (1989; see also Metzner, 1989; Müller-Hartmann, 1989a). Consider a given diagram (Fig. 2), in which the interaction term $Un_{i\uparrow}n_{i\downarrow}$ is depicted as a four-leg vertex at site i, and in which each line stands for a free-fermion propagator between two sites (it is easier to proceed in real space). The crucial observation is that whenever two internal vertices (i,j) can be connected by at least three paths, they must correspond to identical sites $i=j$. This property is of course only true for $d=\infty$, and can be shown by simple power counting. Since the hopping has been scaled by $1/\sqrt{d}$, each path made of fermion propagators connecting i to j will involve at least a factor $(1/\sqrt{d})^{|i-j|}$. On the other hand, i being held fixed, the eventual summation to be performed on the internal vertex j will bring in a factor

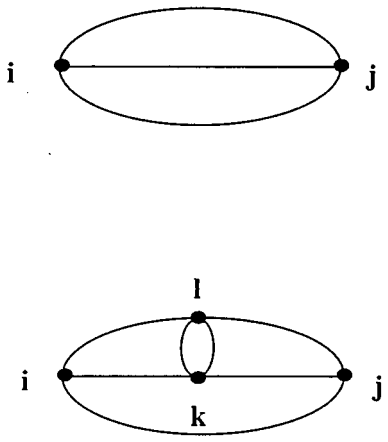

FIG. 2. Example of diagrams contributing to the self-energy at second and fourth order which can be "collapsed" to a single-site.

of order d^R. Indeed, this is the number of sites j located at a (Manhattan) distance $|i-j|\equiv R$ from i (R can be summed over afterwards). Hence, one obtains an overall factor of $d^R(1/\sqrt{d})^{R\mathscr{P}_{ij}}$ where $\mathscr{P}_{ij}$ is the number of (independent) paths joining i to j in the diagram. Thus, if $\mathscr{P}_{ij}>2$, only those contributions with $i=j$ ($R=0$) will survive the $d\to\infty$ limit. (Notice that this argument compares the contribution with $i=j$ to that with $i\neq j$, for a given value of the external vertices of the Green's function). Alternatively, in the perhaps more familiar momentum-space formulation of perturbation theory, this property means that whenever two vertices can be "collapsed" according to the rule above, the fermion propagators $G^{(0)}(\mathbf{k},i\omega_n)$ connecting them can be replaced by their local, $\mathbf{k}$-independent counterpart $\Sigma_k G^{(0)}(\mathbf{k},i\omega_n)$, ignoring momentum conservation at the vertices. Frequency conservation is retained however as $d\to\infty$. Figure 2 illustrates these considerations with two diagrams contributing to the self-energy at second and fourth orders.

This simplification of weak-coupling expansions is of course very useful in practice, since evaluating momentum sums is the main practical obstacle in going to high orders. In fact, discarding momentum conservation at some vertices has sometimes been used in perturbative calculations as a simplifying "local approximation" (see, e.g., Treglia, Ducastelle, and Spanjaard, 1980). The $d=\infty$ limit provides a framework in which this approximation can be justified. Various authors have exploited this simplification to perform weak-coupling studies of various models much beyond what is commonly feasible if one attempts to perform Brillouin-zone summations. Müller-Hartmann (1989b, 1989c) and Menge and Müller-Hartmann (1991) have studied self-consistent perturbation theory schemes for the Hubbard model. Similar schemes were applied to the periodic Anderson model by Schweitzer and Czycholl (1989, 1990a, 1991b). Schweitzer and Czycholl (1990b, 1991a) also used the $d=\infty$ simplifications in order to facilitate the weak-coupling studies of *finite-dimensional* models. The main idea is to

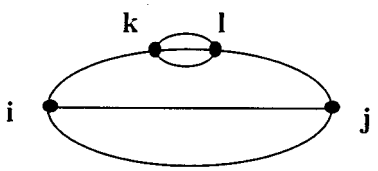

FIG. 3. Example of a diagram that cannot be "collapsed" to a single-site, because only two independent paths connect site i to site k (or j to l). Note that this is not a skeleton diagram, since it contains a correction to the ij propagator.

perform a summation over successive shells of neighbors in real space, rather than momentum summations.

Besides this practical use, these properties of perturbation theory in $d=\infty$ can also be used to formally derive the dynamical mean-field equations. Consider the real-space self-energy $\Sigma_{ij}(i\omega_n)$. It is clear that not all diagrams of a standard weak-coupling expansion for this quantity can be fully collapsed to a local form. An example of a diagram which cannot be collapsed is provided by Fig. 3. We can consider making, however, a "skeleton" expansion of Σ rather than a direct expansion: this amounts to grouping together all corrections to internal propagators, so that all lines of a skeleton diagram stand for the full *interacting* fermion propagator G_{ij}. The diagrams in Fig. 2 are skeleton diagrams, but the one in Fig. 3 is not. In this way, the self-energy can be viewed as a functional of the interacting Green's functions:

$$\Sigma_{ij}=\Sigma_{ij}^{\rm skel}[\{G_{kl}\}]. \tag{39}$$

It is easily seen that two internal vertices of a *skeleton* diagram can always be connected by more than two paths, so that all diagrams contributing to Σ in a skeleton perturbation expansion can be fully collapsed to a single-site. More generally, this is true of the Luttinger-Ward free-energy functional $\Phi[\{G_{ij}\}]$, which is the sum of all vacuum-to-vacuum skeleton graphs (Fig. 4). This functional is such that (see, e.g., Abrikosov *et al.*, 1965):

$$\Sigma_{ij}(i\omega_n)=\frac{\delta\Phi}{\delta G_{ij}(i\omega_n)}. \tag{40}$$

Hence, as $d\to\infty$, Φ and $\Sigma_{ij}^{\rm skel}$ depend *only* on the local (site-diagonal) Green's functions G_{ii}:

$$\Phi=\sum_i \phi[G_{ii}], \quad d\to\infty, \tag{41}$$

in which ϕ is a functional of the local Green's function at site i *only*. An obvious consequence is that the self-energy is site diagonal:

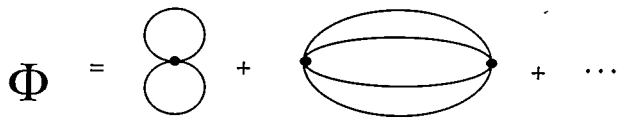

FIG. 4. First two contributions to the Luttinger-Ward functional.

$$\Sigma_{ij}(i\omega_n)=\delta_{ij}\Sigma(i\omega_n). \tag{42}$$

Furthermore, it must be possible to generate the functionals $\phi[G]$ and $\Sigma^{\rm skel}[G]$ from a purely local theory. A simple inspection of Feynman rules shows that the effective action $S_{\rm eff}$ in Eq. (6) precisely achieves this goal. From this point of view, the Weiss function $\mathcal{G}_0$ just plays the role of a dummy variable which never enters the final forms of ϕ, $\Sigma^{\rm skel}$. Once these functionals are known, the actual *value* of Σ is found by writing that the local lattice Green's function is given by $\Sigma_{\mathbf{k}}G(\mathbf{k},i\omega_n)$, namely:

$$G(i\omega_n)=\int_{-\infty}^{+\infty} d\epsilon\,\frac{D(\epsilon)}{i\omega_n-\epsilon-\Sigma^{\rm skel}[G(i\omega_n)]}. \tag{43}$$

This should be viewed as a functional equation for $G(i\omega_n)$, which is of course equivalent to the self-consistency condition (7). This point of view is formally useful to prove reduction to a single-site problem, but is not practical because of the difficulty in handling skeleton functionals. In fact, it has been so far impossible to obtain exact or even approximate expressions of $\Sigma^{\rm skel}$ for the Hubbard model, which would give reasonable results when inserted in (43), except for very small U. A remarkable case for which $\Sigma^{\rm skel}[G]$ can be obtained in closed form is the Falicov-Kimball model (Sec. VIII.B), which is exactly solvable as $d\to\infty$ (Brandt and Mielsch, 1989–1991). For most models, it is much more useful in practice to think of all quantities as *functionals* of $\mathcal{G}_0$ and to promote the latter to the rank of a fundamental quantity which has a clear physical interpretation as a "Weiss function" (Georges and Kotliar, 1992).

This formalism is also useful for establishing the relation between the lattice and the impurity model free-energies, Ω and $\Omega_{\rm imp}$ (Brandt and Mielsch, 1991). Indeed, Ω is related to the Luttinger-Ward functional Φ by (see, e.g., Abrikosov *et al.*, 1965):

$$\Omega=\Phi+T\sum_{n,\mathbf{k},\sigma}[\ln G_\sigma(\mathbf{k},i\omega_n)-\Sigma_\sigma(i\omega_n)G_\sigma(\mathbf{k},i\omega_n)], \tag{44}$$

while, for the impurity model (6),

$$\Omega_{\rm imp}=\phi[G]+T\sum_{n\sigma}[\ln G_\sigma(i\omega_n)-\Sigma_\sigma(i\omega_n)G_\sigma(i\omega_n)]. \tag{45}$$

Eliminating the functional Φ between these two equations [using Eq. (41)], and taking into account translation invariance, one obtains the following expression for the free-energy:

$$\frac{\Omega}{N}=\Omega_{\rm imp}-T\sum_{n\sigma}\left(\int_{-\infty}^{+\infty}d\epsilon\,D(\epsilon)\right.$$
$$\left.\times\ln[i\omega_n+\mu-\Sigma_\sigma(i\omega_n)-\epsilon]+\ln\,G_\sigma(i\omega_n)\right), \tag{46}$$

Note also that the internal energy can be expressed in terms of local quantities only (see, e.g., Fetter and Walecka, 1971):

$$\frac{E}{N}=T\sum_{n,\sigma}\int_{-\infty}^{+\infty}d\epsilon\,\frac{\epsilon D(\epsilon)}{i\omega_n+\mu-\Sigma_\sigma(i\omega_n)-\epsilon}$$

$$+\frac{1}{2}\,T\sum_{n,\sigma}\Sigma_\sigma(i\omega_n)G_\sigma(i\omega_n). \tag{47}$$

C. Derivation based on an expansion around the atomic limit

In this section we derive the LISA equations on the basis of an expansion around the atomic limit. This is more than an academic exercise since a successful resummation of the atomic expansion has long been sought, starting with the pioneering work of Hubbard (1964). It is reassuring to see that a systematic analysis of this expansion leads one back to the LISA equations.

This section builds upon early work of Metzner (1991; see also, Hülsenbeck and Stephan, 1994). For any spatial dimension, one can write a general expansion of the free energy and the correlation functions in terms of hopping matrix elements t_{ij} and bare cumulants c_r^0 which are local in space but nonlocal in time. The bare cumulants are defined by

$$c_r^0(\tau_1\cdots\tau_r\ \tau_1'\cdots\tau_r')=\frac{\delta\ln Z_{\rm at}}{\delta\bar\eta(\tau_1)\cdots\delta\bar\eta(\tau_r)\delta\eta(\tau_1')\cdots\delta\eta(\tau_r')},$$

in which $Z_{\rm at}$ is the partition function in the atomic limit,

$$Z_{\rm at}[\eta,\bar\eta]=\int dc^+dc\ e^{-\int_0^\beta\mathscr{L}_{\rm at}+\int_0^\beta\bar\eta c+c^+\eta},$$

where $\mathscr{L}_{\rm at}=\Sigma_\sigma c_\sigma^+(\partial_\tau-\mu)c_\sigma+Un_\uparrow n_\downarrow$ is the Lagrangian in the atomic limit. The rules for the calculation of a Green's function are given by Wortis (1974) and by Metzner (1991). The basic idea is to carry out an expansion of physical quantities in powers of the hopping matrix element, and eliminate all disconnected graphs using linked-cluster type arguments. The diagrammatic rules for the one-particle Green's function $G_{ij,\sigma}(\tau-\tau')$ follow.

(i) Draw all topologically distinct connected diagrams composed of point vertices, directed "internal" lines connecting two vertices (corresponding to hopping matrix elements), and two "external" lines (one entering and one leaving a vertex) such that at each vertex (bare cumulant) the number of entering lines equals the number of exiting lines.

(ii) Label each line with a time and a spin variable. The entering external line is labeled by τ',σ, the exiting one by τ,σ. Label each vertex with a lattice site index; the vertex with the entering external line is labeled by j', the one with the exiting line by j (the external vertices may coincide: in this case $j=j'$).

(iii) Each line running from a vertex j to a vertex i yields a factor t_{ij}; each vertex j with m entering lines (labeled by $s_1',\ldots,s_m'$) and m exiting lines (labeled by $s_1,\ldots,s_m$) yields a factor $c_m^0(s_1,\ldots,s_m|s_1',\ldots,s_m')$.

(iv) Determine the sign of each diagram (plus/minus for an even/odd number of loops).

(v) Determine the symmetry factor $g(D)$ for each diagram D, i.e., the number of distinct permutations of (labeled) vertices and lines which do not alter the topological structure of the diagram.

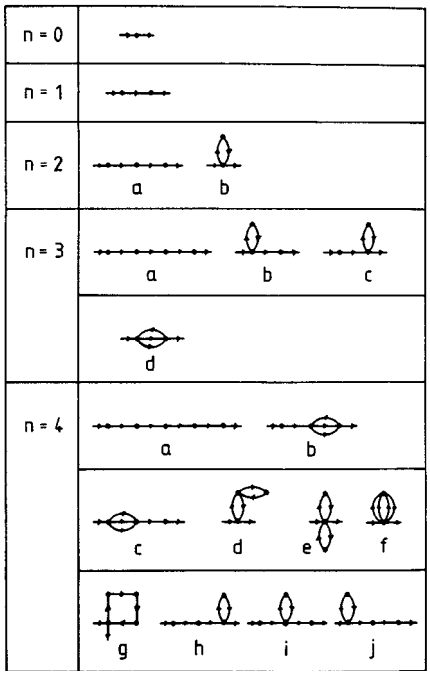

FIG. 5. First few diagrams for the expansion around the atomic limit for the Hubbard model [from Metzner (1991)]. The dots represent bare cumulants.

(vi) For each diagram D, multiply the associated hopping matrix elements and cumulants, integrate each time variable from 0 to β, sum each spin variable and lattice vector *on internal lines* over the whole lattice, and multiply by the sign; the labels of external lines and vertices are kept fixed.

Collecting all these factors, one obtains the weight $w(D)$ of a given diagram D. The one-particle Green's function is finally given by the sum of the weights $w(D)$ of all connected diagrams. The lowest-order diagrams are shown in Fig. 5 from Metzner (1991).

The expansion around the atomic limit is quite complex, and different truncations lead to the Hubbard I and Hubbard III (Hubbard, 1964) approximations (Metzner, 1991). It is natural to define the notion of irreducibility with respect to one line (representing t_{ij}). This leads to the definition of an irreducible cumulant M_1 as the sum of all graphs with two external legs, which cannot be divided into two parts by cutting a single line. Fourier transforming the spatial dependence, one obtains the exact relation between the one-particle irreducible cumulant and the one-particle Green's function,

$$G(\mathbf{k},i\omega_n)=\frac{1}{[M_1^{-1}(\mathbf{k},i\omega_n)-\epsilon_{\mathbf{k}}]} \tag{48}$$

in which $\epsilon_{\mathbf{k}}$ is the Fourier transform of the hopping matrix element. An exact relation between the irreducible one-particle cumulant and the self-energy is thus obtained:

$$M_1^{-1}(\mathbf{k},i\omega_n)=i\omega_n+\mu-\Sigma(\mathbf{k},i\omega_n). \tag{49}$$

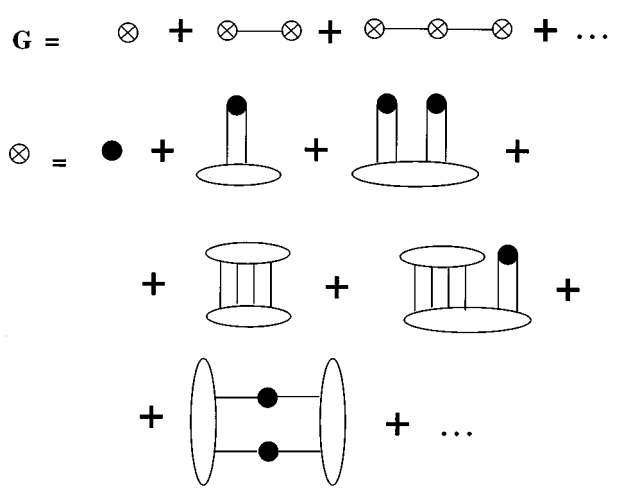

FIG. 6. Diagrammatic representation of the Dyson equation defining the irreducible cumulant M_1 (crossed circle), and its expansion in terms of bare cumulants.

Equation (48) is represented graphically in Fig. 6, in which the first terms in the expansion of M_1 in terms of bare t_{ij} lines and bare cumulants (c^0's) are also depicted.

The expansion described so far is completely general and valid in arbitrary dimensions. The summation over sites are totally unrestricted except for the external vertices which are taken at the same site, say o. In infinite dimensions several important simplifications occur, which are easily explained by means of an example. Consider the diagram in Fig. 7. One shows, just as in the discussion of the weak-coupling expansion in the previous section, that all the bare cumulants connected by more than two lines give a nonzero contribution in $d=\infty$ only when evaluated at the same site. In Fig. 7, i and l have to be equal to o. The contribution from sites $i, l \neq 0$ are of higher order in $1/d$. Notice that the index j in that figure is free. Hence, the irreducible cumulant $M_1(\mathbf{k}, i\omega_n)$ becomes *local* ($\mathbf{k}$ independent) in $d=\infty$, and so does the self-energy.

With this observation, we can identify all the graphs that survive in the $d \to \infty$ limit as originating from the expansion of an Anderson impurity model (AIM) in powers of the hybridization. For the model

$$Z_{\mathrm{AIM}} = \int dc^+ dc \; e^{-\int \Sigma_\sigma c_\sigma^+(\tau)[\partial_\tau - \epsilon_f - \tilde{\Delta}(\tau-\tau')]c_\sigma(\tau') + Un_\uparrow n_\downarrow}. \tag{50}$$

one can derive a diagram expansion in powers of $\tilde{\Delta}$. The elements of a diagram are the bare local cumulants (which we still denote by a dot as in the lattice case), and wavy lines corresponding to $\tilde{\Delta}(\tau-\tau')$. One can introduce the notion of irreducibility with respect to lines, and express the local Green's function in terms of irreducible cumulants. The relation between the impurity orbital Green's function and the renormalized cumulant then becomes

$$G(i\omega) = \frac{1}{[M_1^{-1}(i\omega) - \tilde{\Delta}(i\omega)]}. \tag{51}$$

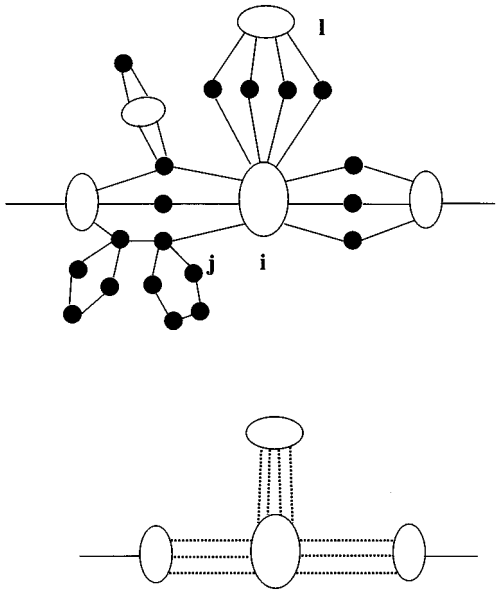

FIG. 7. Examples of the simplifications that take place in the $d=\infty$ limit. The upper plot is a typical graph for M_1. The lower plot is the corresponding Anderson impurity model representation [the dotted lines stand for the hybridization function $\tilde{\Delta}(\tau-\tau')$].

This allows us to identify the renormalized cumulant as

$$M_1^{-1}(i\omega) = i\omega - \epsilon_f - \Sigma(i\omega).$$

Finally, one can express $M_1^{-1}(i\omega)$ in terms of cumulants and $\tilde{\Delta}(\tau-\tau')$. The diagrammatic expansion is identical to that in Fig. 6 for the Hubbard model, provided that one identifies the dotted line representing $\tilde{\Delta}$ with the lines beginning with t_{oi} and ending with t_{jo} as described in Fig. 7. Thus, we conclude that the two expansions coincide provided

$$\tilde{\Delta}(i\omega) = \sum_{(ij)} t_{oi} t_{oj} G_{ij}^{(o)}(i\omega), \tag{52}$$

where $G_{ij}^{(o)}$ denotes, as in Sec. III.A, the Green's function between sites i and j in the absence of site o (and bonds connected to it). This is because the contributions from the site o to the hopping lines that originate from the site labeled j in Fig. 7 vanish in the $d \to \infty$ limit. Other contributions from site o to the diagram described in this figure (such as $l=o$) have been included explicitly in the diagram, thus they should not be included also in the dotted line so as to avoid double counting. The correspondence between the diagrams of the Anderson model and of the $d=\infty$ Hubbard model is illustrated in the case of a specific example in Fig. 7.

Equation (52) is precisely the self-consistency condition (35) derived in the previous sections following different methods. It would be interesting to analyze the effects of the leading order $1/d$ corrections in this framework, in conjunction with a high-temperature expansion.

D. Effective medium interpretation

The dynamical mean-field equations also have a simple interpretation as an effective medium (or "coher-

ent potential") approximation (Janis, 1991; Janis and Vollhardt, 1992a; see also Janis 1986, 1989). (For a review of the coherent potential approximation in the noninteracting case, see, e.g., Elliott, Krumhansl, and Leath, 1974). In this approach, one envisions replacing the interacting lattice model by a *noninteracting medium* with a propagator specified by a local self-energy $\Sigma(i\omega_n)$ to be determined self-consistently. The action of this effective medium thus reads

$$\mathcal{S}_{\rm med}=-\int d\tau\int d\tau'\sum_{\mathbf{k}\sigma} c^{+}_{\mathbf{k}\sigma}(\tau)G^{-1}_{\rm med}(\mathbf{k},\tau-\tau')c_{\mathbf{k}\sigma}(\tau'), \tag{53}$$

$$G_{\rm med}(\mathbf{k},i\omega_n)^{-1}=i\omega_n+\mu-\epsilon_{\mathbf{k}}-\Sigma(i\omega_n). \tag{54}$$

One then imagines that the local interaction $Un_{o\uparrow}n_{o\downarrow}$ is introduced *at a single site o* of this effective medium, and that the self-energy Σ has simultaneously been removed at this single-site only. The action of this new lattice model with a single-site embedding thus reads

$$\mathcal{S}_{\rm emb}=\mathcal{S}_{\rm med}+U\int d\tau\, n_{o\uparrow}n_{o\downarrow} - \int d\tau\int d\tau'\sum_{\sigma} c^{+}_{o\sigma}(\tau)\Sigma(\tau-\tau')c_{o\sigma}(\tau'). \tag{55}$$

This can be turned into an effective action for site o only, by integrating out all other sites. Note that sites $i\neq o$ enter only quadratically in $\mathcal{S}_{\rm emb}$, and that this integration is thus performed *exactly*. This is to be contrasted with the cavity method which is rather different in spirit. One obtains

$$S_{\rm eff}=-\int d\tau\int d\tau'\sum_{\sigma} c^{+}_{o\sigma}(\tau)\mathcal{G}_0^{-1}(\tau-\tau')c_{o\sigma}(\tau') + U\int d\tau\, n_{o\uparrow}n_{o\downarrow} \tag{56}$$

with

$$\mathcal{G}_0^{-1}(i\omega_n)=\tilde{D}(i\omega_n+\mu-\Sigma)^{-1}+\Sigma(i\omega_n). \tag{57}$$

One then requires that the interacting Green's function obtained from $S_{\rm eff}$ for the embedded site coincides with the on-site (local) Green's function of the medium:

$$G(i\omega_n)\equiv-\langle Tc^{+}(i\omega_n)c(i\omega_n)\rangle_{S_{\rm eff}} =\sum_{\mathbf{k}} G_{\rm med}(\mathbf{k},i\omega_n)\equiv\tilde{D}(i\omega_n+\mu-\Sigma). \tag{58}$$

Hence, Σ is identified with the self-energy of the effective (impurity) model itself, and this set of self-consistent equations is seen to be exactly identical to the dynamical mean-field equations above.

IV. RESPONSE FUNCTIONS AND TRANSPORT

In this section, we show that the response functions for the lattice can be obtained from the knowledge of the self-energy and of two-particle Green's functions of the impurity model only (Brandt and Mielsch, 1989; Zlatić and Horvatić, 1990; Jarrell, 1992; Jarrell and Pruschke, 1993a, 1993b; Pruschke, Cox, and Jarrell, 1993a, 1993b). Note that, in the $d\to\infty$ limit, no precursor effect of the instability of a given phase towards some kind of symmetry breaking can, in general, be observed at the level of *one-particle* properties (Müller-Hartmann, 1989b). Indeed, the self-energy only probes local properties in this limit, and is thus sensitive only to those instabilities arising simultaneously from all wave vectors in the Brillouin zone. One such example is the Mott transition discussed in Sec. VII. Instabilities associated with a specific wave vector (such as a ferromagnetic or antiferromagnetic transition) will not be detectable from the knowledge of $\Sigma(i\omega_n)$ in the high-temperature phase. Hence it is very important to be able to evaluate response functions within the LISA framework. Alternatively, dynamical mean-field equations directly adapted to the study of phases with some symmetry breaking can also be established, as described in Sec. V.

A. General formalism

Consider the response function $\chi(\mathbf{q},i\omega_n)$ associated with some operator $\mathcal{O}(\mathbf{R},\tau)$, namely,

$$\chi(\mathbf{q},i\omega_n)=\int_0^{\beta} d\tau\, e^{i\omega_n\tau}\sum_j e^{i\mathbf{q}.\mathbf{R}_j}\langle T\mathcal{O}(\mathbf{R}_j,\tau)\mathcal{O}(\mathbf{0},0)\rangle. \tag{59}$$

Some examples are the charge susceptibility, with $\mathcal{O}(\mathbf{R}_j)=\Sigma_\sigma c^{+}_{j\sigma}c_{j\sigma}$; spin susceptibilities χ^{ab} $(a,b=x,y,z)$, with $\mathcal{O}^a(\mathbf{R}_j)=1/2\Sigma_{\sigma\sigma'}c^{+}_{j\sigma}\sigma^a_{\sigma\sigma'}c_{j\sigma'}$; and the frequency-dependent conductivity tensor $\sigma^{ab}(\omega)$ related to the real-frequency current-current correlation function by $\sigma^{ab}(\omega)=[\chi^{ab}_{jj}(\omega+i0^+)-\chi^{ab}_{jj}(i0^+)]/i\omega$, with the x-component of the current on the hypercubic lattice given by $j^x(\mathbf{R}_j)=i\Sigma_\sigma c^{+}_{j\sigma}(c_{j+\hat{x},\sigma}-c_{j\sigma})$.

All these expressions can be Fourier transformed to yield

$$\mathcal{O}(\mathbf{q},\tau)=\sum_{\mathbf{k}\sigma} v_{\mathbf{k}\sigma}c^{+}_{\mathbf{k}\sigma}c_{\mathbf{k}+\mathbf{q},\sigma}, \tag{60}$$

where the vertex factor $v_{\mathbf{k}\sigma}$ equals 1, $\mathrm{sgn}(\sigma)$, $2\sin(k_x)$ in the three examples above, respectively.

Let us define the two-particle vertex function $\Gamma^{\sigma\sigma'}_{\mathbf{k}\mathbf{k}'\mathbf{q}}(i\nu,i\nu';i\omega)$ appropriate to each of these cases and irreducible in the particle-hole channel (Fig. 8). $\chi(\mathbf{q},i\omega_n)$ is obtained from the ladder sum depicted in Fig. 8, in which a thick line stands for the *interacting* fermion propagator $G(\mathbf{k},i\omega_n)$. Explicitly,

$$\chi(\mathbf{q},i\omega_n)=-\sum_{\mathbf{k},i\nu,\sigma} v_{\mathbf{k},\sigma}G(\mathbf{k},i\nu)G(\mathbf{k}+\mathbf{q},i\nu+i\omega)v_{\mathbf{k}+\mathbf{q},\sigma} + \sum_{\mathbf{k},i\nu,\sigma}\sum_{\mathbf{k}',i\nu',\sigma'} v_{\mathbf{k},\sigma}G(\mathbf{k},i\nu)G(\mathbf{k}+\mathbf{q},i\nu+i\omega) \times\Gamma^{\sigma\sigma'}_{\mathbf{k}\mathbf{k}'\mathbf{q}}(i\nu,i\nu';i\omega)G(\mathbf{k}',i\nu') \times G(\mathbf{k}'+\mathbf{q},i\nu'+i\omega)v_{\mathbf{k}'+\mathbf{q},\sigma'}+\cdots. \tag{61}$$

A crucial simplification arises in the $d\to\infty$ limit: Γ can be replaced in this equation by a purely local quantity

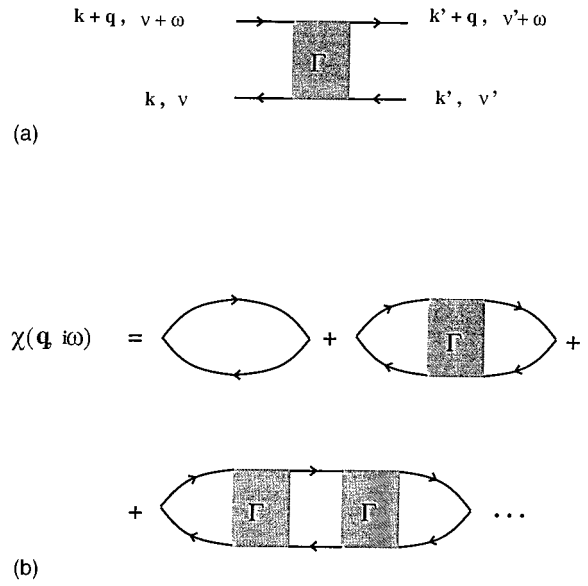

FIG. 8. (a) Two-particle irreducible vertex function. (b) Ladder decomposition of the response function $\chi(\mathbf{q},i\omega_n)$; the *momentum* dependence of Γ can be ignored inside the ladder sum in $d=\infty$.

$\Gamma^{\sigma\sigma'}(i\nu,i\nu';i\omega)$ depending on frequencies only (Zlatić and Horvatić, 1990). This results from the power-counting rules stated in Sec. III.B, since any two sites belonging to Γ in the real-space representation of the ladder series are certainly connected by more than two independent paths. If it were not so, the diagram could be disconnected by cutting two internal propagators in contradiction with the assumption that Γ is irreducible. Note that this assumes that all vertices in Γ can be considered internal (i.e., summed over) and thus Γ can be collapsed to a fully local form *only when inserted in the ladder sum above*. (When considered by itself, Γ does have some momentum dependence, but only its local component contributes to the ladder sum.) As a result of this simplification, the summation over momenta can be performed in each particle-hole bubble independently, ignoring momentum conservation at the vertex Γ. In contrast, note that frequency conservation must be fully taken into account.

For the sake of simplicity, we shall proceed with the example of the spin susceptibility χ^{zz}. All the other response functions can be obtained in an analogous manner. The special case of the frequency-dependent conductivity will also be dealt with in detail below. Only the spin-antisymmetric component Γ^A contributes to χ^{zz} (the superscript A will be omitted everywhere below). We denote by $\tilde{\chi}_{\mathbf{q}}(i\nu,i\nu';i\omega)$ the result of the above ladder sum in which the summation over the first and last frequencies ν,ν' have been omitted [so that the dynamical susceptibility is obtained by summing over frequencies, $\chi(\mathbf{q},i\omega)=\Sigma_{\nu\nu'}\tilde{\chi}_{\mathbf{q}}(i\nu,i\nu';i\omega)$]. $\tilde{\chi}$ satisfies an integral equation:

$$\tilde{\chi}_{\mathbf{q}}(i\nu,i\nu';i\omega)=\tilde{\chi}^0_{\mathbf{q}}(i\nu;i\omega)\delta_{\nu,\nu'} + \tilde{\chi}^0_{\mathbf{q}}(i\nu;i\omega)\,\frac{1}{\beta}\sum_{\nu''}\Gamma(i\nu,i\nu'';i\omega) \times\tilde{\chi}_{\mathbf{q}}(i\nu'',i\nu';i\omega) \tag{62}$$

in which $\tilde{\chi}^0_{\mathbf{q}}(i\nu;i\omega)$ is obtained by performing the summation over the internal momentum $\mathbf{k}$ in the elementary particle-hole bubble,

$$\tilde{\chi}^0_{\mathbf{q}}(i\nu;i\omega)=-\sum_{\mathbf{k}} G(\mathbf{k},i\nu)G(\mathbf{k}+\mathbf{q},i\nu+i\omega). \tag{63}$$

It is clear from Eq. (62) that the $\mathbf{q}$ dependence of $\chi(\mathbf{q},i\omega_n)$ stems entirely from that of $\tilde{\chi}^0_{\mathbf{q}}$. We shall now characterize more precisely this momentum dependence, concentrating on the case where one really studies a $d=\infty$ lattice model (we choose for simplicity the hypercubic lattice). Later in this section, we shall describe how dynamical mean-field approximations for $\mathbf{q}$-dependent response functions of a finite-dimensional model can be generated in the general spirit of the LISA approach.

For the $d=\infty$ hypercubic lattice, the momentum dependence of the response functions simplifies drastically: as shown in Appendix A, $\tilde{\chi}^0_{\mathbf{q}}$ depends on $\mathbf{q}$ (for the hypercubic lattice) only through the following quantity (Brandt and Mielsch, 1989; Müller-Hartmann, 1989a):

$$X(\mathbf{q})=\frac{1}{d}\sum_{i=1}^{d}\cos q_i \tag{64}$$

Let us discuss in more detail the quite peculiar $\mathbf{q}$ dependence of this quantity [and hence of $\chi(\mathbf{q},i\omega_n)$ in the $d\to\infty$ limit]. For a "generic" $\mathbf{q}$ vector (i.e., for all $\mathbf{q}$'s except a set of measure zero), the summation in Eq. (64) is over arguments that are random in sign, and hence is of order $\sqrt{d}$, so that, as $d\to\infty$,

$$X(\mathbf{q})=0 \quad (\text{"generic" } \mathbf{q}). \tag{65}$$

This implies that, for any generic $\mathbf{q}$, $\chi(\mathbf{q},i\omega_n)$ coincides with its *local* (on-site) component:

$$\chi(\mathbf{q},i\omega_n)=\sum_{\mathbf{q}}\chi(\mathbf{q},i\omega_n)\equiv\chi_{\rm loc}(i\omega_n) \quad (\text{"generic" } \mathbf{q}). \tag{66}$$

$X(\mathbf{q})$ may take arbitrary values $-1\leqslant X\leqslant 1$ for specific values of $\mathbf{q}$, however. Important examples are the uniform wave vector $\mathbf{q}=\mathbf{0}$ (appropriate for ferromagnetic ordering) and the zone-corner wave vectors $\mathbf{q}=(\pm\pi,\ldots,\pm\pi)$ (appropriate for two-sublattice commensurate antiferromagnetic ordering):

$$X(\mathbf{0})=+1, \quad X(\pm\pi,\ldots,\pm\pi)=-1. \tag{67}$$

Intermediate values $-1<X<1$ correspond to *incommensurate orderings*. It is important to realize that even though these types of ordering are not very easy to visualize in real space in the $d\to\infty$ limit, they can be studied through the $X(\mathbf{q})$ dependence of χ and indeed are

known to occur in several models including the $d=\infty$ Falicov-Kimball model (Freericks, 1993a, 1993b, 1993c cf. Sec. VIII.B), Hubbard model (Freericks and Jarrell, 1995a, cf. Sec. VII.H), and Holstein model (Ciuchi *et al.*, 1993, cf. Sec. VIII.E), away from half-filling.

Because of this specific $\mathbf{q}$ dependence, the calculation of response functions for a $d=\infty$ model can be reduced to the evaluation of correlation functions of the effective impurity model only. In order to see this, we apply Eq. (62) to a "generic" wave vector $\mathbf{q}$. This allows us to express the irreducible vertex function in terms of local quantities:

$$\Gamma=[\tilde{\chi}^0_{\rm loc}]^{-1}-[\tilde{\chi}_{\rm loc}]^{-1} \tag{68}$$

in which the $\tilde{\chi}$'s are viewed as matrices in the two indices ν,ν' and $[\tilde{\chi}]^{-1}$ denotes matrix inversion. This equation can be used to reexpress Γ in Eq. (62), leading to the important expression (Zlatić and Horvatić, 1990; Jarrell, 1992)

$$\tilde{\chi}^{-1}_{\mathbf{q}}=[\tilde{\chi}_{\rm loc}]^{-1}+[\tilde{\chi}^0_{\mathbf{q}}]^{-1}-[\tilde{\chi}^0_{\rm loc}]^{-1}. \tag{69}$$

The right-hand side of this equation involves impurity model quantities *only*, since $\tilde{\chi}^0_{\mathbf{q}}$ requires only the knowledge of the self-energy $\Sigma(i\omega_n)$, and the local quantities $\chi_{\rm loc}(i\omega_n)$ and $\tilde{\chi}_{\rm loc}(i\nu,i\nu';i\omega)$ are response functions of the impurity model effective action $S_{\rm eff}$. For the example of the spin susceptibility χ^{zz}, we have explicitly

$$\begin{aligned}\tilde{\chi}_{\rm loc}(i\nu,i\nu';i\omega)=&\frac{1}{4}\int_0^\beta d\tau_1\int_0^\beta d\tau_2\int_0^\beta d\tau_3\int_0^\beta d\tau_4\\ &\times e^{i\nu(\tau_1-\tau_2)}e^{i\nu'(\tau_4-\tau_3)}\\ &\times e^{i\omega(\tau_4-\tau_2)}\Sigma_{\sigma\sigma'}(-1)^{\sigma}(-1)^{\sigma'}\\ &\times\langle Tc^+_\sigma(\tau_1)c_\sigma(\tau_2)c^+_{\sigma'}(\tau_3)c_{\sigma'}(\tau_4)\rangle_{S_{\rm eff}}.\end{aligned} \tag{70}$$

The numerical methods reviewed in Sec. VI for the calculation of the impurity model Green's function can be used to evaluate such a local correlation function (cf. Sec. VI.A.5).

The other ingredients entering Eq. (69) are the uncorrected response functions $\tilde{\chi}^0_{\mathbf{q}}$. These are obtained from the knowledge of the one-particle Green's function by evaluating the momentum sum in Eq. (63). On the $d=\infty$ hypercubic lattice, this sum can be evaluated further in order to show that $\tilde{\chi}^0_{\mathbf{q}}$ only depends on $\mathbf{q}$ through $X(\mathbf{q})$. The relevant expressions for an arbitrary $X(\mathbf{q})$ are given in Appendix A. Here, we shall simply note the important expressions for a generic $\mathbf{q}$ and for $\mathbf{q}=0$, valid for an arbitrary density of states:

$$\tilde{\chi}^0_{\mathbf{q}}=\tilde{\chi}^0_{\rm loc}=-\tilde{D}(\zeta_\nu)\tilde{D}(\zeta_{\nu+\omega})\quad(\text{"generic" }\mathbf{q}), \tag{71}$$

$$\tilde{\chi}^0_{\mathbf{q}=\mathbf{0}}=-\frac{\tilde{D}(\zeta_\nu)-\tilde{D}(\zeta_{\nu+\omega})}{\zeta_{\nu+\omega}-\zeta_\nu} \tag{72}$$

with $\zeta_\nu\equiv i\nu+\mu-\Sigma(i\nu)$, as usual.

Hence, Eq. (69) is crucial in that it allows the determination of any $\mathbf{q}$ dependent response function for a $d=\infty$ lattice model from the knowledge of the effective impurity model self-energy and correlation functions. It is instructive to have a closer look at this equation for the case of a uniform and static response $\mathbf{q}=0$, $\omega=0$. Using the above expressions of $\tilde{\chi}^0$ and Eq. (69), we obtain, in that case,

$$\tilde{\chi}^{-1}_{\mathbf{q}=0}(\omega=0)=\tilde{\chi}^{-1}_{\rm loc}(\omega=0)+\delta_{\nu,\nu'}\left(\frac{1}{\tilde{D}(\zeta_\nu)^2}+\frac{1}{\tilde{D}'(\zeta_\nu)}\right) \tag{73}$$

with $\tilde{D}'=\partial\tilde{D}/\partial\zeta$. This expression simplifies in two special cases. For a Lorentzian density of states, $\tilde{D}(\zeta)^{-1}=\zeta+it$ so that the second term in the right-hand side of Eq. (73) vanishes and one obtains that uniform and local response functions coincide for this model: $\tilde{\chi}_{\mathbf{q}=0}=\tilde{\chi}_{\rm loc}$. This parallels the observation made in Sec. II.C that the self-consistency condition becomes trivial for this model, which is really just an impurity model without the interesting feedback effects from the lattice. For all other cases however, the additional term on the right-hand side of Eq. (73) reflects how a static field applied to the lattice induces a spin dependence of the Weiss function $\mathcal{G}_{0\sigma}(i\omega_n)$ (see Sec. V). For the $z=\infty$ Bethe lattice (with our standard normalization), this term simplifies to yield

$$\tilde{\chi}^{-1}_{\mathbf{q}=0}(\omega=0)=\tilde{\chi}^{-1}_{\rm loc}(\omega=0)+t^2\delta_{\nu,\nu'}. \tag{74}$$

This formula has a simple physical interpretation. Even when the local susceptibility diverges, e.g., near the Mott transition $\tilde{\chi}^{-1}_{\rm loc}\to 0$ the uniform susceptibility may remain finite due to the t^2 term. This term cuts off the divergence in the frequency summation $\chi(\mathbf{q}=0,\omega=0)=\Sigma_{\nu\nu'}\tilde{\chi}_{\mathbf{q}=0}(\omega=0)=\Sigma_{\nu\nu'}[\tilde{\chi}^{-1}_{\rm loc}+t^2\delta_{\nu,\nu'}]^{-1}$, and generates the finite spin-exchange scale $J\simeq t^2/U$.

Finally, we conclude this section by mentioning how approximations of $\mathbf{q}$ dependent response functions for a *finite-dimensional* lattice can be obtained in the LISA framework, in the spirit of a dynamical mean-field approximation. The idea is to neglect the momentum-dependence of the irreducible vertex function Γ, and to use again Eq. (62) in order to relate Γ to local quantities. However, it is no longer strictly true that $\chi_{\mathbf{q}}$ coincides with $\chi_{\rm loc}$ for a "generic" value of $\mathbf{q}$, so that using Eq. (68) to calculate Γ is in fact a supplementary approximation. Other choices could be made to define Γ, but Eq. (68) is certainly a natural possibility. Thus, one can follow the strategy of computing the self-energy and the *local* response function $\tilde{\chi}_{\rm loc}$ from the self-consistent impurity model, and to compute $\mathbf{q}$-dependent response functions from Eq. (69). For an arbitrary lattice, the quantities $\tilde{\chi}^0_{\mathbf{q}}$ are obtained from their definition (63) and the knowledge of the self-energy as

$$\begin{aligned}\tilde{\chi}^0_{\mathbf{q}}(i\nu;i\omega)=&-\int_{-\infty}^{+\infty}d\epsilon_1 D(\epsilon_1)\int_{-\infty}^{+\infty}d\epsilon_2 D(\epsilon_2)\\ &\times\frac{\Delta_{\mathbf{q}}(\epsilon_1,\epsilon_2)}{(\zeta_\nu-\epsilon_1)(\zeta_{\nu+\omega}-\epsilon_2)},\end{aligned} \tag{75}$$

where $\zeta_\nu \equiv i\nu+\mu-\Sigma(i\nu)$, and $\Delta_{\mathbf{q}}$ is the lattice-dependent function:

$$\Delta_{\mathbf{q}}(\epsilon_1,\epsilon_2)=\sum_{\mathbf{k}} \delta(\epsilon_{\mathbf{k}}-\epsilon_1)\delta(\epsilon_{\mathbf{k}+\mathbf{q}}-\epsilon_2). \tag{76}$$

For a $d=\infty$ lattice, $\Delta_{\mathbf{q}}$ only depends on $\mathbf{q}$ through $X(\mathbf{q})$, as mentioned above, and the distribution $\Sigma_{\mathbf{q}}\delta(X-X(\mathbf{q}))$ is a delta function $\delta(X)$, so that the above approximation becomes exact.

B. Frequency-dependent conductivity, thermopower and Hall effect

We now deal in detail with the case of the frequency dependent conductivity $\sigma(\omega,\mathbf{q}=0)$. In this case, we have seen that the current vertex $v_{\mathbf{k}}$ is *odd* under parity $\mathbf{k}\to-\mathbf{k}$. Since all $\mathbf{k}$ dependence of Γ can be ignored and $\epsilon_{\mathbf{k}}$ is even under parity, this implies that *all* vertex corrections drop out of the current-current correlation function at $\mathbf{q}=0$ in the $d\to\infty$ limit. This observation was first made by Khurana (1990). A more detailed proof follows from the Ward identity

$$\Omega\Gamma^0(\mathbf{k}+\mathbf{q},\mathbf{k})+\sum_{i=1,d}\Delta(\mathbf{q})^i\Gamma^i(\mathbf{k}+\mathbf{q},\mathbf{k}) = G^{-1}(\mathbf{k}+\mathbf{q},\omega+\Omega)-G^{-1}(\mathbf{k},\omega), \tag{77}$$

where Γ^0 and Γ^i denote the density and current vertex respectively and $\Delta(q)^i=2\sin[(q_i)/2]$ on the hypercubic lattice. Since in large dimensions the self-energy is independent of momentum, and the density vertex is even in $\mathbf{q}$ while the current vertex is odd in $\mathbf{q}$, expanding Eq. (77) to lowest order in $\Delta(\mathbf{q})$ proves that the current vertex is unrenormalized. Notice that this conclusion is false as soon as $\mathbf{q}$ is finite, because there are nontrivial cancellations between the density and the current vertex at finite $\mathbf{q}$ so as to obey Eq. (77).

Hence, only the elementary particle-hole bubble survives in Eq. (62) for the current-current correlator at $\mathbf{q}=0$, and one obtains, for the paramagnetic contribution to the optical conductivity (the diamagnetic term cancels the $1/\omega$ divergence of the real part of the retarded current-current correlator),

$$\sigma(i\omega)=\frac{1}{\omega}\frac{1}{\beta}\sum_{\mathbf{k}\nu_n\sigma}\frac{1}{d}\sum_{l=1}^{d}4\sin^2(k_l)G(\mathbf{k},i\nu_n) \times G(\mathbf{k},i\nu_n+i\omega). \tag{78}$$

One could make use of this expression (inserting the self-energy calculated from the impurity model) to generate approximations of the optical conductivity of a finite-dimensional lattice, in the general spirit of the LISA method. For a $d=\infty$ model however, the sum over momenta can be further simplified by expressing it as an energy integration, and noting that $\Sigma_{\mathbf{k}}\Sigma_l\sin^2(k_l)\delta(\epsilon-\epsilon_{\mathbf{k}})\simeq dD(\epsilon)/2$ for $d\to\infty$. This leads to the final form (Schweitzer and Czycholl, 1991b; Moeller, Ruckenstein, and Schmidt-Rink, 1992; Pruschke, Cox, and Jarrell, 1993a, 1993b):

$$\sigma(i\omega)=\frac{1}{\omega}\frac{1}{\beta}\sum_{\nu_n}\int_{-\infty}^{+\infty}d\epsilon\, D(\epsilon)G(\epsilon,i\nu_n)G(\epsilon,i\nu_n+i\omega). \tag{79}$$

Using the spectral representation of the Green's functions, this is also conveniently expressed in terms of the one-particle spectral density $\rho(\epsilon,\nu)=-(1/\pi)\,\mathrm{Im}G(\epsilon,\nu+i0^+)$:

$$\sigma(i\omega)=\frac{1}{\omega}\int_{-\infty}^{+\infty}d\epsilon\int_{-\infty}^{+\infty}d\nu\int_{-\infty}^{+\infty}d\nu' \times D(\epsilon)\rho(\epsilon,\nu)\rho(\epsilon,\nu')\frac{f(\nu)-f(\nu')}{\nu-\nu'+i\omega}, \tag{80}$$

where f is the Fermi function. Performing the analytic continuation yields (reintroducing dimensional prefactors):

$$\mathrm{Re}\;\sigma(\omega+i0^+)=\pi\frac{e^2}{\hbar a d}\int_{-\infty}^{+\infty}d\epsilon\int_{-\infty}^{+\infty}d\nu\; D(\epsilon)\rho(\epsilon,\nu) \times\rho(\epsilon,\nu'+\omega)\frac{f(\nu)-f(\nu+\omega)}{\omega}. \tag{81}$$

Finally, we conclude by noting that the absence of vertex corrections to the current-current correlation function for $d=\infty$ models is not restricted to that correlation function, but actually applies to the $\mathbf{q}=0$ correlation function of any operator such that the vertex factor $\nu_{\mathbf{k}}$ satisfies

$$\sum_{\mathbf{k}} v_{\mathbf{k}}=0. \tag{82}$$

One additional example is the thermopower Q, associated with the heat current $(\epsilon_k-\mu)\nabla_k\epsilon_k$. The following $d=\infty$ expression can be established (Schweitzer and Czycholl, 1991b; Pruschke, Jarrell, and Freericks, 1996):

$$Q=\frac{\int d\omega\int d\epsilon(\omega-\mu)\frac{\partial f}{\partial\omega}\rho(\epsilon,\omega)^2}{eT\int d\omega\int d\epsilon\frac{\partial f}{\partial\omega}\rho(\epsilon,\omega)^2}. \tag{83}$$

Notice, however, that this expression neglects the contribution to the thermal current due to the transport of doubly occupied sites, which has not been analyzed in detail yet.

Vertex corrections can also be shown to drop out from the Hall coefficient. The proof in this case is more involved, since one needs to consider three-point correlations at finite $\mathbf{q}$, and the limit of small wave vector is taken only at the end of the calculation. Following the careful analysis of Kohno and Yamada (1988), it may be shown that the diagrams neglected in their treatment on the basis of being higher in the small damping constant are in fact higher order in an expansion in $1/d$ relative to the leading terms. This leads to the following expression at finite temperature:

$$\sigma_{xy} \propto B \int d\omega \, \frac{\partial f}{\partial \omega} \sum_k \rho(k,\omega)^3 \left(\frac{\partial \epsilon_k}{\partial k_x} \right)^2 \times \left[\frac{\partial^2 \epsilon_k}{\partial k_y^2} - \left(\frac{\partial \epsilon_k}{\partial k_y} \right)^2 \frac{\partial^2 \epsilon_k}{\partial k_x \partial k_y} \right] \tag{84}$$

Taking the zero-temperature limit of this expression, one observes that the *noninteracting* result is recovered, leading to the Hall number:

$$R_H = -\frac{a^3}{e} \frac{\frac{1}{N} \Sigma_{k,\sigma} \delta(\epsilon_k - \mu_0) \left(v_x^2 \frac{\partial v_y}{\partial k_y} - v_y^2 \frac{\partial v_y}{\partial k_x} \right)}{\left(\frac{1}{N} \Sigma_{k,\sigma} \delta(\epsilon_k - \mu_0) v_x^2 \right)^2}, \tag{85}$$

where $v_k \equiv \nabla_k \epsilon_k$. It is quite remarkable that the Hall coefficient is given by the bare band structure at $T=0$ even when the correlations are strong. This has been applied to the case of $La_{1-x}Sr_xTiO_3$ near the Mott transition by Kajueter, Kotliar, and Moeller (1995).

These expressions can all be simplified further if one considers the special case of the $d=\infty$ hypercubic lattice Eq. (19), in which case summations over $\mathbf{k}$ can be replaced by averages weighted by the bare density of states $D(\epsilon)$, leading to (Pruschke, Jarrell, and Freericks, 1995; Kajueter, Kotliar, and Moeller, 1995; Majumdar and Krishnamurthy, 1995b):

$$\sigma_{xy} \propto -B \int d\epsilon \, D(\epsilon) \epsilon \int d\omega \, \rho(\epsilon,\omega)^3 \frac{\partial f}{d\omega}, \tag{86}$$

$$R_H(T=0) = \frac{a^3}{t^2 e} \frac{\mu_0}{D(\mu_0)}. \tag{87}$$

V. PHASES WITH LONG-RANGE ORDER

For simplicity, the dynamical mean-field equations have been derived in Secs. II and III under the assumption that no long-range order is present. In the previous section, it was shown how response functions signalling some symmetry breaking can be computed. In this section, it will be shown that the dynamical mean-field equations can be generalized to phases with broken symmetry, and a description of the mapping onto an impurity model for these cases will be given (see, e.g., Brandt and Mielsch, 1990, 1991; Georges, Kotliar, and Si, 1992).

A. Ferromagnetic long-range order

In the presence of a magnetic field h coupled to S_z, or if there is a spontaneous uniform magnetization, the Green's functions for up and down electrons are not equivalent. Then one has to retain the spin dependence of the local Green's functions and of the Weiss function in the derivations of Sec. III. The local effective action associated with the Hubbard model in a ferromagnetic phase or in the presence of a uniform field reads

$$S_{\rm eff} = -\int_0^\beta d\tau \int_0^\beta d\tau' \sum_\sigma c_\sigma^+(\tau) \mathcal{G}_{0,\sigma}^{-1}(\tau - \tau') c_\sigma(\tau') + U \int_0^\beta d\tau \, n_\uparrow(\tau) n_\downarrow(\tau). \tag{88}$$

The self-consistent equations for the two functions $G_\uparrow$, $G_\downarrow$ and their corresponding Weiss functions are straightforward generalizations of Eq. (7) to this spin-dependent case. They read

$$G_\sigma(i\omega_n) = \int_{-\infty}^{+\infty} d\epsilon \, \frac{D(\epsilon)}{i\omega_n + \mu + h\sigma - \Sigma_\sigma(i\omega_n) - \epsilon}, \tag{89}$$

where

$$G_\sigma(i\omega_n) \equiv \langle c_\sigma^+(i\omega_n) c_\sigma(i\omega_n) \rangle_{S_{\rm eff}},$$
$$\Sigma_\sigma(i\omega_n) = \mathcal{G}_{0,\sigma}^{-1} - G_\sigma^{-1}. \tag{90}$$

Note that the dependence of $\mathcal{G}_0^{-1}$ on the external field h is, in general, more complicated than just a linear term $h\sigma$: a uniform field coupling linearly to the lattice model induces a nonlinear, frequency dependent term in the impurity effective action.

From the solution of Eqs. (88) and (89), one can reconstruct the lattice Green's functions:

$$G_\sigma(\mathbf{k}, i\omega_n) = \frac{1}{i\omega_n + \mu + h\sigma - \epsilon_{\mathbf{k}} - \Sigma_\sigma(i\omega_n)}. \tag{91}$$

The magnetization as a function of the external field is given by

$$m = \frac{1}{\beta} \sum_n e^{i\omega_n 0^+} [G_\uparrow(i\omega_n) - G_\downarrow(i\omega_n)]. \tag{92}$$

A ferromagnetic phase is signalled by a non-zero spontaneous magnetization $\lim_{h\to 0} m(h) \neq 0$. It is a straightforward but lengthy exercise to check that Eq. (73) for the uniform magnetic susceptibility can be recovered by expanding Eqs. (88) and (89) for small h.

B. Antiferromagnetic long-range order

Similar considerations can be used to study commensurate antiferromagnetic long-range order in the Hubbard model. Note that the $1/\sqrt{d}$ scaling of the hopping amplitude is such that the exchange coupling obtained at large U for a *given* pair of sites, $J_{ij} \simeq t_{ij}^2/U$, scales as $1/d$, which is just the scaling to be performed on a spin model to preserve a Néel transition at a finite temperature $T_N = O(1)$. For simplicity we shall again concentrate on the Hubbard model and we shall add to the Hamiltonian in Eq. (5) a staggered magnetic field:

$$h_s \sum_{i\sigma} e^{i\mathbf{Q}\cdot R_i} c_{\sigma i}^+ c_{\sigma i} \tag{93}$$

with $\mathbf{Q} = (\pi, ..., \pi)$.

Let us first derive the mean-field equations in the ordered phase using the cavity method on the $z=\infty$ Bethe lattice. There are two inequivalent sublattices, A and B and a simple relation in the Néel phase between the

local Green's functions on each sublattice: $G_{ii,\sigma}=G_{A,\sigma},G_{B,\sigma}$ for $i\in A,B$ with

$$G_{A\sigma}(i\omega_n)=G_{B,-\sigma}(i\omega_n). \tag{94}$$

Let us focus on a site belonging to sublattice A, and eliminate all other degrees of freedom. The resulting effective action is identical to Eq. (88), but in the present case the Weiss functions read $\mathcal{G}_{0,\sigma}^{-1}=i\omega_n+\mu-h_s\sigma-t^2G_{B\sigma}$. Using Eq. (94), we see that a single-site description still holds, with (on the Bethe lattice)

$$\mathcal{G}_{0,\sigma}^{-1}=i\omega_n+\mu-t^2G_{-\sigma}-\sigma h_s. \tag{95}$$

This is easily generalized to an arbitrary lattice. The $d\to\infty$ skeleton functional Φ now depends on the two local Green's functions: $\Phi=\Phi[G_{A\sigma},G_{B\sigma}]$. The self-energy is purely local and can take two values with $\Sigma_{A\sigma}(i\omega_n)=\Sigma_{B,-\sigma}(i\omega_n)$. It is convenient to write the Hamiltonian in terms of two sublattice operators in the reduced Brillouin zone (RBZ):

$$H_0=\sum_{\sigma\mathbf{k}\in\mathrm{RBZ}}\epsilon_{\mathbf{k}}(c_{A\mathbf{k}\sigma}^{+}c_{B\mathbf{k}\sigma}+c_{B\mathbf{k}\sigma}^{+}c_{A\mathbf{k}\sigma}) + \sum_{\sigma\mathbf{k}\in\mathrm{RBZ}}\sigma h_s(c_{A\mathbf{k}\sigma}^{+}c_{A\mathbf{k}\sigma}-c_{B\mathbf{k}\sigma}^{+}c_{B\mathbf{k}\sigma}). \tag{96}$$

The Green's functions are obtained by inverting the matrix:

$$\begin{pmatrix}\zeta_{A\sigma} & -\epsilon_{\mathbf{k}}\\ -\epsilon_{\mathbf{k}} & \zeta_{B\sigma}\end{pmatrix}$$

with $\zeta_{A\sigma}=i\omega_n+\mu-\sigma h_s-\Sigma_{A\sigma}$ and $\zeta_{B\sigma}=i\omega_n+\mu+\sigma h_s-\Sigma_{B\sigma}$. The impurity model to be considered is still Eq. (88), but the self-consistency conditions now read (Brandt and Mielsch, 1990, 1991):

$$G_{\alpha\sigma}=\zeta_{\bar{\alpha}\sigma}\int_{-\infty}^{\infty}d\epsilon\,\frac{D(\epsilon)}{\zeta_{A\sigma}\zeta_{B\sigma}-\epsilon^2} \tag{97}$$

with $\alpha=A,B$ and $\bar{\alpha}=B,A$. When a semicircular density of states is inserted in this equation, Eq. (95) is recovered. The staggered magnetization and the free energy of the antiferromagnetic phase are given by similar equations as above.

It is instructive to notice that the simplest approximation to the self-energies, $\Sigma_{A\sigma}=(U/2)(n_{A\sigma}-n_{B\sigma})$, reproduces the usual Hartree-Fock approximation for the staggered magnetization. Also, as soon as Néel order is established and $\Sigma_{A\sigma}\neq\Sigma_{B\sigma}$, it is possible to open a gap in the single particle spectrum, i.e., $\mathrm{Im}G(\omega+i0^+)=0$ if $|\omega+\mu+(\Sigma_B-\Sigma_A)/2|\leq(\Sigma_A+\Sigma_B)/2$. This will always be the case, particularly at half-filling for a nested, bipartite lattice. Note that the effective conduction electron bath entering the impurity model is then also gapped. These are peculiarities of the $d\to\infty$ limit, in which long-wavelength spin-wave excitations are absent. Nevertheless, the LISA method has proven useful for studying the quantum transition between a strongly correlated paramagnetic metal and a metal with spin-density wave order, and some of the results are expected to hold in finite dimensions as well (Sachdev and Georges, 1995; see also Sec. VII.D.3).

In order to study the phase transitions between different magnetic phases we have to compare the free energies of all possible magnetic states, using straightforward generalizations of Eqs. (46) and (47). Alternatively, one can calculate directly the relevant divergent susceptibility, along the lines of Sec. IV (keeping in mind, however, the possibility of first-order transitions). For *incommensurate* magnetic orderings, no simple set of mean-field equations can be written inside the ordered phase in the general case, and one must resort to the study of susceptibilities.

C. Superconductivity and pairing

The LISA mean-field equations are easily extended to take into account superconducting long-range order (Georges, Kotliar, and Krauth, 1993). We illustrate this on the one-band Hubbard model, but the equations are easily generalized to other models, such as the multiband Hubbard model described in Sec. VIII.C. One introduces anomalous Green's functions:

$$F(\mathbf{k},\tau)\equiv-\langle Tc_{\mathbf{k}\uparrow}(\tau)c_{-\mathbf{k}\downarrow}(0)\rangle. \tag{98}$$

In the following, we shall consider only pure singlet pairing, for which $F(-\mathbf{k},-\tau)=F(\mathbf{k},\tau)$ and pure triplet pairing with $S_z=0$ for which $F(-\mathbf{k},-\tau)=-F(\mathbf{k},\tau)$. Within the present $d=\infty$ formalism, the $\mathbf{k}$ dependence of F will be only through $\epsilon_{\mathbf{k}}$, so that only pairing states having the symmetry of the *original* lattice are possible in the limit of $d=\infty$. This can be shown using the absence of vertex corrections to the pair susceptibility (Sec. IV) for pairing states with a different symmetry (Jarrell and Pruschke, 1993a). Pairing with a different symmetry, such as d wave, requires an extension of the LISA formalism to self-consistent clusters, see Sec. IX). However, the *time dependence* of F can be highly nontrivial, which is in fact expected to be crucial for models with repulsive interactions. The underlying physical idea is that on-site *equal-time* pairing is likely to be strongly suppressed in the presence of a strong on-site repulsion, but that pairing involving a time-lag between the members of a pair may occur. This idea dates back to Berezinskii's proposal (Berezinskii, 1974) for triplet pairing in ^{3}He, a generalization of which has been recently considered for cuprate superconductors by Balatsky and Abrahams (1992).

In the presence of a nonzero F, it is convenient to work with Nambu spinors $\Psi_i^{+}\equiv(c_{i\uparrow}^{+},c_{i\downarrow})$—or, in Fourier space, $\Psi_{\mathbf{k}}^{+}\equiv(c_{\mathbf{k}\uparrow}^{+},c_{-\mathbf{k}\downarrow})$—and with the matrix formulation of one-particle Green's functions:

$$\hat{G}(\mathbf{k},\tau)\equiv-\langle T\Psi_{\mathbf{k}}(\tau)\Psi_{\mathbf{k}}^{+}(0)\rangle = \begin{pmatrix}G(\mathbf{k},\tau) & F(\mathbf{k},\tau)\\ F(\mathbf{k},\tau)^* & -G(-\mathbf{k},-\tau)\end{pmatrix}. \tag{99}$$

With these notations, the kinetic term of the Hubbard Hamiltonian reads $-\Sigma_{\langle ij\rangle}t_{ij}\Psi_i^{+}\sigma_3\Psi_j$, where σ_3 denotes the Pauli matrix. We shall first illustrate the derivation of the mean-field equations on the $z=\infty$ Bethe lattice. Following the cavity method, we integrate out fermionic

variables on all sites except a single one. The impurity action obtained in this way now reads

$$S_{\rm eff}=U\int_0^\beta d\tau\, n_\uparrow(\tau)n_\downarrow(\tau) - \int_0^\beta d\tau\int_0^\beta d\tau'\Psi^+(\tau)\mathscr{G}_0^{-1}(\tau-\tau')\Psi(\tau'), \quad (100)$$

where the self-consistency equation relating $\mathscr{G}_0$ to the interacting (matrix) Green's function of $S_{\rm eff}$ reads

$$\mathscr{G}_0^{-1}(i\omega_n)=i\omega_n+\mu\sigma_3-t^2\sigma_3\hat{G}(i\omega_n)\sigma_3. \quad (101)$$

We can account for an externally applied dynamic pairing field on all sites in the original lattice problem by adding a forcing term $\Delta(i\omega_n)$ to the off-diagonal components of the right-hand side of Eq. (101).

For an arbitrary lattice, the impurity action keeps the same form, and we introduce a matrix self-energy:

$$\mathscr{G}_0^{-1}-\hat{G}^{-1}=\begin{pmatrix}\Sigma(i\omega_n) & S(i\omega_n)\\ S(i\omega_n) & -\Sigma(i\omega_n)^*\end{pmatrix}. \quad (102)$$

$S(i\omega_n)$ contains information on the time dependence of the pairing. Here and in the following, we have assumed that the symmetry of the pairing is such that the off-diagonal self-energy obeys: $S(i\omega_n)=S(-i\omega_n)^*$. The lattice Green's function reads, in matrix form,

$$\hat{G}^{-1}(\mathbf{k},i\omega_n) =\begin{pmatrix} i\omega_n+\mu-\epsilon_{\mathbf{k}}-\Sigma(i\omega_n) & -S(i\omega_n)\\ -S(i\omega_n) & i\omega_n-\mu+\epsilon_{\mathbf{k}}+\Sigma(i\omega_n)^*\end{pmatrix}. \quad (103)$$

The self-consistency equation is obtained by requiring that the impurity Green's function coincides with the on-site Green's function of the lattice. This yields the relations

$$G(i\omega_n)=\int_{-\infty}^{+\infty}d\epsilon\, D(\epsilon)\,\frac{\zeta^*-\epsilon}{|\zeta-\epsilon|^2+S^2},$$

$$F(i\omega_n)=-S(i\omega_n)\int_{-\infty}^{+\infty}d\epsilon\, D(\epsilon)\,\frac{1}{|\zeta-\epsilon|^2+S^2} \quad (104)$$

with $\zeta\equiv i\omega_n+\mu-\Sigma(i\omega_n)$ as above.

The impurity action (100) describes an Anderson impurity in a superconducting medium. This model is thus the effective local model associated with the superconducting state of a strongly correlated system. Since this problem is known to be highly nontrivial, even with static pairing, we may expect that the self-consistent solution of Eqs. (104) will allow for very intricate densities of states.

The existence of superconducting phases in concrete models is only beginning to be explored. Odd and even frequency pairing is absent in the single-band Hubbard model (Jarrell and Pruschke, 1993a). Some hints that the *two-band* Hubbard model may have a stable superconducting phase were reported by Georges, Kotliar, and Krauth (1993) and Caffarel and Krauth (1994).

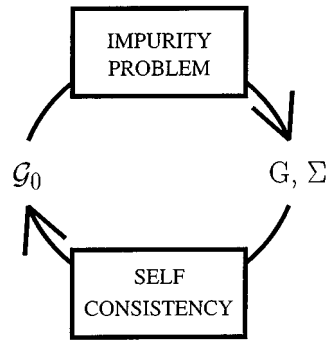

FIG. 9. All methods of solution of the coupled LISA equations involve going through the iteration schematically depicted here. Given $\mathscr{G}_0$, a local interacting Green's function G is obtained by solving the impurity model. This function is used in the self-consistency condition to produce a new bath Green's function $\mathscr{G}_0$. This loop is iterated until a converged set $(G, \mathscr{G}_0)$ is reached.

VI. METHODS OF SOLUTION

As explained in the previous sections, lattice models of correlated fermions can be mapped, in the limit of infinite coordination number, onto a single-impurity model which has to satisfy a self-consistency condition. This condition specifies, for a given lattice, the relation between the Weiss function $\mathscr{G}_0$ (entering the impurity model effective action) and the local Green's function G. On the other hand, G itself is obtained by solving the effective impurity model. Hence, we have a coupled problem to solve for both G and $\mathscr{G}_0$. In practice, all methods deal with this coupled problem in an *iterative* manner: the local Green's function is obtained by solving the impurity effective action given a $\mathscr{G}_0$ (in the first step a guess for $\mathscr{G}_0$ is used). Then, the calculated G (and the self-energy Σ) is used as an input into the self-consistency condition to produce a new Weiss function $\mathscr{G}_0$. The process is iterated until a converged solution $(G,\mathscr{G}_0)$ is reached (Fig. 9). Knowing this converged solution, all $\mathbf{k}$-dependent response functions can be constructed from the impurity model response functions, along the lines of Sec. IV.

To be definite, we concentrate in this section on the case in which the impurity model effective action has the form given by Eq. (6):

$$S_{\rm eff}=-\int_0^\beta d\tau\int_0^\beta d\tau'\sum_\sigma c_\sigma^+(\tau)\mathscr{G}_0^{-1}(\tau-\tau')c_\sigma(\tau') + U\int_0^\beta d\tau\, n_\uparrow(\tau)n_\downarrow(\tau) \quad (105)$$

that corresponds to the local site of the single-impurity Anderson model. In the LISA framework, the $\{c,c^+\}$ operators are associated with a local fermionic variable of the lattice problem.

The most difficult step in the iterative procedure is the repeated solution of the impurity model, for an essentially arbitrary $\mathscr{G}_0$ (i.e., an arbitrary conduction electron effective bath). Even though spatial degrees of freedom

have been eliminated, the impurity model remains a true many-body problem. It is crucial to use *reliable* methods to handle it. Fortunately, quantum impurity models have been studied for over thirty years, and several techniques are available. In this section we review some of these techniques along with some recently developed ones. In particular, we describe in detail a general numerical method which is based on the exact diagonalization of small clusters. We then describe a projective technique, inspired by the renormalization-group method for impurity models, which can be applied to problems with a separation of energy scales.

In contrast to the solution of the single-impurity problem, the implementation of the self-consistency condition in the numerical methods is relatively straightforward. Even though no rigorous proof exists concerning the convergence of the iterative process, practice has shown that it is usually not difficult to reach a self-consistent solution of the LISA equations. Convergence is usually attained after a few iterations. Close to transition points one encounters critical slowing down of the convergence (in the broken symmetry phase) which can however be easily overcome by standard accelerated convergence methods.

This section is organized as follows: we first describe in Sec. VI.A two numerical techniques. These methods are based on a quantum Monte Carlo method and an exact diagonalization solution of the effective impurity problem, and are discussed in full detail. Section VI.A.4 is devoted to the discussion of the problem of the analytic continuation of data from the imaginary to the real axis, which is relevant for some numerical techniques, most notably, the quantum Monte Carlo method. In Sec. VI.A.5, we discuss the calculation of susceptibilities and vertex functions. In Sec. VI.B we review various analytical approximate methods. Among these we devote special attention to the iterated perturbation theory method (Georges and Kotliar, 1992) that is based on the perturbation theory for impurity problems of Yosida and Yamada (1970, 1975). In Sec. VI.C we describe a projective method which allows the detailed solution of problems with separation of energy scales.

The reader is not assumed to have any previous knowledge of the algorithms, which will be thoroughly described in this section. Moreover, we provide with this article a FORTRAN library of programs. The directions to obtain these programs via the internet are explained in Appendix D.

A. Numerical solutions

In this section we review two techniques, the quantum Monte Carlo (QMC) and the exact diagonalization. Both are fully numerical in the sense that the only approximation that is used is a discretization of the mean-field equations. Both methods, when extrapolated to the limit of vanishing discretization, give the exact answer to the problem.

The numerical schemes applied to the LISA equations involve a *discrete* parametrization of the Green's function, and the Weiss field $\mathcal{G}_0$, through a finite number N_P of parameters. This reduces the system of functional equations to a system of N_P nonlinear equations in N_P unknowns. The hope is that as N_P increases, physical quantities converge relatively quickly to their physical values so that the $N_P \to \infty$ value can be inferred by extrapolating results obtained from a finite (and usually small) number of parameters N_P.

We quickly characterize the two numerical techniques and then turn to a detailed description:

(i) The quantum Monte Carlo (QMC) method, and more specifically, the Hirsch-Fye (1986) algorithm considers the single-impurity problem in *discretized imaginary time*. The effective bath only enters through $\mathcal{G}_0$, and there is no need to discretize the conduction band. The first numerical solutions of the LISA equations using this QMC method were obtained independently by Jarrell (1992), Rozenberg, Zhang, and Kotliar (1992), and Georges and Krauth (1992; see also Jarrell, Akhlaghpour, and Pruschke, 1993b).

(ii) The exact diagonalization method (Caffarel and Krauth, 1994; Rozenberg, Moeller, and Kotliar, 1994; Si *et al.*, 1994). In this method, the single-impurity problem is solved exactly with an effective bath that is approximated by a few orbitals only. This introduces a *parametrization* of the effective bath. The parameters correspond to the site energies and hopping amplitudes of the fictitious electrons and to an appropriate choice of the geometry of their connections. Obviously, many different geometries of the electronic bath are possible (cf. Fig. 10). It is the physical insight on a particular problem that indicates the most appropriate choice, which allows one to determine an appropriate parametrization. The number of orbitals that one can effectively treat is severely limited by the size of an exponentially growing Hilbert space. In spite of this limitation, it turns out that the freedom associated with the parametrization more than makes up for the limitations. This freedom concerns the geometry of the electronic bath, and the physical parameters of the orbitals—the site energies and hopping amplitudes. As a consequence, the exact diagonalization algorithm has proven to be very powerful, and in our opinion, clearly superior to the Monte Carlo method.

1. Quantum Monte Carlo method

a. Introduction: A heuristic derivation

The most successful Quantum Monte Carlo method for solving a general impurity problem is due to Hirsch and Fye (1986). Before embarking on a rigorous and self-contained derivation of their method, we describe in this section the algorithm taking a rather different, though less rigorous, approach for the sake of an intuitive understanding of the key ingredients of this method. The method is concerned with the calculation of the local Green's function at finite temperature, which was first introduced in Eq. (8).

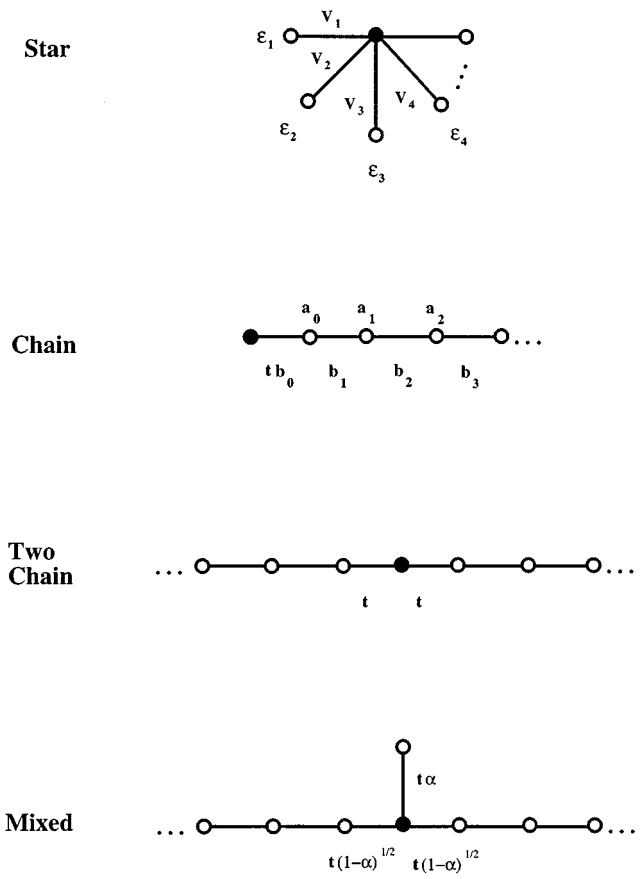

FIG. 10. Various possible geometries used to represent the effective conduction bath in the exact diagonalization algorithm.

(i) The basic principle of the method can be understood as a discretization of the impurity model effective action, Eq. (105):

$$S_{\rm eff}\rightarrow\sum_{\tau\tau'\sigma} c_\sigma^+(\tau)\mathscr{G}_0^{-1}(\tau,\tau')c_\sigma(\tau')+U\sum_\tau n_\uparrow(\tau)n_\downarrow(\tau), \tag{106}$$

where the imaginary time is discretized in L "slices" $\tau=1,2,\ldots,L$ of size $\Delta\tau$, and the timestep $\Delta\tau$ is defined by $\beta=L\Delta\tau$.

(ii) The remaining quartic term can be decoupled using a discrete Hubbard-Stratonovich transformation (Hirsch, 1983):

$$e^{-\Delta\tau U n_\uparrow n_\downarrow+(\Delta\tau U/2)(n_\downarrow+n_\uparrow)}=\frac{1}{2}\sum_{s=\pm1} e^{\lambda s(n_\uparrow-n_\downarrow)}, \tag{107}$$

where $\lambda=\operatorname{arccosh}(e^{\Delta\tau U/2})$ and the discrete field s is an Ising-like variable taking the values ±1. Performing this transformation at every time slice, we are led to a quadratic action, and the partition function becomes

$$Z=\sum_{s_\tau=\pm1}\int D[c,c^+]\exp\left\{-\sum_{\tau\tau'} c_\sigma^+(\tau)\mathscr{G}_0^{-1}(\tau,\tau')c_\sigma(\tau')+\lambda\sum_\tau s_\tau[n_\uparrow(\tau)-n_\downarrow(\tau)]\right\} \tag{108}$$

with

$$G_\sigma^{-1}(\tau_l,\tau_{l'})\equiv\mathscr{G}_{0\sigma}^{-1}(\tau_l,\tau_{l'})+\sigma\lambda s_l\delta_{l,l'+1} \tag{109}$$

the inverse propagator for a particular realization of the Ising spins $(s_1,\ldots,s_L)$. The antiperiodic delta function is defined by $\delta_{l,l'+1}=1$ if $l=l'+1, l=2,\ldots,L-1$, $\delta_{l,l'+1}=-1$ if $l=1$, $l'=L$, and is zero otherwise. Its origin is in the proper time ordering of the creation and destruction operators (Blankenbecler, Scalapino, and Sugar, 1981). In the actual implementation of the algorithm, Eq. (109) is replaced by

$$G^{-1}_{\sigma,(s_1,\ldots,s_L)}(\tau,\tau')\equiv\mathscr{G}^{-1}_{0\sigma}(\tau,\tau')e^V+e^V-1, \tag{110}$$

where e^V is the diagonal matrix with elements $e^V(\tau,\tau)=e^{\sigma\lambda s_\tau}$. This choice of discretization results from the rigorous derivation in Sec. VI.A.1.b following the original Hamiltonian formulation of Hirsch and Fye (1986).

(iii) The replacement of a quartic term for an extra summation on the auxiliary Ising variables $(s_1,\ldots,s_L)$ renders the action quadratic and allows us to apply Wick's theorem at each time slice. We can now perform the Gaussian integration of the Grassmann variables, to obtain

$$Z=\sum_{\{s_1,\ldots,s_L\}}\det[G_\uparrow^{-1}(s_1,\ldots,s_L)]\det[G_\downarrow^{-1}(s_1,\ldots,s_L)]. \tag{111}$$

In principle, the trace over the auxiliary field gives the full interacting Green's function:

$$G_\sigma=\frac{1}{Z}\sum_{\{s_1,\ldots,s_L\}}\det[G_\uparrow^{-1}(s_1,\ldots,s_L)]\times\det[G_\downarrow^{-1}(s_1,\ldots,s_L)]G_\sigma(s_1,\ldots,s_L); \tag{112}$$

this requires the sum over 2^L configurations. Each term in the sum (112) involves the inversion of an $L\times L$ matrix as is clear from Eq. (110). In practice, the full trace can only be performed for small values of L.

(iv) Usually, the interacting Green's function is therefore calculated by stochastic Monte Carlo sampling: the term $\det[G_\uparrow^{-1}(s_1,\ldots,s_L)]\det[G_\downarrow^{-1}(s_1,\ldots,s_L)]$ in Eq. (112) is interpreted as a stochastic weight, and configurations $(s_1,\ldots,s_L)$ are generated by a Markov process with a probability corresponding to their statistical weight.

(v) The Markov process visits configurations of Ising variables $(s_1,\ldots,s_L)$ with a single spin-flip dynamic, in which a possible movement consists in $(s_1,s_2,\ldots,s_k,\ldots,s_L)\rightarrow(s_1,s_2,\ldots,-s_k,\ldots,s_L)$. The formulas given in Sec. VI.A.1.b will allow a rapid calculation of the change in statistical weight, and of the new Green's function for a single spin-flip change.

b. The Hirsch-Fye algorithm: Rigorous derivation

The above derivation leaves us with the impression that there are two discretizations involved: the one of the bath Green's function, and the subsequent discretization of the functional integral. Using a Hamiltonian description of the general Anderson impurity model one

can show (Hirsch and Fye, 1986) that only a single well-defined discretization of the partition function needs to be performed (given by the Trotter breakup). Green's functions corresponding to this discretized partition function can be defined naturally (with the help of the transfer operators). Then, the decoupling using the binary Ising field is performed, and Equation (110) appears as an (exact) Dyson equation relating different discretized Green's functions.

This section is intended mainly for the reader interested in a detailed understanding of the algorithm [this reader should also realize that, in accordance with the *entire* QMC literature, we define in this section temporal Green's functions *without* the minus sign in Eq. (8)]. In order to make it self-contained, the section is accompanied by Appendix B which contains mest derivations.

We temporarily introduce the Hamiltonian description of the local impurity problem, which permits a local-in-time description of the partition function. In order to preserve the standard notations for this model, the impurity orbital (that is associated with a local degree of freedom of the original lattice) will be taken as a d orbital in this section. The conduction bath orbitals are numbered from $p=2,\ldots,n_s$, and the impurity orbital is equivalently denoted by $a_{1\sigma}\equiv d_\sigma$, i.e., corresponds to $p=1$. The Hamiltonian of a general Anderson impurity model reads

$$\mathscr{H}=\sum_{p\geqslant 2,\sigma}\tilde{\epsilon}_p a^+_{p\sigma}a_{p\sigma}+\sum_{p\geqslant 2,\sigma}V_p(a^+_{p\sigma}d_\sigma+d^+_\sigma a_{p\sigma}) + \epsilon_d\sum_\sigma d^+_\sigma d_\sigma+Un_{d\uparrow}n_{d\downarrow}. \tag{113}$$

It is written as a sum of terms $\mathscr{H}=\mathscr{H}^0+\mathscr{H}^i$, where $\mathscr{H}^0$ is quadratic in the fermion operators:

$$\mathscr{H}^0\equiv\sum_{p\geqslant 2,\sigma}\tilde{\epsilon}_p a^+_{p\sigma}a_{p\sigma}+\sum_{p\geqslant 2,\sigma}V_p(a^+_{p\sigma}d_\sigma+d^+_\sigma a_{p\sigma}) +(\epsilon_d+U/2)\sum_\sigma n_{d\sigma}, \tag{114}$$

whereas $\mathscr{H}^i$ is the interaction term:

$$\mathscr{H}^i=U[n_{d\uparrow}n_{d\downarrow}-\tfrac{1}{2}(n_{d\uparrow}+n_{d\downarrow})]. \tag{115}$$

As in Sec. VI.A.1.a, the imaginary time interval $[0,\beta]$ is now discretized into L time slices, but on the level of the original Hamiltonian $\mathscr{H}$. With $\tau_l=l\Delta\tau$, with $l=1,\ldots,L$ and $\Delta\tau\equiv\beta/L$, the partition function is written as

$$Z=\mathrm{Tr}\ e^{-\beta\mathscr{H}}=\mathrm{Tr}\prod_{l=1}^{L}e^{-\Delta\tau[\mathscr{H}^0+\mathscr{H}^i]} \tag{116}$$

Using the Trotter breakup: $\exp[-\Delta\tau(\mathscr{H}^0+\mathscr{H}^i)]\simeq\exp(-\Delta\tau\mathscr{H}^0)\exp(-\Delta\tau\mathscr{H}^i)$, Z can be approximated by the discretized partition function:

$$Z\simeq Z^{\Delta\tau}\equiv\mathrm{Tr}\prod_{l=1}^{L}e^{-\Delta\tau\mathscr{H}^0}e^{-\Delta\tau\mathscr{H}^i}. \tag{117}$$

Green's functions corresponding to $Z^{\Delta\tau}$ can be defined analogously, by using $U_{\Delta\tau}\equiv\exp(-\Delta\tau\mathscr{H}^0)\exp(-\Delta\tau\mathscr{H}^i)$ as an evolution operator between time slices:

$$g^{\Delta\tau}_{p_1,p_2}(\tau_{l_1},\tau_{l_2})\equiv\langle a_{p_1}(\tau_{l_1})a^+_{p_2}(\tau_{l_2})\rangle =\frac{\mathrm{Tr}U^{L-l_1}_{\Delta\tau}a_{p_1}(\tau_{l_1})U^{l_1-l_2}_{\Delta\tau}a^+_{p_2}(\tau_{l_2})U^{l_2}_{\Delta\tau}}{\mathrm{Tr}\ U^L_{\Delta\tau}} \quad (\text{for } l_1>l_2) \tag{118}$$

(and similarly for $l_1<l_2$). It is important to understand that the object $g^{\Delta\tau}$ will be obtained essentially exactly: The only systematic error of the QMC method will consist in the replacement of $\exp(-\Delta\tau\mathscr{H})$ by $U_{\Delta\tau}$ as an evolution operator between time slices. We are then ultimately interested in the d-site Green's function, which we denote by a capital letter $G^{\Delta\tau}(\tau_{l_1},\tau_{l_2})\equiv g^{\Delta\tau}_{1,1}(\tau_{l_1},\tau_{l_2})$.

After the decoupling of $\mathscr{H}^i$ by the transformation Eq. (102)

$$\exp[-\Delta\tau\mathscr{H}^i]=\frac{1}{2}\sum_{s=\pm 1}\exp[\lambda s(n_{d\uparrow}-n_{d\downarrow})], \qquad \cosh(\lambda)\equiv\exp(\Delta\tau U/2) \tag{119}$$

and after inserting Eq. (119) into Eq. (117), the partition function $Z^{\Delta\tau}$ is reduced to

$$Z^{\Delta\tau}=\frac{1}{2^L}\sum_{s_1,\ldots,s_L=\pm 1}Z^{\Delta\tau}_{s_1,\ldots,s_L} \tag{120}$$

with

$$Z^{\Delta\tau}_{s_1,\ldots,s_L}=\prod_{\sigma=\pm 1(=\uparrow,\downarrow)}\mathrm{Tr}e^{-\Delta\tau\mathscr{H}^0}e^{V^\sigma(s_1)} \times e^{-\Delta\tau\mathscr{H}^0}e^{V^\sigma(s_2)}\cdots e^{-\Delta\tau\mathscr{H}^0}e^{V^\sigma(s_L)}. \tag{121}$$

In Eq. (121), the $n_s\times n_s$ matrix $V^\sigma(s)$ is diagonal with

$$e^{V^\sigma(s)}=\begin{pmatrix} e^{\lambda\sigma s} & \ldots & \ldots & 0\\ \ldots & 1 & \ldots & \ldots\\ \ldots & \ldots & 1 & \ldots\\ 0 & \ldots & \ldots & 1\end{pmatrix}. \tag{122}$$

An important observation is that $Z^{\Delta\tau}_{s_1,\ldots,s_L}$ can be written as $Z^{\Delta\tau}_{s_1,\ldots,s_L}=\det\mathscr{O}_{s_1,\ldots,s_L}$ (cf. Appendix B), with the $n_sL\times n_sL$ matrix

$$\mathscr{O}_{s_1,\ldots,s_L}=\begin{pmatrix} 1 & 0 & \cdots & 0 & B(s_L)\\ -B(s_1) & 1 & \cdots & \cdots & 0\\ 0 & -B(s_2) & 1 & \cdots & \cdots\\ \cdots & \cdots & \cdots & 1 & 0\\ \cdots & \cdots & \cdots & -B(s_{L-1}) & 1\end{pmatrix}, \tag{123}$$

where $B(\sigma s)\equiv\exp[-\Delta\tau\mathscr{H}^0]\exp[V^\sigma(s)]$, and $\mathscr{O}$ has been written as an $L\times L$ matrix of $n_s\times n_s$ matrices [$\mathscr{O}$

$\equiv \mathscr{O}_{\{i_l,i_s\},\{i'_l,i'_s\}}$ with $i_l=1,\ldots,L$ and $i_s=1,\ldots,n_s$]. $\mathscr{O}$ is related to the discretized Ising-spin dependent Green's function by the identity (cf. Appendix B)

$$g^{\Delta\tau}_{s_1,\ldots,s_L}=\mathscr{O}^{-1}_{s_1,\ldots,s_L}. \tag{124}$$

The matrix $\mathscr{O}_{s_1,\ldots,s_L}$ is large (of size $n_sL\times n_sL$), but it need not be manipulated explicitly, as will be shown below.

The crucial fact noted by Hirsch and Fye is that the Green's functions for two different Ising spin configurations, $(s_1,\ldots,s_L)$ and $(s'_1,\ldots,s'_L)$, are related to each other by a Dyson equation (also derived in Appendix B). Abbreviating $g\equiv g^{\Delta\tau}_{s_1,\ldots,s_L}$ and $g'\equiv g^{\Delta\tau}_{s'_1,\ldots,s'_L}$, etc, this Dyson equation reads

$$g'=g+(g-1)(e^{V'-V}-1)g'. \tag{125}$$

This equation brings us back to the description of the impurity problem given in paragraph (a). In fact, Eq. (125) relates two Green's functions g and g' via a projection operator on the d site, namely $[\exp(V'-V)-1]$

$$[\exp(V'-V)-1]_{\{i_l,i_s\},\{i'_l,i'_s\}}\propto\delta_{i_l,i'_l}\delta_{i_s,1}\delta_{i'_s,1}. \tag{126}$$

The presence of this projection operator comes from the possibility of integrating out the conduction band. As a consequence, the Dyson equation Eq. (125) directly relates the Green's functions on the d site one to another, and this equation remains equally valid in the subspace $i_s=1,i'_s=1$. Hence, the d site Green's functions $G^{\Delta\tau}_{s_1,\ldots,s_L}$ also satisfy

$$G'=G+(G-1)(e^{V'-V}-1)G', \tag{127}$$

viewed as an $L\times L$ matrix equation. As a first application of this Dyson equation, we use it to derive Eq. (110), which follows by putting $G'\equiv G_{s_1,\ldots,s_L}$, $G\equiv\mathscr{G}_0$. Notice that the Dyson equation allows arbitrary values for the auxiliary spins s_i.

Rearranging Eq. (125), it is straightforward to see that $G_{s'_1,\ldots,s'_L}$ for an Ising configuration $(s'_1,\ldots,s'_L)$ can be obtained from $G_{s_1,\ldots,s_L}$ by inversion of an $L\times L$ matrix $\mathscr{A}$, defined in the following equation

$$\mathscr{A}G'=G,\quad \mathscr{A}\equiv 1+(1-G)[e^{V'-V}-1]$$

(any two configurations). (128)

In the special case in which $(s'_1,\ldots,s'_L)$ differs from $(s_1,\ldots,s_L)$ by the value of a single spin, say s_l, $\mathscr{A}$ takes on a special form

$$\mathscr{A}=\begin{pmatrix} 1 & 0 & \mathscr{A}_{1l} & 0 & \cdots \\ 0 & 1 & \mathscr{A}_{2l} & \cdots & \cdots \\ \cdots & 0 & \mathscr{A}_{ll} & \cdots & \cdots \\ \cdots & \cdots & \cdots & 1 & 0 \\ \cdots & \cdots & \mathscr{A}_{Ll} & 0 & 1 \end{pmatrix}. \tag{129}$$

In that case, $\det\mathscr{A}=\mathscr{A}_{ll}=1+(1-G_{ll})[\exp(V'_l-V_l)-1]$. Expanding $\mathscr{A}^{-1}$ in minors, it can easily be seen that $(\mathscr{A}^{-1})_{lk}=0$ for $k\neq l$. In that case Eq. (128) simplifies to

$$G'_{l_1l_2}=G_{l_1l_2}+(G-1)_{l_1l}e^{V'_l-V_l}(\mathscr{A}_{ll})^{-1}G_{ll_2}$$

(single flip), (130)

which is a special case of a Sherman-Morrison formula (cf. Press *et al.*, 1991). Equation (125) can also be used to show that

$$\frac{\det\mathscr{O}'}{\det\mathscr{O}}=\frac{\det G}{\det G'}$$

$$=\det\mathscr{A}=1+(1-G_{ll})[\exp(V'_l-V_l)-1] \tag{131}$$

It is remarkable that all the Eq. (127)–(131) express *exact* relations between discretized Green's functions $G^{\Delta\tau}$. The only error committed is related to the Trotter breakup [cf. Eq. (121)]. Further comments on this discretization error can be found in Appendix B.

c. Implementation of the Hirsch-Fye algorithm

We can now assemble the essential ingredients of the Hirsch-Fye algorithm:

(1) The calculation starts from the Green's function $G^{\Delta\tau}_{s_1,\ldots,s_L}(\tau_i,\tau_j)$, with all Ising spins formally set to $s_1=\cdots=s_L=0$. In the LISA context, $G^{\Delta\tau}_{s_1=0,\ldots,s_L=0}(\tau_i-\tau_j)$ is a discretized version $\mathscr{G}_0^{\Delta\tau}$ of the Weiss function $\mathscr{G}_0$, which generally has been determined in the previous iteration by the self-consistency condition (whose implementation will be discussed shortly). At the first step of the iteration, an initial guess is made for $\mathscr{G}_0^{\Delta\tau}$.

(2) The Green's function $G^{\Delta\tau}_{s_1,\ldots,s_L}(\tau_l,\tau_{l'})$ for an arbitrary initial configuration with $s_1=\pm1\cdots s_L=\pm1$ is calculated by explicit inversion of the matrix $\mathscr{A}$ in Eq. (128).

(3) From then on, configurations are visited using single spin flips. In that case, Green's functions can be updated using Eq. (130) (every so often, one checks that the precision has not degraded by doing a complete update as indicated above).

(4) Physical Green's functions $G^{\Delta\tau}(\tau_l-\tau_{l'})$ are determined as averages of the configuration-dependent functions $G^{\Delta\tau}_{s_1,\ldots,s_L}(\tau_l,\tau_{l'})$ with the Ising spin configurations weighted according to Eq. (131).

The last point may benefit from some additional remarks. From Eqs. (118) and (120), it is easily seen that the physical Green's function is given by

$$G^{\Delta\tau,\uparrow\downarrow}(\tau_l,\tau_{l'})$$

$$=\frac{\Sigma_{s_1,\ldots,s_L}\Pi_{\sigma=\pm1}\det\mathscr{O}(\sigma)_{s_1,\ldots,s_L}\mathscr{O}^{-1}(\uparrow\downarrow)_{s_1,\ldots,s_L}(\tau_l,\tau_{l'})}{\Sigma_{s_1,\ldots,s_L}\Pi_{\sigma=\pm1}\det\mathscr{O}(\sigma)_{s_1,\ldots,s_L}} \tag{132}$$

[in order to be explicit, we have reintroduced the dependence on physical spin in Eq. (132)]. If a complete enumeration of Ising spin configurations is possible, the Green's function can be readily evaluated using this formula. It is advisable in this case (Georges and Krauth, 1993) to perform this enumeration using the so-called Gray code, which allows enumerating all the configurations of the Ising spins via single spin flips (cf. Appendix

B). The Gray code enumeration of Eq. (132) produces *numerically exact* results for $G^{\Delta\tau}$.

In a Monte Carlo simulation, Ising spin configurations are generated with a probability proportional to $\det\mathcal{O}^{\uparrow}\det\mathcal{O}^{\downarrow}$, and the physical Green's function $G^{\Delta\tau}$ is then given from Eq. (132) as an average of $G^{\Delta\tau}_{s_1,\ldots,s_L}$ with this measure. As usual, there is some freedom in the choice of the Monte Carlo dynamics, which must, however, satisfy the detailed balance property:

$$\frac{P(s\to s')}{P(s'\to s)}=\frac{\Pi_\sigma \det\mathcal{O}(\sigma)_{s'}}{\Pi_\sigma \det\mathcal{O}(\sigma)_s}. \tag{133}$$

Both the heat-bath and the Metropolis dynamics satisfy this condition:

$$P(s\to s')=\frac{\Pi_\sigma \det\mathcal{O}(\sigma)_{s'}}{[\Pi_\sigma \det\mathcal{O}(\sigma)_{s'}+\Pi_\sigma \det\mathcal{O}(\sigma)_s]} \quad \text{(Heat bath)}, \tag{134}$$

$$P(s\to s')=\begin{cases} 1 & \text{if } \Pi_\sigma \det\mathcal{O}(\sigma)_{s'}>\Pi_\sigma \det\mathcal{O}(\sigma)_s \\ \dfrac{\Pi_\sigma \det\mathcal{O}(\sigma)_{s'}}{\Pi_\sigma \det\mathcal{O}(\sigma)_s} & \text{otherwise} \end{cases} \quad \text{(Metropolis)}. \tag{135}$$

In both cases, the transition probability is a function of the ratio of determinants, which can be computed easily [cf. Eq. (131)] with a computational effort of $O(1)$. If the move $s\to s'$ is accepted, $G^{\Delta\tau}_{s_1,\ldots,s_L}$ is updated with a computational burden of $O(L^2)$, using Eq. (130). The computational effort is thus large for each *accepted* move only. This fact renders the simulation rather insensitive to the problem of small acceptance probabilities. Notice also that the physical Green's function $G^{\Delta\tau}$ is translation invariant in time $G^{\Delta\tau}(\tau_i,\tau_j)=G^{\Delta\tau}(\tau_i-\tau_j)$, a property which the Ising spin dependent quantities $G^{\Delta\tau}_{s_1\cdots s_L}$ lack. This property can be used to reduce statistical noise. We also note that the fermionic sign problem plays no role in any of the calculations. The determinants in Eq. (133) generally have the same sign, and their ratio can be interpreted as a ratio of probabilities.

d. The LISA-QMC algorithm and a practical example

The Hirsch-Fye algorithm is remarkably stable, and a full-size program (such as the program LISAQMC.F provided with this article) can be written relatively easily. The only problem consists in reducing the statistical uncertainties as much as possible, since $G^{\Delta\tau}(\tau_l-\tau_{l'})$ is needed as an input for the self-consistency condition at the next iteration step.

The numerical implementation of this condition—the second building block of the full QMC-LISA algorithm—is contained in the program LISASELF.F also provided with this article. The self-consistency condition is expressed in terms of the Fourier-transformed Green's functions $G(i\omega_n)$ and $\mathcal{G}_0(i\omega_n)$. The direct Fourier transform (FT)—say, calculated by a standard fast Fourier transform (FFT) algorithm—is not applicable here, since the periodicity of $G^{\Delta\tau}(\tau_l)$ would imply that its FFT is a *periodic* function of $i\omega_n$, rather than show the correct asymptotic behavior $G(i\omega_n)\sim 1/i\omega_n$ for large arguments. As detailed in Appendix B, it is more convenient to calculate $G(i\omega_n)$ as the Fourier transform of a (linear or spline) interpolation of $G^{\Delta\tau}(\tau_i)$, with due care paid to the discontinuity of the Green's function at $\tau=0$. Finally, we also need to perform inverse Fourier transforms (IFT), from the Matsubara frequency to imaginary time. Again, we do not use the FFT for this purpose, since L, the number of τ values, is usually very much smaller than the number $n_{\max}$ of frequencies (typical values are $L\sim 64,128$ and $n_{\max}\sim 2^{13}$).

We have now described all the ingredients required to set up the full QMC algorithm for the iterative solution of the LISA equations. One loop of this iteration consists in two steps. In the first step, the self-energy $\Sigma(i\omega_n)$ is computed by performing the following operations:

$$\mathcal{G}_0(\tau)\to\left\{\begin{array}{ll} \xrightarrow{\text{Hirsch-Fye}} G(\tau) & \xrightarrow{\text{FT}} G(i\omega_n) \\ \xrightarrow{\text{FT}} & \mathcal{G}_0(i\omega_n) \end{array}\right\}\to\Sigma(i\omega_n)$$
$$\equiv \mathcal{G}_0(i\omega_n)^{-1}-G(i\omega_n)^{-1}. \tag{136}$$

The self-energy determined in Eq. (136) is then used for the computation of a "new" Green's function by evaluating the Hilbert transform:

$$G^{\text{new}}(i\omega_n)=\int_{-\infty}^{+\infty} d\epsilon\,\frac{D(\epsilon)}{i\omega_n+\mu-\Sigma(i\omega_n)-\epsilon}. \tag{137}$$

From $G^{\text{new}}(i\omega_n)$, the self-consistency loop is then closed as follows:

$$G^{\text{new}}(i\omega_n)\xrightarrow{\mathcal{G}_0^{-1,\text{new}}=G^{-1}+\Sigma}\mathcal{G}_0^{\text{new}}(i\omega_n)\xrightarrow{\text{IFT}}\mathcal{G}_0^{\text{new}}(\tau). \tag{138}$$

The reader may find additional technical comments in the programs LISAQMC.F and LISASELF.F implementing these various steps. Directions to obtain the FORTRAN codes may be found in Appendix D.

The self-consistency loop in Eqs. (136) and (138) is iterated until a converged solution $(G,\mathcal{G}_0)$ is reached. It is remarkable that the process actually converges in almost all cases that have been considered so far. Occasionally, simple cycles appear. To avoid the cycles it is generally sufficient to use $[\mathcal{G}_0(\tau)+\mathcal{G}_0^{\text{new}}(\tau)]/2$ instead of $\mathcal{G}_0^{\text{new}}(\tau)$ in Eq. (138). A direct implementation of the self-consistency loop does however not *always* converge. A counter example is the Hubbard model in a magnetic field close to the Mott transition. The solution to the convergence problem in this case is described in Laloux *et al.* (1994).

As a practical illustration of the LISA-QMC algorithm, we invite the reader to perform the computation of Green's functions for the half-filled Hubbard model with a semicircular density of states for $U=3(D/\sqrt{2})$ and $\beta D/\sqrt{2}=6,8,\ldots,16$. As will be discussed in Sec. VII, for this choice of parameters solutions with and without long range magnetic order may be obtained. To select the paramagnetic solution it suffices to enforce the sym-

metry of spin by averaging the spin up and down Green's functions entering the self-consistency condition. On the other hand, to obtain solution with magnetic order one must include a small difference in the initial guess for $\mathcal{G}_{0\sigma}$.

Using the programs LISAQMC.F and LISASELF.F provided with this paper, it is a simple matter to reproduce the results given in Fig. 11. Another simple calculation consists in reproducing the results of Fig. 14, which will be compared to the exact diagonalization results for the same values of the parameters in Sec. VI.A.3.

e. Relationship with other QMC algorithms

Historically, the first applications of Quantum Monte Carlo methods to impurity models did not use the Hirsch-Fye algorithm, but the original method for performing QMC calculations for lattice fermions, which is due to Blankenbecler, Scalapino, and Sugar (1981). The two methods are very closely related: The Blankenbecler, Scalapino, and Sugar algorithm simply computes the determinant of $\mathcal{O}_{s_1,\ldots,s_L}$, as follows:

$$Z^{\Delta\tau}_{s_1,\ldots,s_L} = \prod_{\sigma=\pm 1} \det[1+B(\sigma s_1)B(\sigma s_2)\ldots B(\sigma s_{L-1})B(\sigma s_L)] \equiv \prod_{\sigma=\pm 1} \det W_{s_1,\ldots,s_L}(\sigma), \tag{139}$$

which is further commented on in Appendix B. Similarly, discretized Green's functions can also be expressed in terms of the matrices B_i:

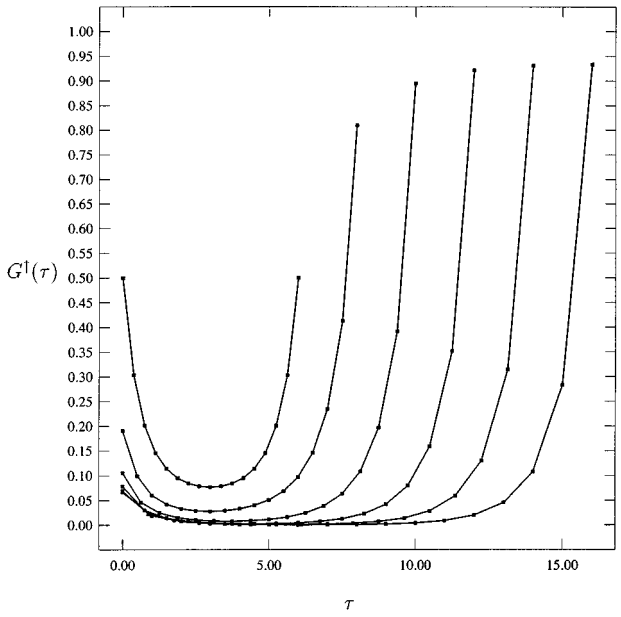

FIG. 11. Self-consistent solution $G^{\uparrow}(\tau)$ of the LISA equations for the half-filled Hubbard model (with a semicircular density of states of half-width D) at $U=3D/\sqrt{2}$ and $\beta D/\sqrt{2}$ =16,14,12,10,8,6 (bottom to bottom) obtained by the QMC method with L=16. The self-consistency condition used in this calculation allows for antiferromagnetic order, which does appear for $\beta \geq 8$ [$G^{\downarrow}(\tau)=G^{\uparrow}(\beta-\tau)$ has not been shown]. The paramagnetic solution can also be continued to larger values of β, by imposing $G^{\downarrow}=G^{\uparrow}$ and using the paramagnetic self-consistency condition (the corresponding result at $\beta D/\sqrt{2}$=32 is displayed in Fig. 14).

$$G^{\Delta\tau}_{s_1,\ldots,s_L}(\tau_l,\tau_{l'}) = \left[B(s_l)B(s_{l-1})\ldots B(s_{l'+1}) \frac{1}{1+B(s'_l)\ldots B(s_1)B(s_L)\ldots B(s_{l'+1})} \right]_{1,1} \quad (l \geq l') \tag{140}$$

[cf. Blankenbecler, Scalapino, and Sugar, (1981) for $l<l'$]. The matrices in Eqs. (139) and (140) are of size $n_s \times n_s$, independently of the number of time slices, and the determinant of $W_{s_1,\ldots,s_L}$ can be computed explicitly. Notice that in this formulation $W_{s_1,\ldots,s_L}$ is a $n_s \times n_s$ matrix, and the number of time slices is reflected solely by the number of matrices appearing in the products of Eqs. (139) and (140). Unfortunately, the product of matrices $B(s_1)B(s_2)\cdots B(s_{L-1})B(s_L)$ is usually very badly conditioned. This generates numerical instabilities that render the calculation of $\det(W_{s_1,\ldots,s_L})$ difficult in practice. As a result of the severe numerical instabilities, the early attempts to treat the single impurity problem with QMC methods (Gubernatis *et al.* 1986), which used the Blankenbecler, Scalapino, and Sugar algorithm, have met with little success. Note, however, that the more recent "balancing schemes" for the Blankenbecler, Scalapino, and Sugar algorithm (Sugiyama and Koonin, 1986; White *et al.*, 1989) have to our knowledge not been applied to impurity models, and could lead to an important improvement.

In order to avoid misunderstandings, we clarify the following: usual (finite-dimensional) QMC calculations, which apply the Blankenbecler, Scalapino, and Sugar algorithm, are haunted by two completely unrelated problems: the bad conditioning of the product of matrices $B(\sigma s_1)\cdots B(\sigma s_L)$, and the fermionic sign problem [$\det(W_{s_1,\ldots,s_L})$ may not always have the same sign]. In impurity problems, one usually encounters neither of these problems, since one is able to use a stable algorithm (Hirsch-Fye), and since the fermionic sign problem is empirically found to play no role. There are techniques—"balancing schemes"—which attempt to solve the problem of the numerical instability.

Rather than expand further on the relationship between the Hirsch-Fye and the Blankenbecler, Scalapino, and Sugar algorithm, we illustrate the above considerations on a toy example in which the Green's function $G^{\Delta\tau}_{s_1,\ldots,s_L}$ is calculated using different approaches. To this aim, a purely pedagogical test program QMCEXAMPLE.F is provided with this paper (cf. Appendices B and D). In this program, the case of an impurity coupled to a small number of conduction electron orbitals (with given values of $\tilde{\epsilon}_p, V_p$) is solved by three possible routes (with identical results):

(1) The original Blankenbecler, Scalapino, and Sugar algorithm: In that case, the two different matrices $B_i(\sigma)$ are calculated for $\sigma=\pm 1$ and the Green's function is obtained by direct matrix multiplication [cf. Eq. (140)]. The eigenvalue spectrum of the large product of matrices appearing in Eq. (139) is computed, and the numerical instabilities can be tracked explicitly.

(2) The explicit calculation of the matrix $\mathcal{O}$: Here $\det\mathcal{O}$ and $\mathcal{O}^{-1}$ are computed by standard matrix inversion. What looks like a very awkward method in this case, in which the conduction orbitals are retained, has in fact been used for calculations in lattice models because of its larger inherent stability (cf. Hirsch, 1988; White *et al.*, 1988 for an application to the two-dimensional Hubbard model).

(3) The use of the Dyson equation, following Hirsch and Fye.

Besides contributing to the reader's understanding of the auxiliary-field QMC method, and helping in the actual implementation of the Hirsch-Fye algorithm, the test can also be used in order to illustrate the numerical instabilities encountered in the Blankenbecler, Scalapino, and Sugar algorithm, which the Hirsch-Fye algorithm overcomes.

Compared to the Blankenbecler, Scalapino, and Sugar algorithm, the method of Hirsch and Fye thus not only yields a very natural numerical implementation of the impurity problem that integrates out the conduction band electrons from the beginning (i.e., allows a general Weiss field $\mathcal{G}_0$). It also presents the enormous advantage of being numerically stable at low temperature, and allows the reaching of temperatures significantly lower than the bandwidth. The remaining limitations of the Hirsch-Fye algorithm can be described as follows:

(i) Only imaginary-time (or Matsubara frequency) quantities can be obtained directly. Real-frequency calculations require analytic continuation algorithms (cf. Sec. VI.A.4).

(ii) The lowest temperatures that can be reached are limited by the number of time slices that one can handle, because the matrices to be multiplied become prohibitively large. On a present-day workstation, the computations with, let us say, 256 time slices already present a considerable investment in computer time. If the problem at hand is not altogether trivial, we may expect (and notice in fact) that the finite $\Delta\tau$ behavior is intricate, which means that we have to choose $\Delta\tau$ sensibly smaller than 1 (cf. the discussion in Appendix B). Thus, even if U is not too big, the range of accessible temperatures is limited to temperatures of the order of $\beta\simeq 30$ or smaller (in the units of the half-bandwidth D). We shall see in the next section that very accurate descriptions of the relevant impurity models, which are much more economical in the number of parameters used (256 in the present example), are possible. The condition for this is that one uses an *adaptive* discretization, which may change with the problem at hand, instead of a fixed grid, as is done in the QMC procedure, in which $\tau_i = i\cdot\Delta\tau$.

2. Exact diagonalization method

In this section we review the implementation of methods that are based on the exact diagonalization of the effective Anderson impurity Hamiltonian Eq. (113). In this method, a rational approximation for $\mathcal{G}_0$ is found. This corresponds to approximating the Anderson impurity Hamiltonian in Eq. (113) by a Hamiltonian made up of a finite number of orbitals n_s (in practice $n_s\sim 5$–12). This Hamiltonian can then be diagonalized exactly using standard algorithms. In order to avoid misunderstandings, we emphasize from the beginning that the exact diagonalization method reviewed here does not deal with a finite-size lattice for the original lattice model: the discretization concerns only the effective conduction bath in the impurity-model formulation. As in all methods of solution of the LISA equations detailed in this article, the infinite-size limit for the actual spatial lattice is implemented from the start. For studies of $d=\infty$ models through a truncation of the physical lattice into subclusters, see the work of Gros *et al.* (1994). We note that analytical approximations involving a continuous fractional expansion of the Green's function, somewhat close in spirit to the Lanczos method detailed below, have recently been considered by Hong and Kee (1995a, 1995b) and Kee and Hong (1995).

All the exact diagonalization algorithms reviewed here to solve the LISA equations adopt the following three basic steps:

(i) The Weiss function

$$\mathcal{G}_0(i\omega_n)^{-1} = i\omega_n + \mu - \int_{-\infty}^{+\infty} d\omega' \, \frac{\Delta(\omega')}{i\omega_n - \omega'} \tag{141}$$

is approximated by a discretized version, for instance:

$$\mathcal{G}_0^{n_s}(i\omega_n)^{-1} = i\omega_n + \mu - \sum_{p=2}^{n_s} \frac{V_p^2}{i\omega_n - \tilde{\epsilon}_p} \tag{142}$$

corresponding to the Anderson impurity Hamiltonian (113). It is also useful to think of this replacement as a *projection* onto a restricted functional subspace (Fig. 12) containing all functions of the form (142) (for a given fixed n_s). The different algorithms that have been used differ only in the choice of the projection operator. From the mathematical point of view one is dealing with the problem of rational approximation of functions. There are many different algorithms (Pade approximation, Continuous fractions, minimization with respect to a given norm) for carrying out the task, and for a small number of approximants the quality of the results may depend on the method used.

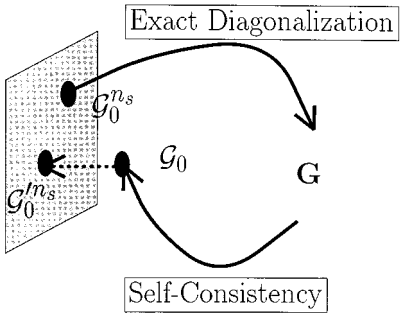

FIG. 12. The exact diagonalization method involves a projection of the bath Green's function $\mathcal{G}_0$ onto the space of functions $\{\mathcal{G}_0^{n_s}\}$ built out of n_s orbitals. At self-consistency $\mathcal{G}_0^{n_s} = \mathcal{G}_0'^{n_s}$. The quality of the approximation can be inferred from the distance that separates $\mathcal{G}_0^{\text{new}}$ and $\mathcal{G}_0^{n_s}$. This distance is usually very small, and decreases approximately by a constant factor as n_s is incremented by one.

(ii) The n_s-orbital Hamiltonian (113) corresponding to Eq. (142) is then diagonalized *exactly*, and the Green's function $G(i\omega_n)$ is computed.

(iii) The self-consistency condition Eq. (137) then leads to a new function $\mathcal{G}_0$, which in turn is approximated by a function $\mathcal{G}_0^{n_s}$ with a *new* set $V_p, \tilde{\epsilon}_p$. The process is iterated until a converged set of parameters is reached. Notice that the bath Green's function $\mathcal{G}_0$ obtained at the previous step of the iteration has no reason to belong to this subspace in general, but that it can be *projected* onto this subspace.

Let us discuss in more detail the various steps of this algorithm, starting with the diagonalization of $\mathcal{H}$. In contrast to the Monte Carlo method, the exact diagonalization algorithm provides a numerically *exact* relationship between $\mathcal{G}_0^{n_s}$ and G, since G is the true Green's function of $\mathcal{H}$. (Note also that the QMC does not in fact determine the Green's function of a specific Hamiltonian, but a related object $G^{\Delta\tau}$, which approaches a Green's function in the limit $\Delta\tau \to 0$). The states of the finite-dimensional Hilbert space of $\mathcal{H}$ are given by

$$|n_1^{\uparrow}, n_2^{\uparrow}, \ldots, n_{n_s}^{\uparrow}\rangle |n_1^{\downarrow}, n_2^{\downarrow}, \ldots, n_{n_s}^{\downarrow}\rangle \tag{143}$$

with $n_p^{\sigma}=0,1$ and $\Sigma_p n_p^{\sigma} \equiv n^{\sigma}$. $\mathcal{H}$ does not mix the different sectors $(n^{\uparrow}, n^{\downarrow})$. In consequence, all sectors can be diagonalized independently. The full diagonalization is feasible for values of n_s of the order of $n_s=6$ [which leads to the diagonalization of a 400×400 matrix in the sector $(n^{\uparrow}=3, n^{\downarrow}=3)$] or $n_s=7$ (1225×1225). At finite temperature, the Green's function is calculated from the full set of states $|i\rangle$ (with eigenvalues E_i) according to

$$G(i\omega_n) = \frac{1}{Z} \sum_{i,j} \frac{(\langle i|d^+|j\rangle)^2}{E_i - E_j - i\omega_n} \times [\exp(-\beta E_i) + \exp(-\beta E_j)]. \tag{144}$$

Using the Lanczos algorithm (cf. Golub and Van Loan, 1983; Gagliano *et al.*, 1986; Lin and Gubernatis, 1993), the *zero-temperature* Green's function of much larger matrices can be computed ($n_s \lesssim 12$). The algorithm is used in a two-step procedure. In the first step, the ground-state wave function $|\Psi_0\rangle^{n^{\uparrow}, n^{\downarrow}}$ is determined in each of the sectors $(n^{\uparrow}, n^{\downarrow})$. This is done in the usual way by picking an arbitrary vector $|p_0\rangle$ [within the sector $(n^{\uparrow}, n^{\downarrow})$], and diagonalizing $\mathcal{H}$ in the linear hull of $|p_0\rangle, \mathcal{H}|p_0\rangle, \ldots, \mathcal{H}^n|p_0\rangle$. In a subsequent application of the Lanczos procedure, the initial vector is taken to be $|p_0\rangle = d^+|\text{g.s.}\rangle$ where $|\text{g.s.}\rangle$ is the *overall* ground state of the Hamiltonian. This second Lanczos procedure allows the computation of the ground-state Green's function, which is written in two continued-fraction expansions that describe the "particle" ($\omega>0$) and "hole" ($\omega<0$) excitations:

$$G(\omega) = G^{>}(\omega) + G^{<}(\omega) \tag{145}$$

with

$$G^{>}(\omega) = \cfrac{\langle \text{g.s.}|d d^{\dagger}|\text{g.s.}\rangle}{\omega - a_0^{>} - \cfrac{b_1^{>2}}{\omega - a_1^{>} - \cfrac{b_2^{>2}}{\omega - a_2^{>} - \cdots}}},$$

$$G^{<}(\omega) = \cfrac{\langle \text{g.s.}|d^{\dagger} d|\text{g.s.}\rangle}{\omega - a_0^{<} - \cfrac{b_1^{<2}}{\omega - a_1^{<} - \cfrac{b_2^{<2}}{\omega - a_2^{<} - \cdots}}}. \tag{146}$$

It is the parameters entering this parametrization that are determined by the second Lanczos procedure, in a way further detailed in Appendix C.

The most subtle aspect of these methods is in the implementation of the projection of $\mathcal{G}_0$ onto $\mathcal{G}_0^{n_s}$. The following methods for carrying out this projection have been proposed.

(i) A distance d between $\mathcal{G}_0$ and the finite-orbital function $\mathcal{G}_0^{n_s}$ is chosen (Caffarel and Krauth, 1994), e.g.:

$$d = \frac{1}{n_{\max}+1} \sum_{n=0}^{n_{\max}} |\mathcal{G}_0(i\omega_n)^{-1} - \mathcal{G}_0^{n_s}(i\omega_n)^{-1}|^2 \tag{147}$$

(where $n_{\max}$ is a very large upper cutoff). For the runs at finite temperatures, the ω_n are of course taken to be the Matsubara frequencies. Even at zero temperature, they are taken to be the Matsubara frequencies associated with a "fictitious" temperature, which serves as a low-energy cutoff. The precise functional form plays a minor role in this formula, but the crucial aspect of the definition is that the Green's functions are compared with each other at *imaginary* frequencies, and *not* on the real axis. This is illustrated pictorially on Fig. 13. As a practical matter, the "projection" is performed using a *minimization* algorithm. A modern conjugate gradient algorithm has of course no trouble in locating the minimum of the $(2n_s)$-dimensional function in Eq. (147) for $n_s \lesssim 12$. Using repeated projection operations, converged solutions $\mathcal{G}_0^{n_s}$ within the subspace (142) can be found. The quality of the solution can be assessed from the "distance" between $\mathcal{G}_0$ and the corresponding $\mathcal{G}_0^{n_s}$, and from the behavior of this distance as a function of n_s.

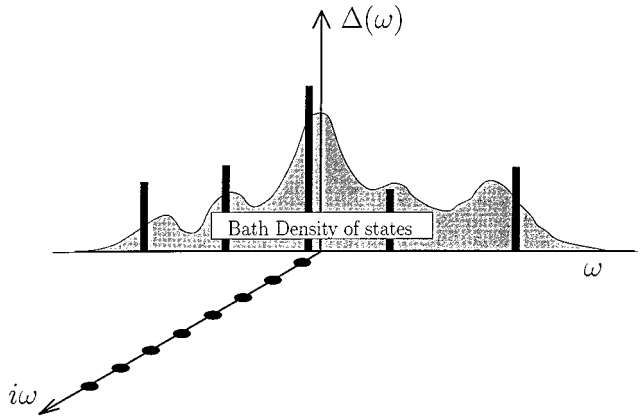

FIG. 13. Schematic representation of the fitting procedure used by Caffarel and Krauth (1994). The spectral density associated with $\mathcal{G}_0^{-1}$ is represented by a finite set of poles ($\tilde{\epsilon}_p$) and weights (V_p^2) on the real frequency axis, but the fitting procedure involves a minimization of the distance between $\mathcal{G}_0(i\omega_n)$ and $\mathcal{G}_0^{n_s}(i\omega_n)$ on the *imaginary frequency* axis.

This distance is an estimate of the distance between the *actual* solution of the LISA equations (which is generically *not* part of the restricted subspace for a finite n_s) and the converged discretized $\mathcal{G}_0^{n_s}$ that has been found within the restricted subspace. This state of affairs is no different in principle from the QMC method (in which a converged solution is found for a given discretization $\Delta\tau$). An illustration of this comparison will be given in Appendix C.

A key to the success of this approximation lies in that *both* the positions of the orbitals $\tilde{\epsilon}_p$ and the hybridizations V_p are free to adjust themselves. The exact diagonalization method is thus formulated on an adaptive "grid" in ω, and shows the excellent convergence and economy common to variable-grid methods. The power of such methods is lost when $d=\infty$ models are studied by exact diagonalization of subclusters of the original lattice itself (cf. Gros *et al.*, 1994).

A second reason behind the fast convergence of this algorithm is related to the fact that the poles of the function $\mathcal{G}_0$ all lie on the real axis, i.e., far away from the region in which we search to fit the functions. Nevertheless, we will show in Sec. VI.A.4 that the real-frequency properties are very well represented.

(ii) An alternative projection method (Si *et al.*, 1994), which avoids the need for a minimization procedure in several variables, is based on the continued-fraction representation of a rational function (cf. Haydock, 1985). The basic idea is to write the hybridization function of the Anderson model as a sum of two continuous fraction expansions (describing the positive and negative parts of the spectral function) $\Delta^>$ and $\Delta^<$ and define the projection as the truncation of the continued fraction down to a given level. Because of the well-known connection between the moments and the coefficients of the continued fraction expansion this can be thought of as a "moment by moment" systematic fitting on the *real axis* of the one-particle spectral density:

$$\Delta^>(\omega)=\cfrac{b_0^{>2}}{\omega-a_0^>-\cfrac{b_1^{>2}}{\omega-a_1^>-\cfrac{b_2^{>2}}{\omega-a_2^>-\cdots}}},$$

$$\Delta^<(\omega)=\cfrac{b_0^{<2}}{\omega-a_0^<-\cfrac{b_1^{<2}}{\omega-a_1^<-\cfrac{b_2^{<2}}{\omega-a_2^<-\cdots}}}. \tag{148}$$

The Hamiltonian that needs to be diagonalized now has a natural representation in the form of two one-dimensional chains, with parameters as shown in Fig. 10 (the $b_i^{>/<}$ are hopping elements between sites of the chains, and the $a_i^{>/<}$ are atomic energies of the sites). It is easy to see that the two chains generate the Weiss field *precisely* in the truncated continued-fraction form (with n_c the length of the chain, $2n_c+1=n_s$):

$$\mathcal{H}=\sum_\sigma \sum_{\rho=>,<}\left(\sum_{\alpha=0}^{n_c-1} a_\alpha^\rho c_{\alpha\sigma}^{\rho+}c_{\alpha\sigma}^\rho + b_0^\rho(c_{0\sigma}^{\rho+}d_\sigma+\text{H.c.}) + \sum_{\alpha=1}^{n_c-2}(b_\alpha^\rho c_{\alpha\sigma}^{\rho+}c_{\alpha+1\sigma}^\rho+\text{H.c.})\right) + U(n_{d\uparrow}-\tfrac{1}{2})(n_{d\downarrow}-\tfrac{1}{2}). \tag{149}$$

This algorithm can be most easily programmed in the case of the $z=\infty$ Bethe lattice at zero temperature, because in this case the self-consistency condition reads $\Delta^>=t^2G^>$ and $\Delta^<=t^2G^<$. Since the Green's function is obtained in a continued-fraction representation [cf. Eq. (146)] the variables a and b are obtained without further work. The self-consistency is thus translated into the self-consistent determination of the parameters of a continued fraction representation of $\mathcal{G}_0^{-1}$, or equivalently, G.

In this case, the approximation consists in the truncation of the length of the continued fractions due to the finite size of the effective electron bath that can be dealt with. This approximation relies on the fact that the continued-fraction representation captures exactly the moments of the Hamiltonian, up to the order retained in the continued fraction.

This method avoids the multidimensional fit of the Green function but has the disadvantage of giving a high weight to the high-frequency features. This is because the low-energy features of the spectral function have a very small contribution to the moments. For this reason, this method is best adapted to the calculation of the total energy (for which it gives very accurate results), and particularly well suited for the study of insulating phases.

(iii) A third implementation of the projection in the LISA exact diagonalization procedure (which is a mixture of the two previous ones) was introduced to describe a strongly correlated metal (Rozenberg, Moeller, and Kotliar, 1994). An extra site at the Fermi energy is added to the scheme (ii) in order to better represent the

low-frequency region. The hopping amplitude to this extra site $t\delta^{1/2}$ is calculated by a (single-parameter) minimization of the expression:

$$\chi^2(\delta)=\sum_{n;\omega_L<\omega_n<\omega_H}|G_A(i\omega_n,\delta)-G(i\omega_n)|^2, \quad (150)$$

where now G is the full Green's function and $G_A(i\omega_n,\delta)=(\delta/i\omega_n)+(1-\delta)G_n(i\omega_n)$. G_n is the truncated Green's function to length $n=n_s/2-1$ and ω_L and ω_H are low and high energy cutoffs that can be defined, for instance, as the lowest poles of G and G_n, respectively. δ decreases as n_s is increased and scales as $1/n_s$ as $n_s\to\infty$. This is the behavior expected from all the residues in the spectral representation of the hybridization function. For the half-filled Hubbard model with a semicircular density of states of half-width D, the quasiparticle residue as a function of U obtained with this procedure vanishes at a value $U_c/D\simeq 3$, which is very close to the more precise value obtained from the projective self-consistent method.

The projection via the moments captures most easily the high-energy features, and is quite insensitive to the low-energy features. Conversely, the χ^2 fit is most sensitive to the low-energy behavior of the spectral features but seems to capture the high-energy features reasonably well when n_s is not too small. Combination of the two approaches optimized for a specific problem are worth exploring.

Working codes for the solution of the LISA equations by exact diagonalization are provided with this article (cf. Appendix D). Two versions of the code are available:

(1) The program LISADIAG.F performs an explicit (sector-by-sector) diagonalization of the Hamiltonian, and constructs the Green's function from the eigenvalues and eigenvectors according to Eq. (144). This is the code that is used for calculations at finite temperature. We will apply it in the next section for a detailed comparison with the QMC calculations. For n_s=6, a single loop of the program will take of the order of one minute to run on a modern workstation (HP 735, or IBM RS6000).

(2) The program LISALANC.F uses the Lanczos algorithm in a two-step procedure.

Naturally, the two completely independent programs agree essentially to machine precision at zero temperature for the values of n_s which can be handled by the full diagonalization. There is also very good agreement between the different ways of choosing the projection operator to compute $\mathcal{G}_0^{n_s}$, given a $\mathcal{G}_0$.

Both codes can more easily be written than explained, and we refer for details to the well-documented FORTRAN programs. Compared to the Monte Carlo programs, they are much faster, and easier to run, since the difficult convergence problems of the stochastic QMC algorithm are absent.

3. Comparison of exact diagonalization and Monte Carlo methods

In this section we compare in detail the QMC and exact diagonalization algorithms. The section serves two purposes:

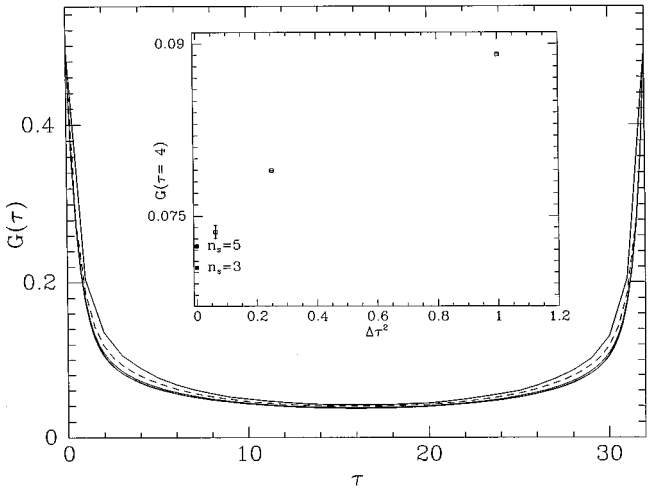

FIG. 14. Comparison between the imaginary-time Green's functions $G(\tau)$ obtained by the QMC and the exact diagonalization methods, for the half-filled Hubbard model with $U=3D/\sqrt{2}$, $\beta D/\sqrt{2}=32$). From top to bottom: $\Delta\tau$=1,1/2,1/4. The bottom curve is the exact diagonalization result for n_s=5 (which cannot be resolved from $\Delta\tau$=1/4 on the scale of the figure). The inset shows the scaling of the QMC results for a fixed value of τ=4 as a function of $(\Delta\tau)^2$: the result converges to a value which is readily obtained within exact diagonalization.

(i) First, by actually comparing the methods, we lend credibility to both. Both methods are able to produce well-converged results which can be taken as they stand, since the thermodynamic limit has been built in from the start. This is quite an exceptional situation in current fermionic many-body simulations. In comparing the two methods we will furthermore be able to clearly expose the advantages of the exact diagonalization algorithm.

(ii) Secondly, we also judge it important to address the wider issue of the confidence limits with which various quantities can presently be computed. Given the importance of the numerical results in the field (in discussions such as the Mott transition, for example), a critical discussion of the numerical methods is needed.

We will first consider three quantities in the context of the $d=\infty$ single-band Hubbard model: the calculation of imaginary-time (or Matsubara frequency) Green's functions at finite temperature, the calculation of the quasiparticle residue Z, and the computation of susceptibilities. The more difficult question of real-frequency quantities will be dealt with in Sec. VI.A.4, where a critical discussion of the results that can be obtained from maximum-entropy analytic continuations of very high precision Monte Carlo data will be given. These calculations will be compared to the discrete spectra obtained from exact diagonalization and to results of analytic approximations.

The most instructive comparison between the QMC and exact diagonalization methods is in imaginary time, where the QMC result is guaranteed to converge quadratically to the exact result [with an error $O(\Delta\tau^2)$, cf. Appendix B]. In Fig. 14 we present results (Caffarel and Krauth, 1994) for the Green's function $G(\tau)$ of the half-filled Hubbard model with a semicircular density of

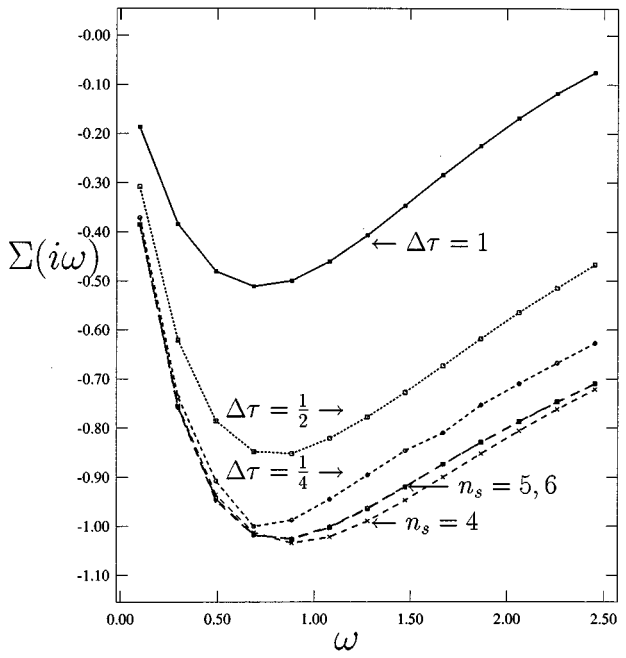

FIG. 15. Finite-temperature self-energy as a function of Matsubara frequency, computed by exact diagonalization (n_s=4,5,6) and QMC $\Delta\tau$=1,1/2,1/4 for the half-filled Hubbard model, with parameters as in Fig. 14.

states of half-width D at $U/D=3/\sqrt{2}$ and $\beta D/\sqrt{2}=32$. The figure shows calculations at $\Delta\tau$=(1,1/2,1/4) for the Monte Carlo algorithm, and n_s=(3,4,5) for the exact diagonalization (in the paramagnetic phase). The excellent agreement between the numerical results is immediately apparent. To see the differences between the methods, we consider a single τ value, as done for τ=4 in the inset of the figure. The Monte Carlo results are plotted against $(\Delta\tau)^2$. It is evident from the figure that the exact diagonalization results for n_s=5 (which the reader can himself reproduce within a few minutes on a regular work station using the program LISADIAG.F) are more precise than the Monte Carlo data at $\Delta\tau$=1/4 (L=128), which necessitate a few *days* of computer time.

The comparison for imaginary frequencies gives a very similar picture, of course with the additional ingredient that, for $\omega>1/(\Delta\tau)$, the Monte Carlo data contain no more information. An illustration of this is shown for the self-energy at finite temperature in Fig. 15, which compares again QMC and the exact diagonalization data. The low-frequency behavior of the self-energy is important in order to determine the nature of the physical state (insulating or metallic), and a good quantitative knowledge is crucial in order to be able to calculate the quasiparticle residue Z, a zero-temperature quantity defined from the retarded self-energy as $Z^{-1}=1-\partial\,\mathrm{Re}\Sigma(\omega+i0^+)/\partial\omega|_{\omega=0}$. A plot of this quantity for the half-filled Hubbard model will be displayed in Sec. VII, in connection with our discussion of the Mott transition. The exact diagonalization method and the (much more costly) QMC method converge to the same values of $\Sigma(i\omega_n)$ down to the first Matsubara frequency at a given finite temperature. Therefore, these values are known up to a precision of the order of 0.3%. Notice however that the error on the quasiparticle residue Z may be much larger, since this is a zero-temperature quantity. More precisely, the estimate $\zeta(T)=[1-\mathrm{Im}\Sigma(i\omega_1)/\omega_1]^{-1}$ suffers from additional systematic errors because at *finite temperature* the analytic continuation of $\Sigma(i\omega_n)$ has a branch cut at zero frequency. For the half-filled Hubbard model, these systematic errors are very small for small or intermediate U, but become larger as the Mott transition is reached. Very close to the transition point, more elaborate methods (Sec. VI.C) are needed to access the true low-frequency regime.

In the process of an actual computation, it is very important to track the behavior of the exact diagonalization algorithm. This is done by analyzing the effect of the "projection" in going from $\mathcal{G}_0$ to $\mathcal{G}_0^{n_s}$ at the self-consistent solution (cf. Fig. 12). The behavior of the mismatch between these functions as a function of n_s allows us to evaluate whether we may trust the results (in the QMC algorithm, we would check whether the data scale properly with $1/\Delta\tau$). In general, $\mathcal{G}_0$ and $\mathcal{G}_0^{n_s}$ differ the most at *small* imaginary frequencies, closest to the real axis and very quickly agree to machine precision for larger values of $i\omega$. An actual example for this comparison is displayed and discussed in Appendix C.

From the discussion of this section, the superiority of the exact diagonalization method over the Monte Carlo method is evident. We would, however, like to mention the very costly scaling of the exact diagonalization algorithm with the size n_s, if we think, e.g., of the obvious generalization to the self-consistent embedded clusters, which are the subject of Sec. IX. Even a small cluster, with a few surrounding orbitals per cluster site, could not possibly be treated with the exact diagonalization method. It seems to us that the QMC method still has a lot of untapped potential: It seems very likely that such systems would most easily be treated by a combination of the Hirsch-Fye algorithm and the original BSS method, suitably stabilized (cf. the detailed discussion of Sec. VI.A.1.e).

4. Spectral densities and real frequency quantities: Comparison of various methods

In this section, we provide some guidelines concerning the calculation of *real-frequency* quantities, such as the one-particle spectral function $\rho(\omega)=-(1/\pi)\,\mathrm{Im}G(\omega+i0^+)$ [or the response functions $\chi''(\omega)=-(1/\pi)\,\mathrm{Im}\chi(\omega+i0^+)$]. The determination of such quantities faces some limitations in both numerical methods treated in Secs. VI.A.1 and VI.A.2. The most severe ones are found in the case of the QMC method. There, only imaginary time/frequency data are obtained directly, and one needs to perform an analytic continuation from numerical data. In the exact diagonalization method, $\rho(\omega)$ is obtained directly, but in the form of an approximation by a set of delta functions (since one is using a finite number of orbitals in the effective bath). Analytic approximation schemes are always best

adapted to computing such quantities, but it is crucial to be able to compare the results to the ones obtained numerically. We present such a comparison here in the case of the half-filled Hubbard model.

The standard algorithm for the analytic continuation of QMC data is the maximum entropy method [Gubernatis *et al.*, 1991; see also Jarrell and Gubernatis (1996) for a recent review]. One is trying to retrieve by inverse Laplace transform the spectral function $\rho(\omega)$ from the imaginary-time Green's function $G(\tau)$, such that

$$G(\tau)=\int_{-\infty}^{\infty} d\omega \, \frac{e^{-\tau\omega}}{1+e^{-\beta\omega}} \, \rho(\omega). \tag{151}$$

The problem is ill-posed and altogether hopeless if the data for $G(\tau)$ are not of extremely good quality, and if the errors and the correlations between errors are not carefully taken into account (Gubernatis *et al.*, 1991). The interplay between statistical errors and systematic ($\Delta\tau$-dependent) errors has also been much discussed in the literature. In addition, the "guess" of the correct density of states $\rho(\omega)$ using Bayesian logic usually brings in an *a priori* choice of a "possible" $\rho(\omega)$, which generally requires an independent approximation method and justification. In the LISA context, all these difficulties are present, and also the additional one associated with the self-consistency condition ($\mathcal{G}_0$ itself is only known up to numerical errors). We will see that a consistent determination of the spectral density is nevertheless possible at sufficiently high temperature. However, in spite of the tremendous effort which has been spent on maximum entropy methods, it is still very difficult, if not impossible, to predict—solely from Monte Carlo calculations—reliable densities of states at low temperature.

The difficulty arises from two different sources: (i) analytic continuation to the real-axis of the *exact* $G(i\omega_n)$ is a numerically "ill-posed" problem, which requires a regularization (see, e.g., the discussion in Press *et al.*, 1991), and (ii) the numerical data for $G(i\omega_n)$ have systematic and/or statistical errors. The first difficulty is alleviated as the temperature decreases because more information becomes available. Unfortunately, the errors in the numerical data (for a given computation efficiency) increase as the temperature decreases.

It is very instructive to deal first with an example in which the interplay between statistical and systematic errors can be disentangled, and for which an exact determination of $\rho(\omega)$ can be achieved, up to discretization errors only. This can be achieved by performing the summation over Ising auxiliary spins using the full Gray-code enumeration mentioned in the QMC section above. In that case we are able to calculate the discretized Green's function $G^{\Delta\tau}(\tau)$ for up to $L=18$ slices exactly, and produce a self-consistent solution to machine precision (the reader can reproduce these calculations with the QMC programs provided). Because of the complete absence of statistical errors we can in this special case perform a Padé transformation (Vidberg and Serene, 1977) in order to compute $\rho(\omega)$, thus avoiding the difficulties of the maximum entropy method. In Fig. 16, we show the results of such a calculation for the

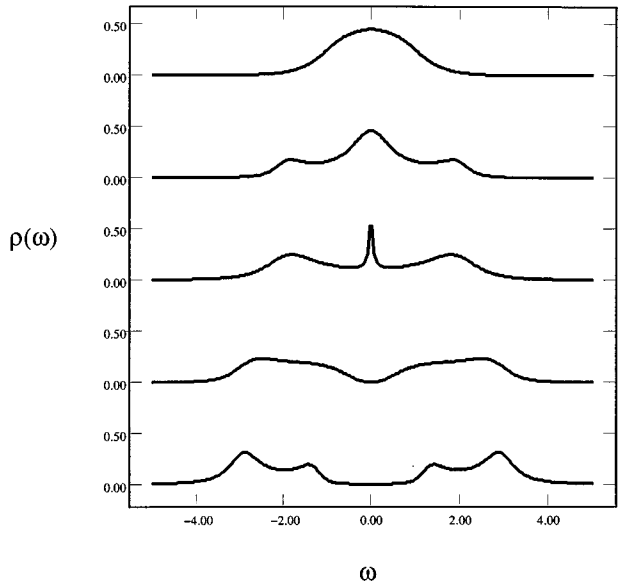

FIG. 16. Finite-temperature spectral densities for the half-filled Hubbard model with a semicircular density of states of half-width D, obtained by the QMC method with $L=16$ time slices at $\beta D/\sqrt{2}=10$ and $U\sqrt{2}/D=1,2,3,4,5$ (top to bottom). An *exact enumeration* of the 2^{16} Ising spin configurations has been used, so that these results correspond to the *exact* analytic continuation of the discretized $G(\tau)$ (for the specific value of $\Delta\tau=10/16$).

half-filled Hubbard model with $\beta=10$ and $L=16$ (i.e., $\Delta\tau=10/16$) as a function of $U=1,2,3,4,5$ (in the units of $D/\sqrt{2}$). Without using any prior knowledge, the results display correctly the buildup of the upper Hubbard band associated with high-energy charge excitations at a scale $\sim\pm U/2$ (cf. Sec. VII). The narrowing of the quasiparticle peak around $\omega=0$ is also apparent. At larger U, a gap opens, indicative of the Mott transition.

It is very interesting to notice that the result of such a simple calculation agrees very well with the results of a full-fledged maximum entropy calculation [along the lines of Gubernatis *et al.* (1991)], as displayed in Fig. 17 at the same values of the physical parameters. Just to indicate the enormous investment needed for the maximum entropy calculation, we indicate that the data were obtained with 100 samples of $G^{\Delta\tau}(\tau)$, which were obtained by performing each time 10^5 sweeps of the Monte Carlo algorithm (with $L=64$). It would be quite inconceivable to redo this calculation at much smaller temperature. In the same figure, we also show the results of the iterated perturbative theory approximation (at finite temperature), which will be discussed in Sec. VI.B.2. It agrees very well with both the maximum entropy and the complete enumeration results. Similar agreement (between maximum entropy and iterated perturbation theory) was obtained for the Hubbard model on a hypercubic lattice (Georges and Krauth, 1993; Jarrell, 1992), again at the rather high temperature accessible to maximum entropy.

Finally, we consider (Caffarel and Krauth, 1994) the spectral densities obtained by the exact diagonalization

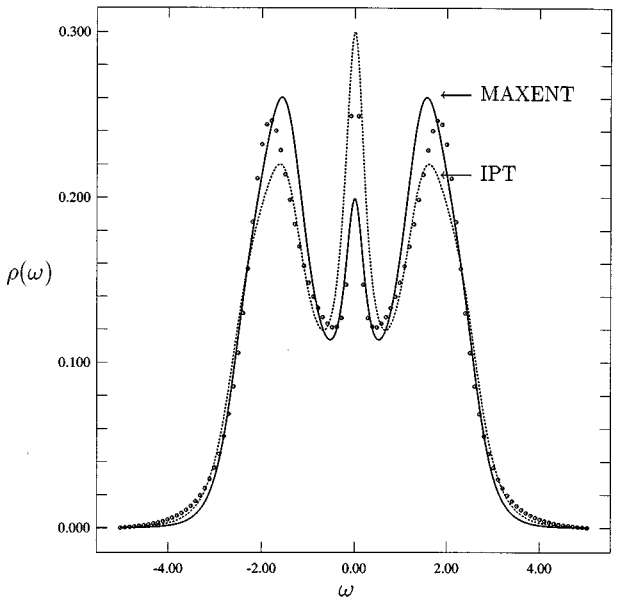

FIG. 17. For the same temperature $\beta D/\sqrt{2}=10$ as in Fig. 16, and $U=3D/\sqrt{2}$, this figure compares spectral densities obtained by the iterated perturbation theory approximation (dotted line), by the QMC method with $L=64$ supplemented by a maximum entropy analytic continuation (full line), and by the Padē interpolation of the exact enumeration data (Fig. 16) with $L=16$ (dots).

method, which consists of a large number of discrete δ functions, directly obtained at $T=0$. The one-particle spectral densities $\rho(\omega)=-\mathrm{Im}G(\omega+i\epsilon)/\pi$ as obtained from the Lanczos calculation ($n_s=10$) are displayed together with the iterated perturbation theory approximation solutions (cf. Sec. VI.B.2) in Fig. 18 for different values of U. In the Fermi-liquid regime the spectrum of the finite-size Anderson model consists of a large number of peaks, while in the insulating phase we systematically observe a simpler structure made of only a few peaks. As U is increased we see that $\rho(\omega)$ develops three well-separated structures: a central quasiparticle feature and two broad high-energy satellite features corresponding to the formation of the upper Hubbard band. At large U, a gap is observed in good agreement with the approximate iterated perturbation theory solution. In the insets of Fig. 18 we also present the integrated single particle density of states corresponding to Lanczos and iterated perturbation theory solutions. The agreement between both curves is seen to be very good, provided we average over a frequency interval of $\omega\sim 0.5$. This indicates that the calculated spectral density contains coarse-grained information about the exact solution, as it should be. Due to the discrete nature of the Anderson model used, the fine details of the spectrum are poorly reproduced, but the agreement of the coarse-grained results with those obtained by the other methods is remarkable.

5. Numerical calculation of susceptibilities and vertex functions

In this short section, we explain how susceptibilities and vertex functions can be computed numerically

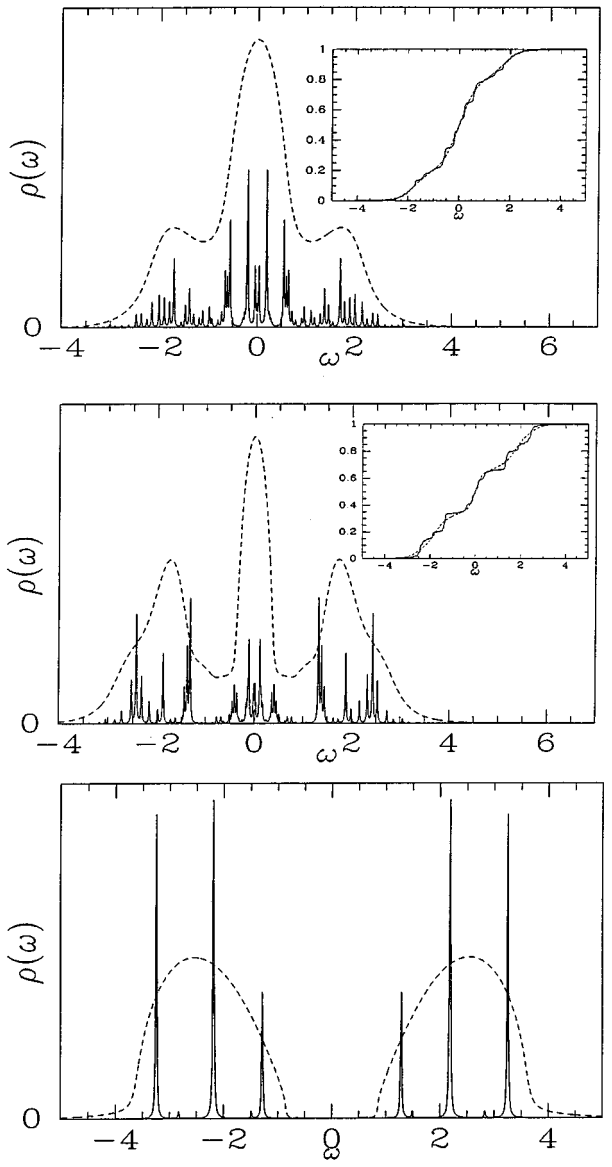

FIG. 18. $T=0$ spectral density for the half-filled Hubbard model at $U\sqrt{2}/D=2,3,4.8$ (top to bottom), as calculated by the exact diagonalization method (Lanczos at $n_s=10$). Also shown are the corresponding results from the iterated perturbation theory approximation (on a different, arbitrary, scale). For a comparison between the two results, the inset contains the integrated density of states $\int_{-\infty}^{\omega}\rho(\omega')d\omega'$ in each case.

within the various methods described above. The theoretical formalism relevant to this section is that of Sec. IV. There, it was shown that **q**-dependent response functions for the lattice model can be related, in the LISA framework, to local response functions of the impurity model through the formula [Eq. (69)]

$$\tilde{\chi}_{\mathbf{q}}^{-1}=\tilde{\chi}_{\mathrm{loc}}^{-1}+\tilde{\chi}_{\mathbf{q}}^{0-1}-\tilde{\chi}_{\mathrm{loc}}^{0-1}, \tag{152}$$

in which $\tilde{\chi}_{\mathrm{loc}}$ is a local response function depending on three frequencies. In the case of the S^z-S^z response function, it reads

$$\tilde{\chi}_{\rm loc}(i\nu,i\nu';i\omega)=\frac{1}{4}\int_0^\beta d\tau_1\int_0^\beta d\tau_2\int_0^\beta d\tau_3\int_0^\beta d\tau_4 e^{i\nu(\tau_1-\tau_2)}\times e^{i\nu'(\tau_4-\tau_3)}e^{i\omega(\tau_4-\tau_2)}\times\sum_{\sigma\sigma'}(-1)^{\sigma}(-1)^{\sigma'}\langle Tc_\sigma^+(\tau_1)c_\sigma(\tau_2)\times c_{\sigma'}^+(\tau_3)c_{\sigma'}(\tau_4)\rangle_{S_{\rm eff}}. \quad (153)$$

A local correlator such as $\langle Tc_\sigma^+(\tau_1)c_\sigma(\tau_2)c_{\sigma'}^+(\tau_3)c_{\sigma'}(\tau_4)\rangle_{S_{\rm eff}}$ can be calculated numerically within both the QMC and exact diagonalization algorithms.

In the QMC method, Wick's theorem applies once the interaction term has been decoupled through the auxiliary Ising variables $s_1\cdots s_L$, so that:

$$\langle Tc_\sigma^+(\tau_1)c_\sigma(\tau_2)c_{\sigma'}^+(\tau_3)c_{\sigma'}(\tau_4)\rangle_{S_{\rm eff}}=\overline{g^{\sigma}_{s_1\cdots s_L}(\tau_2,\tau_1)g^{\sigma'}_{s_1\cdots s_L}(\tau_4,\tau_3)}-\delta_{\sigma\sigma'}\overline{g^{\sigma}_{s_1\cdots s_L}(\tau_2,\tau_3)g^{\sigma}_{s_1\cdots s_L}(\tau_4,\tau_1)}. \quad (154)$$

The overlines denote an average over the Ising spin configurations, with the measure given above. As in the case of the calculation of Green's functions from the QMC, the physical four-point correlation function has symmetries that the Ising-spin dependent quantities lack. This fact can again be used to reduce the importance of statistical noise.

In the exact diagonalization algorithm, a spectral representation can be derived for such a correlator, by inserting a complete set of eigenstates. Since the full formula is rather lengthy, we simply quote it for the local spin correlator $\chi_{\rm loc}(\tau)=\langle S_z(0)S_z(\tau)\rangle$ [i.e., $\chi_{\rm loc}(i\omega)=\Sigma_{\nu\nu'}\tilde{\chi}_{\rm loc}(i\nu,i\nu';i\omega)$]:

$$\chi_{\rm loc}(i\omega)=\frac{1}{Z}\sum_{i,j}\frac{|\langle i|S_z|j\rangle|^2}{i\omega+E_i-E_j}(e^{-\beta E_j}-e^{-\beta E_i}). \quad (155)$$

In this expression, Z is the partition function $Z\equiv\Sigma_i e^{-\beta E_i}$. At finite temperature in the exact diagonalization algorithm, such an expression can be evaluated explicitly. At $T=0$, the Lanczos procedure for the Green's function can be adapted to the calculation of $\chi_{\rm loc}$, by starting the (second) Lanczos iteration with the vector $S_z|{\rm g.s.}\rangle$ instead of $d^+|{\rm g.s.}\rangle$ (cf. Appendix C).

In Fig. 19, we show a comparison of the QMC and exact diagonalization results for the local correlator $\chi_{\rm loc}(\tau)$ of the half-filled Hubbard model at $U/D=3/\sqrt{2}$. Again we notice the almost complete absence of finite-n_s effects, this time in a response function (at lower temperature, however, these effects are more pronounced for the susceptibility than for the Green's functions).

A word of caution is in order however. In the metallic phase at $T=0$, the ground state of an impurity model with a *finite* number of orbitals is a singlet, and there is a finite gap to excited states, so that Eq. (155) should yield a vanishing result at $T=0$ as long as n_s is finite. The correct method for obtaining the asymptotic $n_s\to\infty$ result is to work at a small but finite temperature $T>T^*(n_s)$, where $T^*(n_s)$ is roughly of the order of the finite-size gap of the Anderson chain. As n_s becomes large, $T^*(n_s)$ does vanish, but the limits $T\to 0$ and $n_s\to\infty$ should not be interchanged.

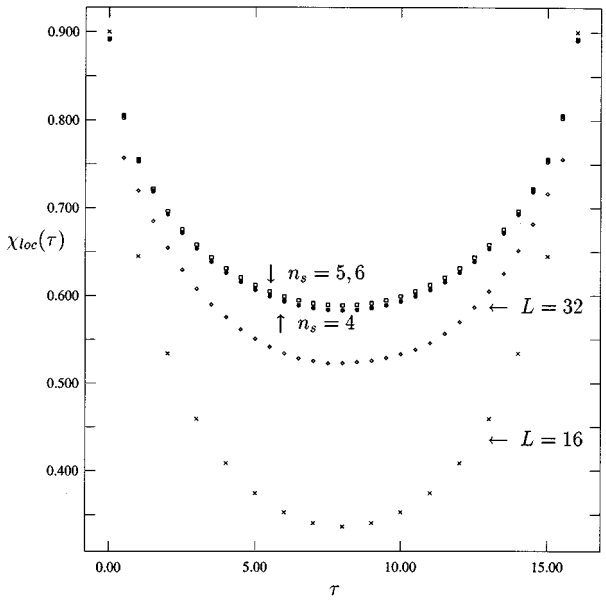

FIG. 19. Local spin correlation function $\chi_{\rm loc}(\tau)=\langle[n_\uparrow(0)-n_\downarrow(0)][n_\uparrow(\tau)-n_\downarrow(\tau)]\rangle$ obtained by the QMC and exact diagonalization methods for the half-filled Hubbard model with $\beta D/\sqrt{2}=16$ and $U=3D/\sqrt{2}$.

Let us finally consider the calculation of the static, uniform susceptibility $\chi=\Sigma_{\mathbf{q}}\chi(\mathbf{q},\omega=0)=\partial m/\partial h|_{h=0}$. This quantity is chosen for illustrative purposes: similar considerations would apply, e.g., to the staggered susceptibility. There are essentially two ways to compute such a quantity numerically:

(i) Compute the *local* response function $\tilde{\chi}_{\rm loc}(i\nu,i\nu';i\omega)$ as described above, and perform the matrix inversion required in (152). The $\tilde{\chi}^0$ can be obtained from the knowledge of the self-energy. A second matrix inversion yields $\tilde{\chi}_{\mathbf{q}=0}(\nu,\nu',\omega=0)$, and finally χ by summing this quantity over ν,ν'. This procedure has been used, e.g., in the work of Jarrell (1992).

(ii) Solve the LISA equations in the presence of a small uniform external field h, and compute the susceptibility as a finite difference $\chi\simeq\Delta m/\Delta h$. The presence of the field enters the self-consistency condition (Sec. V), resulting in a spin-dependent Weiss function $\mathcal{G}_{0\sigma}$ in the impurity effective action.

The second method is probably the simplest if one is interested only in the zero-frequency static susceptibility.

The same method can be used for the static susceptibility at other values of $\mathbf{q}$, such as the staggered susceptibility obtained by including a small staggered field. Note that a similar procedure can be used to obtain the local static susceptibility $\chi_{\rm loc}=\Sigma_{\mathbf{q}}\chi(\mathbf{q})$, instead of the explicit evaluations described above. To do this, one has first to compute the self-consistent solution $G(h=0)$, $\mathcal{G}_0(h=0)$ at zero external field. In a second step, one

then calculates the Green's function $G(h)$ while keeping the Weiss field $\mathcal{G}_0(h=0)$ (this means that the calculation is done for a spin-dependent chemical potential $\mu \to \mu - h\sigma$). The local susceptibility is then given by

$$\chi_{\rm loc} = \lim_{h=0} [G^{\uparrow}(\tau=0,h)|_{\mathcal{G}_0(h=0)} - G(\tau=0,h=0)]/h, \tag{156}$$

which corresponds to putting a magnetic field solely onto the impurity site.

The finite-field method for calculating both local and uniform susceptibilities is perfectly practical, especially in the exact diagonalization framework, where the complete absence of *statistical* noise allows calculations at arbitrarily small h (such as $h \sim 1.0\times10^{-5}$, i.e., fully in the linear regime). Equation (155) describes a linear-response formula which is valid for any Hamiltonian. It is numerically equivalent to the calculation at very small magnetic field. This is of course only true if no further approximations are introduced, as in the exact diagonalization framework [where the sum over states in Eq. (155) is actually computed]. In the Monte Carlo procedure, an exact linear response formula to an external field (at finite $\Delta\tau$) can be derived by expanding the Dyson equation in a field h with respect to h at $h=0$. The method using four-point functions agrees with the finite-field procedure only in the limit of $\Delta\tau \to 0$.

In phases with broken symmetry (where there is a finite effective field), it is again evident that the two procedures result in the same determination of the critical temperatures whenever we are able to write a self-consistency condition for the broken-symmetry phase. An illustration of this point is the calculation of the Néel temperature of the Hubbard model for the hypercubic lattice obtained by Jarrell (1992) by following the first method, and reproduced by Georges and Krauth (1993) following the second one, and on the Bethe lattice calculated by Rozenberg, Kotliar, and Zhang (1994) using the first method and by Ulmke, Janis, and Vollhardt (1994) using both methods.

B. Analytic methods

This article is not the place for an exhaustive review of the rather large variety of analytical methods designed to handle quantum impurity models. These methods can rather generally be divided into two broad classes. On one side, we find several analytical tools for the study of *low-energy* universal properties of these models. These are important in the LISA context since they allow for a classification of the various low-energy behaviors that are *a priori* possible, on a qualitative level. In Sec. VI.B.1 we simply give a list of such methods, with appropriate references. A second class of analytical methods is designed for a full quantitative solution of impurity models, including the calculation of dynamical quantities such as the impurity Green's function. This is precisely what is needed for a full quantitative solution of the LISA equations. Unfortunately, these methods are less numerous and are most of the time *approximate methods* (which may become exact in some extreme limit of the model). We briefly describe in the following three of these methods that have proven useful in the LISA context, namely, weak-coupling perturbation theory (leading to the iterated perturbation theory approximation in the LISA context), the non-crossing approximation, and the (high-temperature) equation of motion method. The description of these methods will be short, and the reader is directed to the original references for a detailed exposition. Two useful general sources on quantum impurity models are the review article by Tsvelick and Wiegmann (1983), and the recent book by Hewson (1993).

1. Exact methods at low energy

When faced with the LISA equations for a specific problem, the first thing to attempt is a characterization of the possible low-energy behaviors. In order to achieve this, one starts by assuming a specific low-energy form for the Weiss function $\mathcal{G}_0(i\omega_n)$ [i.e., for the effective conduction bath density of states $\Delta(\omega)$]. Then, one uses some of the various analytical tools listed below in order to access the low-energy behavior of the impurity Green's function $G(i\omega_n)$ [i.e., of the spectral density $\rho(\omega)$]. This is subsequently inserted into the self-consistency condition in order to decide whether the initial assumption made for $\mathcal{G}_0$ and Δ is indeed compatible with the coupled LISA equations. One may also proceed in the reverse order, namely postulate a low-energy behavior of $G(i\omega_n)$, insert it into the self-consistency condition in order to find the corresponding behavior of $\mathcal{G}_0$ and Δ, and then analyze the impurity problem at low-energy in order to decide on the validity of the initial ansatz for G. For a concrete illustration of this procedure, the reader is directed to the qualitative analysis of the LISA equations for the half-filled Hubbard model in Sec. VII.C, and for the doped case in Sec. VII.H.1. Of course, this analysis only results in a classification of the low-energy behavior that is *a priori* possible, and does not allow for a quantitative determination of the regions of parameter space of the original lattice model that lead to a specific, allowed low-energy behavior. In order to achieve this, these low-energy methods must be combined with some information on the high-energy physics. This information must be obtained either from the numerical methods described above, or from some quantitative analytic approximation technique, like the ones described below in Secs. VI.B.2 and VI.B.3.

The method to be employed for the analysis of the low-energy problem depends crucially on the low-energy behavior of the effective conduction bath density of states $\Delta(\omega)$ parametrizing the Weiss function $\mathcal{G}_0$. Different fixed points (in the renormalization group sense) will generally control the low-energy behavior of the impurity model for different low-frequency behaviors of Δ. An important distinction is whether the effective bath has states at low-energy [i.e., $\Delta(\omega)$ is nonzero in some finite range around $\omega=0$], or whether $\Delta(\omega)$ displays a gap.

In the latter case, the low-energy analysis is generally rather easy to perform. Since there are no low-energy states in the effective bath, the expansion in the hybridization coupling the impurity to the bath (i.e., in Δ itself) is free of singularities and can be used in order to understand the low-energy physics. However, when the effective hybridization becomes comparable to the gap, this expansion may break down, leading to a different low-energy behavior.

The gapless case requires more sophisticated techniques, since in that case the naive expansion in powers of the hybridization generally has vanishing energy denominators, leading to singularities. (Other expansions may be regular though, and quite useful, such as the weak-coupling expansion in powers of the interaction U in the Anderson model case, cf. Sec. VI.B.2). For the convenience of the reader, we provide here a list of techniques that have proven useful in analyzing the low-energy behavior of quantum impurity models with a gapless conduction bath. No details or description of these techniques is given here. Instead, for each of them, the reader is directed to a short nonexhaustive list of convenient references.

(i) Renormalization-group methods. The purpose of these methods is to obtain the effective low-energy theory by integrating out the high-energy parts of $\Delta(\omega)$ in a recursive manner. This method can be used, for example, as an analytical tool to handle the singular expansion in the hybridization. Standard references are the papers by Anderson, Yuval, and Hamann (1970); Anderson (1970); Haldane (1978a). The renormalization group can also be extended beyond the weak coupling regime using recursive numerical diagonalizations (Wilson, 1975; Krishnamurthy, Wilkins, and Wilson, 1980). Extension of the numerical renormalization group to the calculation of Green's functions and dynamical quantities has been investigated by Frota and Oliveira (1986), Sakai, Shimizu, and Kasuya (1989), and Costi and Hewson (1990). (See the book by Hewson, 1993, for additional references). Numerical renormalization-group methods have been recently applied in the LISA context by Sakai and Kuramoto (1994) and Shimizu and Sakai (1995); see, however, the remarks below in Sec. VI.C.

(ii) Mapping onto Coulomb gas models. The expansion in the hybridization (or in the spin-flip term for the Kondo model) leads to a mapping of quantum impurity models onto one-dimensional Coulomb gas models (Anderson, Yuval, and Hamann, 1970; Haldane, 1978b). For a general discussion of the Anderson impurity model using this mapping, and an application in the LISA context, see Si and Kotliar, 1993 (cf. Sec. VIII.D).

(iii) Bosonisation methods. When $\Delta(\omega)$ is constant at low frequency, the effective conduction bath can be parametrized as a one-dimensional model. This maps the quantum impurity model at low energies onto a (1+1)-dimensional field theory model. Bosonisation methods can be used in order to study this field theory model. The Coulomb gas mapping mentioned above can also be derived in this way (for an early study of the Kondo model along these lines, see Schotte and Schotte, 1969). For recent applications of bosonisation methods to quantum impurity models, see, e.g., Emery and Kivelson (1992); Sire, Varma, and Krishnamurthy (1993); Clarke, Giamarchi, and Shraiman (1993); Sengupta and Georges (1994); Georges and Sengupta (1995).

(iv) Special solvable points. The Coulomb gas representation and the bosonization method can also be used to derive explicit solutions at special values of the coupling constants. These solvable points may have the universal low-energy physics of the infrared fixed point controlling the model. Notorious examples are the Toulouse point of the single-channel Kondo model (Toulouse, 1970) and the Emery-Kivelson point in the two-channel case (Emery and Kivelson, 1992; see also Clarke, Giamarchi, and Shraiman, 1993; Sengupta and Georges, 1995). For a recent application in the LISA context to the mixed valence problem, see Kotliar and Si (1995).

(v) Large degeneracy and slave boson methods. Solvable limits of quantum impurity models can be found when the spin degeneracy is extended from SU(2) to SU(N) and the large-N limit is taken. These solutions can be used as approximation techniques for the N=2 case, and will be described in more detail in Sec. VI.B.3 below. For reviews, see, e.g., Newns and Read (1987), Coleman (1987), Bickers (1987), and Kotliar (1993a, 1994).

(vi) Conformal field theory methods. Recently, Affleck and Ludwig combined the mapping onto a (1+1)-dimensional field theory with the techniques of conformal field theory in the presence of a boundary in order to devise a new powerful approach for the study of low-energy properties of quantum impurity models. See the original articles by Affleck and Ludwig (1991).

(vii) Bethe-ansatz solutions. Exact solutions of quantum impurity models can be found in the limit of a flat conduction bath density of states with infinite bandwidth [$\Delta(\omega)$=const for $-\infty<\omega<+\infty$]. For a review, see Tsvelick and Wiegmann, 1983; Andrei, Furuya, and Lowenstein, 1983. Because of this restriction, these solutions are of little direct use in the LISA context, but they do yield the generic low-energy physics corresponding to a regular gapless $\Delta(\omega)$. Furthermore, as observed by Georges and Kotliar (1992) and Georges, Kotliar, and Si (1992), the LISA equations for lattice models with a Lorentzian noninteracting density of states $D(\epsilon)$ (corresponding to long-range hopping) map onto the integrable case.

All of these techniques have been mostly developed in the case where the effective bath density of states is constant and free of singularities at low frequency ($0<\Delta(0)<\infty$). It is conceivable that the LISA equations for some problems lead to consider densities of states $\Delta(\omega)$ having some low-energy singularity (e.g., vanishing or diverging as a power law). Some of the above techniques (such as renormalization-group methods) can be adapted to such cases (see, e.g., Withoff and Fradkin, 1990).

In the next three sections, we turn to analytic approximation methods that lead to explicit expressions for the

impurity orbital Green's function at all energies, and can be used for an approximate quantitative solution of the LISA equations.

2. The iterated perturbation theory approximation

The first approximation method that we describe has turned out to be very useful in investigating the half-filled Hubbard model and the physics of the Mott transition (Sec. VII). This method relies on early weak-coupling studies of the half-filled single-impurity Anderson model (Yosida and Yamada, 1970, 1975; Yamada, 1975; Salomaa, 1981; Zlatić, Horvatić, and Sokcević, 1985). In these works, it was shown that the second-order perturbation theory in U is a very good approximation up to values of $U/\Delta(0)\simeq 6$. In particular, it succeeds in capturing not only the quasiparticle (Abrikosov-Suhl) resonance, but also the upper and lower incoherent bands. Motivated by this observation, Georges and Kotliar (1992) first studied the $d=\infty$ Hubbard model by solving the effective impurity model using the second-order weak-coupling approximation to Σ (for a given Weiss field $\mathcal{G}_0$). Explicitly, one makes use of the approximate form for the self-energy:

$$\Sigma(i\omega_n)\simeq \frac{U}{2}+U^2\int_0^\beta d\tau\, e^{i\omega_n\tau}\hat{\mathcal{G}}_0(\tau)^3 \tag{157}$$

in which the shift $\hat{\mathcal{G}}_0^{-1}(i\omega_n)\equiv \mathcal{G}_0^{-1}-U/2$ has been made to enforce particle-hole symmetry. A self-consistent solution $(G,\mathcal{G}_0)$ is then found by going through the usual iteration. This is the iterated perturbation theory (IPT) approximation. The method is easily implemented by using fast Fourier transforms on the Matsubara axis. At zero temperature, it is most conveniently implemented by working with real-frequency Green's functions. Programs for both the zero-temperature and the finite-temperature iterated perturbation theory approximation are provided with this article (cf. Appendix D).

It was later realized (Zhang, Rozenberg, and Kotliar, 1993) that this method is actually not limited to moderate couplings (at half-filling), but it also correctly reproduces the exact strong-coupling limit. This is easily shown by considering the atomic limit $D/U\to 0$, for which $\hat{\mathcal{G}}_0^{-1}\approx i\omega_n$, and the exact Green's function and self-energy read $G(i\omega_n)\approx \frac{1}{2}[1/(i\omega_n+U/2)+1/(i\omega_n-U/2)]$, $\Sigma(i\omega_n)\approx U/2+U^2\mathcal{G}_0(i\omega_n)/4$. Hence, Eq. (157) correctly reproduces this limit. Thus, the iterated perturbation theory approximation provides an "interpolation" scheme between the weak-coupling and strong-coupling limits that are both captured exactly. The fact that a weak coupling expansion happens to work in the strong coupling case is a "fortunate" coincidence. It no longer holds in the particle-hole asymmetric case. At half filling, the iterated perturbation theory approximation displays a Mott transition of the paramagnetic solution, as will be reviewed in detail in Sec. VII. The iterated perturbation theory approximation gives results in very good agreement with the QMC and exact diagonalization results (except very close to the Mott transition point), as reviewed in Sec. VI.A.4 and detailed in the studies of Zhang, Rozenberg, and Kotliar, 1993; Georges and Krauth, 1993; Rozenberg, Kotliar, and Zhang, 1994. The rationale behind this success is that the Anderson impurity model is *analytic* in U irrespectively of the nature of the bath, so that it can be treated perturbatively. The nonanalyticities (such as the opening of a gap) stem from the lattice aspects of the problem and are brought in by the self-consistency condition. The value of the iterated perturbation theory approximation relies largely on its simplicity: it is much easier to implement than the full numerical solution of the model, and allows a fast scan of parameter space. The iterated perturbation theory approximation has been successfully extended to various other models in the LISA framework, such as the Holstein model (Freericks and Jarrell, 1994a, 1994b; cf. Sec. VIII.E).

Various other methods based on weak-coupling approximations have been used in the literature for $d=\infty$ lattice models, namely (i) *the direct weak-coupling perturbation theory* to $O(U^2)$ in which the *free* local Green's function $G_{U=0}=\tilde{D}(i\omega_n)$ is used in (157) in place of $\hat{\mathcal{G}}_0$ (Schweitzer and Czycholl, 1991a); and (ii) *the "self-consistent" weak-coupling approaches*, which look for a solution with the *interacting* G replacing $\hat{\mathcal{G}}_0$ in Eq. (152) (Müller-Hartmann, 1989b; Schweitzer and Czycholl, 1991b), and has also been generalized to include bubble and ladder summations by Menge and Müller-Hartmann (1991). [See Freericks (1994) for a comparison of various methods.]

These approaches should not be confused with the iterated perturbation theory approximation. All three methods of course coincide for small values of U. However, only the iterated perturbation theory provides an interpolation scheme between weak and strong coupling at half-filling and therefore correctly captures the formation of the incoherent band and the physics of the Mott-Hubbard transition. Specifically, it is found (Georges and Kotliar, 1992) that already for intermediate values of U, the metallic spectral density displays incoherent features around energies $\pm U/2$, corresponding to the upper and lower Hubbard bands. As will be shown in Sec. VI.A.4, these features are indeed present in the spectral density obtained numerically (with which the iterated perturbation theory approximation is in good agreement). In contrast, they are absent from the self-consistent weak-coupling approximations. Note that, for intermediate coupling, these features are indeed predicted by the direct weak-coupling expansion. This remark has been known for a long time in the context of the single impurity Anderson model (for recent work, see, e.g., White, 1992).

It would be quite interesting and of great practical use to develop a reliable extension of the iterated perturbation theory approximation away from half-filling. However, this is not so easy to achieve because naive extensions of the original iterated perturbation theory method do not automatically fulfill the Luttinger theorem away from half-filling. Specifically, if one computes the total density at $T=0$ from $n/2=\int_{-\infty}^{0} d\omega\rho(\omega)$, the iterated perturbation theory approximation for Σ does not satisfy in

general the Luttinger condition, which reads in the present case $\mu-\Sigma(i0^+)=\mu_0(n)$, where μ_0 is the noninteracting chemical potential corresponding to the density n. Only at half-filling is this preserved by the iterated perturbation theory approximation.

Very recently, Kajueter and Kotliar (1995) proposed an extension of the iterated perturbation theory for arbitrary filling, using an interpolation scheme that becomes exact in various limits: (a) the atomic limit, (b) in an expansion in powers of U up to second order in U (c) at very high frequencies, and (d) at zero frequency. Furthermore it fulfills the Luttinger theorem and is in excellent agreement with exact diagonalization results.

3. Slave boson methods and the noncrossing approximation

Slave boson methods for quantum impurity models can be viewed as a way of handling the singular perturbation in the hybridization. When the spin degeneracy is extended from SU(2) to SU(N) and the limit $U=\infty$ is taken, these methods can be viewed as a systematic reorganization of this perturbation theory as a $1/N$ expansion. In the following, we review two slave-boson approximations which differ from each other in that the auxiliary boson is condensed or not. The former is adapted to the low-energy description of a Fermi liquid state but does not capture the high-energy incoherent features to dominant order, while the latter (known as the noncrossing approximation) provides a description of these high-energy features but does not capture correctly the low-energy Fermi liquid behavior. The aim of this section is to convey only the general spirit of those methods, and mention their application in the LISA context. The reader is directed to the articles of Bickers (1987), Coleman (1987), Newns and Read (1987), and Kotliar (1993a, 1994) for further details. Also, the equations are explicitly quoted only for the $U=\infty$ single-impurity Anderson model. Extension to the case of finite U is discussed in the papers of Kotliar and Ruckenstein (1986) (for approximations in which the bosons are condensed) and Pruschke and Grewe (1989) (finite-U noncrossing approximation).

In the following, we deal with the single-impurity Anderson model effective action (105), with the Weiss function written in the form

$$\mathcal{G}_0^{-1}(i\omega_n)=i\omega_n-\epsilon_d-\tilde{\Delta}(i\omega_n), \tag{158}$$

where $\tilde{\Delta}$ is the Hilbert transform of the effective conduction electron bath density of states:

$$\tilde{\Delta}(i\omega_n)=\int_{-\infty}^{+\infty}d\omega\,\frac{\Delta(\omega)}{i\omega_n-\omega}. \tag{159}$$

We introduce a slave boson representation of the impurity orbital. When the latter is empty, we represent it as $b^+|0\rangle$, and when it is occupied by an electron of spin σ, we represent it as $f_\sigma^+|0\rangle$, so that the original impurity creation operator reads

$$d_\sigma^+=f_\sigma^+ b. \tag{160}$$

The spin degeneracy is extended from SU(2) to SU(N) ($\sigma=1,\ldots,N$), and we concentrate on the $U=\infty$ limit with a constraint of no double occupancy (for $N=2$) generalized to

$$b^+b+\sum_\sigma f_\sigma^+ f_\sigma=\frac{N}{2}. \tag{161}$$

With this representation, the effective action of the impurity model can be written in the form:

$$\begin{aligned}S_{\rm eff}=&\int_0^\beta d\tau\Bigg\{\sum_\sigma f_\sigma^+[\partial_\tau+\epsilon_d]f_\sigma\\&+i\lambda(\tau)\Bigg(\sum_\sigma f_\sigma^+ f_\sigma+b^+b-\frac{N}{2}\Bigg)\Bigg\}\\&+\frac{2}{N}\int_0^\beta d\tau\int_0^\beta d\tau'\sum_\sigma f_\sigma^+(\tau)b(\tau)\\&\times\tilde{\Delta}(\tau-\tau')b^+(\tau')f_\sigma(\tau')\end{aligned} \tag{162}$$

In this expression, $\lambda(\tau)$ is a Lagrange multiplier field associated with the constraint (161), over which it has to be integrated.

a. Slave boson mean-field theory

The first approximation that we consider consists in taking the $N\to\infty$ limit of this model. With the above scaling, the model can be solved in this limit by a saddle-point method, such that the Lagrange multiplier becomes static at the saddle point, and the boson field has negligible fluctuations around a nonzero vacuum expectation value (boson condensate):

$$\langle b\rangle\equiv\sqrt{N/2}r_0,\quad \langle i\lambda\rangle=\lambda_0. \tag{163}$$

The pseudofermion Green's function reads, at the saddle point,

$$\begin{aligned}G_f(i\omega_n)\equiv&\langle f_\sigma^+(i\omega_n)f_\sigma(i\omega_n)\rangle\\=&\frac{1}{i\omega_n-\epsilon_d-\lambda_0-r_0^2\tilde{\Delta}(i\omega_n)},\end{aligned} \tag{164}$$

and the values of r_0,λ_0 are determined by the following saddle-point equations obtained by minimizing the free energy associated with (162);

$$\frac{r_0^2}{2}+\frac{1}{\beta}\Sigma_n G_f(i\omega_n)e^{i\omega_n 0^+}=\frac{1}{2}, \tag{165}$$

$$\lambda_0+\frac{2}{\beta}\Sigma_n G_f(i\omega_n)\tilde{\Delta}(i\omega_n)e^{i\omega_n 0^+}=0. \tag{166}$$

For a discussion of the solution of these equations, we refer the reader to the articles by Newns and Read (1987) and Kotliar (1993a, 1994). An extension of the slave-boson mean-field theory to finite U has been given by Kotliar and Ruckenstein (1986). In this case, the saddle-point approximation is no longer controlled by a large-N limit.

Let us discuss the form of the *physical* impurity orbital spectral function. The corresponding Green's function reads, from (160) and (164),

$$G_d(i\omega_n)=\langle b\rangle^2 G_f(i\omega_n)=\frac{Nr_0^2/2}{i\omega_n-\epsilon_d-\lambda_0-r_0^2\tilde{\Delta}(i\omega_n)}. \tag{167}$$

Since $\tilde{\Delta}(\omega+i0^+)\simeq -i\pi\Delta(0)$ for $\omega\simeq 0$, it is clear from this expression that $\rho_d(\omega)$ basically consists of a (quasiparticle) resonance centered on the effective d level $\epsilon_d+\lambda_0$. The width of this resonance is of order $\pi r_0^2\Delta(0)$, which must be interpreted as the low-energy coherence scale (Kondo temperature). Below this scale, a Fermi-liquid description of the low-energy properties is obtained.

The overall spectral weight carried by $\rho_d(\omega)$ is given (for $N=2$) by just r_0^2. The missing spectral weight corresponds to the high-energy incoherent features, which are absent at the saddle-point level. These features are reintroduced when fluctuations around the saddle point are taken into account (Bang *et al.*, 1992; Castellani *et al.*, 1992; Raimondi and Castellani, 1993; Kotliar, 1993a, 1994).

When applied to the LISA equations for e.g., the $U=\infty$ Hubbard model or the $U=\infty$ periodic Anderson model, the slave boson mean-field theory simply amounts to solve directly these lattice models in the simultaneous $d=\infty$ and $N=\infty$ limits. For finite U, one can apply the four-boson mean-field approximation of Kotliar and Ruckenstein (1986) to the effective impurity model. When combined with the LISA self-consistency condition, this leads to the same equations as the Gutzwiller (1965) approximation applied directly to the lattice model. We note in passing that, in the $d\to\infty$ limit, the Gutzwiller approximation was demonstrated by Metzner and Vollhardt (1989) to yield the exact average value of various physical quantities in the Gutwiller wave function (i.e., $\langle \mathrm{GWF}|O|\mathrm{GWF}\rangle$ can be computed exactly from the Gutzwiller approximation in $d=\infty$). However, the Gutzwiller wave function is still not the exact ground-state wave function of the Hubbard model, even for $d=\infty$.

One of the strongest motivations for the LISA approach, which is to treat the low-energy and incoherent spectral features on an equal basis, is thus lost when a slave boson mean-field approximation is made on the LISA equations. It would be quite interesting however to perform a full calculation of the impurity spectral function to order $1/N$ and to use this calculation in the LISA framework. The variational $1/N$ result of Gunnarson and Schönhammer (1983a, 1983b) could also be used in the LISA context (Lelievre, Misguich, and Georges, 1995).

b. The noncrossing approximation

In order to capture the high-energy features of the spectral function at dominant order, the slave-boson effective action can be handled in a different manner. The idea is to perform a particular resummation of the perturbative expansion in powers of the hybridization $\tilde{\Delta}$ (which was scaled by $1/N$ in the effective action (162) above. This resummation can actually be viewed as a controlled procedure if the slave boson is supplemented with an additional "color index" b_α, $\alpha=1,\ldots,M$ and a simultaneous $N\to\infty$, $M\to\infty$ limit is taken with M/N fixed (Newns and Read, 1987; Cox and Ruckenstein, 1993). The resummation takes into account all self-energy diagrams for both the pseudofermion and the slave boson, which contain no crossing of the internal propagators, hence the name noncrossing approximation. These diagrams are depicted in Fig. 20. For references to the rather vast literature on the noncrossing approximation method, the reader is directed to the review article by Bickers (1987).

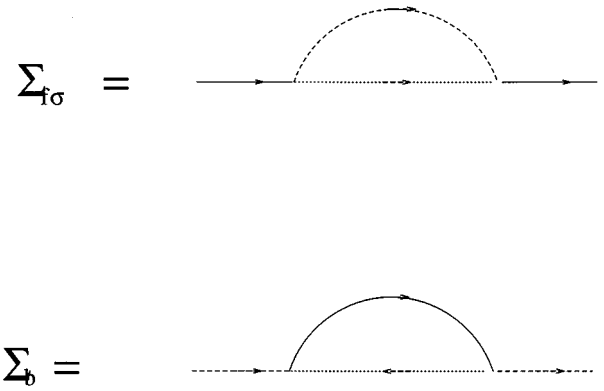

FIG. 20. Diagrams contributing to the pseudofermion and slave boson self-energies in the noncrossing approximation resummation. Plain lines stand for the full fermion propagator, dashed lines for the full boson propagator and dotted lines for the hybridization function.

Higher-order terms in this expansion have been recently considered by Anders (1995), and have been shown to substantially improve some of the noncrossing approximation pathologies. Application of these methods to the LISA would certainly be of interest.

The equations corresponding to the resummation of the diagrams in Fig. 20 are coupled equations for the pseudofermion and slave boson Green's functions and self-energies. The latter are defined as

$$\begin{aligned} G_f(i\omega_n)_\sigma &\equiv \frac{1}{i\omega_n-\epsilon_d-\Sigma_f(i\omega_n)}, \\ G_b(i\omega_m) &\equiv \frac{1}{i\omega_m-\Sigma_b(i\omega_m)}. \end{aligned} \tag{168}$$

The $U=\infty$ noncrossing approximation equations read

$$\begin{aligned} \Sigma_f(\tau-\tau') &= \frac{2}{N}\tilde{\Delta}(\tau-\tau')G_b(\tau-\tau'), \\ \Sigma_b(\tau-\tau') &= 2\tilde{\Delta}(\tau'-\tau)G_f(\tau-\tau'), \end{aligned} \tag{169}$$

and, using (160), the physical impurity Green's function is obtained as a convolution of the pseudofermion and slave boson propagators:

$$G_d(\tau)=G_f(\tau)G_b(-\tau). \tag{170}$$

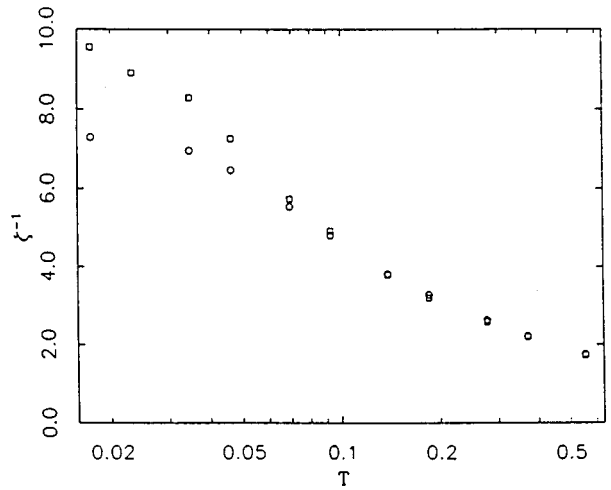

FIG. 21. Inverse of the temperature-dependent quasiparticle weight as defined in the text for the Hubbard model on the hypercubic lattice ($t_{ij}=\frac{1}{2}\sqrt{d}$) with $U=4$, $\mu=1$ ($n\simeq 0.94$). The circles are the QMC results and the squares the noncrossing approximation. (From Pruschke, Cox, and Jarrell, 1993b.)

These equations have been extended to the finite-U case by Pruschke and Grewe (1989).

A low-energy analysis of the noncrossing approximation equations can be performed analytically at zero temperature (Müller-Hartmann, 1984). A low-energy scale is generated as before, which can be interpreted as the Kondo temperature. Below this scale however, the NCA equations fail to reproduce Fermi-liquid properties. For example, the spectral function develops a low-frequency power-law singularity $\rho_d(\omega)\sim\text{const}+\omega^{1/(N+1)}+\cdots$. This is not surprising in retrospect since the noncrossing approximation equations become justified for a large number of conduction electron channels and actually yield the *exact* non-Fermi liquid behavior characteristic of multichannel models (Cox and Ruckenstein, 1993). Above this low-energy scale however, the noncrossing approximation produces a reasonable description of the spectral features even in the one-channel case, at least when the system is dominated by spin fluctuations, i.e., not too far from the particle-hole symmetric case.

The noncrossing approximation has been extensively applied in the LISA context as an approximate way of solving the effective impurity model, and as a default model supplementing the maximum entropy analytic continuation of QMC data. For applications to the Anderson lattice, see the early works of Kuramoto (1985) and Kim, Kuramoto, and Kasoya (1990). For applications to the Hubbard model, see the work of Jarrell and Pruschke (1993a, 1993b) and Pruschke, Cox, and Jarrell (1993a, 1993b). The plot in Fig. 21, reproduced from the work of these authors, allows one to assess the degree of validity of the noncrossing approximation for the Hubbard model on the hypercubic lattice with $U=4t$ ($t_{ij}=t/\sqrt{d}$) and a density $n\simeq 0.94$. It displays the quantity $\zeta(T)^{-1}=1-\text{Im}\Sigma(i\omega_0)/\omega_0$, where $\omega_0=\pi T$ is the first Matsubara frequency corresponding to the temperature T, and Σ is the self-energy. $\zeta(T=0)$ coincides with the quasiparticle residue Z. In Fig. 21 the QMC and noncrossing approximation results for this quantity are compared to each other. It is seen that the noncrossing approximation is reliable down to $T/T_{\text{coh}}\simeq 1/5$, where T_{coh} is the low-energy coherence scale (estimated by the authors to be $T_{\text{coh}}\simeq t/8$ in this case). Below $T_{\text{coh}}/5$, the noncrossing approximation suffers from the low-energy singularities mentioned above. It should also be noted that the noncrossing approximation results for the spectral density of the Mott insulating phase display unphysical peaks at the gap edge.

4. Equations of motion decoupling schemes

Another method to obtain approximations of the high-frequency parts of the impurity spectral function is to use decoupling schemes for the hierarchy of exact relations between Green's functions resulting from the equations of motion. These decoupling schemes can in general be justified at sufficiently high temperature. At low temperature, the resulting approximations suffer from singularities reflecting the singularities in the perturbative expansions in the hybridization. These singularities can be more or less severe depending on the crudeness of the approximations made in the decoupling scheme. Such approximation schemes have been used for the single impurity Anderson model by various authors (see, e.g., Appelbaum and Penn, 1969; Theumann, 1969; Lacroix, 1981). In the LISA context, they have been investigated recently by Gros (1994).

Let us briefly describe the simplest nontrivial approximation obtained in this way. Decoupling the equations of motion at second order yields the following approximation for the impurity Green's function (Theumann, 1969):

$$G(i\omega_n)=\frac{1-n/2}{\mathcal{G}_0^{-1}(i\omega_n)+\dfrac{U\Pi_1(i\omega_n)}{\mathcal{G}_0^{-1}(i\omega_n)-U-\Pi_3(i\omega_n)}}+\frac{n/2}{\mathcal{G}_0^{-1}(i\omega_n)-U-\dfrac{U\Pi_2(i\omega_n)}{\mathcal{G}_0^{-1}(i\omega_n)-\Pi_3(i\omega_n)}}. \tag{171}$$

In which the "self-energies" Π_i read

$$\Pi_i(i\omega_n)=\int_{-\infty}^{+\infty}d\omega\ \Delta(\omega)\left(\frac{1}{i\omega_n-\omega}-\frac{1}{U+2\epsilon_d-i\omega_n-\omega}\right)\times F_i(\omega) \tag{172}$$

with $F_1(\omega)=f(\omega)$, $F_2(\omega)=1-f(\omega)$, $F_3(\omega)=1$, where $f(\omega)$ is the Fermi factor. The total density has to be determined self-consistently from $n/2=-(1/\pi)\int d\omega\ \text{Im}G(\omega+i0^+)$. In the $T=0$ limit, the Π's have logarithmic singularities signalling the Kondo effect, which is not correctly treated at this level of approximation. Lacroix (1981) has shown how to extend

this scheme so that a finite Kondo resonance is obtained (which however does not have the correct Fermi-liquid Lorentzian shape).

In the LISA context, the above equations have to be supplemented with the self-consistency condition (and ϵ_d set to $-\mu$), resulting in an integral equation for the effective bath density of states $\Delta(\omega)$. This integral equation simplifies considerably at half-filling (particle-hole symmetric case $n=1$, $\epsilon_d=-U/2$). Indeed, one then has $\Pi_1=\Pi_2=\Pi_3/2=\tilde{\Delta}(i\omega_n)$.

Specializing to the case of the half-filled Hubbard model on the Bethe lattice with $t_{ij}=t/\sqrt{z}$, for which the self-consistency condition reads $\tilde{\Delta}(i\omega_n)=t^2G(i\omega_n)$, a closed algebraic equation for G is obtained:

$$3t^4G^3-4t^2\omega G^2+\left(\omega^2-\frac{U^2}{4}+3t^2\right)G-\omega=0. \quad (173)$$

This approximation was first obtained by Hubbard (1964) and is known as the Hubbard III approximation. It displays a Mott transition with the opening of a gap at $U_c=2\sqrt{3}t=\sqrt{3}D$ (with D the half-width of the semicircular density of states). At strong coupling, when the gap is finite, or at high temperatures, the approximation is reasonable, as we explain in more detail in Sec. VII. Below U_c, however, the approximation fails to comply with Fermi-liquid theory because the Kondo effect is not properly described. Gros (1994) has studied the extension of this approximation to higher order in the decoupling scheme.

C. The projective self-consistent technique

As will be discussed in Secs. VII and VIII, many strongly correlated electron systems exhibit a wide range of energy scales. A clear example is the Hubbard model for intermediate and large values of the interaction ($U\geqslant 2.5D$) and for zero and small doping δ. This causes unsurmountable problems to the fully numerical methods described above, which are unable to resolve the interesting low-energy features at the heart of the strong correlation problem. The difficulty can be traced to the finite number of time-slices in the quantum Monte Carlo method or the finite number of orbitals n_s in the exact diagonalization technique.

Let us take as a concrete example the Hubbard model at half-filling, which will be studied in detail in Sec. VII. The spectrum can be separated into three distinct features (cf. Fig. 22). The high energy features are given by the broad upper and lower Hubbard bands which are centered at energies $-\mu$ and $U-\mu$. At half-filling $\mu=U/2$, such that they are centered symmetrically about the Fermi level at $\pm U/2$. These are well separated from the narrow Kondo resonance at the Fermi level, the weight of which, w, goes to zero at the metal-insulator transition. When w becomes small the LISA system of equations contains two vastly different energy scales, given by the chemical potential μ or U and the width of the Kondo resonance, wD, rendering an accurate direct numerical treatment impossible.

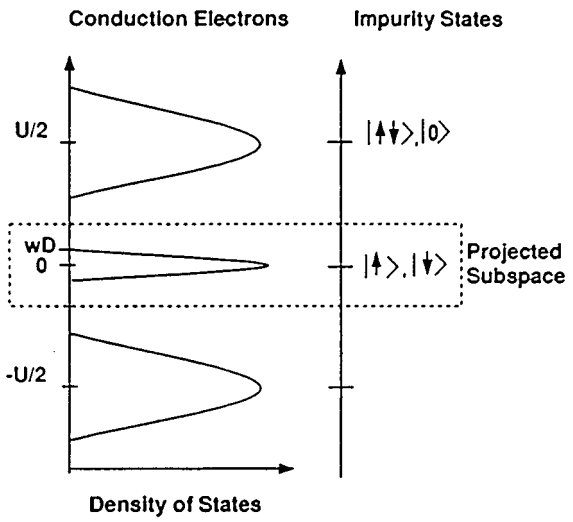

FIG. 22. Schematic plot of the conduction bath spectral function and impurity orbital configurations, illustrating the separation of energy scales at half-filling, close to the Mott transition.

While the need to resolve features that are one hundredth of the bandwidth may seem unnatural from the point of view of numerical analysis it is in fact the common situation that one faces in condensed matter theory. For the copper oxides, to give an example, the LDA calculations, used to derive the one-band Hubbard model, give a hopping integral of the order of 0.5 eV or a full bandwidth of 2.0 eV. This means that the parameter D in the LISA equations is of the order of 10 000 K. On the other hand, measurements on these systems are performed in a temperature range from 1 to 600 K, that is from 10^{-4} to 6×10^{-2} of the natural energy scale. Band structure calculations of transition metal oxides give bands which are about 4 eV wide, i.e., D is about 20 000 K. Metal-insulator transitions occur below temperatures of the order of 400 K, so the interesting physics takes place at a scale which is 50 times smaller than the bare energy scales of the problem. More examples are discussed in Sec. VIII.

In this section we will describe the projective self-consistent method developed by Moeller *et al.* (1995) which exploits the natural separation of scales present in the strong correlation problem by *eliminating* the high-energy degrees of freedom, thereby reducing the full problem to an effective low-energy problem containing only *one scale*, which can be tackled numerically. From the resulting effective problem one can obtain low-frequency (temperature) results, as well as information about the critical behavior of the models considered. The self-consistent projective method has been successfully used in the study of the Mott transition problem, but we stress that the main ideas are widely applicable because the method only relies on the separation of scales.

Before discussing the formalism in detail, it is useful to make an analogy with the Landau-Ginzburg theory.

Faced with a complicated problem, say a magnetic phase transition in a metallic alloy, such as Fe, a time-honored strategy is to divide the problem into two parts. To discuss the problem at low energies one writes down an effective Landau theory which contains the low-energy degrees of freedom (coarse-grained slowly varying magnetization), which one treats with the methods of statistical mechanics. All the details of the high-energy physics, i.e., the band structure of the alloy, the relevant atomic configurations, and their interactions, are buried in a few coefficients, the parameters of the Landau-Ginzburg Hamiltonian. A complete first-principles solution for a given material requires a microscopic calculation of these coefficients, which is sometimes done using LDA methods.

It is worthwhile to stress several points of this methodology: (1) much can be learned from the existence of a Landau expansion without having to calculate the Landau coefficients, (2) the techniques used in the solution of high-energy part and the low-energy part are completely different and (3) a direct numerical solution of the Schrödinger equation for an iron alloy in order to understand the critical behavior near the ferromagnetic phase transition is computationally intractable. These points are relevant to the application of the LISA to complex problems.

The projective self-consistent method applies this philosophy to the solution of the LISA equations. An early discussion of these ideas in the context of a two-band model with repulsive interactions can be found in the work of Kotliar and Si (1993; see also Si and Kotliar, 1993) and illustrates the main points. In that work, the model with repulsive interactions is mapped onto an impurity model where the charge-charge interactions between the different bands is repulsive. The high-energy part of the spectral function of the impurity and of the bath has a rich structure, and is treated by using a canonical transformation in order to obtain a low-energy effective problem, a new impurity model with a featureless bath and *attractive* charge-charge interactions. At this point, a renormalization group can be used to analyze the low-energy behavior leading to various possible phases (including non-Fermi liquid ones), as described in Sec. VIII.D.

In this section, we shall take the Hubbard model as an example in order to demonstrate how the self-consistent projective technique enables us to analyze the physical properties near the Mott transition. The emphasis is on the methodology since many of the results on this physical problem are reviewed in detail in Sec. VII.

As one can see immediately from the spectral functions described in Fig. 22, the separation of scales implies that it is possible to decompose the single particle density of states $\rho(\epsilon)$ of the Hubbard model into high- and low-frequency parts as $\rho(\epsilon)=\rho^{\rm low}(\epsilon)+\rho^{\rm high}(\epsilon)$. Given the mapping of the Hubbard model onto a single impurity Anderson model,

$$\mathscr{H}_{\rm AM}=\sum_{k\sigma}\epsilon_k c^\dagger_{k\sigma}c_{k\sigma}+\sum_{k\sigma}V_k(f^\dagger_\sigma c_{k\sigma}+\text{H.c.})+Un_{f\uparrow}n_{f\downarrow}-\mu(n_{f\uparrow}+n_{f\downarrow}) \tag{174}$$

with self-consistency condition (on the Bethe lattice):

$$\sum_k \frac{4V_k^2/D^2}{i\omega_n-\epsilon_k}=G[\epsilon_k,V_k](i\omega_n), \tag{175}$$

we separate the variables ϵ_k and V_k describing the self-consistently determined bath of conduction electrons into sets $\{\epsilon_{k,H},V_{k,H}\}$, corresponding to the high-energy features, and $\{\epsilon_{k,L},V_{k,L}\}$, containing the low-energy states, up to a cutoff given by the Kondo temperature or renormalized Fermi energy of the Hubbard model and carrying spectral weight

$$w=4/D^2\sum_{k\in\text{low}}V_{k,L}^2. \tag{176}$$

In order to eliminate the high-energy degrees of freedom, we first separate the impurity Hamiltonian $\mathscr{H}_{\rm AM}$ into three parts as

$$\mathscr{H}_{\rm AM}=\mathscr{H}_{\rm at}+\mathscr{H}_b+\mathscr{H}_M. \tag{177}$$

$\mathscr{H}_{\rm at}$ is given as

$$\mathscr{H}_{\rm at}=Un_{f\uparrow}n_{f\downarrow}-\mu(n_{f\uparrow}+n_{f\downarrow})+\sum_{\sigma k\epsilon\,\text{high}}V_{k,H}(c^+_{k\sigma}f_\sigma+\text{H.c.})+\sum_{\sigma k\epsilon\,\text{high}}\epsilon_{k,H}c^+_{k\sigma}c_{k\sigma}, \tag{178}$$

and can be thought of as an Anderson impurity in a semiconductor.

$$\mathscr{H}_b=\sum_{k\epsilon\,\text{low},\sigma}wD\,\tilde\epsilon_k c^+_{k\sigma}c_{k\sigma} \tag{179}$$

describes a narrow band of low energy conduction electrons. Since the energy will turn out to be of order wD, we have introduced dimensionless, rescaled variables $\tilde\epsilon_k=\epsilon^L_k/(wD)$. The hybridization $\mathscr{H}_M$ with the low-energy electrons is given by

$$\mathscr{H}_M=\sqrt{w}D\sum_\sigma(c^\dagger_{L\sigma}f_\sigma+\text{H.c.}) \tag{180}$$

with

$$c_{L\sigma}\equiv\sum_{k\epsilon\,\text{low}}2\tilde V_k c_{k\sigma} \tag{181}$$

the local low-energy conduction electron operators normalized to have canonical anticommutation relations

$$\{c_{L\sigma},c^\dagger_{L\sigma}\}=1, \tag{182}$$

$$\{c_{L\sigma},c_{L\sigma}\}=\{c^\dagger_{L\sigma}c^\dagger_{L\sigma}\}=0. \tag{183}$$

Again we have rescaled the $V_{k,L}$ by introducing the variables $\tilde V_k=V_{k,L}/(\sqrt{w}D)$, which shows explicitly the perturbative nature of the hybridization with the low-energy band.

As long as we are in the local moment regime of the impurity model, which is the case in the critical region, the contribution to the Hamiltonian containing the high-energy states, $\mathscr{H}_{\rm at}$, has low-lying spin doublet ground states $|\sigma\rangle_{H_{\rm at}}$ with energy $E^{\rm at}_{\rm g.s.}$. These are separated by a gap of order μ from the high-energy excited states. These high-energy states (i.e., the excited states of $\mathscr{H}_{\rm at}$) are denoted by $|\alpha\rangle$. This structure of the eigenstates can be seen most clearly by considering the impurity orbital *only*. The four possible states in that case are the doublet ground state $|\sigma\rangle = f^\dagger_\sigma|0\rangle$ with energy $-\mu$, which is well separated from the doubly occupied and empty states, $f^\dagger_\uparrow f^\dagger_\downarrow|0\rangle$ and $|0\rangle$, at energies $U-2\mu$ and 0, respectively. Hybridizing the single impurity with lower and upper Hubbard bands simply renormalizes the states by "dressing" them with particle-hole excitations without altering their transformation properties, i.e. the ground state remains a degenerate doublet.

Upon diagonalizing $\mathscr{H}_{\rm at}$, the full Hamiltonian can thus be decomposed into a high-energy sector spanned by the states $\{|\alpha\rangle_{H_{\rm at}}\} \otimes \{|\psi_L\rangle\}$, a low-energy sector spanned by the states $\{|\sigma\rangle_{H_{\rm at}}\} \otimes \{|\psi_L\rangle\}$ with $\{|\psi_L\rangle\}$ states of the $c^L_{k\sigma}$, and mixing terms. In order to obtain the effective low-energy Hamiltonian, we perform a *canonical transformation* which eliminates the coupling between high- and low-energy subspaces and thus yields effective low- and high-energy Hamiltonians. We thus have to find an operator S mediating the transformation such that the effective Hamiltonian is block diagonal, i.e., find S such that

$$\mathscr{H}^{\rm eff} = e^{-S}\mathscr{H}_{\rm AM}e^{S} = \mathscr{H}^{\rm eff}_L + \mathscr{H}^{\rm eff}_H, \tag{184}$$

where the subscripts L and H denote operators acting exclusively on the low- and high-energy sectors, respectively. Notice that if the high-energy band just consisted of a single state, this procedure would be equivalent to a Schrieffer-Wolff canonical transformation (Schrieffer and Wolff, 1966). The information about virtual excitations to high- and low-energy sectors is contained in the coefficients of the terms in the effective low- and high-energy Hamiltonians, respectively.

Having decomposed the Hamiltonian into high- and low-energy parts, we now have to transform operators, Green's functions, and self-consistency condition accordingly. The canonical transformation amounts to a *basis transformation*, implying that *all operators* have to be transformed correspondingly. In particular, for the determination of the single-particle Green's function, we obtain projected fermion operators

$$F_\sigma \equiv F^{LL}_\sigma + F^{LH}_\sigma + F^{HL}_\sigma + F^{HH}_\sigma \equiv e^{-S} f_\sigma e^{S}. \tag{185}$$

The superscripts HL and LH denote operators connecting low- and high-energy sectors. The low- and high-energy contributions to the Green's function assume the form (at zero temperature):

$$G_{\rm low}(i\omega_n) = \left\langle F^{LL}_\sigma \frac{1}{i\omega - (\mathscr{H}^{\rm eff}_L - E_{\rm g.s.})} F^{LL\dagger}_\sigma \right\rangle + \left\langle F^{LL\dagger}_\sigma \frac{1}{i\omega + (\mathscr{H}^{\rm eff}_L - E_{\rm g.s.})} F^{LL}_\sigma \right\rangle \tag{186}$$

and

$$G_{\rm high}(i\omega_n) = \left\langle F^{LH}_\sigma \frac{1}{i\omega - (\mathscr{H}^{\rm eff}_H - E_{\rm g.s.})} F^{\dagger HL}_\sigma \right\rangle + \left\langle F^{LH\dagger}_\sigma \frac{1}{i\omega + (\mathscr{H}^{\rm eff}_H - E_{\rm g.s.})} F^{HL}_\sigma \right\rangle. \tag{187}$$

The self-consistency condition (175) can then be decomposed as

$$0 = \sum_k \frac{V^2_{k,L}}{i\omega_n - \epsilon_{k,L}} - t^2\, G_{\rm low}[i\omega_n; V_{kL}, \epsilon_{kL}, V_{kH}, G_{kH}], \tag{188}$$

$$0 = \sum_k \frac{V^2_{k,H}}{i\omega_n - \epsilon_{k,H}} - t^2\, G_{\rm high}[i\omega_n; V_{kL}, \epsilon_{kL}, V_{kH}, G_{kH}]. \tag{189}$$

Equations (188) and (189) are strictly equivalent to the original problem and form the basis of the self-consistent projective technique.

The crucial observation is that a detailed analysis of the low-frequency region equation (188) depends only weakly on the high-energy part of the spectrum, which enters *only* through a few numerical coefficients, as we will see in the case of the Hubbard model. Conversely, the high-energy part Eq. (189) only depends weakly on the low-energy part.

There are therefore various levels on which the equations can be studied. In the model at hand, in which the physics is well understood, a *quantitative* analysis of the equations has been achieved. In less well understood problems one can start by making crude approximations for the high-energy parameters and obtain *qualitative* insights by investigating the corresponding consequences for the low-energy part. Again it is illuminating to make the connection to a Landau-Ginzburg approach, in which qualitative insights about a physical problem can be gained without knowledge of the numerical details.

The formalism described so far is quite general, and can in principle be carried out numerically by solving for the canonical transformation S along the lines of (Kutzelnigg, 1982; Kutzelnigg and Koch, 1983). Alternatively one can use semianalytic schemes to get insight into the nature of the problem. For example, replacing the insulator by a three-site system turns out to be within 15% of the more precise results.

Near the transition it turns out that one can use the weight w as an expansion parameter anticipating that it will be of order $U_c - U$ in the half-filled case or $|\mu_c - \mu|$ for large U away from half-filling. The canonical transformation is then implemented in a systematic expansion in the "small parameter" w and in $\Delta = U - U_c$ or

$\mu-\mu_c$. Then one solves for w as a function of Δ and shows that this expansion is justified, i.e., that it is vanishingly small as Δ approaches zero. This procedure is standard in singular perturbation problems.

The generator of the canonical transformation has an expansion

$$S=\sqrt{w}S^{(1)}+w^{3/2}S^{(3)}+\cdots . \tag{190}$$

The expansion yields

$$\mathscr{H}_L^{\rm eff}=w.\mathscr{H}_L^{{\rm eff}(1)}+w^2.\mathscr{H}_L^{{\rm eff}(3)}+\cdots , \tag{191}$$

$$\mathscr{H}_H^{\rm eff}=\mathscr{H}_H^{{\rm eff}(0)}+w.\mathscr{H}_H^{{\rm eff}(1)}+\cdots \tag{192}$$

and

$$F_\sigma^{LL}=\sqrt{w}F_\sigma^{LL(1)}+w^{3/2}F_\sigma^{LL(3)}+\cdots , \tag{193}$$

$$F_\sigma^{LH}=F_\sigma^{LH(0)}+wF_\sigma^{LH(2)}+\cdots , \tag{194}$$

Correspondingly the high- and low-energy contributions to the Green's function can be expanded order by order as

$$G_{\rm high}(i\omega_n)=G_{\rm high}^{(0)}(i\omega_n)+wG_{\rm high}^{(1)}(i\omega_n), \tag{195}$$

$$G_{\rm low}(i\omega_n)=wG_{\rm low}^{(1)}(i\omega_n)+w^2G_{\rm low}^{(2)}(i\omega_n). \tag{196}$$

Depending on whether we are interested in the properties *at* the critical point, at which $w\to 0$, or *near* the critical point, we have to solve the self-consistency equations (188) and (189) to order w or to order w^2. For the purpose of determining the low-energy parameters, the expansion in w of the high-energy Green's function is regular.

For the determination of the physical properties *at* the critical point coming from the metallic side, for which $w\to 0^+$, it is clearly sufficient to treat equations (188) and (189) to *lowest order* in w, i.e., we have to solve

$$0=\sum_k \frac{V_{k,H}^2}{i\omega_n-\epsilon_{k,H}}-t^2G_{\rm high}^{(0)}(i\omega_n), \tag{197}$$

which to lowest order is independent of w, and

$$0=\sum_k \frac{wD^2\tilde{V}_k^2}{i\omega_n-\epsilon_{k,L}}-t^2wG_{\rm low}^{(1)}(i\omega_n). \tag{198}$$

We thus see that—as is intuitively obvious—at the critical point the *high-energy* contributions are unaffected by the presence of the vanishing Kondo resonance at low energies. One can therefore proceed in two steps:

(1) One solves the lowest-order high-energy part described by the Hamiltonian $\mathscr{H}_H^{{\rm eff}(0)}$ self-consistently. For a vanishing quasiparticle weight this simply corresponds to the solution to the insulating problem. This yields the lowest-order coefficients entering the low-energy Hamiltonian $w.\mathscr{H}_L^{{\rm eff}(1)}$ and thus determines the low-energy properties.

(2) One can then proceed by solving the low-energy part at the critical point self-consistently using the coefficients obtained from the insulating solution.

Note that to lowest order the low-energy spectral weight w drops out in Eq. (198), so that this equation is soluble only at the critical point. This is analogous to the familiar case of a Landau-Ginzburg expansion, where in order to obtain a finite value for the order parameter in a second-order phase transition, terms in the Landau functional to fourth order need to be retained. It is also typical of bifurcation problems where the values of the control parameter at which a bifurcation takes place appears as a solvability condition.

To determine the behavior of w as a function of Δ one has to solve the equations

$$0=\sum_k \frac{V_{k,H}^2}{i\omega_n-\epsilon_{k,H}}-t^2G_{\rm high}^{(0)}(i\omega_n)-wt^2G_{\rm high}^{(1)}(i\omega_n), \tag{199}$$

$$0=\sum_k \frac{wD^2\tilde{V}_k^2}{i\omega_n-\epsilon_{k,L}}-t^2wG_{\rm low}^{(1)}(i\omega_n)-t^2w^2G_{\rm low}^{(2)}(i\omega_n) \tag{200}$$

simultaneously. While this is a possible procedure, it is desirable to have, at least in principle, a procedure in which one is left with a *single* equation for the low-energy part *only*. This can be achieved in the following way.

(1) We first solve the self-consistent insulator, i.e., the high-energy part to lowest order in w, as done when determining the properties of the model at the critical point.

(2) One now has to determine how the high-energy $V_{k,H}$ are modified if the low-energy $V_{k,L}$ change. This can be done in principle by expanding Eq. (189) around the insulating solution. Let us define

$$\begin{aligned}\Lambda[V_{k,L},\epsilon_{k,L};V_{k,H},\epsilon_{k,H};\Delta]&\\ \equiv\sum_k \frac{V_{k,H}^2}{i\omega_n-\epsilon_{k,H}}&\\ -t^2G_{\rm high}[i\omega_n;V_{k,H},\epsilon_{k,H},V_{k,L},\epsilon_{k,L}],&\end{aligned} \tag{201}$$

where Δ is the formally small parameter determining the proximity to the critical point and is thus given as $\Delta=U-U_c$ at half-filling and as $\Delta=\mu-\mu_c$ for finite doping. In terms of Λ the high-energy part of the self-consistency then simply reads

$$\Lambda[V_{k,H},\epsilon_{k,H};V_{k,L},\epsilon_{k,L};\Delta]=0. \tag{202}$$

Close to the transition this can be expanded to lowest order in w and one obtains

$$\begin{aligned}0=&\frac{\partial\Lambda}{\partial(V_{k,L}^{(1)}V_{k',L}^{(1)})}V_{k,L}^{(1)}V_{k',L}^{(1)}+\frac{\partial\Lambda}{\partial\epsilon_{k,L}^{(1)}}\epsilon_{k,L}^{(1)}\\ &+\frac{\partial\Lambda}{\partial V_{k,H}^{(2)}}V_{k,H}^{(2)}+\frac{\partial\Lambda}{\partial\epsilon_{k,H}^{(2)}}\epsilon_{k,H}^{(2)}+\frac{\partial\Lambda}{\partial\Delta}\Delta.\end{aligned} \tag{203}$$

Solving this matrix equation for $\epsilon_{k,H}^{(2)}$ and $V_{k,H}^{(2)}$ by performing a matrix inversion in principle gives explicit expressions for the $V_{k,H}^{(2)}$ and $\epsilon_{k,H}^{(2)}$ in terms of the low-frequency parameters $V_{k,L}$ and $\epsilon_{k,L}$.

(3) We can now insert these expressions into the low-frequency self-consistency condition (188) and thus obtain the correct high-energy coefficients (to order w) as

functions of the low-frequency parameters. The low-frequency condition is now consistently given to order w^2 and can be iterated until convergence is achieved. This gives the consistent solution of the low-energy problem to order w^2.

We now provide the *explicit* form of the operators entering the effective low-energy problem to the order which is necessary to derive the results quoted in Sec. VII. Notice that since the canonical transformation is formally very similar to the Schrieffer-Wolff transformation, the expressions are very similar to the results of the cited paper.

The low-energy Hamiltonian is given by

$$\mathscr{H}_{\rm low}^{\rm eff(1)} = D\sum_{k\sigma} \tilde{\epsilon}_k n_{k\sigma} - \frac{D}{4}\sum_{\sigma} J^{\perp(1)} X_{\bar{\sigma}\sigma} c^{\dagger}_{L\sigma} c_{L\bar{\sigma}} - \frac{D}{4}\sum_{\sigma\sigma'} J^{(1)}_{\sigma\sigma'} X_{\sigma'\sigma'} n_{L\sigma} \tag{204}$$

with

$$J^{\perp(1)} = D\left(\langle \bar{\sigma}| f_\sigma \frac{1}{H - E^{\rm at}_{\rm g.s.}} f^{\dagger}_{\bar{\sigma}} |\sigma\rangle_{H_{\rm at}} - \langle \bar{\sigma}| f^{\dagger}_{\bar{\sigma}} \frac{1}{H - E^{\rm at}_{\rm g.s.}} f_\sigma |\sigma\rangle_{H_{\rm at}} \right) \tag{205}$$

and

$$J^{(1)}_{\sigma\sigma'} = D\left(\langle \sigma'| f_\sigma \frac{1}{H - E^{\rm at}_{\rm g.s.}} f^{\dagger}_{\sigma} |\sigma'\rangle_{H_{\rm at}} - \langle \sigma'| f^{\dagger}_{\sigma} \frac{1}{H - E^{\rm at}_{\rm g.s.}} f_\sigma |\sigma'\rangle_{H_{\rm at}} \right). \tag{206}$$

We have used the standard Hubbard operators defined as $X_{\sigma\sigma'} = |\sigma\rangle\langle\sigma'|$ acting on the low-energy impurity doublet.

Due to the fact that the system is rotationally invariant, we observe that $J_{\uparrow\uparrow} = J_{\downarrow\downarrow}$ and $J_{\uparrow\downarrow} = J_{\downarrow\uparrow}$. Defining the quantities

$$J^{(1)}_{\rm pot} \equiv J^{(1)}_{\uparrow\uparrow} + J^{(1)}_{\uparrow\downarrow} \tag{207}$$

and

$$J^{(1)}_{\rm spin} \equiv J^{(1)}_{\uparrow\uparrow} - J^{(1)}_{\uparrow\downarrow} \tag{208}$$

and again using rotational invariance we see that, furthermore $J^{(1)}_{\rm spin} = J^{\perp(1)}$ such that the Hamiltonian can be written as a Kondo Hamiltonian. In contrast to the more common definition of J, we have defined J such that it is *negative*, i.e., $J_{\rm spin} < 0$, and the low-energy effective Hamiltonian reads

$$\mathscr{H}_{\rm low}^{\rm eff(1)} = D\sum_{k\sigma} \tilde{\epsilon}_k n_{k\sigma} - \frac{D}{2} J^{(1)}_{\rm spin} \vec{S}\cdot\vec{s}_L - \frac{D J^{(1)}_{\rm pot}}{8}(n_{L\uparrow} + n_{L\downarrow}) \tag{209}$$

with $\vec{S} = 1/2 \Sigma_{\sigma\sigma'} X_{\sigma\sigma'} \vec{\sigma}_{\sigma\sigma'}$ the spin-$\frac{1}{2}$ operator acting on the $|\sigma\rangle_{\rm at}$ states and $\vec{s}_L = 1/2 \Sigma_{\alpha\beta} c^{+}_{L\alpha} \vec{\sigma}_{\alpha\beta} c_{L\beta}$ the local spin operator of the low-energy conduction electrons. Notice that the identity $X_{\uparrow\uparrow} + X_{\downarrow\downarrow} = 1$ has been used to simplify the result.

The explicit expressions for the F^{LL}_{σ} operators describing the low-energy excitations to lowest order are

$$F^{LL(1)}_{\uparrow} = -\frac{1}{2}\left((J^{(1)}_{\uparrow\uparrow} X_{\uparrow\uparrow} + J^{(1)}_{\uparrow\downarrow} X_{\downarrow\downarrow}) c_\uparrow + J^{\perp(1)} X_{\downarrow\uparrow} c_\downarrow \right), \tag{210}$$

or, in terms of $J^{(1)}_{\rm spin}$ and $J^{(1)}_{\rm pot}$, as

$$F^{LL(1)}_{\sigma} = -\frac{1}{4}\left(J^{(1)}_{\rm pot} + J^{(1)}_{\rm spin}(X_{\sigma\sigma} - X_{\bar{\sigma}\bar{\sigma}}) \right) c_\sigma - \frac{1}{2} J^{(1)}_{\rm spin} X_{\bar{\sigma}\sigma} c_{\bar{\sigma}}. \tag{211}$$

Using these results we now write explicitly Eq. (198) (with $F \equiv F^{LL(1)}$):

$$\sum_k \frac{D^2 \tilde{V}^2_k}{i\omega_n - \epsilon_{k,L}} = t^2 G^{(1)}_{\rm low}(i\omega_n) = -t^2 \int_0^\beta d\tau\, e^{i\omega_n \tau} \langle T\left(F(\tau) F^{\dagger}(0)\right)\rangle_{H_{\rm eff}}. \tag{212}$$

The condition for a vanishing resonance, i.e., for the critical point, is most easily obtained by noticing that at high frequencies Eq. (212) simplifies to $1 = \{F^{(1)}_{\sigma}, F^{(1)\dagger}_{\sigma}\}$ which is easily evaluated to give

$$1 = -\frac{1}{2}\left[J^{(1)2}_{\rm spin}\left(\langle \vec{S}\cdot\vec{s}_L\rangle - \frac{3}{8} \right) - \frac{J^{(1)2}_{\rm pot}}{8} \right]. \tag{213}$$

Here $\langle\ \rangle$ denotes the expectation value of an operator in the ground state of (209). For a given value of U, this equation can be satisfied for only two values of the chemical potential, $\mu^{\pm}_c(U)$, the position of the resonance at infinitesimal particle and hole doping, respectively. In the half-filled case $\mu = U/2$, $J_{\rm pot} = 0$, and Eq. (213) determines the value of U_{c2}. The instability of the insulator can be analyzed by adding an infinitesimal perturbation to the insulating state (Fisher, Kotliar, and Moeller, 1995). All the previous analysis carries through for the insulator, except that now $\langle \vec{S}\cdot\vec{s}_L\rangle = 0$, since an infinitesimal Kondo coupling cannot induce a finite correlation. The criteria for the destruction of the insulator becomes [dropping from thereon the superscript (1)]:

$$1 = \frac{1}{2}\left(\frac{3}{8} J^2_{\rm spin} + \frac{1}{8} J^2_{\rm pot} \right). \tag{214}$$

Notice that at half-filling, $J_{\rm pot}$ is zero because of particle-hole symmetry, and the equations for U_{c1} (instability of the insulator) and U_{c2} (instability of the metal) become, respectively,

$$1 = \frac{3}{16} J^2_{\rm spin}, \tag{215}$$

$$1 = \frac{1}{2} J^2_{\rm spin}\left(\frac{3}{8} - \langle \vec{S}\cdot\vec{S}_L\rangle \right). \tag{216}$$

Comparing these two equations, and noting that $\langle \vec{S} \cdot \vec{s}_L \rangle < 0$ and that $J_{\text{spin}}(U)$ decreases as U increases, proves analytically that $U_{c1} < U_{c2}$ (Fisher, Kotliar, and Moeller, 1995). This is in complete agreement with the numerical work described in Sec. VII which tackles the full problem numerically with exact diagonalization methods (Rozenberg, Moeller, and Kotliar, 1994).

The projective method described in this section is a particular implementation of the idea of renormalization. It was taylored specifically to solve the LISA equations. It is worth stressing the reasons why the renormalization group invented by Wilson to solve the single impurity Kondo model does not work for the impurity models arising in the context of the LISA applications. The essential insight is that because of the self-consistency conditions the energy scales of the impurity are also the energy scales of the bath. The impurity models are thus in an *intermediate coupling* regime. The logarithmic discretization of Wilson's mesh and the Wilson recursion procedure was intended to deal with a mismatch in energy scales, typical of a weak-coupling situation in which the Kondo coupling was much smaller than the conduction electron bandwidth. Notice that, even in the Kondo model, the calculation of Green's functions is not possible to very high precision for all energies (cf. Hewson, 1993). In the LISA context, we are not interested in the low-energy eigenvalue spectrum (which we can calculate using the renormalization group), but in the whole single-particle excitation spectrum (Green's function), which is fed back into the low-energy sector via the self-consistency condition. It is thus not surprising that a direct numerical renormalization group approach in the LISA context is faced with rather serious difficulties. For early attempts to implement the Wilson scheme to solve the LISA equations see Sakai and Kuramoto (1994) and Shimizu and Sakai (1995).

VII. THE HUBBARD MODEL AND THE MOTT TRANSITION

In this section, we review the application of the LISA method to the physics of the Hubbard model. We shall be concerned with the phase diagram, thermodynamics, one-particle spectra, and two-particle response functions. The control parameters are the temperature T, and the interaction strength U/t. In order to reveal the full variety of possible behavior, we shall also consider models with different degrees of magnetic frustration. This introduces a third parameter, which can be for example the ratio of nearest-neighbor to next-nearest neighbor hopping amplitudes t_1/t_2. As a function of these parameters, the Hubbard model at half-filling has, within the LISA, four possible phases: a paramagnetic metallic phase, a paramagnetic insulating phase, an insulating antiferromagnetic phase, and (in the presence of magnetic frustration) an antiferromagnetic metallic phase. The effect of doping away from half-filling will also be considered towards the end of this section (Sec. VII.H).

A. Early approaches to the Mott transition

We shall put a special emphasis in this section on the transition between the paramagnetic metal and the para-

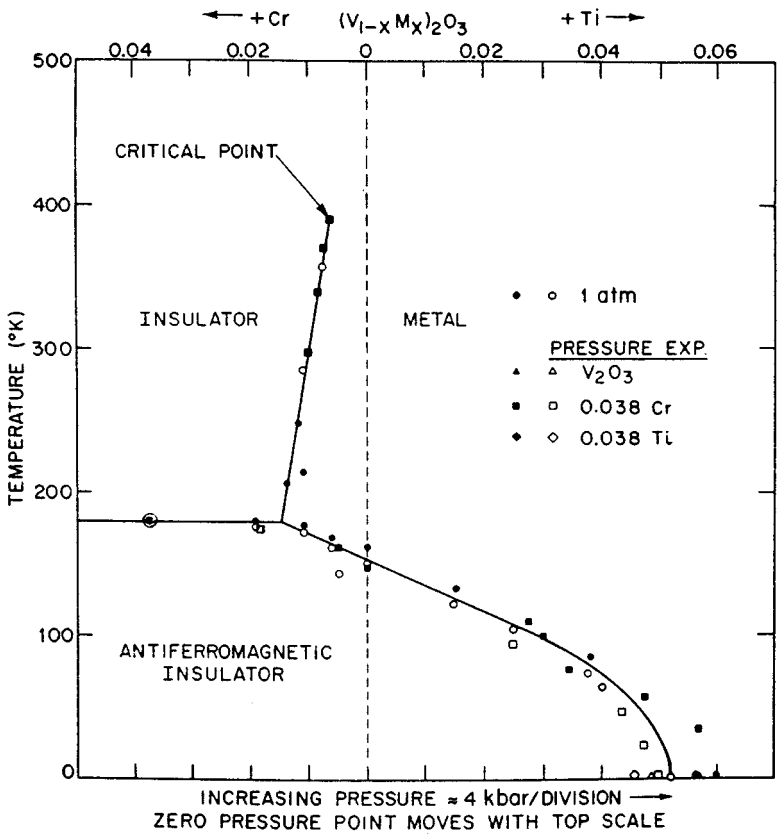

FIG. 23. Experimental phase diagram for the metal-insulator transition in V_2O_3 as a function of doping with Cr or Ti and as a function of pressure (after McWhan *et al.*, 1973). See also recent results by Carter *et al.* (1992, 1993) that report a low temperature metallic phase with antiferromagnetic order in $V_{2-y}O_3$.

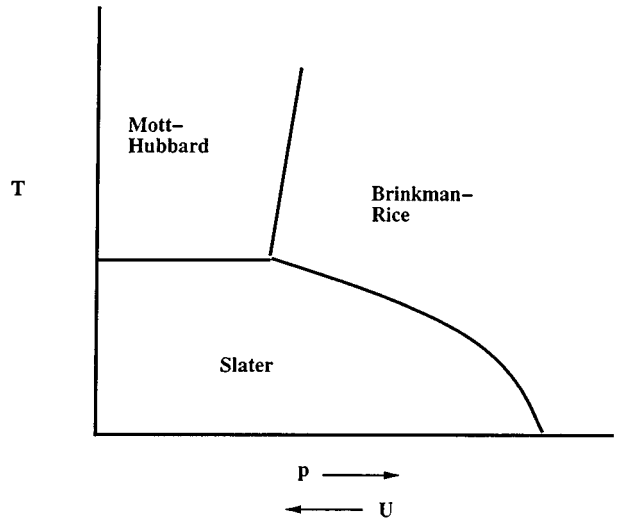

FIG. 24. Classic theories for the description of the various phases.

magnetic insulator. This is an example of a Mott transition, i.e., of a metal-insulator transition driven by the strength of electron-electron interactions in a homogeneous system. It is realized experimentally in three-dimensional transition metal oxides, such as V_2O_3, and can be driven by varying pressure, temperature, and composition (for general references, see, e.g., Mott, 1990; Tsuda *et al.*, 1991). Figure 23 reproduces the experimental phase diagram found for V_2O_3 by varying these parameters (McWhan *et al.*, 1973). Since the early ideas of Mott (1949, 1956, 1961), this transition has been the subject of numerous experimental and theoretical investigations. From a theoretical point of view, several ideas have been put foward that we shall briefly review. They are rather different from one another and correspond to the various possible ways of approaching the transition in the phase diagram of Fig. 23, coming from different phases (Fig. 24). The LISA provides for the first time a unified framework in which the various phases (and their relative stability) can be studied within a single model, so that the validity of the previous approaches can be assessed and put in perspective.

Early work of Hubbard (1964) provided a description of the transition rather close in spirit to Mott's original views. He attempted to give an effective band description of the correlated system (Fig. 25), and proposed that the original density of states (of half-width D) gets split for large U into a lower Hubbard band (corresponding to holes, or empty sites) and an upper Hubbard band (corresponding to doubly occupied sites). For large U these bands are separated by a gap of order $U-2D$. As U is reduced there is a critical value of U where the two bands merge again and a metal is recovered. Hence, the Hubbard picture of the metal-insulator transition is associated with the closure of a gap. This description obviously relies on the large U insulating limit as a starting point, and as we shall see is actually qualitatively valid there. It fails however to provide a description of the metal consistent with Fermi-liquid properties.

On the other hand, Brinkman and Rice (1970), building on the work of Gutzwiller (1965), started from the metallic phase which they described as a strongly renormalized Fermi liquid with a reduced low-energy scale (or effective Fermi energy). This scale is of the order of ZD, where Z is the quasiparticule residue, related to the quasiparticle effective mass in this approach by $m^*/m=1/Z$. As the interaction strength increases, this energy scale vanishes at a critical value of the interaction U_{BR}, with $Z\propto(U_{\mathrm{BR}}-U)$. In this framework, the metal insulator transition is driven by the localization of the Fermi-liquid quasiparticles, $m^*/m\propto 1/(U_{\mathrm{BR}}-U)\rightarrow\infty$, and their disappearance in the insulator. This approach is a consistent low-energy description of the strongly correlated metal, but does not account for the high-energy excitations forming the Hubbard bands, which should be present already in the metallic state. Furthermore, it gives an oversimplified picture of the insulator, which is caricatured as a collection of independent local moment with no residual antiferromagnetic exchange and an infinite susceptibility at $T=0$. The Brinkman-Rice approach can be justified formally using slave bosons methods (Kotliar and Ruckenstein, 1986). In that case, the Hubbard bands and incoherent features, absent at the saddle point level, are reintroduced by the fluctuations around the slave-boson condensate, and the disappearance of the resonance coincides with the closing of the gap (Castellani *et al.* 1992; Raimondi and Castellani, 1993; see also Kotliar, 1993a).

Finally, early arguments by Slater (1951) focus on the possibility of long-range antiferromagnetic order at low enough temperature. At weak coupling, this possibility is confirmed (on bipartite lattices) by a simple Hartree-Fock approximation. In this picture, the driving force behind the metal-insulator transition is the doubling of the unit cell which makes the band structure of the sys-

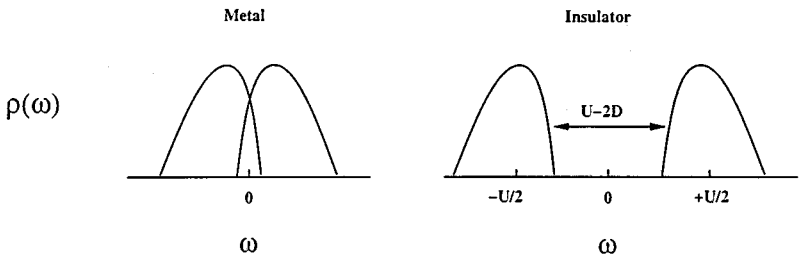

FIG. 25. Schematic evolution of the density of states with U in the Hubbard picture.

tem that of a band insulator. For strong coupling, Anderson's superexchange mechanism yields an antiferromagnetic exchange $J \propto t^2/U$, and suggests again an antiferromagnetic ground state. The high degeneracy of the paramagnetic Mott insulating state indeed suggests that some kind of long-range order should take place at low temperature. This is indeed observed experimentally, for instance in the case of V_2O_3 (McWhan *et al.*, 1973).

B. Models and self-consistent equations

Throughout this section, we shall deal with the single-band Hubbard model at or close to half-filling. Since the chemical potential at half-filling is $\mu = U/2$, it is convenient in this section to define the Hamiltonian as

$$H = -\sum_{\langle ij\rangle,\sigma} t_{ij}(c_{i\sigma}^{+}c_{j\sigma} + c_{j\sigma}^{+}c_{i\sigma}) + U\sum_{i} (n_{i\uparrow} - \tfrac{1}{2})(n_{i\downarrow} - \tfrac{1}{2}) \tag{217}$$

and to make use of a shifted chemical potential $\Delta\mu \equiv \mu - U/2$. Various forms of the hopping term t_{ij} and various lattices will be considered. For simplicity, all the cases that we shall consider in this section correspond to a semicircular density of states:

$$D(\epsilon) = \frac{2}{\pi D}\sqrt{1-(\epsilon/D)^2}. \tag{218}$$

Other density of states have also been investigated in the literature. In order to compare results obtained with different densities of states in a qualitative manner, it is useful to normalize U to an effective half-bandwidth (typical kinetic energy):

$$W = 2\left(\int_{-\infty}^{+\infty} \epsilon^2 D(\epsilon) d\epsilon\right)^{1/2}. \tag{219}$$

For the semicircular density of states (218), this definition is chosen so that $W = D$. The half-filled Hubbard model with a Gaussian density of states (corresponding to a $d=\infty$ hypercubic lattice) has been studied by Jarrell (1992), Georges and Krauth (1992, 1993), and Pruschke, Cox, and Jarrell (1993a, 1993b). The diamond lattice has been studied by Santoro *et al.* (1993). The overall structure of the spectral function far from the Mott transition turns out to be rather independent of the precise form of the density of states. For density of states that have (unphysical) tails up to infinite energies, such as the Gaussian one, the precise nature of the Mott transition is however modified as compared to a bounded density of states. In particular the insulator is not expected to display a sharp gap. A detailed analysis of the critical properties of the transition in those cases has not yet been performed.

In this section, the impurity model effective action will be written as

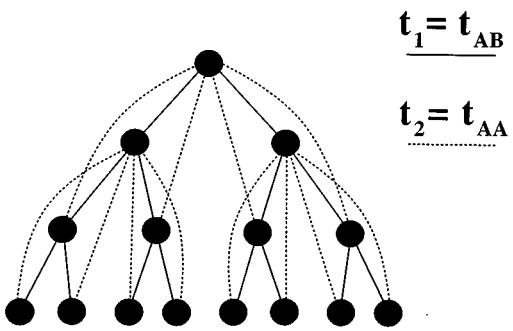

FIG. 26. Schematic representation of the Bethe lattice with nearest-neighbor hopping $t_1/\sqrt{z}$ and next-nearest neighbor hopping t_2/z.

$$S_{\rm eff} = -\int_0^\beta d\tau \int_0^\beta d\tau' \sum_\sigma c_\sigma^{+}(\tau)\mathcal{G}_{0\sigma}^{-1}(\tau-\tau')c_\sigma(\tau') + U\int_0^\beta d\tau [n_\uparrow(\tau) - \tfrac{1}{2}][n_\downarrow(\tau) - \tfrac{1}{2}]. \tag{220}$$

As defined here, the Weiss function has been shifted by $\mathcal{G}_0^{-1} \to \mathcal{G}_0^{-1} - U/2$ in comparison to the previous sections.

The simplest realization of the density of states (218) is the Bethe lattice with connectivity $z \to \infty$. In order to mimic a varying degree of magnetic frustration, we shall allow for a nearest neighbor hopping $t_1/\sqrt{z}$ and a next-nearest neighbor hopping t_2/z (Fig. 26). In the absence of symmetry breaking, the self-consistency condition reads (dropping spin indices)

$$\mathcal{G}_0^{-1} = i\omega_n + \Delta\mu - (t_1^2 + t_2^2)G(i\omega_n), \tag{221}$$

and the half-width of the noninteracting density of states reads

$$D = 2\sqrt{t_1^2 + t_2^2}. \tag{222}$$

In the antiferromagnetic Néel phase, where the A and B sublattices magnetize in opposite directions, the self-consistency equations read

$$\mathcal{G}_{0A\sigma}^{-1} = i\omega_n + \Delta\mu - t_1^2 G_{B\sigma} - t_2^2 G_{A\sigma},$$
$$\mathcal{G}_{0B\sigma}^{-1} = i\omega_n + \Delta\mu - t_1^2 G_{A\sigma} - t_2^2 G_{B\sigma} \tag{223}$$

with the additional relations $G_{A\sigma} = G_{B-\sigma}$ (and similarly for the $\mathcal{G}_0$'s). Note that, in the paramagnetic phase, everything depends only on the magnitude of $t = \sqrt{t_1^2 + t_2^2}$, but that the tendency to form a magnetically ordered phase depends crucially on the ratio t_1/t_2 (measuring the degree of magnetic frustration).

The same semicircular density of states is also realized in models defined on a fully connected lattice of N sites with some randomness on the hopping t_{ij}. A first example is the fully frustrated model (Georges and Krauth, 1993; Rozenberg, Kotliar, and Zhang, 1994) defined by

$$H_{FF} = -t\sum_{i,j=1,N} \epsilon_{ij} c_{i\sigma}{}^{\dagger} c_{j\sigma} + U\sum_i (n_{i\uparrow} - \tfrac{1}{2})(n_{i\downarrow} - \tfrac{1}{2}). \tag{224}$$

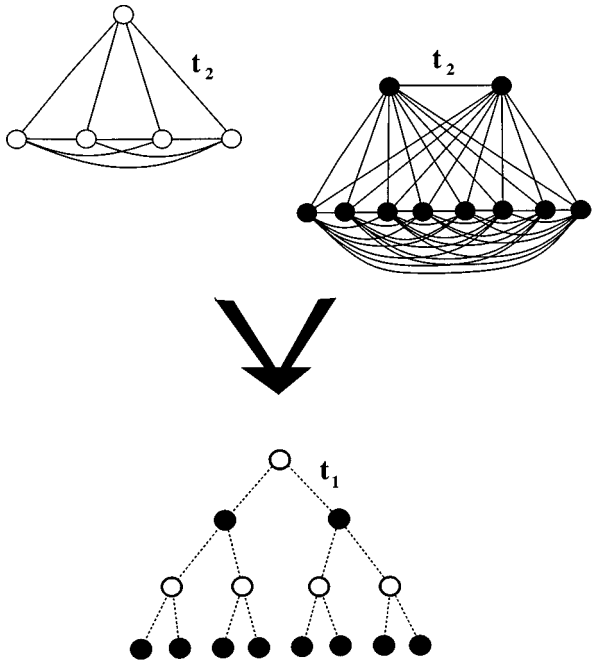

FIG. 27. Schematic construction of the two-sublattice fully frustrated model (TSFF). The fully connected, fully frustrated sublattices A (white sites) and B (black sites) at the top of the figure are combined into a single lattice through the interlattice hopping elements t_1.

Summation over repeated spin indices is assumed. Here ϵ_{ij} are quenched independently distributed Gaussian random variables with zero mean and a variance $\langle \epsilon_{ij}^2 \rangle = 1/N$. This model has the same density of states as the Bethe lattice with nearest neighbor hopping t, and thus has identical one-particle properties in the high-temperature disordered phase. However, it is not expected to display Néel order at any finite temperature. Finally, we can also vary the degree of frustration for such models by studying a two sublattice frustrated model (TSF), defined by (Rozenberg, Kotliar, and Zhang, 1994)

$$H_{\mathrm{TSF}} = -t_2 \sum_{i,j \in A \text{ or } B} \epsilon_{ij} c_{i\sigma}{}^{\dagger} c_{j\sigma} - t_1 \sum_{i \in A, j \in B} \epsilon_{ij} c_{i\sigma}{}^{\dagger} c_{j\sigma} + U \sum_{i \in A \cup B} (n_{i\uparrow} - \tfrac{1}{2})(n_{i\downarrow} - \tfrac{1}{2}). \quad (225)$$

The self-consistency equations for this model are the same [Eqs. (223)] as for the Bethe lattice with two types of hopping described above. The unfrustrated case is recovered for $t_2=0$ and the fully frustrated case corresponds to $t_1 = t_2$. Figure 27 displays a schematic representation of the TSF model. Notice that the Hamiltonians (224) and (225) contain randomness but that the single-particle properties are self-averaging in the $N \to \infty$ limit. The single-particle Green's functions are the same for any typical realization of the random variables ϵ_{ij}. This is due to the scaling chosen for ϵ_{ij}. For the same reason, no spin-glass order is expected.

The available techniques for the study of the coupled dynamical mean-field equations have been reviewed in Sec. VI. The first applications of the QMC method (Jarrell, 1992; Rozenberg, Zhang, and Kotliar, 1992; Georges and Krauth, 1992) were carried out at temperatures much higher than the metal-insulator transition critical temperature (see below), but did display a clear crossover from metallic to quasi-insulating behavior as a function of U. The existence of a Mott transition in the half-filled case was demonstrated on the basis of analytic arguments (Rozenberg, Zhang, and Kotliar, 1992; Georges and Krauth, 1992). Later, the Mott transition was investigated in great detail with a variety of methods: QMC was used in conjunction with the iterated perturbation theory approximation introduced by Georges and Kotliar (1992; see Sec. VI.B.2 and Georges and Krauth, 1993; Zhang, Rozenberg, and Kotliar, 1993; Rozenberg, Kotliar, and Zhang, 1994), or in conjunction with maximum entropy and the noncrossing approximation (Jarrell and Pruschke, 1993a, 1993b; Pruschke, Cox, and Jarrell, 1993a, 1993b). Exact diagonalization methods (Caffarel and Krauth, 1994; Rozenberg, Moeller, and Kotliar, 1994), and the projective method of Sec. VI.C (Moeller *et al.*, 1995) played a key role in recent work. Approximate continuous fraction resummations of the Green's function (Hong and Kee, 1995a, 1995b; Kee and Hong, 1995), equation of motion decoupling schemes (Gros, 1994), and diagonalizations of lattices involving successive shells of neighbors (Gros *et al.*, 1994) have also been used. An important point here is that no single technique can be pointed out as the most suitable one, but the insights obtained on the Mott transition problem rely on a combined use of different techniques in order to elucidate the different aspects of the physics. In this section, we shall put the emphasis on the physics rather than on the techniques. The reader is directed to Sec. VI for a detailed discussion of the capabilities and range of applicability of the various methods.

C. Existence of a Mott transition at half-filling

We first present a simple *qualitative analysis* of the zero-temperature behavior of the dynamical mean-field Eqs. (220) and (221) in the paramagnetic phase at half-filling ($\Delta\mu = \mu - U/2 = 0$). This analysis establishes the existence of a $T=0$ metal-insulator transition as U is increased.

1. Metallic phase

In the limit of small U, the self-energy of the Anderson impurity model is a smooth function of frequency that can be computed perturbatively in the interaction. At half-filling, particle-hole symmetry implies $\Sigma(i0^+) = U/2$. The self-consistency condition then implies that as long as one is in the Fermi-liquid phase the value of $G(i0^+) = 2/(iD)$ is independent of the interaction strength, and similarly $\mathcal{G}_0^{-1}(i0^+) = iD/2$. Since the latter is the low-frequency limit of the hybridization function of the Anderson impurity model (220) and (221) we have a standard Anderson model describing an impurity embedded in a bath of conduction electrons

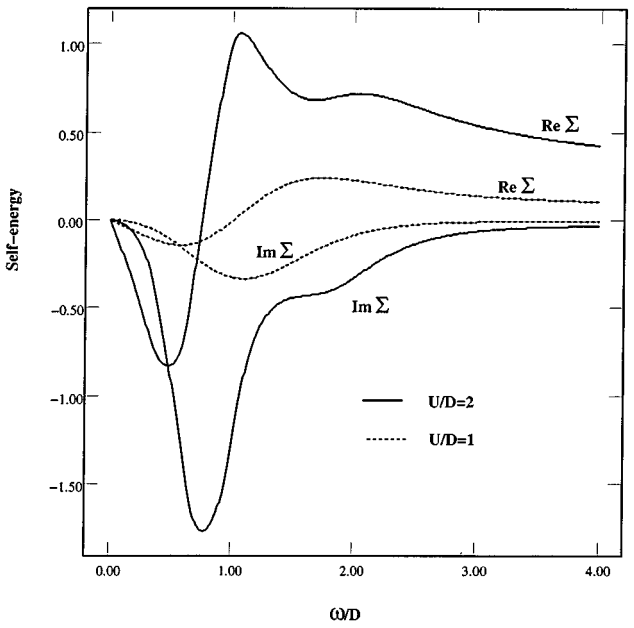

FIG. 28. Real and imaginary parts of the real-frequency self-energy $\Sigma(\omega+i0^+)$, as obtained from the iterated perturbation theory approximation, for two metallic values of $U/D=1$ and 2 (dotted and full lines).

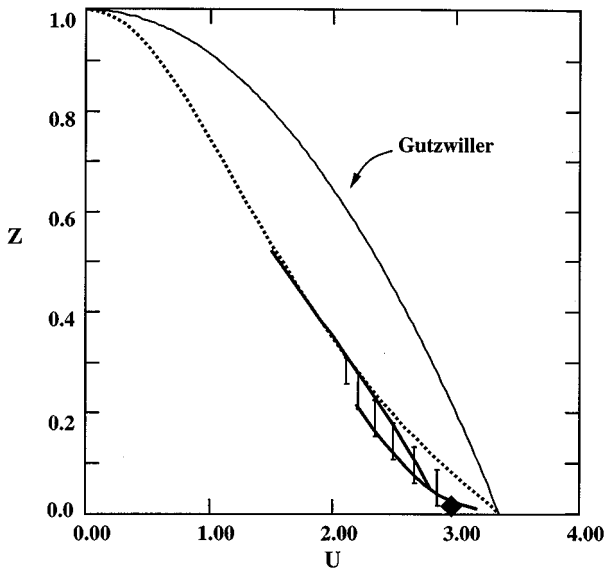

FIG. 29. The quasiparticle weight Z as a function of the interaction U. The solid bold line corresponds to exact diagonalization results with eight sites. The dotted line is obtained from iterated perturbation theory. For comparison we also plot the results using the Gutzwiller variational method (full line). The error bars near U_c reflect the uncertainties inherent to the various methods. The diamond represents the exact location of U_c obtained from the projective method.

with a *nonsingular density of states at the Fermi level* $\Delta(\omega=0)=D/2\pi$. As the interaction U is increased, we expect the Kondo effect to take place, leading to a singlet nondegenerate ground state of the impurity model. The low-frequency behavior of $\Sigma(\omega)$ is that of a local Fermi liquid:

$$\mathrm{Re}\Sigma(\omega+i0^+)=U/2+(1-1/Z)\omega+O(\omega^3), \tag{226}$$

$$\mathrm{Im}\Sigma(\omega+i0^+)=-B\omega^2+O(\omega^4). \tag{227}$$

The quasiparticle residue Z defines the renormalized Fermi energy of the problem:

$$\epsilon_F^*\equiv ZD \tag{228}$$

This is also the Kondo temperature of the impurity model. Since the self-energy is momentum independent, Z directly yields the effective mass of quasiparticles (Müller-Hartmann, 1989c):

$$\frac{m^*}{m}=\frac{1}{Z}=1-\frac{\partial}{\partial\omega}\mathrm{Re}\Sigma(\omega+i0^+)\big|_{\omega=0}. \tag{229}$$

All these quantities can be computed quantitatively using the techniques described in Sec. VI. A plot of the self-energy obtained within the iterated perturbation theory approximation is given in Fig. 28 for two values of U representative of the metallic regime. The quasiparticle residue Z (obtained by exact diagonalization) is plotted in Fig. 29 as a function of U [and compared to the Gutzwiller approximation (Brinkman and Rice, 1970)]. Z is close to 1 for small U, and goes to zero at $U=U_{c2}(T=0)\simeq 3D$, signalling the disappearance of quasiparticles, and hence of the metallic solution. The precise nature of this transition at U_{c2} will be further reviewed in Sec. VII.E.

A plot of the local spectral function

$$\rho(\omega)\equiv-\frac{1}{\pi}\sum_{\mathbf{k}}\mathrm{Im}G(\mathbf{k},\omega+i0^+) \tag{230}$$

is shown in Fig. 30 for various values of U. The results displayed have been obtained with the iterated perturbation theory, and it was shown in Sec. VI that this is a quite accurate approximation in the metal, for all values of U (except very close to U_{c2}). For small U, the spectral function is featureless and similar to the bare lattice density of states. For larger values of U, a narrow quasiparticle peak is formed at the Fermi level of width ϵ_F^* and weight Z. This is the Abrikosov-Suhl resonance in the impurity model language. Notice the pinning of $\rho(0)$ at its noninteracting value:

$$\rho(\omega=0)=D(0), \tag{231}$$

as required by the Luttinger theorem for a momentum-independent self-energy (Müller-Hartmann, 1989c). Two additional features at frequencies $\pm U/2$ (corresponding to energies $\omega+\mu=0,U$) are associated with the upper and lower Hubbard band (empty and doubly occupied sites).

Finally, we mention a very simple argument showing that the LISA equations cannot sustain a metallic solution up to arbitrary large U at half-filling (Georges and Krauth, 1992; Rozenberg, Zhang, and Kotliar, 1992). Imagine solving the system of Eqs. (220) and (221) by iteration, with a conduction electron half-bandwidth D_n at step n. For large U, solving the Kondo problem produces a bandwidth $D_{n+1}=e^{-U/t}D_n$. Therefore, D_n iterates to zero for large U. In fact, the metallic solution

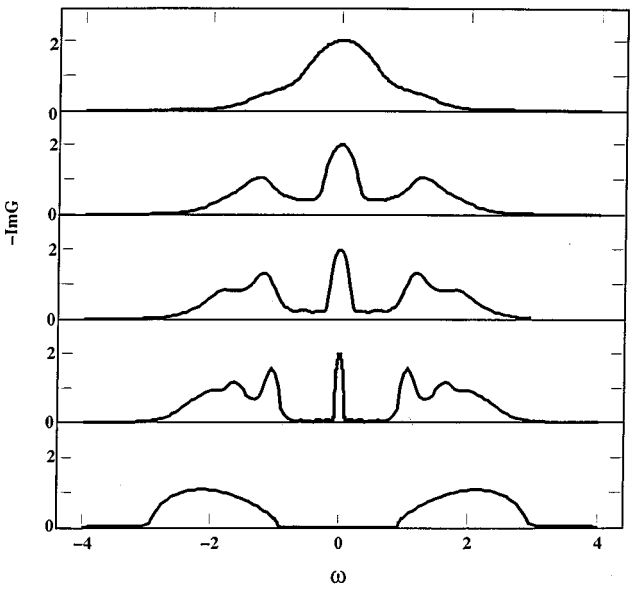

FIG. 30. Local spectral density $\pi D\rho(\omega)$ at $T=0$, for several values of U, obtained by the iterated perturbation theory approximation. The first four curves (from top to bottom, U/D =1,2,2.5,3) correspond to an increasingly correlated metal, while the bottom one ($U/D=4$) is an insulator.

disappears continuously (at $T=0$) at a critical value $U_{c2}/D\simeq 2.92$, as explained in more detail in Sec. VII.E.

2. Insulating phase

When U/t is large, we begin with a different ansatz based on the observation that in the "atomic limit" $t=0$ ($U/t=\infty$), the spectral function has a gap equal to U. In this limit the exact expression of the Green's function reads

$$G(i\omega_n)_{\rm at}=\frac{1/2}{i\omega_n+U/2}+\frac{1/2}{i\omega_n-U/2}. \tag{232}$$

Since $\mathrm{Im}G(\omega+i0^+)$ also plays the role of the density of states of the effective conduction electron bath entering the impurity model, we have to deal with an impurity embedded in an *insulator* [$\Delta(\omega=0)=0$]. It is clear that an expansion in powers of the hybridization t does not lead to singularities at low frequency in this case. This is very different from the usual expansion in the hybridization V with a given (flat) density of states that is usually considered for an Anderson impurity in a metal. Here, t also enters the conduction bath density of states (via the self-consistency condition) and the gap survives an expansion in t/U. An explicit realization of this idea is to make the following approximation for the local Green's function (Rozenberg, Zhang, and Kotliar, 1992):

$$G(i\omega_n)\simeq\frac{1/2}{\mathscr{G}_0^{-1}(i\omega_n)-U/2}+\frac{1/2}{\mathscr{G}_0^{-1}(i\omega_n)+U/2}, \tag{233}$$

which can be motivated as the superposition of two magnetic Hartree-Fock solutions or as a resummation of an expansion in Δ/U. This implies that $G(i\omega)\sim i\omega$ for small ω, and the substitution into the self-consistency condition implies that $\mathscr{G}_0^{-1}\sim i\omega$, which is another way of saying that the effective bath in the Anderson model picture has a gap. We know from the theory of an Anderson impurity embedded in an *insulating medium* that the Kondo effect does not take place. The impurity model ground state is a doubly degenerate local moment. Thus, the superposition of two magnetic Hartree-Fock solutions is qualitatively a self-consistent ansatz. If this ansatz is placed into Eq. (221), we are led to a closed (approximate) equation for $G(i\omega_n)$:

$$D^4G^3-8D^2\omega G^2+4(4\omega^2+D^2-U^2)G-16\omega=0. \tag{234}$$

This approximation corresponds to the first-order approximation in the equation of motion decoupling schemes reviewed in Sec. VI.B.4. It is similar in spirit to the Hubbard III approximation Eq. (173) (Hubbard, 1964), which would correspond to pushing this scheme one step further. These approximations are valid for very large U but become quantitatively worse as U is reduced. They would predict a closure of the gap at $U_c=D$ for (234) ($U_c=\sqrt{3}D$ for Hubbard III). The failure of these approximations, when continued into the metallic phase, is due to their inability to capture the Kondo effect which builds up the Fermi-liquid quasiparticles. They are qualitatively valid in the Mott insulating phase however.

The spectral density of insulating solutions vanish within a gap $-\Delta_g/2<\omega<+\Delta_g/2$. Inserting the spectral representation of the local Green's function into the self-consistency relation, Eq. (221) implies that $\Sigma(\omega+i0^+)$ must be purely real inside the gap, except for a δ-function piece in $\mathrm{Im}\Sigma$ at $\omega=0$, with

$$\mathrm{Im}\Sigma(\omega+i0^+)=-\pi\rho_2\delta(\omega)\quad\text{for }\omega\in[-\Delta_g/2,\Delta_g/2] \tag{235}$$

and that $\mathrm{Re}\Sigma$ has the following low-frequency behavior:

$$\mathrm{Re}\Sigma(\omega+i0^+)-U/2=\frac{\rho_2}{\omega}+O(\omega). \tag{236}$$

In these expressions, ρ_2 is given by

$$\frac{1}{\rho_2}=\int_{-\infty}^{+\infty}d\epsilon\,\frac{\rho(\epsilon)}{\epsilon^2}. \tag{237}$$

ρ_2 can be considered as an order parameter for the insulating phase [the integral in Eq. (237) diverges in the metallic phase]. A plot of the spectral function and self-energy in the insulating phase, obtained within the iterated perturbation theory approximation, is also displayed in Figs. 30 and 31. The accuracy of these results is more difficult to assess than for the metal, since exact diagonalization methods are less efficient in this phase. A plot of the gap Δ_g vs U estimated by the iterated perturbation theory and exact diagonalization is given in Fig. 32. Within both methods, the insulating solution is found to disappear for $U<U_{c1}(T=0)$, with $U_{c1}^{\rm ED}\simeq 2.15D$ (while the iterated perturbation theory method yields $U_{c1}^{\rm IPT}\simeq 2.6D$). As discussed below in more detail (Sec. VII.F), the precise mechanism for the disappear-

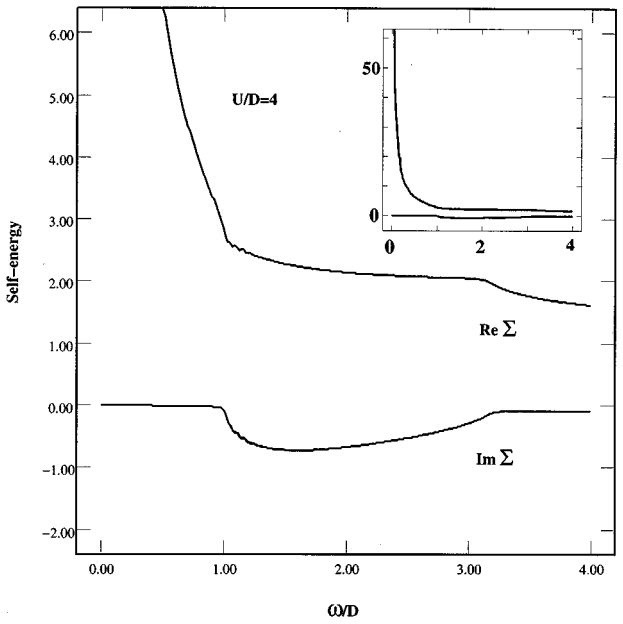

FIG. 31. Real and imaginary parts of the self-energy $\Sigma(\omega+i0^+)$, as obtained from the iterated perturbation theory approximation, for a value of $U/D=4$ in the insulating phase. The inset contains the same quantities on a larger scale that shows the $1/\omega$ singularity in $\mathrm{Re}\Sigma$.

ance of the insulating solution at U_{c1}, the behavior of the gap at this point, and the value of U_{c1} have not yet been fully settled.

In summary, the existence of two classes of solutions of the paramagnetic LISA equations at zero temperature can be established analytically. Metallic solutions are characterized by a nonzero density of states $\rho(0)=D(0)$ $[=2/(\pi D)$ for the Bethe lattice], while insulating solutions have $\rho(0)=0$, for both the impurity and the effective conduction bath at zero frequency. The density of states at zero energy is an order parameter for this problem, and can be shown to be self-consistently nonzero for small U/D and zero for large U/D.

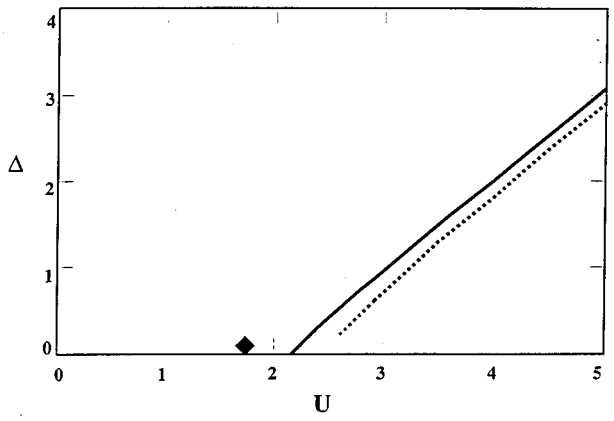

FIG. 32. Paramagnetic gap (solid line) as a function of the interaction U obtained from exact diagonalization. For comparison, the corresponding results from iterated perturbation theory (dotted line) and the value of $U_{c1}^{\mathrm{H\ III}}=\sqrt{3}D$ within the Hubbard III approximation (diamond) are also shown.

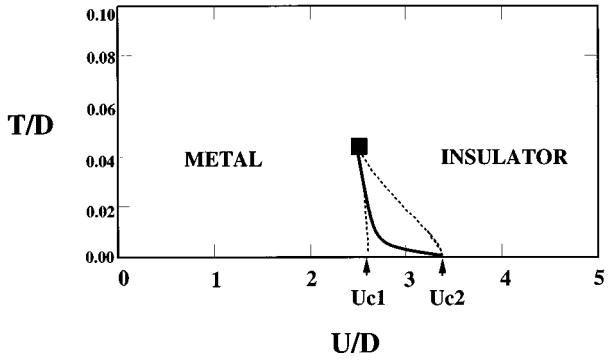

FIG. 33. Phase diagram of the fully frustrated model at half-filling. It is possible to move continuously from one phase to the other since at high temperature the transition becomes a crossover. Within the region delimited by the dashed lines, the metallic and insulating solutions coexist. The full line is the approximate location of the actual first-order transition line. Both ends of this line [at the full square and at $U_{c2}(T)=0$] are second-order points.

D. Phase diagram and thermodynamics

1. Paramagnetic phases

The qualitative distinction between a metal and an insulator is precise at zero temperature. At finite but small temperatures a sharp distinction between a metallic and an insulating solution can still be made in the present problem, since a region of the (U,T) parameter space defined by $U_{c1}(T)<U<U_{c2}(T)$ is found where *two* paramagnetic solutions are allowed within the LISA, as shown on Fig. 33 (Georges and Krauth, 1993; Rozenberg, Kotliar, and Zhang, 1994). This is evidenced by the plot of the double occupancy $\langle n_\uparrow n_\downarrow\rangle$ given in Fig. 34. One of these solutions is continuously connected to the $T=0$ metallic solution, and its density of states displays a peaklike feature at the Fermi energy. The other solution can be connected to the $T=0$ insulating solution, and the Green's function extrapolates to zero at zero frequency. As the temperature is further increased, this region of coexistent solutions disappears and we are left with a rapid crossover from a metallic-like solution to an insulating-like one. This is possible because at finite temperature there is no *qualitative* distinction between a metallic and an insulating state. The two lines $U_{c1}(T)$ and $U_{c2}(T)$ defining the coexistence region merge at a second-order critical point (Fig. 33). The actual metal-insulator transition at finite temperature is first order, and takes place at the coupling $U_c(T)$ where the free energy of the two solutions cross. Note that this is the case even though *no lattice deformations* have been included in the model. For early discussions of the occurrence of a first-order metal-insulator transition at finite temperature in the Hubbard model, see the works of Cyrot (1972); Castellani, DiCastro, Feinberg, and Ranninger (1979); Spalek, Datta, and Honig, 1987); Spalek

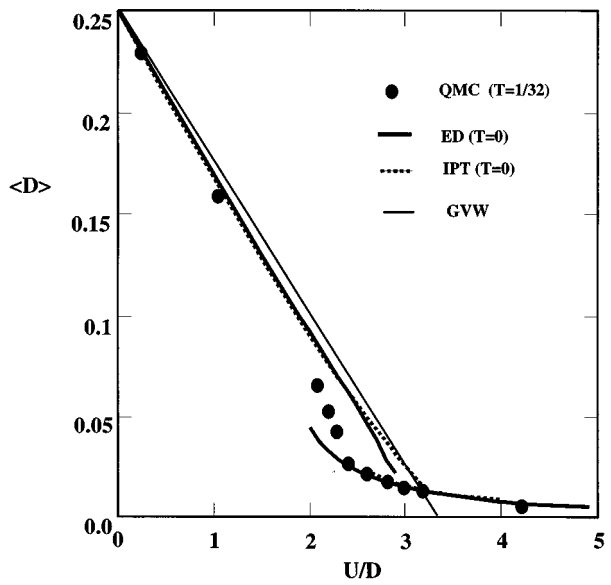

FIG. 34. Double occupancy $\langle D\rangle=\langle n_\uparrow n_\downarrow\rangle$ as a function of the interaction U/D. The data corresponds to QMC simulations at βD=32 (dots), eight sites exact diagonalization (bold line) and iterated perturbation theory at T=0 (dotted line). For comparison, the results of the Gutzwiller approximation is also plotted (thin line).

(1990) and references therein. It is interesting in this respect to note that the compound $Y_{1-x}Ca_xTiO_3$ has been recently reported by Iga *et al.* (1995) to display a first-order metal-insulator transition without a structural change. At zero temperature $U_c=U_{c2}(T=0)$ (Rozenberg, Moeller, and Kotliar, 1994; Moeller *et al.*, 1995), but the line $U_c(T)$ remains very close to $U_{c1}(T)$ down to very small temperatures, because of the higher entropy (N ln 2) of the insulating solution.

In addition to these paramagnetic solutions, the mean field Eqs. (220) and (223) also have nontrivial solutions with antiferromagnetic long-range order. The range of parameters where the antiferromagnetic solution exists depends on the details of the lattice structure and in particular on the degree of magnetic frustration t_1/t_2, as described in detail below.

As in any mean-field theory, the complete determination of a phase diagram in the LISA method involves the following steps: (i) first, the *possible* competing phases have to be determined, and their region of coexistence located, (ii) then, the free-energy of each competing solution is calculated within the coexistence region. The solution with lowest free-energy gives the stable phase, and the procedure also yields the actual critical boundary. Notice that (i) the nature of the various competing phases must be guessed *a priori* on the basis of physical intuition in order to get the correct phase diagram, and that (ii) the determination of the free-energy may be ambiguous when approximate techniques are used to solve the LISA equations, if these approximations are not "conservative" in the sense of Baym and Kadanoff. For these reasons only a few complete phase diagrams have appeared in the literature.

In the case of the half-filled Hubbard model on the *fully frustrated* lattice, magnetically ordered phases need not be considered since they are suppressed by the magnetic frustration. In this case, the only two competing phases are the paramagnetic metal and the paramagnetic insulator. These phases coexist in a region of the (U,T) parameter space, as described above. The location of this coexistence region (Georges and Krauth, 1993) and the location of the actual critical line obtained by comparing free energies (Rozenberg, Kotliar, and Zhang, 1994) has only been studied in detail within the iterated perturbation theory approximation. The resulting phase diagram is displayed on Fig. 33. The first-order metal insulator critical line ends at a finite-temperature critical point (in a manner analogous to a liquid-gas transition). Furthermore, the zero-temperature end point of this line can be shown analytically (see Sec. VII.E below) to correspond to a second-order transition associated with the disappearance of the metallic solution (Moeller *et al.*, 1995): $U_c(T=0)=U_{c2}(T=0)$. Note that the iterated perturbation theory approximation yields $U_{c1}(T=0)^{\rm IPT}/D\simeq 2.6$ and $U_{c2}(T=0)^{\rm IPT}/D\simeq 3.3$, while the more precise determinations from zero-temperature exact diagonalization studies and the projective technique yield $U_{c1}(T=0)/D=2.15\pm 0.25$ and $U_{c2}(T=0)/D=2.92\pm 0.05$. [The iterated perturbation theory values for the critical U's found by Georges and Krauth (1993) for the $d=\infty$ hypercubic lattice are close but slightly smaller to the ones above, when normalized by the effective half-width W.] Detailed comparisons between the iterated perturbation theory approximation and the QMC method at finite temperature have shown excellent agreement for T/D of the order of 1/50 or higher. In this region, the iterated perturbation theory phase diagram is quite reliable. The detailed shape of the very-low-temperature coexistence region as obtained from exact diagonalization studies does reveal some differences with the iterated perturbation theory approximation however. In this respect, and in connection with the remark (ii) made above, let us mention that the free energy within the iterated perturbation theory approximation must be evaluated from a functional that gives the mean-field equations by differentiation, rather than from the one-particle Green's function. This is crucial in order to obey the exact property of a second-order transition at T=0.

Two physical remarks must be made on the phase-diagram of Fig. 33. First, the slope of the first-order phase boundary is such that the insulator is reached upon heating. This reflects the fact that the paramagnetic insulator has higher entropy than the metal. It is a generic feature of the phase diagram of many strongly correlated systems, such as the first-order metal-insulator transition line of V_2O_3 (Fig. 23), and the solidification line of ^{3}He below the Pomeranchuk temperature. The same qualitative reason is responsible for the behavior of the fraction of doubly occupied sites as a function of temperature, shown in Fig. 35. One observes that in the metallic regime, $\langle n_\uparrow n_\downarrow\rangle$ starts by *decreasing* upon heating (thus indicating an *increasing* degree of

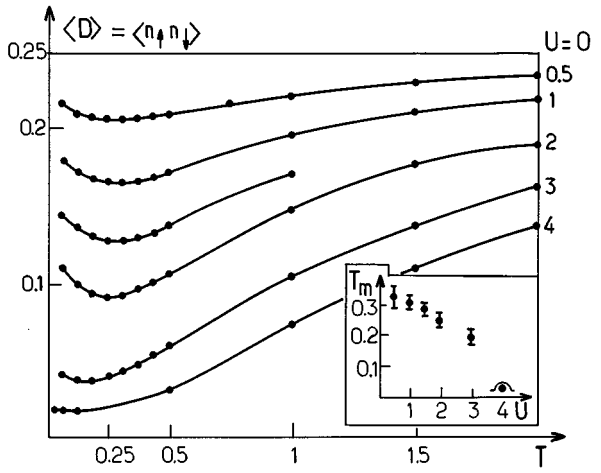

FIG. 35. Double occupancy as a function of temperature. These QMC data were obtained for the hypercubic lattice (Gaussian density of states with $t_{ij}=t/2\sqrt{d}$). Note the presence of a minimum at $T=T_m$ for metallic values of U. The inset displays T_m as a function of U.

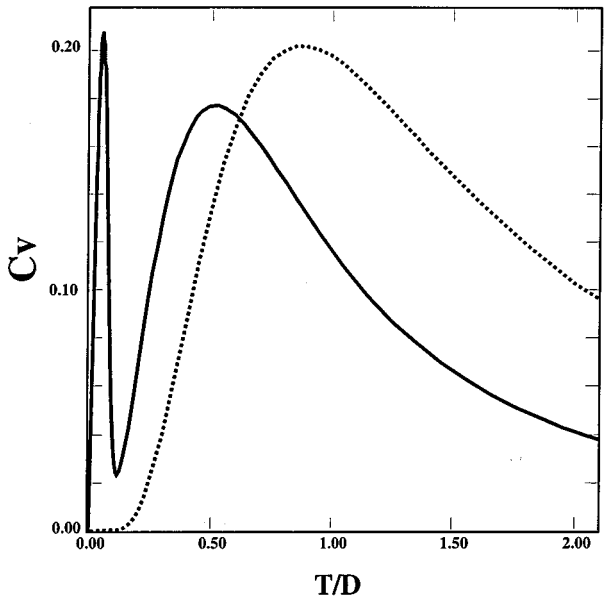

FIG. 36. The specific heat C_v as a function of temperature. The solid line is for U/D=2 and the dashed line corresponds to U/D=4. The separation between the spin-fluctuation scale ϵ_F^* at low energies and the charge-fluctuations scale at high energy ($\sim U-2D$) is apparent in the metallic case (U/D=2). Note also the linear behavior at low temperature in the metal, in contrast to the activated behavior in the insulator.

localization). Secondly, the first-order line ends at a critical point where a crossover region starts. In this region the metal is sustained by activation across the Mott-Hubbard gap. As a result the slope of the crossover region between the metal and the insulator is $T\approx U-2D$, opposite to that of the transition line.

2. Thermodynamics

Now we turn to the behavior of thermodynamic quantities as a function of temperature, in both the metallic and insulating phase. The LISA is a powerful technique for the study of thermodynamics. This represents a significant improvement over earlier methods like the Gutzwiller variational approach or the slave boson method, which did not have satisfactory extensions to finite temperatures (because of the neglect of incoherent excitations).

In the paramagnetic case, the energy is computed from the Green function using Eq. (47) and the entropy is given by

$$S(T)=\int_0^T \frac{C_v(T')}{T'}\,dT'+S(0)$$

$$=N\ \ln 4-\int_T^{+\infty}\frac{C_v(T')}{T'}\,dT', \tag{238}$$

where C_v is evaluated by numerical differentiation of the energy. $S(0)$ is zero for the metallic side and N ln2 for the insulating side, reflecting the double degeneracy of the impurity model ground state in this phase. The physical critical line where the first-order phase transition takes place is determined by equating the free energies of the two states,

$$F_M-F_I=E_M-E_I-(S_M-S_I)T. \tag{239}$$

Figure 36 shows the specific heat C_v as a function of temperature for two values of the interaction U, in the metallic and insulating phases, respectively. The characteristic low-energy scale in the metallic phase is set by the renormalized Fermi energy $\epsilon_F^* = ZD$. Below this scale (in practice, below $\sim \epsilon_F^*/5$), the specific heat has the characteristic Fermi-liquid behavior $C_v=\gamma T$, with the slope γ proportional to $m^*/m\sim(U_{c2}-U)^{-1}$. At higher temperatures we see a thermal activation of the incoherent features corresponding mainly to density fluctuations. In the insulating phase, we observe only this last effect, which takes place at an energy scale $U-2D$. The main features of the thermodynamics in the strongly correlated metallic state can be understood from the existence of these two energy scales: ϵ_F^*, the renormalized Fermi energy, is the scale for low-energy (local) spin fluctuations, and U is the energy scale for charge (density) fluctuations. In the correlated metal, these two scales are well separated and give rise to two peaks in the specific-heat, while they coalesce for small U (Fig. 37).

The entropy as a function of temperature, obtained by integrating C_v/T, is displayed in Fig. 38. The quasiparticle peak in C_v corresponds to a spin entropy of ln2, which is reached at a scale of order ϵ_F^*, while the integral over the second peak at around U-2D contains the ln2 entropy of the charge degrees of freedom. Figure 39 shows the evolution of the spectral function of the metal as a function of temperature. Note that the quasiparticle peak is suppressed above a temperature of order ϵ_F^*. At higher temperatures, the curvature at low frequencies

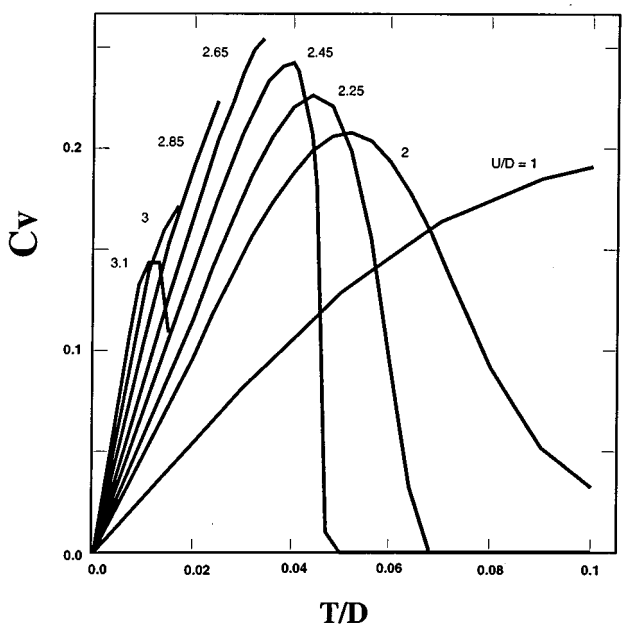

FIG. 37. Low-temperature part of the specific heat C_v as a function of temperature for several (metallic) values of U/D, showing the gradual increase of the slope γ and gradual decrease of ϵ_F^*.

changes sign, and $\rho(\omega)$ has a "pseudogap" shape.

In Figs. 36 and 38, we also display the specific heat and entropy of the Mott insulating phase. They feature the expected activated behavior $\sim\exp(-\Delta_g/T)$ at low temperature. Note that, as mentioned above, the insulator has a residual ground-state entropy $S(0)=N\ln 2$. This is also the result found in the Gutzwiller approximation, where the insulator is caricatured as a collection

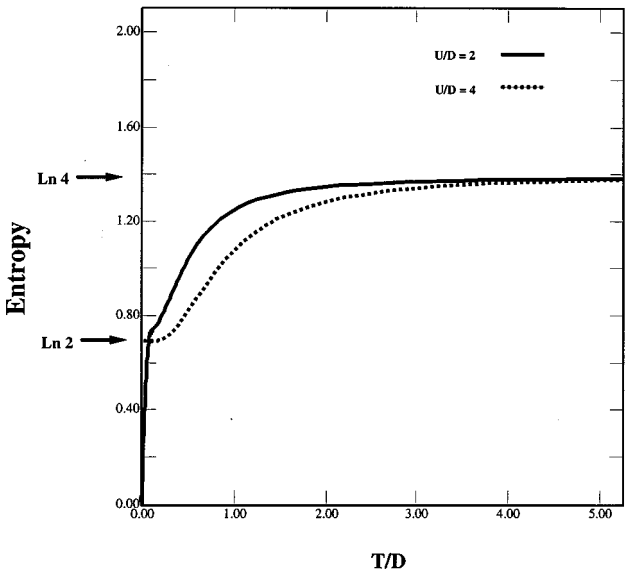

FIG. 38. Entropy *per site* as a function of temperature for two different values of interaction U/D=2,4. Note that the spin-fluctuation entropy ln2 is reached at a scale $\sim\epsilon_F^*$ in the metal.

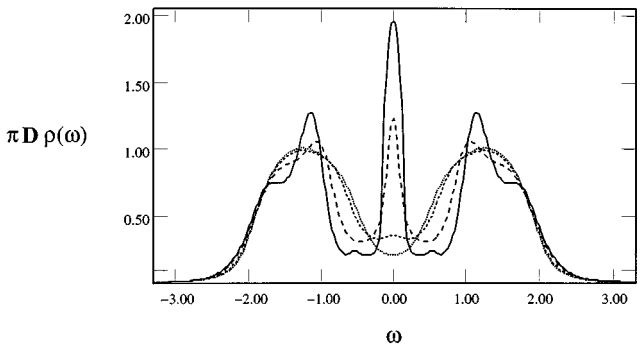

FIG. 39. Local spectral density $\pi D\rho(\omega)$ for various temperatures T/D=0.03 (full), 0.05 (dashed), 0.08 (short-dashed) and 0.10 (dotted), as obtained by iterated perturbation theory (U/D=2.5). Note the disappearance of the quasiparticle peak at a scale $\sim\epsilon_F^*$, and the corresponding transfer of spectral weight over large energy scales.

of independent magnetic moments. This result may seem surprising in the present context since the LISA *does not* neglect charge fluctuations and residual magnetic exchange. The explanation is that there are actually *two* different exchange scales in the $d=\infty$ limit: one is the exchange coupling between two fixed spins $J_{ij}\sim t_{ij}^2/U\sim O(1/d)$ while the other is the exchange energy between a spin and its shell of d antiparallel neighbors. Since the latter is d times the former, it remains $O(1)$ and sets the scale for the Néel temperature. The first scale controls the splitting between the ($\sim 2^N$) states with total S_z=0, and does vanish as $d\to\infty$. Hence, the $d\to\infty$ limit *does* lead to a degenerate ground state whenever the Mott insulating phase is not unstable to long-range antiferromagnetic order (i.e., for highly frustrated lattices). These considerations will also be crucial in order to understand the behavior of local and uniform spin susceptibilities.

The comparison of the kinetic energy $K=\langle\Sigma_k\epsilon_k c_k^+ c_k\rangle/N$ and the potential energy per site $V=U\langle n_\uparrow n_\downarrow\rangle$ of the two solutions is shown in Fig. 40. We find that the difference in the internal energy of the two states within the iterated perturbation theory is much smaller than the corresponding difference in the kinetic

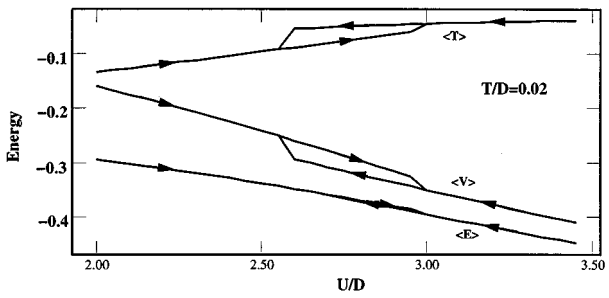

FIG. 40. The kinetic, potential and internal energy as a function of U for T/D=0.02 from iterative perturbation theory. The hysteresis effect is clearly observed.

and potential energy taken separately. The gain in kinetic energy by delocalization is almost perfectly canceled by the loss in potential energy due to the Coulomb repulsion on doubly occupied sites. The small energy difference between the two states is a generic feature of the problem, and has been verified in exact diagonalization calculations. In fact the near degeneracy of the metallic and the insulating state near U_{c2} follows from the bifurcation of two stationary points of the free-energy functional at U_{c2}. This issue will be revisited later in this section.

3. Antiferromagnetic phases

Let us now consider the solution of the model with magnetic order. In the absence of magnetic frustration, on a bipartite lattice, one expects to find an antiferromagnetically ordered state at low temperature. For small U, this is expected from Hartree-Fock and variational calculations (Penn, 1966; Langer, Plischke, and Mattis, 1969; Yokoyama and Shiba, 1987; for next-to-leading corrections to Hartree-Fock, see also Georges and Yedidia, 1991 and van Dongen, 1991b). For large values of the interaction, the magnetic moments become fully developed and the model maps onto the Heisenberg model. It will consequently also display an antiferromagnetic state with a Néel temperature that is inversely proportional to U. The low-temperature solution of the model, on a bipartite lattice, is therefore expected to be that of an antiferromagnetic insulating state for all U, due to the effective doubling of the lattice parameter.

This scenario is fully realized in the limit of large dimensions as is demonstrated by the solution of the self-consistent equations (223) with $t_2=0$ that defines the model on a Bethe lattice without magnetic frustration. Analytic arguments for an antiferromagnetic ground state for arbitrary U on the $d=\infty$ hypercubic lattice have also been given by Kopietz (1994). In Fig. 41 (top plot) we show the local spectral densities for each spin species in the antiferromagnetic phase at $U/D=1.5$, as obtained by exact diagonalization. A gap is present in the spectrum, and the solution is insulating. The difference between the total densities of the up and down spin on each sublattice is clearly apparent.

The Néel temperature as a function of U has been calculated with the QMC method (Jarrell, 1992; Georges and Krauth, 1993; Rozenberg, Kotliar and Zhang, 1994). In Fig. 42, we show the results for the unfrustrated Bethe lattice ($t_2=0$). Comparison with Fig. 33 shows that, in this case, the Néel temperature is always well above any metal-insulator transition temperature. Hence, the phase diagram just consists in a high-temperature paramagnetic phase and a low-temperature insulating antiferromagnet. On such unfrustrated lattices, it is clear that Slater's point of view is correct for understanding the metal to insulator transition. The onset of antiferromagnetism makes the metal insulator transition within the paramagnetic phase completely irrelevant on bipartite lattices.

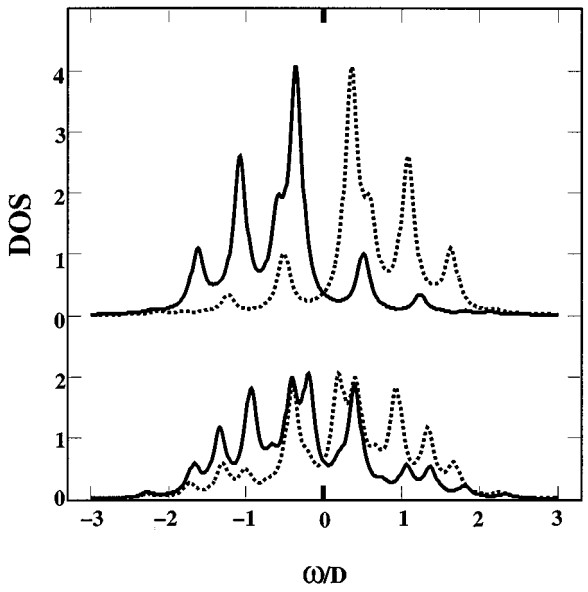

FIG. 41. The local spectral density for spin-σ and $-\sigma$ electrons (full and dotted line), obtained from eight sites (exact diagonalization) with $U/D=1.5$. ($\sigma=\uparrow$ on the A sublattice, $\sigma=\downarrow$ on the B sublattice.) The top plot corresponds to the bipartite Bethe lattice and to an insulating AF, while the lower plot corresponds to the TSF model with $t_1^2=\frac{1}{4}t^2$ and $t_2^2=\frac{3}{4}t^2$, and to a metallic AF. The exact diagonalization results in a set of δ-function peaks to which a small broadening has been applied.

Also shown on Fig. 42 is a comparison between the QMC determination of the Néel temperature and the Hartree-Fock and iterated perturbative theory approximations. As it turns out, T_N is considerably reduced by local quantum fluctuations as compared to the Hartree-Fock approximation. Unfortunately, the iterated perturbative approximation is also rather poor and underestimates T_N for large U.

We finally turn to the interesting case of a model having some intermediate degree of frustration. Rozenberg,

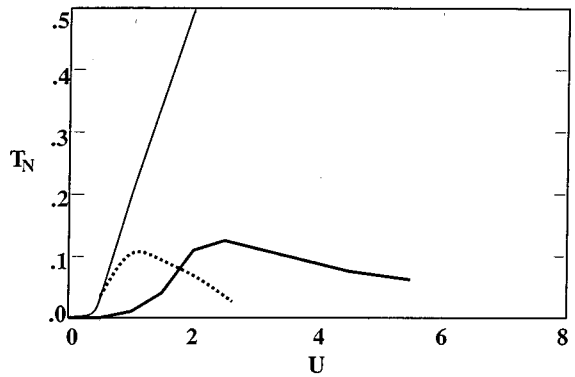

FIG. 42. QMC determination of the Néel temperature (and phase diagram) of the half-filled bipartite Bethe lattice as a function of U/D (bold line). For comparison, the Hartree-Fock (thin line) and iterated perturbation theory approximations (dotted line) are also displayed.

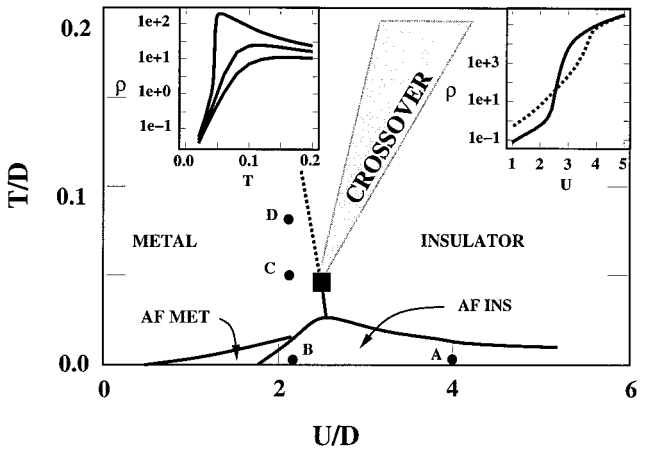

FIG. 43. Approximate phase diagram for the model with nearest-neighbor and next-to-nearest-neighbor hopping $(t_2/t_1) = \sqrt{1/3}$. The first-order PM metal-insulator transition ends at the critical point T_{MIT} (square). The dotted line and the shaded region describe two crossovers as discussed in the text. The full circles indicate values of the parameters chosen to model the optical spectra of V_2O_3 in Sec. VII.I.3. A, insulator (y=0); B, insulator (y=0.013); C, metal (y=0, 170 K); D, metal (y=0, 300 K). For comparison with the experimental results, note that increasing U/D is associated with decreasing pressure. Left inset: $\rho_{\mathrm{dc}}(T)$ for U/D=2.1,2.3,2.5 (bottom to top). The maxima of $\rho_{\mathrm{dc}}(T)$ is defined by the dotted line. Right inset: $\rho_{\mathrm{dc}}(U)$ for $T=0.06D$ (full) and $T=0.15D$ (dotted).

Kotliar, and Zhang (1994) studied the TSF model, with $t_1^2=1/4t^2$ and $t_2^2=3/4t^2$, but the general features are expected to be representative of more realistic frustrated lattices. A schematic representation of the phase diagram of the two sublattice frustrated model is shown in Fig. 43. The partial frustration reduces the Néel temperature. For large U, the Néel temperature is given by $2(t_2^2-t_1^2)/U$ while, for small U, Rozenberg, Kotliar, and Zhang were able to obtain upper bounds on the Néel temperature, showing that its maximum lies *below* the critical temperature for the Mott transition. This establishes the relevance of the finite-temperature metal to the paramagnetic insulator transition in this case.

As shown in Fig. 41 (lower plot) and Fig. 43, the partial frustration is also able to drive the system into an *antiferromagnetic (AF) metallic state* at small values of U (in contrast to an antiferromagnetic insulator in the absence of frustration). The Néel temperature on the metallic side is smaller than the one on the insulating side. The addition of frustration has also dramatic consequences for the density of states in the ordered phase. The order of the different magnetic transitions for small and intermediate U is still an open problem in this case.

Let us finally mention that the quantum transition between a strongly correlated paramagnetic metal and a metal with spin-density wave (AF) order has been studied in a rather general framework by Sachdev and Georges (1995), using the LISA method. These authors demonstrated that at low energies $T,\omega \ll \epsilon_F^*$, the order parameter fluctuations are characterized by $z\nu$=1 (where ν is the exponent associated with the correlation length and z is the dynamical exponent), while there is an intermediate energy range $\epsilon_F^* < T,\omega < \sqrt{U\epsilon_F^*}$ in which a universal regime with $z\nu$=1/2 is found.

It is very interesting to note that most of the main features of the experimental phase diagram of V_2O_3 (McWhan *et al.*, 1973; Kuwamoto, Honig, and Appel, 1980; Carter *et al.*, 1992) are very close to the phase diagram of the TSF model in Fig. 43. In particular, if we associate decreasing pressure with increasing interaction U, we find the correct sign of the slope of the first-order line that separates the paramagnetic metallic and the paramagnetic insulating state. In both the theoretical and experimental case, this line ends in a second-order critical point where a crossover region starts and which is tilted in the opposite way. The topology of the phase diagram is also captured in detail, including the small antiferromagnetic metallic region recently found by Carter *et al.* (1992) for $V_{2-y}O_3$.

The experimentally observed phase diagrams of transition metal oxides display incommensurate metallic magnetism. This can in principle be studied by extending the mean field theory to account for incommensurate phases, as described in Sec. IV, and has been investigated by Freericks (1993a, 1993b, 1993c) for the Falicov-Kimball model (Sec. VIII.B) and Freericks and Jarrell (1995a, 1995b) for the Hubbard model (Sec. VII.H). These orderings depend on the detailed shape of the Fermi surface, and it would be interesting to perform a calculation taking into account a realistic band structure for some transition metal oxide. This seems feasible within the LISA (cf. Sec. VIII.C), but has not been investigated yet.

E. The zero-temperature metal-insulator transition

As discussed above, a metallic solution is found at zero temperature for $U<U_{c2}(0)$, while an insulating solution exists for $U>U_{c1}(0)$. A fairly detailed understanding of the critical behavior at $U_{c2}(0)$ has been achieved, which we review in this section. This understanding is based to a large extent on the projective self-consistent method described in Sec. VI.C, to which the reader is referred for technical details. The evidence that $U_{c1}(0)<U_{c2}(0)$ also relies on this method. The detailed mechanism for the disappearance of the insulator at $U_{c1}(0)$ is understood in less detail, and will be discussed in Sec. VII.F.

Let us first mention that the existence of a continuous T=0 transition at which the metallic solution of the LISA equations disappears can be established by various methods. The general idea common to all methods is to characterize the Green's function in the metal by a single parameter Z (the quasiparticle residue, or weight of the Kondo resonance), and to project the full LISA dynamical mean-field equations onto that single "relevant direction." This yields an equation for Z which is reminiscent of the slave-boson mean field equations near the Brinkman-Rice transition and which takes the form

$$(1-U/U_{c2})Z-aZ^2=0. \tag{240}$$

This equation can be derived, together with the value of the positive coefficient a, by using the iterated perturbation theory approximation (Zhang, Rozenberg, and Kotliar, 1993), and has yet to be calculated with the more accurate projective self-consistent method of Sec. VI.C. This method yields a very accurate determination of $U_{c2}(0)$ [from Eq. (211) in Sec. VI.C]:

$$U_{c2}(T=0)/D=2.92\pm 0.05. \tag{241}$$

The Gutzwiller-Brinkman-Rice approximation would yield the somewhat larger value $U_{\mathrm{BR}}=3.37D$, virtually identical to the value obtained in the iterated perturbation theory approximation ($U_{c2}^{\mathrm{IPT}}\simeq 3.37D$).

We now mention an argument of Moeller *et al.* (1995), showing that the actual *zero-temperature* metal-insulator transition takes place at $U_{c2}(0)$, and is second order, so that the first-order transition line $U_c(T)$ ends at $U_{c2}(0)$ for $T=0$. [In the following, we shall for this reason use U_c in place of $U_{c2}(0)$]. The argument uses the fact that the derivative of the ground-state energy is the density of doubly occupied sites:

$$\frac{dE}{dU}=\langle n_\uparrow n_\downarrow\rangle. \tag{242}$$

The fraction of doubly occupied sites can be computed numerically at $T=0$ using exact diagonalization, as shown above in Fig. 34. As expected, $\langle n_\uparrow n_\downarrow\rangle$ is larger for the metallic solution than for the insulating solution. Integrating Eq. (242) from U up to U_{c2} (where the two solutions merge), one thus finds that $E_{\mathrm{ins}}>E_{\mathrm{metal}}$ whenever the two solutions coexist, which proves that the $T=0$ transition takes place at $U_{c2}(0)\equiv U_c$. Using the projective technique of Sec. VI.C, Moeller *et al.* (1995) have proved furthermore that $E_{\mathrm{ins}}-E_{\mathrm{metal}}\propto(U-U_c)^2$ and hence that the transition is second order. It is interesting to note that the total energy difference between the two states is much smaller than the difference in kinetic and potential energy taken separately. The gain in kinetic energy by delocalization is almost perfectly cancelled by the loss in potential energy due to the Coulomb repulsion on doubly occupied sites. (Fig. 40).

It is instructive to compare the calculation of $\langle n_\uparrow n_\downarrow\rangle$ in Fig. 34 to the results of the Gutzwiller approximation (Brinkman and Rice, 1970). In contrast to this approximation, the actual double occupancy *does not* vanish at the transition, and cannot be used as an order parameter. This is to be expected, since virtual hopping in the insulator produces a very small but nonzero double occupancy. There is however a singular contribution to $\langle n_\uparrow n_\downarrow\rangle$ that vanishes at U_c, and is correctly captured by the BR approximation. The numerical results close to U_c can be parametrized as

$$\langle n_\uparrow n_\downarrow\rangle\approx 0.015+0.235\,\frac{U_c-U}{U_c}. \tag{243}$$

Also note that the magnetic moment is obtained from the double occupation through $\langle m_z^2\rangle=1-2\langle n_\uparrow n_\downarrow\rangle$, and is thus not quite saturated at the transition.

The destruction of the metallic state at U_c is driven by the collapse of the renormalized Fermi-energy scale (or Kondo temperature) $\epsilon_F^*=ZD$. Because of the self-consistency equation (221), this is also the *bandwidth* of the effective conduction bath entering the impurity model. The critical behavior of this quantity at U_c has been investigated using the approximate iterated perturbation theory method (Rozenberg, Kotliar, and Zhang, 1994), and more recently by Moeller *et al.* (1995) using the more accurate self-consistent projective method. It has been established that the quasiparticle residue (and hence ϵ_F^*) vanishes linearly at U_c, with a prefactor obtained from the numerical results as

$$Z=C_Z\left(1-\frac{U}{U_c}\right)+\cdots,\quad C_Z=0.9\pm 0.15. \tag{244}$$

So, the effective mass $m^*/m=1/Z$ and linear coefficient of the specific heat $\gamma=4\pi k_B^2/(3Z)$ diverge at the transition. For comparison, the BR approximation yields the much larger slope $Z\approx 2(1-U/U_{BR})$. Also note that, as compared to an Anderson impurity model with a fixed conduction band, the self-consistency has the effect of changing the dependence of the quasiparticle energy scale (or Kondo scale) from an exponential behavior [$\sim\exp-(U/D)$] to linear in (U_c-U).

Close to U_c, there is a clear separation of energy scales and the local spectral density can be written as a sum of low-energy and high-energy parts: $\rho(\omega)=\rho_l(\omega)+\rho_h(\omega)$. The high-energy part resembles the solution of an atomic problem, with two Hubbard bands centered around $\pm U/2$, while the low-energy part obeys a scaling form:

$$\rho_l(\omega)=\frac{1}{D}\,f\left(\frac{\omega}{\epsilon_F^*}\right). \tag{245}$$

The scaling function f, which resolves the low-energy peak in the spectral function, has been calculated by Moeller *et al.* (1995) using the projective methods of Sec. VI.C. The scaling form (245) implies that the quasiparticle lifetime has a stronger singularity than the quasiparticle residue, and behaves as

$$\mathrm{Im}\Sigma(\omega+i0^+)\simeq -0.4D\left(\frac{\omega}{\epsilon_F^*}\right)^2+\cdots, \tag{246}$$

where the prefactor has been determined by a fit to the scaling function.

F. On the $T=0$ instability of the insulating solution

We have just seen that, in the region of the phase diagram around U_{c2}, many of the Brinkman-Rice predictions for the destruction of the metal are qualitatively valid (when suitably interpreted). In this section, we consider the mechanism for the destruction of the insulating solution, which occurs at U_{c1}, and we address the question of whether the $T=0$ values of U_{c1} and U_{c2} are actually different (in contrast to the Brinkman-Rice scenario where $U_{c1}=U_{c2}$). The original Hubbard scenario

predicts a continuous closure of the gap at U_{c1}, and a divergence of the dielectric constant.

In order to gain insights on the destruction of the insulating state, a simple parametrization of the Green's function can be used in this phase:

$$\mathcal{G}_0(\tau)=\alpha\left(\theta(\tau)-\tfrac{1}{2}\right)+\mathcal{G}_0^{\rm inc}(\tau) \tag{247}$$

with $\theta(\tau)$ being the step function. The first term represents an insulating solution in the atomic limit (t=0). $\mathcal{G}_0^{\rm inc}$ is the "incoherent part" of the insulating solution, which decays exponentially to zero as $\tau\to\infty$ at zero temperature. Physically, this decomposition is motivated by viewing the self-consistent equations as describing a Kondo spin in an insulator. The spin operator $\vec{S}$ has a low energy part which is responsible for a Curie type of local spin susceptibility and a high frequency part. We write $\vec{S}=\sqrt{\alpha}\vec{S}_{\rm low}+\vec{S}_{\rm high}$, α is a quantity similar to the "quasiparticle weight," describing the weight of a pure free spin in an interacting system made of the impurity and the insulating host. In frequency space, $\mathcal{G}_0^{\rm inc}$ is only responsible for the details of the shape of the Hubbard bands which are high frequency features. The step function part gives rise to a divergency in $\mathcal{G}_0(i\omega_n)\sim 1/i\omega_n$ and is solely responsible for the existence of a gap. In the atomic limit α approaches unity, while on the contrary, the vanishing of α signals the complete screening (or Kondo quenching) of the spin and the destruction of the insulating phase.

Using the parametrized form of $\mathcal{G}_0$, we can relate α to the density of states $\rho(\epsilon)$ of the local Green function. At half-filling, because of the particle-hole symmetry,

$$G=2i\omega_n\int_0^\infty \frac{\rho(\epsilon)d\epsilon}{(i\omega_n)^2-\epsilon^2}. \tag{248}$$

Therefore, using (221) and comparing linear terms in $i\omega$,

$$\alpha^{-1}=1+2t^2\int_0^\infty \frac{\rho(\epsilon)d\epsilon}{\epsilon^2}\equiv 1+2t^2\rho_2. \tag{249}$$

Note that in the metallic phase, α^{-1} would diverge.

Further progress can be made within the iterated perturbation theory approximation (Rozenberg, Kotliar, and Zhang, 1994). Inserting the parametrized $\mathcal{G}_0$ into the expression of the self-energy at second order [Eq. (157)], and identifying the most singular terms in the self-consistency condition, one obtains a closed equation for α:

$$\alpha=\left(1+\frac{D^2}{U^2\alpha^3}\right)^{-1}. \tag{250}$$

There are two solutions α^* for $U>U_{c1}$, with $U_{c1}^{\rm IPT}=3\sqrt{3}/2D\approx 2.6D$ (in good agreement with the value obtained from solving numerically the iterated perturbation theory equations). The one with a smaller α^* is always unstable and unphysical since it is not connected continuously to α=1 as U tends to infinity. At the transition U_{c1}, the unstable fixed point merges with the stable one, and the fixed point solution disappears. Note that α is finite at U_{c1} within the iterated perturbative theory approximation, but the gap may well close continuously.

Studies of the full numerical solution of the model within exact diagonalization indicate a closure of the gap at a critical value of $U=U_{c1}$ appreciably below $U_{c1}^{\rm IPT}\simeq 2.6D$. The numerical data indicate that $\Delta_{\rm gap}\sim(U-U_{c1})$ and that α^{-1} may diverge at U_{c1} (Rozenberg, Kotliar, and Kajueter, 1995). However, the detailed critical behavior near U_{c1} requires much more precise numerics and analytic techniques, and is still an open problem. These results can be compared to the corresponding ones from the Hubbard III approximation. In that case the critical value for the destruction of the insulating state is $U_{c1}^{\rm HIII}=\sqrt{3}D$, and $\Delta^{\rm HIII}\sim(U-U_{c1}^{\rm HIII})^{3/2}$. Diagonalizations of truncated lattices involving successive shells of neighbors of the $z=\infty$ Bethe lattice have been investigated by Gros *et al.* (1994), with results quite comparable to the Hubbard III approximation and to a more elaborated equation of motion decoupling scheme (Gros, 1994; cf. Sec. VI.B.4). These methods may ultimately shed some light on the behavior near U_{c1}. We emphasize however that they are unable to access the metallic phase in a reliable way, and thus that they should not be used to draw conclusions on the transition taking place at U_{c2} (which is missed by these methods).

Neither the iterated perturbation theory approximation nor the Hubbard III approximation are reliable near U_{c1}, and it would be interesting to have a detailed determination of the exact critical behavior and compare it to these approximations.

As a final remark, let us mention that even though the paramagnetic insulating phase is strictly unstable at zero temperature, it is relevant to very frustrated magnetic insulators. Since the energy difference between the metal and the paramagnetic insulator is very small in the full coexistence region, departures from full frustration will stabilize a magnetic solution that will resemble the paramagnetic insulating solution.

G. Response functions close to the Mott-Hubbard transition

We present in this section a combination of theoretical arguments and numerical results, in order to discuss the behavior of the response functions in the vicinity of the Mott transition (Rozenberg, Kotliar, and Zhang, 1994).

1. Magnetic susceptibilities

The local spin-spin correlation function has a very different behavior in the metallic and insulating phase. In the metal, we have the Fermi-liquid behavior (at T=0):

$$\langle S_z(0)S_z(\tau)\rangle\sim\frac{1}{\tau^2}\quad(\tau\gg 1/\epsilon_F^*), \tag{251}$$

while in the insulator, it develops long-term memory signalling the formation of a local moment:

$$\langle S_z(0)S_z(\tau)\rangle\sim m_0^2-O(e^{-\Delta_g\tau})\quad(\tau\to\infty). \tag{252}$$

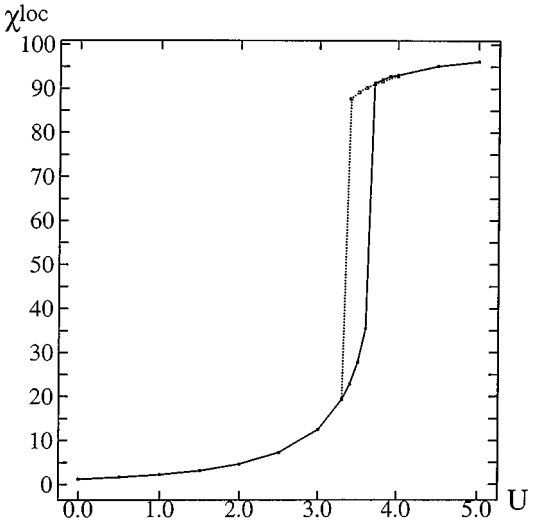

FIG. 44. Local spin susceptibility $\chi_{\rm loc}$ as a function of $U\sqrt{2}/D$ for $\beta D/\sqrt{2}=100$ obtained by exact diagonalization. Note that $\chi_{\rm loc}$ is of order $1/T$ in the insulator. The hysteresis corresponding to the first-order metal-insulator transition is apparent at this temperature between $U_{c1}=3.3D/\sqrt{2}$ and $U_{c2}=3.8D/\sqrt{2}$.

As shown in Sec. IV, the local spin susceptibility of the lattice model coincides (Sec. IV) with the local susceptibility of the impurity model (in units where $g\mu_B=2$): $\chi_{\rm loc}=\Sigma_{\mathbf{q}}\chi(\mathbf{q})=\int_0^\beta d\tau\langle S_z(0)S_z(\tau)\rangle$. It diverges at the transition and follows the Curie law in the insulating phase:

$$\chi_{\rm loc}=\frac{C_\chi}{\epsilon_F^*},\quad C_\chi=4.7\pm0.3\quad (U\to U_c^-), \tag{253}$$

$$\chi_{\rm loc}\sim\frac{1}{T}\quad (U>U_c). \tag{254}$$

Figure 44 illustrates this behavior. Using Eq. (244) and $\epsilon_F^*\equiv ZD$, the divergence of $\chi_{\rm loc}$ can also be written: $\chi_{\rm loc}/\chi_{\rm loc}^0=(3.1\pm0.2)(1-U/U_c)^{-1}$, with $\chi_{\rm loc}^0=16/(3\pi D)$ the noninteracting local susceptibility. Also, the nuclear magnetic resonance (NMR) relaxation rate is predicted to diverge as

$$\frac{1}{T_1T}=\lim_{\omega\to0}\frac{\chi''_{\rm loc}(\omega+i0^+)}{\omega}\simeq12.5\,\frac{1}{(\epsilon_F^*)^2}. \tag{255}$$

The *uniform* ($\mathbf{q}$=0) susceptibility has a very different behavior. Its relation with the impurity model response functions has been discussed in Sec. IV. It can be calculated by applying an external magnetic field on the impurity and solving the self-consistency equations for the bath and the Green's functions in the presence of the field. The uniform susceptibilities differ from the local ones because of the polarization of the Weiss function due to the external perturbation. We will illustrate how this effect, which is at the heart of the Fermi-liquid theory, affects the $\mathbf{q}$=0 response functions near U_c. In the presence of a field, the self-consistency equation reads (on the $z=\infty$ Bethe lattice)

$$\mathcal{G}_{0\sigma}^{-1}=i\omega_n+\sigma h-t^2G_\sigma. \tag{256}$$

Further qualitative insight can be gained by using an approximate analytic parametrization of the Green's function near U_c. It has been demonstrated that at $U\sim U_c$ the upper and lower Hubbard bands are already well developed, so that we can separate high energies from low energies. The high frequency part of the Green's function is polarized by the field and can be described as a superposition of Hartree-Fock solutions. As a first approximation, one can assume that the low-frequency part is unaffected by the field and consists in a resonance centered at zero frequency, of width ϵ_F^* and height $D(0)\simeq1/D$. This leads to the following approximate parametrization of the local spin-dependent Green's function:

$$G_\sigma=\frac{\langle n_{-\sigma}\rangle}{i\omega_n-U/2}+\frac{\langle n_\sigma\rangle}{i\omega_n+U/2}+\frac{1}{D}\,\frac{\epsilon_F^*}{i\omega_n+i\epsilon_F^*{\rm sgn}(\omega_n)} \tag{257}$$

Inserting (257) in (256), we have, for small frequencies,

$$\mathcal{G}_{0\sigma}^{-1}=\mathcal{G}_0^{-1}|_{h=0}+h\sigma-2\,\frac{t^2m}{U}\,\sigma, \tag{258}$$

where $\langle n_\sigma\rangle=(1+m\sigma)/2$, and m is the magnetization. Equation (258) describes an Anderson model in the presence of an effective external field $h_{\rm eff}=h-2(t^2/U)m$ acting on the impurity. The magnetization is obtained as $m=\chi_{\rm loc}h_{\rm eff}$ with $\chi_{\rm loc}$ given by (253). Solving for m we find

$$\chi\equiv\left[\frac{dm}{dh}\right]_{h=0}=\frac{1}{\chi_{\rm loc}^{-1}+2\,\dfrac{t^2}{U}}=\frac{1}{\epsilon_F^*/C'_\chi+J}, \tag{259}$$

where we have defined the magnetic exchange energy:

$$J=2\,\frac{t^2}{U}=\frac{D^2}{2U}. \tag{260}$$

In practice, however, the uniform susceptibility obtained numerically appears to be well described by the form (259), but with a value of the constant somewhat different from that entering the local susceptibility: $C'_\chi\simeq2.2\simeq C_\chi/2$ (Laloux, 1995). This is because the change in the quasiparticle peak was neglected in the above argument.

The physical interpretation of Eqs. (259) and (260) is transparent: the exchange arises from high-energy virtual processes which are largely unaffected by the Mott transition. As a result, the susceptibility varies continuously at T=0, as U passes through U_c. The result in Eq. (259) should be contrasted to the behavior of $\chi_{\rm loc}$ in Eq. (254).

These findings are consistent with the QMC results displayed in Fig. 45 for χ as a function of U. For smaller U, an initial fast increase in χ is observed as ϵ_F^* rapidly decreases. However, unlike the Brinkman-Rice approach, χ remains finite at the transition due to the existence of a nonzero superexchange constant in the uniform response. The numerical result can be parametrized according to the analytic expression obtained above. We find $\chi^{-1}\simeq0.4(1-U/U_c)+J$ for the me-

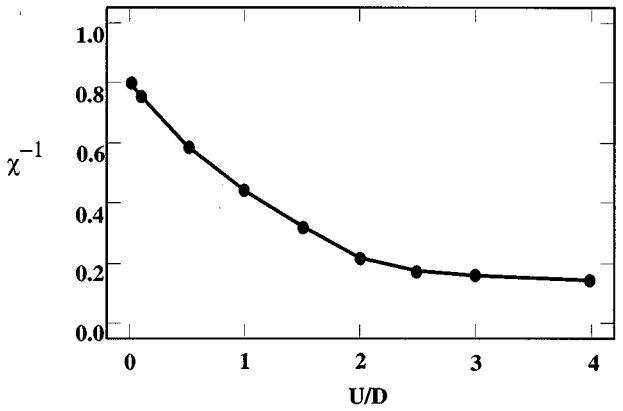

FIG. 45. Inverse of the uniform magnetic susceptibility (solid dots) as a function of the interaction U/D. Obtained from QMC at $\beta=16/D$.

tallic phase, and $\chi^{-1}\simeq J$ in the insulator phase. In comparison, the Gutzwiller-Brinkman-Rice approximation gives for the spin susceptibility (see, e.g., Vollhardt, 1984)

$$\chi^{\mathrm{BR}}=\mu_B^2 D(0)^2\left(1-\frac{U^2}{U_c^2}\right)^{-1}\left(1-\frac{D(0)U}{2}\frac{1+U/2U_c}{1+U/U_c}\right)^{-1}, \tag{261}$$

where $D(0)$ denotes the free density of states at the Fermi level. Within this approximation, the magnetic susceptibility is predicted to diverge as $\chi^{-1}_{\mathrm{BR}}\approx 0.74(1-U/U_c)$. This is an artefact of the approximation, which fails to take the exchange into account in the magnetic response. Consequently, we find that the Wilson ratio

$$R_W\equiv\frac{\chi/\chi^0}{\gamma/\gamma_0}=\frac{1}{1+F_0^a} \tag{262}$$

vanishes at U_c within the LISA, instead of approaching a constant (close to 4) as in the Brinkman-Rice approximation (Vollhardt, 1984). The Wilson ratio as a function of interaction U is displayed in Fig. 46. One can, however, define a *local* Wilson ratio which remains finite at the transition, obtained from Eqs. (244) and (253) as

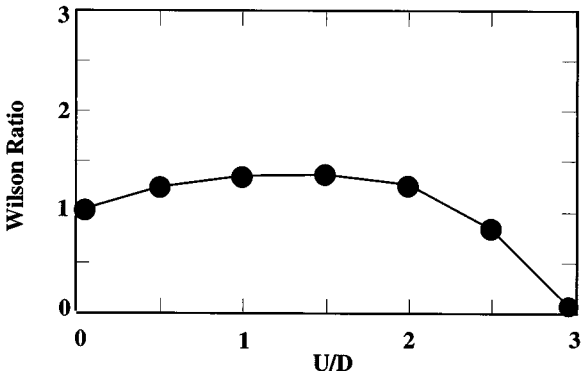

FIG. 46. Wilson ratio as a function of the interaction U/D. From QMC at $\beta=16/D$.

$$R_W^{\mathrm{loc}}\equiv\frac{\chi_{\mathrm{loc}}/\chi^0_{\mathrm{loc}}}{\gamma/\gamma_0}\quad(\simeq 2.8\pm 0.2\quad\text{for}\quad U\simeq U_{c2}). \tag{263}$$

2. Charge response and compressibility

The charge-charge response (compressibility) can be analyzed along similar lines. A chemical potential shift away from half-filling $\delta\mu=\mu-U/2$ is applied. This does not cause a change (to order δn) in the distribution of integrated spectral weight between the upper and lower Hubbard bands, as can be readily checked close to the atomic limit. The resonance width does not change to order $\delta\mu$ because of particle hole symmetry. Denoting by $\delta\epsilon$ the shift of the resonance location, we can parametrize approximately the low-energy part of the spectral function as a Lorentzian peak of unmodified width ϵ_F^* and height $D(0)$ centered around $\delta\epsilon$, so that the low-energy part of the Green's function is approximated by

$$G(i\omega_n)\simeq\frac{2}{D}\frac{\epsilon_F^*}{i\omega_n+\delta\epsilon+i\epsilon_F^*\,\mathrm{sgn}(\omega_n)}\quad(\omega_n<\epsilon_F^*). \tag{264}$$

The change of the particle number, δn, is obtained from the change in the integrated spectral function as $\delta n\simeq\delta\epsilon/(\pi D)$. In order to obtain the corresponding shift in the chemical potential $\delta\mu$, we make use of the Luttinger theorem to obtain $\delta n=\delta\epsilon/\epsilon_F^*-D\,\delta\mu/U^2$. The last term in this equation comes from the response of the Hubbard bands to a chemical potential, which is identical to that of an insulator. Combining these two equations, we see that the compressibility $\delta n/\delta\mu$ is proportional to ϵ_F^* and thus vanishes as U_c-U as the Mott transition is approached by varying U at half-filling. The numerical results using ED yield

$$\kappa=\frac{\delta n}{\delta\mu}\simeq 0.93\,\frac{\epsilon_F^*}{D^2}. \tag{265}$$

This is in qualitative agreement with the Brinkman-Rice approximation, which yields

$$\kappa^{\mathrm{BR}}=\frac{4}{U_c}\frac{1-U/U_c}{1+U/U_c}. \tag{266}$$

Close to the critical point, this reads $\kappa^{\mathrm{BR}}/\kappa_0\simeq 0.47(1-U/U_c)$, in mediocre quantitative agreement with the result (265) $\kappa/\kappa_0\simeq 0.66(1-U/U_c)$, with $\kappa_0=4/(\pi D)$ the noninteracting compressibility. On the other hand, we have seen above that the double occupancy does not vanish as the transition is crossed. This is consistent with the *local* charge susceptibility being finite.

3. Response to a finite magnetic field and metamagnetism

The effect of a finite uniform magnetic field on the half-filled Hubbard model close to the Mott transition has been investigated by Laloux, Georges, and Krauth (1994). The results of these authors for the magnetization as a function of applied field, for various values of U, is displayed in Fig. 47. In the weakly correlated metal at small U, the magnetic field reduces the effect of the

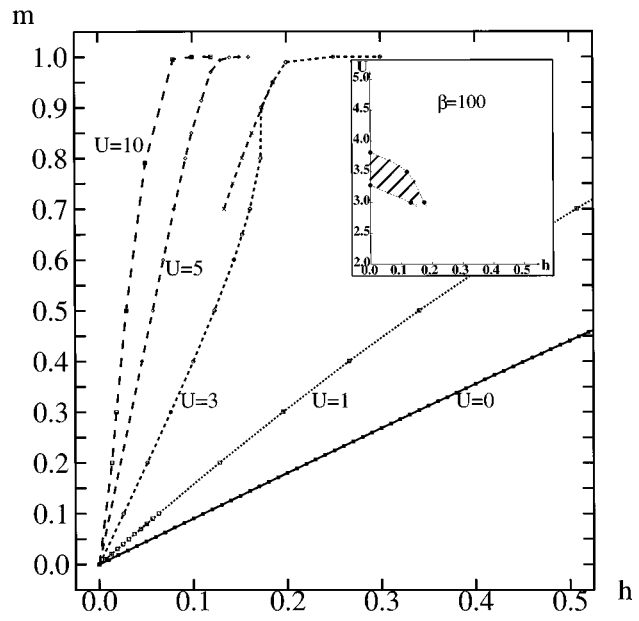

FIG. 47. Magnetization m_z as a function of an external magnetic field, for different values of the interaction U (in units of $D/\sqrt{2}$) domain of coexisting metallic and insulating solutions in the (U,h) plane, at $\beta D/\sqrt{2}=100$ (from Laloux, Georges, and Krauth, 1994).

interaction because of the Pauli principle, and a smooth crossover is found between the unpolarized metal and the fully polarized band insulator, with a mass enhancement m^*/m decreasing smoothly to unity. Close enough to the Mott transition, however, and at very low temperature, the magnetic field is found to induce a first-order metamagnetic transition between the strongly correlated metal at low field and the high-field Mott insulator, forcing a jump in the magnetization curve. This is in qualitative agreement with the predictions of the Gutzwiller approximation (Vollhardt, 1984), except for the important difference that the magnetization jump is always significantly smaller than unity, and *vanishes* at U_c (in contrast to being maximal there as in the Gutzwiller approximation). This is because the exchange is not neglected in the LISA method, and the $T=0$ uniform susceptibility is continuous at U_c. Also, the critical field for the transition is significantly larger than in the Gutzwiller approximation.

Metamagnetism in the antiferromagnetic phase has been recently studied by Held, Ulmke, and Vollhardt (1995).

H. The Hubbard model away from half-filling: Doping the Mott insulator

The properties of the Hubbard model away from half-filling are of great interest. In one dimension the Hubbard model at half-filling is a solvable model of a Mott insulator and away from half-filling the low-energy properties are those of a Luttinger liquid. In finite dimensions, this problem is currently the subject of a lively debate. It is therefore quite instructive to review what has been learned from the opposite limit: that of infinite dimensions.

1. Qualitative arguments

From the mapping onto an Anderson impurity model subject to a self-consistency condition it is possible to make some exact statements. Georges and Kotliar (1992) showed that when the system is metallic and there is no broken symmetry, it is necessarily a Fermi liquid. The argument is based on the observation that the *paramagnetic* mean-field equations only allow $G(i\omega_n)\sim i\omega_n$ or $G(i\omega_n)\sim i\,\mathrm{sgn}(\omega_n)$ as consistent solutions in the low-frequency limit. The first possibility describes an insulator (since it corresponds to a density of states with a gap at the Fermi energy), and the second case describes a metal with $G(i0^+)\neq 0$. In the latter, the self-consistency condition relating the local Green's function to the bath of the Anderson impurity model implies that the density of states $\mathrm{Im}\mathcal{G}_0^{-1}(\omega+i0^+)$ of the bath of conduction electrons [i.e., the hybridization function $\Delta(\omega)$ of the impurity model] is regular and finite at $\omega=0$. Then the low-energy theory of the Anderson impurity model (Haldane, 1978a; Krishnamurthy, Wilkins, and Wilson, 1980) can be used to show that Fermi-liquid properties (Langreth, 1966) hold at low temperature and low frequency. In particular, $\mathrm{Im}\Sigma(\omega)\sim\omega^2$ as $\omega\to 0$. This is true irrespectively of the value of the interaction U or chemical potential (as long as these values are such that the assumption of a metallic state is realized).

Fermi liquid sum rules for the *single-impurity model* (Langreth, 1966) imply that the Luttinger theorem is satisfied by the $d=\infty$ Hubbard model, with a Fermi surface unchanged by the interactions. Let us briefly repeat the proof here (Müller-Hartmann, 1989b). Denoting by $G(\mathbf{k},z)$ the lattice Green's function (for a complex frequency z), we have the obvious identity

$$G(\mathbf{k},z)=\frac{\partial}{\partial z}\ln[z+\mu-\epsilon_{\mathbf{k}}-\Sigma(z)]+G(\mathbf{k},z)\,\frac{\partial\Sigma}{\partial z}. \tag{267}$$

Summing this equation over $\mathbf{k}$, and using the impurity-model sum-rule for the *local* Green's function (Luttinger and Ward, 1960; Langreth, 1966),

$$\int_{-i\infty}^{+i\infty}\frac{dz}{2\pi i}\,G(z)\,\frac{\partial\Sigma}{\partial z}=0, \tag{268}$$

one obtains the total density n in the form

$$\frac{n}{2}\equiv\int_{-i\infty}^{+i\infty}\frac{dz}{2\pi i}\,G(z)=\int_{-\infty}^{+\infty}d\epsilon D(\epsilon)\,\theta(\mu-\Sigma(i0^+)-\epsilon). \tag{269}$$

From this we conclude that

$$\mu-\Sigma(i0^+)=\mu_0(n) \tag{270}$$

with $\mu_0(n)$ the noninteracting chemical potential corresponding to a density n. Hence the location of the poles of $G(\mathbf{k},\omega)$ are unchanged by the interaction. Because the

self-energy is momentum independent, not only the volume but also the shape of the Fermi surface is unchanged.

For small doping, the Fermi liquid regime applies below a certain coherence temperature $T_{\rm coh}$ reminiscent of the Kondo temperature of the single impurity Anderson model, below which a narrow quasiparticle resonance appears at Fermi energy in the single-particle spectrum. The width $Z\epsilon_F$ of this peak is proportional to doping. QMC studies (Prushke, Jarrell, and Freericks, 1995) and ED studies (Kajueter and Kotliar, 1995) suggest that $T_{\rm coh}$ is smaller than $Z\epsilon_F$. A more detailed investigation of this issue is certainly needed. At temperatures much larger than $T_{\rm coh}$ we have free spins at each site and therefore the local spin response has Curie-like behavior, while at very low temperatures the moment is quenched by the effective conduction electrons and the spin susceptibility is finite. This picture of the low-energy physics is similar to the one resulting from the slave boson approach to the Hubbard or the t-J model when the exchange interactions are not introduced explicitly via bond variables (Kotliar and Liu, 1988; Grilli and Kotliar, 1990).

2. Single-particle properties

An important question in the light of the revival of the photoemission spectroscopy technique is the position of the quasiparticle resonance relative to the rather broad Hubbard bands. One possibility is that, upon doping the paramagnetic Mott insulator, the resonance appears at the top of the lower Hubbard band (for hole doping $n=1-\delta<1$). In this picture the jump in the chemical potential $\mu(\delta=0^+)-\mu(\delta=0^-)$ *equals* the Mott-Hubbard gap Δ_g, in agreement with the slave boson calculations using the Kotliar-Ruckenstein (1986) technique (Bang *et al.*, 1992; Castellani *et al.*, 1992; Frezard and Wölfle, 1992). Another possibility is that this jump is *strictly less* than the gap, $\mu(\delta=0^+)-\mu(\delta=0^-)<\Delta_g$, and that doping induces "midgap" states inside the Mott-Hubbard gap. Note that this is not in contradiction with the exact statement that $\mu(N+1)-\mu(N-1)=\Delta_g$, where N is the number of electrons (equal to the number of lattice sites at half-filling): this statement does not apply to a *finite concentration* of added holes or electrons.

The first quantitative calculations for this problem were performed by means of the QMC method supplemented by the maximum entropy algorithm and the noncrossing approximation (Jarrell and Pruschke, 1993a, 1993b; Pruschke, Cox, and Jarrell, 1993a, 1993b). We reproduce in Fig. 48(a) the spectral function of the lightly doped Mott insulator obtained in these works. It is hard to decide which of the two possibilities above is correct, on the basis of these results. Indeed, finite-temperature effects are quite significant, and these results have been obtained for an unbounded Gaussian bare density of states. The results are not in contradiction however with a resonance appearing at the top of the lower Hubbard band.

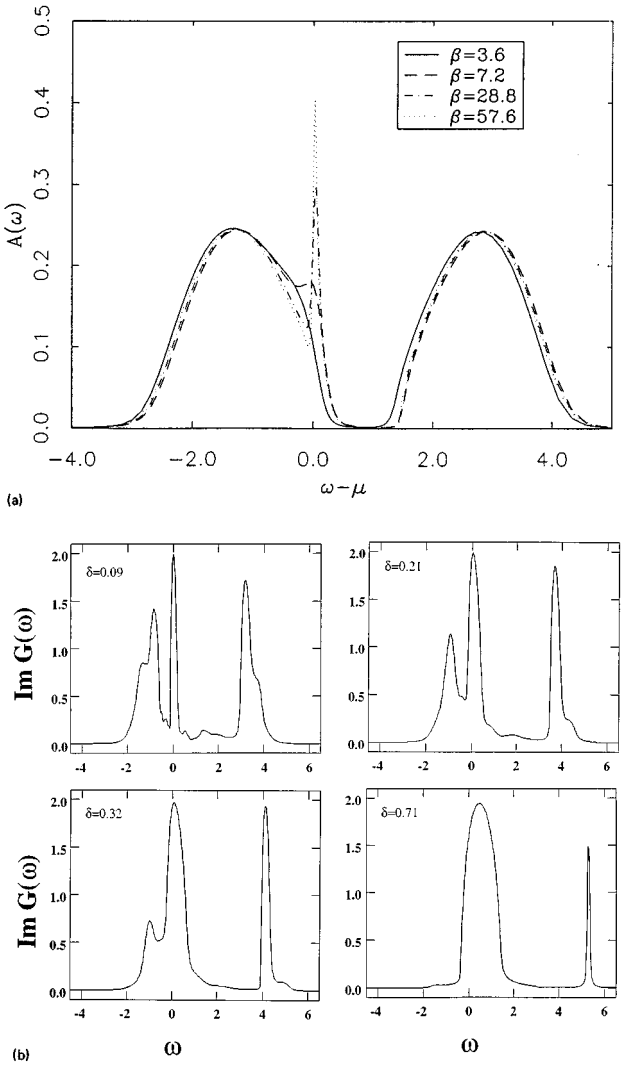

FIG. 48. (a) Temperature dependence of the local spectral density for U=4 and n=97 obtained from analytically continued QMC data on a hypercubic lattice with $t_{ij}=1/2\sqrt{d}$ (from Pruschke, Cox, and Jarrell, 1993b). (b) T=0 local spectral density for the Hubbard model on the Bethe lattice at U/D=4 for increasing (hole-) doping δ=0.09, 0.21, 0.32, 0.71 obtained from the generalized iterated perturbative theory approximation (Kajueter and Kotliar, 1995).

Using the projective self-consistent technique, however, it was shown (Fisher, Kotliar, and Moeller, 1995) that, for any value of U larger than U_c, doping does induce states *inside* the Mott-Hubbard gap. Therefore the jump in chemical potential for infinitesimal doping is strictly less than the single-particle gap of the insulator, and the second possibility described above holds. This applies to the fully frustrated situation, with no magnetic order, and a bounded semicircular bare density of states. Moreover, the shift of the quasiparticle band relative to the Hubbard band edge is a fraction of the bare kinetic energy, and remains finite even in the limit where U is infinite. These results were obtained by solving numerically Eq. (213) which does not contain a small energy scale. We reproduce the results of this analysis in Fig. 49,

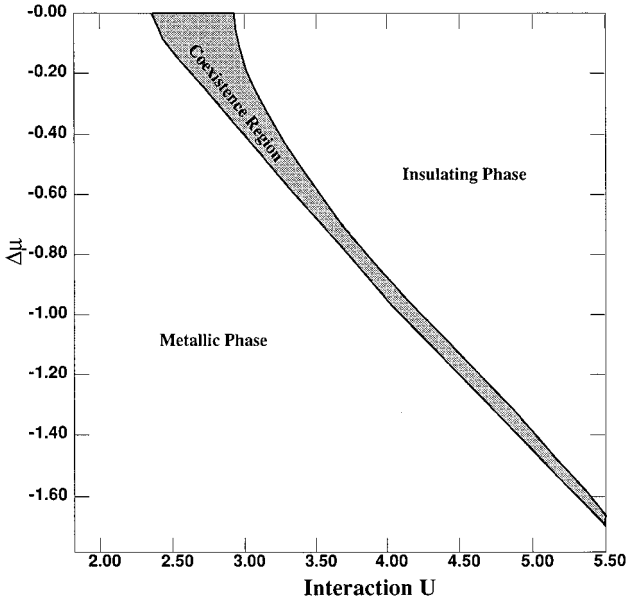

FIG. 49. Phase diagram of the fully frustrated Hubbard model as a function of U/D and $\Delta\mu \equiv \mu - U/2$. The shaded region is the region of coexistence between a metallic and an insulating solution of the LISA equations. The boundary of this coexistence region with the metallic phase directly yields the position of the top of the lower Hubbard band as a function of U. The curve corresponding to the boundary with the insulating region gives the position of the quasiparticle resonance as a function of U, for infinitesimal doping.

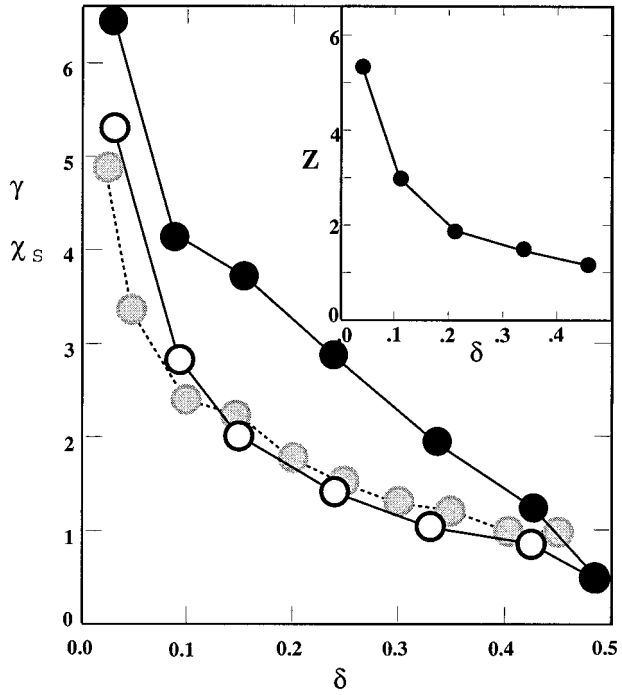

FIG. 50. Slope of the specific heat $C_v \sim \gamma T$ (white dots) and spin susceptibility (black dots) as a function of doping for $U/D=3$ and $\beta D=32$. The experimental results for the specific heat of $La_{1-x}Sr_xTiO_3$ (Tokura *et al.*, 1993) are plotted for comparison (grey dots). The plots are in units of γ_0 (for γ) and χ_0 (for χ). The inset shows the renormalized mass $m^*/m = Z^{-1}$ as a function of doping.

which gives the position of the top of the lower Hubbard band and of the quasiparticle resonance for infinitesimal doping, as a function of U.

These conclusions are also supported by a recent extension of the iterated perturbative theory approximation away from half-filling (Kajueter and Kotliar, 1995). Spectral functions obtained in this approximation are also reproduced in Fig. 48(b) for various dopings. For the smaller ones, the quasiparticle resonance is clearly seen to appear inside the Mott gap.

The fact that the resonance appears near the middle of the Mott gap when $U \approx U_c$ can be understood from a continuity argument. The essential point is that as long as the system is *away from half-filling*, the self-energy is a continuous function of frequency, chemical potential, and U. Since at $U = U_c$ when the doping goes to zero μ approaches $U/2$ for U slightly bigger than U_c, μ has to approach values slightly above (below) $U/2$ for electron (hole) doping to obey the Luttinger condition in Eq. (269) as n approaches 1 from above or below. The insulating gap, in contrast, is already preformed and finite at U_c. We note that the prediction that new states appear inside the insulating gap upon doping is also consistent with recent approximate continuous-fraction resummations of the single-particle Green's function (Kee and Hong, 1995). It should finally be mentioned that midgap states have also been predicted to occur on the basis of phase separation (Emery and Kivelson, 1995), but the physical mechanism responsible for these states in our case seems rather different.

3. Thermodynamics

The Mott transition as a function of doping is driven by the collapse of the small energy scale $T_{\rm coh}$, which vanishes as one approaches half-filling. Thermodynamic properties as a function of doping have been investigated by Jarrell and Pruschke (1993a, 1993b) and Pruschke, Cox, and Jarrell (1993a, 1993b) for a Gaussian density of states, and by Rozenberg, Kotliar, and Zhang (1994), who concentrated on a semicircular density of states with $U/D = 3 \simeq U_c/D$ in order to make a connection with the experiments of Tokura *et al.* (1993) on Sr-doped $LaTiO_3$, a compound which lies on the brink of the Mott transition.

A simple estimate of the doping dependence of the effective mass m^*/m (with m the band effective mass) can be obtained from the quasiparticle residue Z ($=m/m^*$ within LISA), which is plotted as a function of doping in the inset of Fig. 50. The results of Rozenberg *et al.* for this quantity (which also yields the slope of the specific heat γ) and for the uniform susceptibility as a function of doping is depicted in Fig. 50. In the same figure, the experimental results of Tokura *et al.* have been reproduced for comparison.

Figure 51 shows the particle occupation $\delta = 1 - n$ as a function of the chemical potential $\Delta\mu$ obtained from QMC at $\beta = 16$. We note that the slope of the curve, i.e., the compressibility, goes to zero at $\Delta\mu = 0$ as U_c is approached from below. For larger values of U, we have a

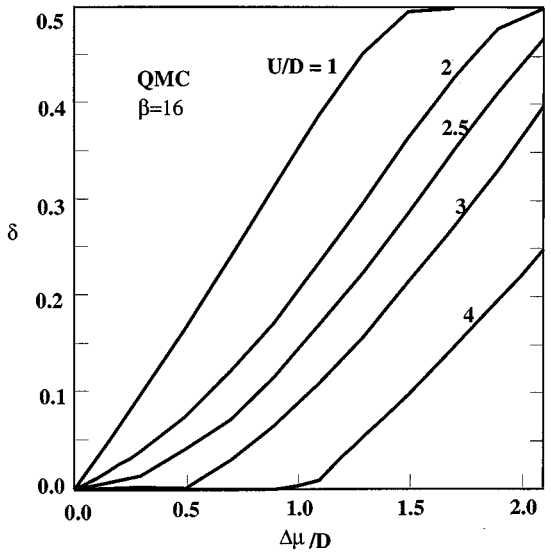

FIG. 51. Particle number $\delta=\langle n\rangle-\frac{1}{2}$ as a function of the chemical potential $\Delta\mu=\mu-U/2$. Data obtained from QMC at $\beta D=16$, for different values of the interaction U.

vanishing compressibility characteristic of an insulating state. It displays a gap approximately equal to $U-2D$ which compares very well with the results for the size of the gap from the exact diagonalization method (Fig. 32). Notice that for $U>U_c$ the δ vs $\Delta\mu$ curves approach half-filling ($\delta=0$) with a finite slope. This is in contrast with the QMC simulations in the two-dimensional case reported by Furukawa and Imada (1993) and Imada (1994).

A very striking feature of the regime $T\geqslant T_{\rm coh}$ is the strong temperature dependence of physical quantities. In this respect it is important to emphasize that while all the calculations are performed at a fixed chemical potential, one obtains results at a given density by carefully adjusting the chemical potential that is needed to keep the density constant and performing the calculations at a temperature-dependent chemical potential.

The discussion presented in Sec. VII.G on the difference between the local and the $\mathbf{q}=0$ susceptibility is very general and applies also away from half-filling. The arguments presented in that section imply that $\chi_{\rm loc}^{-1}\simeq T+T_{\rm coh}$, where $T_{\rm coh}$ vanishes as the doping goes to zero, while the $\mathbf{q}=0$ susceptibility behaves as $\chi^{-1}\simeq(T+T_{\rm coh}+J)$ where C is a coefficient of order unity and J remains finite as the doping goes to zero. The plots of these quantities from QMC calculations are consistent with this picture and are displayed in Fig. 52 (Jarrell and Pruschke, 1993b).

4. Transport properties and response functions

Using the QMC method and the maximum entropy technique for analytic continuation, Pruschke, Cox, and Jarrell (1993a, 1993b) and Jarrell and Pruschke (1993a, 1993b) have computed various transport quantities and response functions as a function of temperature. Their

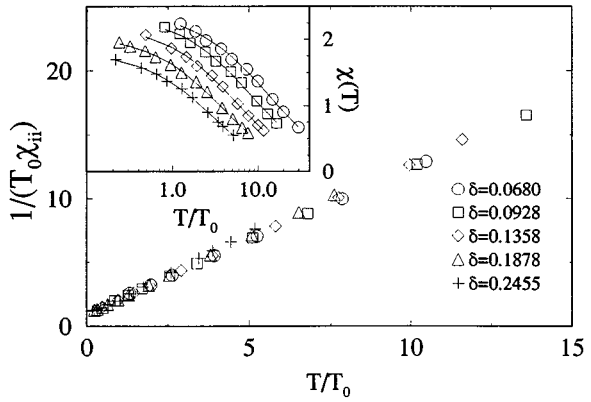

FIG. 52. QMC results for the local susceptibility (main plot) and the uniform susceptibility (inset) for the Hubbard model away from half-filling on a hypercubic lattice with $U=4$ and $t_{ij}=1/(2\sqrt{d})$ (from Jarrell and Pruschke, 1993b). The plot demonstrates the scaling of $\chi_{\rm loc}$ (but not of χ) vs $T/T_{\rm coh}$.

results for the NMR relaxation rate and for the resistivity are displayed in Figs. 53 and 54. Above the coherence temperature $T_{\rm coh}$ they found that there are regions where the resistivity is linear and the NMR relaxation rate is constant. Similar observations were made by Qin and Czycholl (1994) using self-consistent perturbation theory. However, given the values of $T_{\rm coh}$ for the range of doping of interest, the temperatures where this behavior is observed are too high to be relevant for the physics of the normal state of high-T_c compounds.

The optical conductivity in the doped case has also been addressed by these authors and by Jarrell, Freericks, and Pruschke (1995). It is possible to give a simple intuitive picture of the various contributions to the opti-

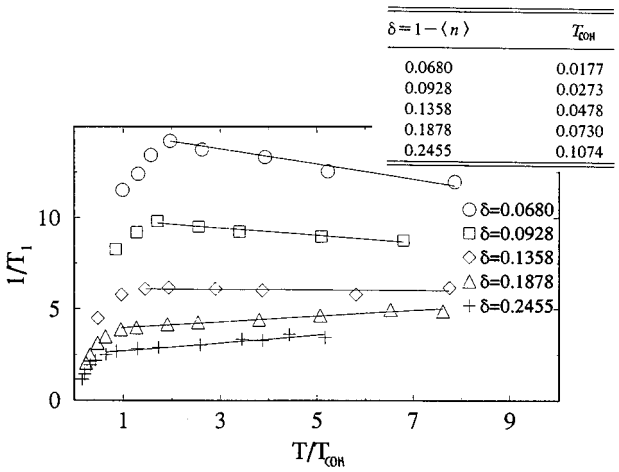

FIG. 53. The NMR relaxation rate $1/T_1$ vs temperature from QMC calculations for the Hubbard model away from half-filling, for the same parameters as in Fig. 52 (after Jarrell and Pruschke, 1993b). The inset gives the determination of $T_{\rm coh}$ as a function of doping found by these authors. A behavior $1/T_1\sim$const is reported in a range of temperature for $T>T_{\rm coh}$, while the low-temperature behavior is expected to obey the Korringa law $1/T_1T\sim$const.

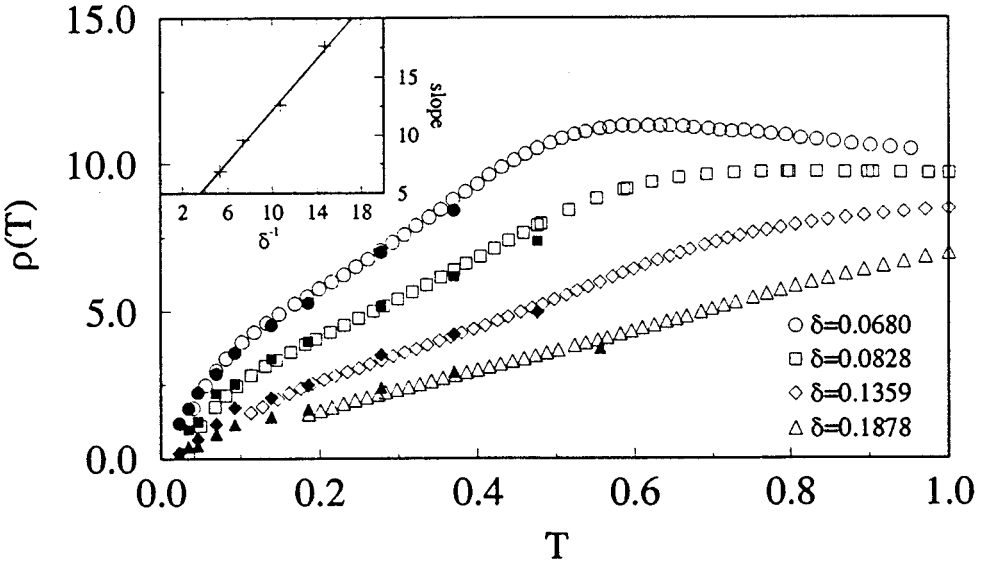

FIG. 54. The dc conductivity ρ_{dc} from QMC calculations away from half-filling, for the same parameters as in Fig. 52 (after Jarrell and Pruschke, 1993b). The low-temperature part has a T^2 dependence, while a linear behavior is reported in a range of temperature for $T > T_{coh}$.

cal response, by noticing that it results, in the LISA method, from the convolution of two single-particle spectral functions. As already shown in Figs. 48(a) and 48(b), the spectral function in the lightly (hole-) doped regime is characterized by a sharp quasiparticle peak at the Fermi level which is close to the top of the lower Hubbard band (a word of caution is in order for very small doping and intermediate U, where midgap states do appear). The lower Hubbard band extends down to $\approx -2D$. A second feature, the upper Hubbard band, is present in the positive side of the spectrum at a frequency $\omega \approx U$. The optical response that results from the convolution of such spectral functions will accordingly present three different contributions:

(i) The first contribution is a narrow low-frequency peak that is due to transitions within the quasiparticle resonance. In the $T=0$ limit this peaks becomes a δ function and is the Drude part of the optical response.

(ii) A second contribution results from transitions from the lower Hubbard band to the unoccupied part of the quasiparticle peak. It gives rise to the so-called "mid infrared band" in $\sigma(\omega)$, which extends from the origin up to frequencies of order D.

(iii) The third contribution appears at much higher frequencies of order U, which corresponds mainly to excitations between the Hubbard bands.

In agreement with the qualitative picture that we just described, we display in Fig. 55 the optical response for small doping ($n=0.97$) obtained by Jarrell, Freericks, and Pruschke (1995) with the QMC method. It is interesting to track how the spectral weights associated with the three different contributions in the optical spectra evolve as one moves away from the half-filled case. The weights resulting from the QMC simulations of Jarrell, Freericks, and Pruschke (1995) are presented in Fig. 56, where the increase in the weight of the Drude peak and the concommitant decrease of the weight associated with incoherent contributions is apparent, as the system evolves to a less correlated state when the doping increases.

5. Phase diagram

The determination of the phase diagram of the Hubbard model away from half-filling is a very difficult prob-

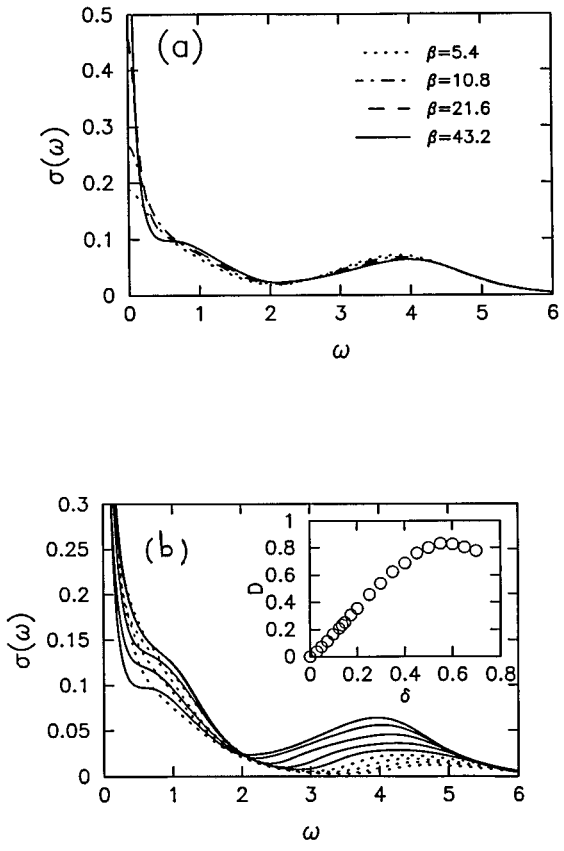

FIG. 55. Temperature (a) and doping (b) dependence of the optical conductivity $\sigma(\omega)$ from QMC calculations with $U=4$ on the hypercubic lattice with $t_{ij}=1/(2\sqrt{d})$ (from Jarrell, Freericks, and Pruschke, 1995). The curves in (b) correspond to $\delta=0.068$, 0.0928, 0.1358, 0.1878, 0.2455, 0.3, 0.4, and 0.45 (top to bottom curve at high ω). The inset shows the evolution of the Drude weight as a function of doping.

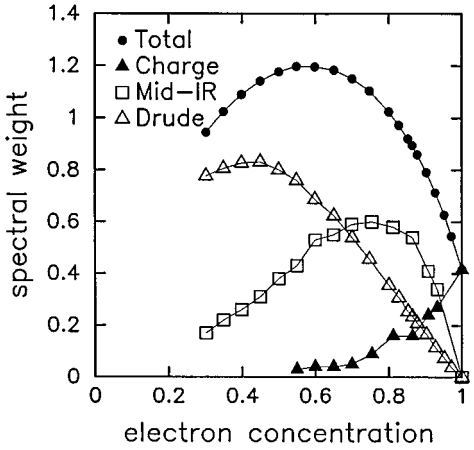

FIG. 56. Total spectral weight (solid dots) as a function of electron density for the same parameters as in Fig. 55 (from Jarrell, Freericks, and Pruschke, 1995). These authors considered a decomposition of the total weight into a Drude part (open triangles), a mid-infrared part (open squares) and a charge-transfer part (solid triangles).

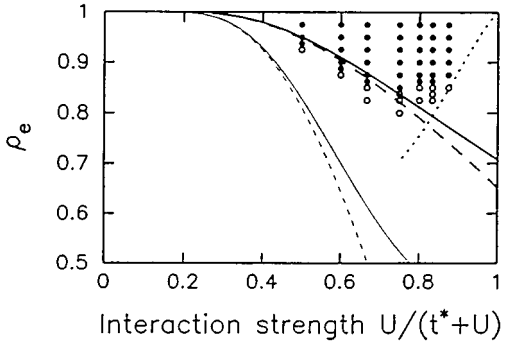

FIG. 57. Phase diagram of the Hubbard model on the $d=\infty$ hypercubic lattice ($t_{ij}=1/2\sqrt{d}$) as a function of electron concentration ρ_e and U (from Freericks and Jarrell, 1995a). The open dots indicate an incommensurate antiferromagnetic ordered state and the solid dots a commensurate state. The lines correspond to various approximations discussed by these authors.

lem because one has to consider the possibility of commensurate and incommensurate magnetic and charge order, and because a certain range of densities may not be allowed in the model. This last possibility, corresponding to phase-separation, was pointed out by Visscher (1974), and investigated intensively by Emery and Kivelson (1993a, 1993b).

In infinite dimensions, the details of the phase diagram in the $U-n$ plane at low temperature depend crucially on the particular lattice chosen, via the degree of magnetic frustration, and this issue is only beginning to be explored.

In the fully frustrated situation, there is no magnetic long-range order and the phase diagram at zero temperature displays a paramagnetic insulating phase and a Fermi-liquid metallic phase, with a region of coexistence of the two phases. The resulting phase diagram is displayed in Fig. 49, as obtained by Kajueter, Kotliar, and Moeller (1995) by the exact diagonalization method. It is in good agreement with the results of the more precise projective method (Fisher, Kotliar, and Moeller, 1995).

Freericks and Jarrell (1995a) investigated the magnetic phase diagram of the $d=\infty$ Hubbard model on the *hypercubic lattice* as a function of doping, temperature, and interaction strength. They used the QMC method, and compared the results with various approximation schemes. Their main finding is that, when doped away from half-filling, the magnetic long-range order of the insulating antiferromagnetic phase remains commensurate up to a limiting value of the doping (that depends on U), after which the order becomes incommensurate. The parameter $X(q)$ characterizing the ordering wave vector (Sec. VII.G) varies continuously with doping. At a higher, critical doping, the long-range order disappears and a paramagnetic metal is found. Figures 57 and 58 display the phase diagram found by these authors, and the inset shows their QMC determination of the ordering temperature as a function of doping. Notice, however, that a comparison of the free energies of the magnetically ordered phases and the paramagnetic phase has not been carried out. In the range of parameters studied, these authors argued for the absence of ferromagnetic order or phase separation. In contrast, at *weak coupling*, van Dongen (1995) found that the doped Hubbard model does possess phase separation between homogeneous low-density regions and antiferromagnetic high-density regions, but that incommensurate order is suppressed.

Furthermore, for large U, a $T=0$ analysis using the projective self-consistent method (Kajueter, Kotliar, and Moeller, 1995) suggests that phase separation occurs between a commensurate magnetic insulator and a Fermi

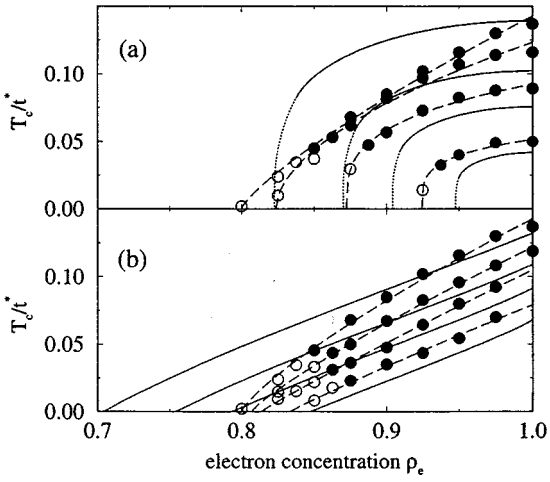

FIG. 58. Critical temperatures corresponding to Fig. 57 as a function of electron concentration (from Freericks and Jarrell, 1995a). (a) Weak coupling regime (U=1,1.5,2,3). (b) Strong-coupling regime (U=3,4,5,7). Solid dots indicate the transition to a commensurate antiferromagnetic ordered state, and open dots denote the incommensurate state.

Liquid phase. Ferromagnetism and incommensurate order was ignored in this analysis however. We also note that a ferromagnetic phase has recently been found by Ulmke (1995) in a $d=\infty$ generalization of the face-centered cubic lattice.

I. Comparison with experiments

The LISA method has already been applied successfully to the description of various three-dimensional strongly correlated materials displaying a Mott transition. The qualitative agreement is very good, and in some cases the quantitative agreement is surprising. We will discuss below a few instances in which the dynamical mean field results can be directly compared to experiments. It should be kept in mind that, at the present stage, this comparison has been made within the one-band Hubbard model and that LISA calculations treating each material in a more realistic manner (including, e.g., orbital degeneracy and disorder) could and should be performed (see Sec. VIII.C).

1. Phase diagrams

The phase diagram of V_2O_3 (Fig. 23) is qualitatively very similar to the phase diagram presented above in Fig. 43. In the inset of Fig. 43, results for the dc conductivity are also displayed. As we discussed before in Sec. VII.D.3, the introduction of frustration in the model plays the key role of lowering the Néel temperature T_N below the critical point T_{MIT} where the first-order transition line ends. Thus, the phase diagram of the single-band Hubbard model, with an intermediate degree of frustration, presents the same topology as the one determined experimentally for V_2O_3. This system has been the subject of extensive studies in the 1970s, and has been revisited again most recently by Carter *et al.* (1992, 1993). Note that the magnetic ordering of V_2O_3 (Castellani, Natoli, and Ranninger, 1978) has indeed a high degree of frustration. The origin of the first-order paramagnetic metal-insulator transition is in the existence of a region where two solutions are allowed (cf. Sec. VII.D.1). This coexistence regime between a metal and a paramagnetic insulator has been observed experimentally (McWhan *et al.*, 1973). The slope of the transition line is such that the insulator can be reached upon heating the metal. Note that the temperature scale for the critical end point of the line T_{MIT} is correctly predicted by the theory to be much smaller than the electronic bandwidth: $T_c \simeq 0.05D$. Setting $D \simeq 0.4$ eV, which is consistent with optical conductivity results and is also close to LDA band structure calculations (Mattheiss, 1994), yields T_c of the order of 250 K, within less than a factor of 2 from the experimental result.

The study of the dc conductivity (displayed in the insets) allows us to characterize two crossover regions that start at T_{MIT}. The dotted line indicates a crossover separating a good metal at low T and a semiconductor at higher T. Between these states ρ_{dc} has an anomalous, rapid increase with T. This crossover retains much of the flavor of the first-order line, as it can be traced to the rapid disappearance of the coherent central quasiparticle peak in the density of states. A similar behavior of ρ_{dc} was experimentally found by McWhan *et al.* (1973). The other crossover, indicated by the shaded area, denotes the evolution from the semiconductor to the insulator regime. The rapid change of the dc conductivity across this regime can be observed in the inset (semilog scale). In this case, the density of states merely consists in the lower and upper Hubbard bands split by a small gap Δ. The crossover then corresponds to the crossing of the two energy scales T and Δ. These crossovers were observed in V_2O_3 by Kuwamoto, Honig, and Appel (1980).

At very low temperature, the insulating phase is found to be unstable to antiferromagnetic order. Interestingly, the partially frustrated model also displays a small region of metallic antiferromagnetism similar to the recent experimental observation of Carter *et al.* (1992) in the Vanadium deficient compound $V_{2-y}O_3$.

Hence the single-band Hubbard model by itself, and its solution within the LISA, can account for all four phases and the various phase transitions observed in this system. In particular, contrary to a rather widespread belief, *lattice deformation is not necessarily the driving force behind the first-order metal-insulator transition at finite temperature*. Of course, a more realistic model of V_2O_3 should take into account lattice deformations. Extensions of the LISA in this direction have recently been considered by Majumdar and Krishnamurthy (1994).

Although we argue that the simple model considered here indeed captures many puzzling behaviors observed in the experimental systems, we expect that the detailed nature of the antiferromagnetic metallic phase (such as incommensurate orderings, etc.) will be very sensitive to the particular band structure of the system. We note that V_2O_3 has three t_{2g} orbitals per vanadium filled with two electrons. Two electrons (one per V) participate in a strong cation-cation bond, leaving the remaining two in a twofold degenerate e_g band (Castellani, Natoli, and Ranninger, 1978). The application of the LISA approach to a model that takes into account some features of the *realistic band structure* of V_2O_3 seems a very promising direction, and is now within the reach of available techniques.

Some of the features of the V_2O_3 phase diagram appear in other strongly correlated systems that undergo a metal insulator transition as a function of applied pressure or chemical substitution. A notable example is the $Y_{1-x}Ca_xTiO_3$ compound that was very recently found to exhibit a metal-to-paramagnetic insulator transition in the range $0.35<x<0.4$ (Iga *et al.*, 1995). As for V_2O_3, this line is first order with evidence of phase coexistence. Also, the study of the dc conductivity shows the behavior associated with the crossovers that we discussed above. It is interesting to point out that, in contrast to V_2O_3, the metal insulator transition in this compound is *not* accompanied by a discontinuity of the lattice parameters. This represents a strong empirical evidence of a transition driven by *purely electronic correlation effects*.

The phase diagram of ^{3}He is also qualitatively similar if we identify the solid phase with the paramagnetic insulator phase and the liquid phase with the metal. Therefore the pressure-induced first-order metal-to-insulator transition upon *heating* or upon decreasing pressure is a very general feature of correlated fermion systems, which can be accounted for by a simple electronic model and need not be driven by the fermion-lattice interaction.

2. Photoemission spectra

Regarding spectroscopic properties, there are two important predictions of the LISA that differ qualitatively from earlier work on the metal insulator transition. It was shown by Georges and Kotliar (1992) that Hubbard bands are already well formed within the correlated metallic state. It would be very interesting to investigate numerically whether this also applies in three dimensions. Secondly, *at zero temperature* in fully frustrated systems, the metal-insulator transition takes place when the Mott Hubbard gap is well formed (Zhang, Rozenberg, and Kotliar, 1993). This prediction is very different from the results obtained in other approximation schemes such as slave boson calculations.

With this theoretical background in mind, we now turn to the comparison of one-particle spectral functions to photoemission experiments on transition metal oxides (for a general reference on experimental results, see Hüfner, 1994). In a recent paper Fujimori *et al.* (1992) examined the spectral function of several transition metal compounds with a (slightly distorted) cubic perovskite structure containing all one d-electron per transition metal ions. In these systems the value of $U_{\rm eff}/D$ changes because the lattice distortion changes the overlap between neighboring d orbitals. The compounds studied were ReO_3, VO_2, $SrVO_3$, $LaTiO_3$, and $YTiO_3$, corresponding to increasing values of $U_{\rm eff}/D$, with the last compound being insulating and the other ones metallic. The photoemission spectra are reproduced in Fig. 59. The progressive separation of a quasiparticle feature close to the Fermi level, and a (lower) Hubbard band at high energy is clearly visible. The weight in the low-energy part of the spectrum vanishes by the time the lower Hubbard band is well formed. All this is in good qualitative agreement with the above results and the plots of the spectral function in Fig. 30. It is clear from the spectra that $LaTiO_3$ is very close to the Mott transition point U_{c2}. It is difficult however to investigate precisely the mechanism of spectral weight transfer as U is increased, since the data correspond to different materials.

Very recently, Inoue *et al.* (1995) studied the $Ca_{1-x}Sr_xVO_3$ system (in which a Sr^{2+} ion is replaced by Ca^{2+} of the same valence), for concentrations ranging from a strongly correlated metal for x=1 to weaker correlations for x=0. In this case the substitution parameter x controls the strength of the interaction U/D by modifying the V—O—V bond angle from ~160° to 180°. Their results are displayed in Fig. 60, where the background has been subtracted and the intensity normalized. The gradual transfer of spectral weight from the quasiparticle feature to the lower Hubbard band as U is increased is clearly seen. Moreover, due to the excellent quality of the data, we can attempt a qualitative fit within the LISA method. Using the iterated perturbation theory approximation with a semicircular free density of states, we obtain the local spectral density at negative frequencies, for values of U close to U_{c2}. In order to compare our results to the experiment we convolute the theoretical spectra with a Gaussian of width

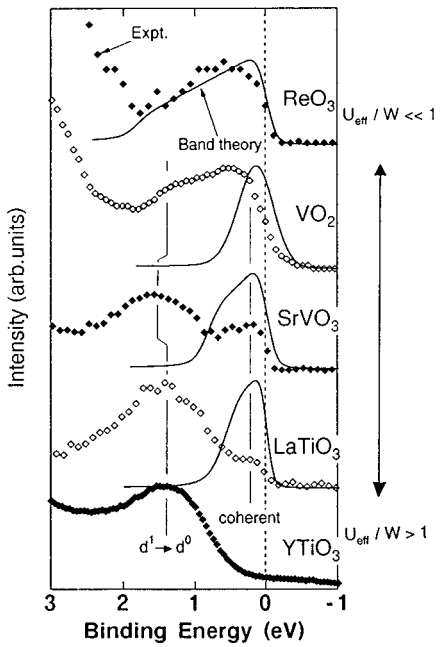

FIG. 59. Photoemission spectra for various oxides. The solid line are the spectra predicted by band-structure calculations (from Fujimori *et al.*, 1992, and references therein).

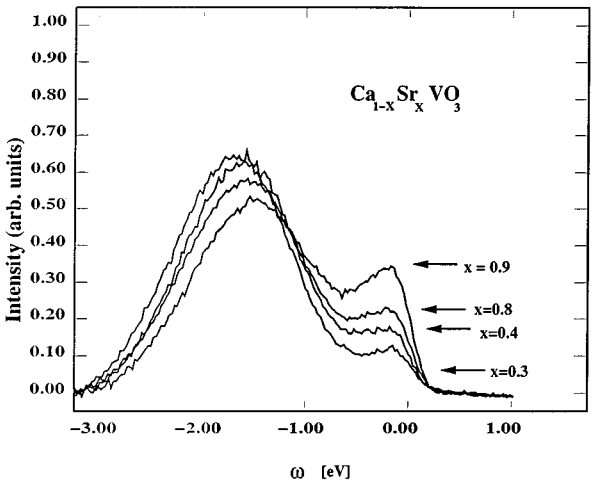

FIG. 60. Photoemission spectra of $Ca_{1-x}Sr_xVO_3$ for x=0.9, 0.8, 0.4, 0.3 (from Inoue *et al.*, 1995). A background substraction and normalization of the spectra has been performed (courtesy of I. Inoue).

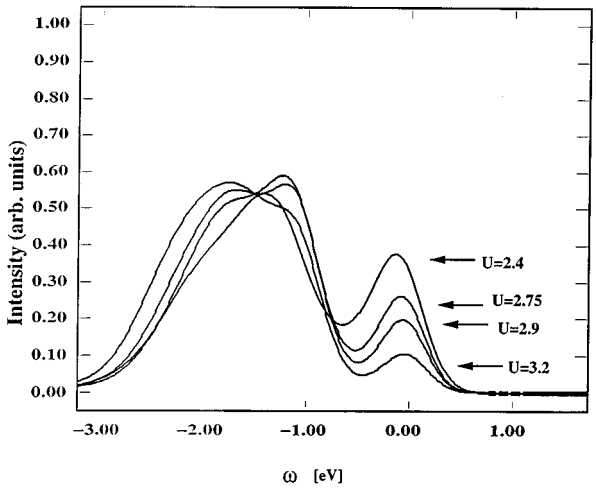

FIG. 61. Photoemission spectra calculated (with the iterative perturbation theory method) for the half-filled single band Hubbard model, with U/D=2.4, 2.75, 2.9, 3.2. The theoretical spectra has been convoluted with a Gaussian of width 0.3 eV that corresponds to the experimental resolution.

0.3 eV that corresponds to the experimental resolution. We plot the results in Fig. 61. The agreement is quite good. We point out that since the width of the incoherent part is $\approx 2D$, and the position of its maximum is $\approx U/2$, the fit is made with essentially *no adjustable parameters* since these quantities can be approximately extracted from the experimental data. One important point to note is that the property of the pinning of the density of states at the Fermi energy characteristic of a momentum-independent self-energy is no longer apparent in Fig. 61. This is just the mere consequence of the convolution with the experimental response. Although many aspects of the experimental results are correctly captured by our simplified model, a detailed description of the shape of the spectra in this system calls for extensions of the LISA framework to include more realistic band structure, density of states, and some degree of momentum-dependence of the self-energy. Indeed, it is apparent from the data that, upon increasing the strength of the interactions, the quasiparticle peak not only becomes narrower in this system, but also becomes flatter. This is evidence for a significant momentum dependence of the self-energy near the Fermi level (Inoue *et al.* 1995), which obviously requires an extension of the LISA formalism. Note, however, that there is no obvious contradiction between this observation and the good overall agreement of the LISA results with the *momentum-integrated* spectrum. For more details on the comparison between the LISA results with photoemission and optical conductivity experiments on $CaVO_3$, the reader is directed to the recent work of Rozenberg, Inoue, *et al.* (1996).

We finally mention another system, $NiS_{1.5}Se_{0.5}$, which undergoes a transition between an antiferromagnetic metal below T=60 K and a charge-transfer insulator at temperatures above 60 K. In this system, angle-resolved photoemission experiments of Matsuura *et al.* (1994) reveal a well-defined quasiparticle peak in the metal, with very little dispersion, in agreement with the description above. In the insulator, however, a sharp feature remains near the gap edge, which is obviously beyond the reach of the present one-band description but might still be explained within the LISA treatment of a multiband model.

We conclude that the LISA treatment of the single-band Hubbard model can account qualitatively for (i) the separation of the quasiparticle peak from the Hubbard bands in a strongly correlated metal, and (ii) the gradual transfer of spectral weight between these features as U is increased. This point, which is sometimes challenged (Chen, 1994), was clearly demonstrated in the first application of the iterated perturbation theory method by Georges and Kotliar (1992), and has been widely confirmed since. Notice, however, that, in many systems, the correlation gap seems to close as the metal-insulator transition is approached (Torrance, Lacorre, and Nazzal, 1992). Furthermore, optical measurements of Tokura *et al.* in a series of compounds with varying Mott Hubbard gap have been interpreted as a result of the collapse of the Mott-Hubbard gap at the metal insulator transition. A more careful investigation of the optical conductivity is necessary before drawing a final conclusion.

Another difficulty is that the *doping dependence* of the coherent and incoherent features observed in photoemission spectroscopy (Fujimori *et al.*, 1992; Sarma *et al.*, 1995) does not agree with the predictions of the single-band Hubbard model treated within LISA. Clearly more detailed studies with higher resolutions, and in particular more extensive use of *angular resolved spectroscopy* will be useful in elucidating these and other issues.

3. Optical conductivity

We now review the application of the LISA to the optical conductivity of the Hubbard model recently performed by Rozenberg *et al.* (1995; see also, Pruschke, Cox, and Jarrell, 1993a, 1993b and Hong and Kee, 1995b), in connection with the recent experiments on V_2O_3 of Thomas *et al.* (1994). We shall argue below that the single-band Hubbard model with an intermediate degree of magnetic frustration can qualitatively account for many features that are experimentally observed in this compound.

Let us recall the expression derived in Sec. IV for the frequency-dependent real part of σ in the limit of large dimensions:

$$\sigma(\omega)=\frac{1}{\omega}\frac{2e^2t^2a^2}{\hbar^2\nu}\int_{-\infty}^{\infty}d\epsilon\, D(\epsilon)\int_{-\infty}^{\infty}\frac{d\omega'}{2\pi}\rho(\epsilon,\omega') \times\rho(\epsilon,\omega'+\omega)[n_f(\omega')-n_f(\omega'+\omega)], \quad (271)$$

where $\rho(\epsilon_{\mathbf{k}},\omega)=-(1/\pi)\,\mathrm{Im}G(\mathbf{k},\omega)$ is the spectral function of the lattice conduction electrons, e is the electron charge, a the lattice constant, and $\nu=a^d$ is the volume of

the unit cell. At $T=0$, the optical conductivity can be parametrized by (Kohn, 1964)

$$\sigma(\omega)=\frac{\omega_P^{*2}}{4\pi}\,\delta(\omega)+\sigma_{\rm reg}(\omega), \tag{272}$$

where the coefficient in front of the δ function is the Drude weight and ω_P^* is the renormalized plasma frequency. In the presence of disorder $\delta(\omega)$ is replaced by a Lorentzian of width Γ. The kinetic energy is related to the conductivity by the sum rule

$$\int_0^\infty \sigma(\omega)d\omega=-\frac{\pi e^2a^2}{2d\hbar^2\nu}\langle K\rangle=\frac{\omega_P^2}{8\pi} \tag{273}$$

The Drude part can be directly obtained in terms of the quasiparticle weight Z in the limit of $d\to\infty$. Using (271), it can be shown that

$$\frac{\omega_P^{*2}}{4\pi}=\frac{4\pi t^2e^2a^2}{\hbar^2\nu}\,ZD(\epsilon_F). \tag{274}$$

In order to apply the Hubbard model to V_2O_3, we recall that this compound has three t_{2g} orbitals per V atom which are filled with two electrons. Two electrons (one per V) are engaged in a strong cation-cation bond, leaving the remaining two in a twofold degenerate e_g band. The Hubbard model ignores the degeneracy of the band which is crucial in understanding the magnetic structure (Castellani, Natoli, and Ranninger, 1978), but captures the interplay of the electron-electron interactions and the kinetic energy. With our simplified single-band model, we shall only focus on the low-frequency behavior of the optical response in the range $\omega<1$ eV. One should keep in mind that at high frequencies the experimental spectra show contributions from higher bands, but these are outside the scope of the present approach. Experimentally, one can vary the parameters U and D, by introducing O and V vacancies or by applying pressure or chemical substitution of the cation. Similarly to what we did for the photoemission data, we proceed by extracting model parameters from the experimental data. We then use them as input for the model calculation and compare the results to the experimental spectra. These parameters should be considered as having merely a phenomenological significance.

We first discuss the insulating state of $V_{2-y}O_3$. The experimental optical spectrum of the insulator is reproduced in Fig. 62 (bottom; Thomas *et al.*, 1994). It is characterized by an excitation gap at low energies, followed by an incoherent feature that corresponds to charge excitations of mainly Vanadium character (Thomas *et al.*, 1994). The procedure to extract the model parameters U,D is indicated in the figure, and the resulting values are given in Table II for the two samples considered. The sample with no vanadium deficiency ($y=0$) is fitted by $U/D\simeq 4$ and corresponds to point A in the phase diagram of Fig. 43, while the sample with $y=0.013$ is fitted by $U/D\simeq 2.1$ and corresponds to point B in this phase diagram. The model results for the optical conductivity, corresponding to these parameters are displayed in Fig. 63. The size of the gaps and the overall

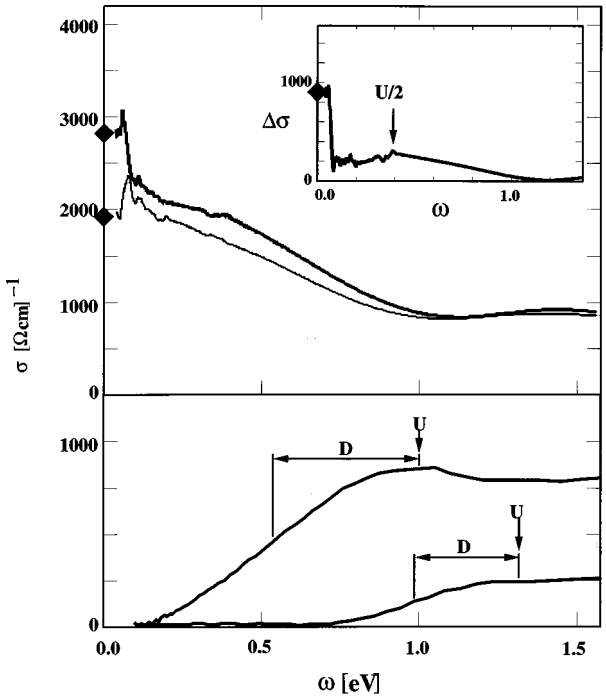

FIG. 62. The experimental $\sigma(\omega)$ of metallic V_2O_3 (full lines) at $T=170$ K (upper) and $T=300$ K (lower), from (Thomas *et al.*, 1994). The inset contains the difference of the two spectra $\Delta\sigma(\omega)=\sigma_{170\ \rm K}(\omega)-\sigma_{300\ \rm K}(\omega)$. Diamonds indicate the measured dc conductivity $\sigma_{\rm dc}$. The lines in the lower panel indicate $\sigma(\omega)$ of insulating $V_{2-y}O_3$ with $y=0.013$ at 10 K (upper) and $y=0$ at 70 K (lower).

shape of the spectrum is found to be in good agreement with the experimental results. The insets contain the kinetic energy $\langle K\rangle$ and the optical gap Δ as a function of U for various degrees of magnetic frustration. Using for the lattice constant $a\approx 3$ Å (the average V-V distance), we compare the former with the experimental integrated spectral weight.

We now discuss the recent data in the metallic phase. The experimental data are for pure samples that become insulating at $T_c\simeq 150$ K and have been taken at $T=170$ and 300 K. They are reproduced in Fig. 62 (top). Both spectra are made up of broad absorption at higher frequencies and some phonon lines in the far infrared. They appear to be rather featureless; however, upon considering their difference (in which the phonons are approximately eliminated) distinct features are observed. As T is lowered, there is an enhancement of the spectrum at intermediate frequencies of order 0.5 eV; more notably, a sharp low-frequency feature emerges that extends from 0 to 0.15 eV.

In Fig. 63 we show the calculated optical spectra for two different values of T. The interaction is set to $U=2.1D$, which places the system in the correlated metallic state. Setting $D\approx 0.4$ eV we find these results to be qualitatively consistent with the experimental data on V_2O_3. The two temperatures $T=170$ and 300 K then correspond to points C and D in the phase diagram of Fig. 43, respectively. As the temperature is lowered, we ob-

TABLE II. Parameters extracted from experiments for the model description of $V_{2-y}O_3$. Points A,B,C refer to the locations indicated in the phase diagram of Fig. 43.

Phase	Location	Parameter D [eV]	U [eV]	U/D	Δ [eV]	$\omega_P^2/(8\pi)$ [eV/Ω cm]
Insulator (y=0)	A	0.33	1.3	4	0.64	170±20
Insulator (y=0.013)	B	0.46	0.98	2.1	0.08	800±50
Metal (170 K)	C	0.4	0.8	2.1	-	1700±300

serve both the enhancement of the incoherent structures at intermediate frequencies of the order $U/2$ to U and the rapid emergence of a feature at the lower end of the spectrum. An interesting prediction of the Hubbard model treated within the LISA framework (Rozenberg *et al.*, 1995) is the T dependence of the lowest frequency feature. From the model calculations we expect a transfer of spectral weight to the low-frequency end as T is decreased. This occurs at a scale $T_{\rm coh}\approx 0.05D\approx 240$ K which correlates well with the experimental data. $T_{\rm coh}$ has the physical meaning of the temperature below which the Fermi-liquid description applies (i.e., at which the quasiparticle resonance is formed, cf. Sec. VII.D.2).

For the total spectral weight we find $\omega_P^2/8\pi\approx 500$ eV/Ω cm which is lower than the experimental result. This could be due to the contribution from tails of bands at higher energies that are not included in our model, or it may indicate that the bands near the Fermi level are degenerate.

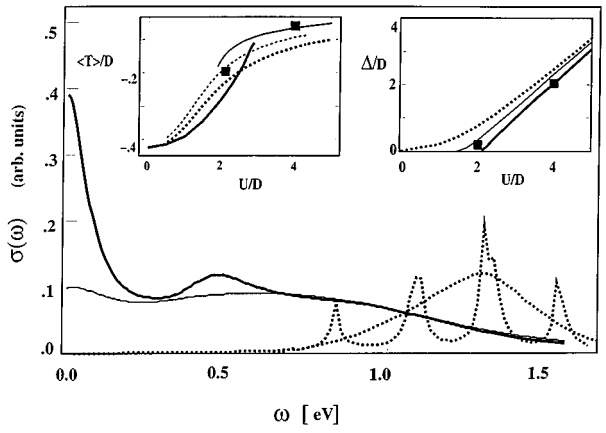

FIG. 63. The model $\sigma(\omega)$ for the metallic solution (full lines) at $U=2.1D$ and $T=0.05D$ (upper, corresponding to point C in Fig. 43) and $0.083D$ (lower, corresponding to point B in Fig. 43). A small Γ=0.3 and $0.5D$ was included to mimic a finite amount of disorder. Dotted lines indicate the insulating solution results at $U=4D$ and T=0 from exact diagonalization (thin) and iterative perturbation theory (bold). Left inset: $\langle K\rangle$ versus U for the AFM (bold-dotted), partially frustrated (thin-dotted) and PM insulators (thin) and PM metal (bold). Right inset: gap Δ versus U for the AFM (dotted), partially frustrated (thin) and PM (bold) insulators. Δ is twice the energy of the lowest pole from the exact diagonalization Green function. The data are for $n_s\to\infty$ from clusters of three, five, and seven sites assuming $1/n_s$ scaling behavior. Black squares show the insulator experimental results.

A final and important point is that experiments show that the slope of the linear term in the specific heat γ in the metallic phase is unusually large. For 0.08 Ti substitution $\gamma\approx 40$ mJ/mol K^2, while for a pressure of 25 Kbar in the pure compound $\gamma\approx 30$ mJ/mol K^2 and with V deficiency in a range of y=0.013 to 0.033 the value is $\gamma\approx 47$ mJ/mol K^2 (McWhan *et al.*, 1971; McWhan *et al.*, 1973; Carter *et al.*, 1993). In our model γ is simply related to the weight in the Drude peak in the optical conductivity and to the quasiparticle residue Z, $\gamma=3/(ZD)$ mJ eV/mol K^2. The chosen model parameters results in $\gamma\approx 25$ mJ/mol K^2 which is close to the experimental findings. Thus, it turns out that the LISA gives a simple interpretation to the experimentally observed temperature dependence of the optical conductivity spectrum and the anomalously large values of the slope of the specific heat γ, as a consequence of the appearance of a single small energy scale, the renormalized Fermi energy $\epsilon_F^*\equiv ZD$.

4. Doped titanates

We finally compare the LISA to experiments on the behavior of a Mott insulator under doping. A particularly interesting system in this respect is $La_{1-x}Sr_xTiO_3$, which has been recently studied in a beautiful set of experiments by Tokura *et al.* (1993) and Fujimori *et al.* (1992). As mentioned above $LaTiO_3$ is poised at the brink of the Mott transition. By substituting La with Sr (corresponding to hole doping), one can move away from the Mott point, thus producing a three-dimensional analog of the $La_{2-x}Sr_xCuO_2$ system.

Measurement of the resistivity ρ, Hall coefficient, magnetic susceptibility χ, and specific heat $C=\gamma T$ were reported. The resistivity is proportional to the square of the temperature ($\rho=AT^2$), demonstrating that these systems are Fermi liquids. Furthermore, the Hall coefficient is electronlike and is in rough agreement with a (large) volume of the Fermi surface (proportional to $1-x$). All three quantities χ, γ, and A are strongly enhanced as the metal-insulator transition is approached, with the ratios χ/γ and A/γ^2 remaining finite.

Because of the nature of the perovskite lattice structure of this three-dimensional compound, one should use a degenerate Hubbard model for its quantitative description. So far the Mott transition as a function of doping has mainly been investigated in the context of the one-band Hubbard model using LISA. Since this is the simplest model exhibiting this phenomenon, it is useful to summarize the results of a comparison of the predic-

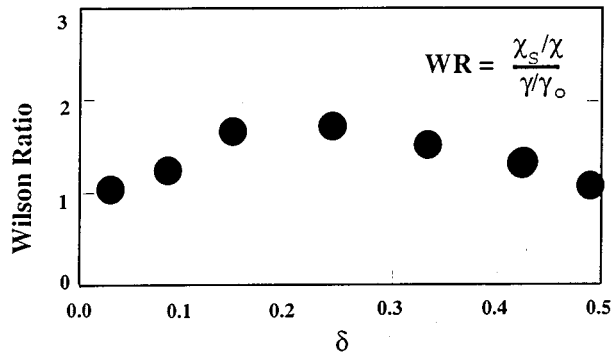

FIG. 64. The Wilson ratio as a function of doping for U=3. In comparison, the $La_{1-x}Sr_xTiO_3$ has an almost constant $R_W \simeq 2$.

tions of this model against the existing experiments, keeping in mind the possible shortcomings of a single-band description.

Rozenberg, Kotliar, and Zhang (1994) have applied a single-band LISA description to this system by choosing a value of U close to the transition point ($U=U_{c2}\simeq 3D$), in agreement with the proximity of $LaTiO_3$ to the transition, and calculating physical quantities as a function of doping x. The renormalized Fermi energy $\epsilon_F^* \simeq xD$ is the energy scale which collapses at the transition. The results for χ and γ were displayed in Fig. 50 above and compared to experiments. The agreement is found to be quite satisfactory (especially for γ), with *no* adjustable parameter.

The Wilson ratio R_W for the same values of parameters was also calculated. The results are shown in Fig. 64 and indicate that R_W is roughly independent of x, for not too small doping because the value of the exchange constant J in Eq. (254) is not very large. For very small doping however, the Wilson ratio vanishes (since χ remains finite and γ diverges, as discussed previously). Also, for large doping $R_W \to 1$, the noninteracting value, since the correlation effects become less important. However, even in the intermediate doping region, the computed value was substantially lower than the experimentally observed value $R_W \simeq 2$ (which turns out to be rather independent of doping). While this discrepancy could in principle be due to limitations of the LISA method, Kajueter, Kotliar, and Moeller (1995) recently argued that orbital degeneracy may account for the observed experimental value $R_W \simeq 2$, at least in the large doping regime. For very small doping, the effect of the magnetic exchange on γ (which is absent within LISA) is also an important question.

As discussed before, the LISA framework allows us to understand the observed scaling of A with γ^2 and calculate the coefficient of proportionality (Moeller *et al.*, 1995). The result $\rho(T)=AT^2$ where

$$A=-\frac{\pi^{5/2}\hbar a}{e^2 D}\frac{\partial^2\Sigma(i\omega_n)}{\partial(i\omega_n)^2}$$

gives rise to a finite ratio

$$\frac{A}{\gamma^2}=8.2\times 10^3 a \quad (\Omega\mathrm{m}), \tag{275}$$

where a is the lattice spacing in units of meter, and Eq. (275) is found in fair agreement with the measured value $A/\gamma^2=8\times 10^{-6}$ Ωm reported by Tokura *et al.* (1993).

The evolution of the spectral function as a function of doping in $La_{1-x}Sr_xTiO_3$ was investigated by Fujimori *et al.* (1992). The observed spectra show the presence of a narrow quasiparticle peak at the Fermi level plus a broad incoherent band at higher frequencies. The line shape is approximately independent of x, while the overall intensity of these features roughly scales with $1-x$. If one naturally associates the higher frequency feature of the observed spectra with the lower Hubbard band, the data seems inconsistent with the results of the one-band Hubbard-model calculation. It should be noted that the experimental results are rather surprising, especially in the region of large doping where correlations are not expected to be important. In order to explain the observed data, Sarma *et al.* (1995) recently introduced two models that involve phase separation on the surface and a strong random site-potential. Their solution within the LISA framework shows better agreement with the observed data. This interesting problem certainly deserves more experimental and theoretical study.

As a general conclusion of this section, we emphasize that the recent attempts that have been made in comparing the LISA results to experimental findings on transition metal oxides are encouraging. Several qualitative features were captured, and in some cases the quantitative agreement is surprising. It is clear however that these attempts must go beyond the single-orbital description, and that the effect of disorder is also likely to be an important issue. Extending the LISA framework to include more realistic features—such as a realistic band structure, crystal structure, and atomic orbitals (Sec. VIII.C)—should be within the reach of current techniques and would result in an improved *ab initio* description of correlated transition-metal oxide systems. Also, more precise experiments (such as angle-resolved photoemission) on improved samples will be necessary to decide whether some of the surprising predictions of the LISA, such as the existence of mid-gap states very near half-filling (Fisher, Kotliar, and Moeller, 1995), indeed occur in real transition-metal oxides.

VIII. APPLICATION OF THE LISA TO VARIOUS MODELS

In this section, we review recent studies of several strongly correlated fermion models in the limit of infinite dimensions, in the LISA framework. For each model, we set up the dynamical mean-field equations and describe the associated single-impurity model, briefly describe the main results and indicate possible directions for future research. Our approach is much less exhaustive than in Sec. VII, and the reader is directed to the original articles for more detailed information.

A. Periodic Anderson model and the Kondo lattice

1. The periodic Anderson model

The periodic Anderson model (PAM) consists of a band of conduction electrons that hybridizes with localized f-electron states at each lattice site. The double occupation of the f sites is disfavored by a repulsive local term that corresponds to the screened Coulomb interaction. With a local hybridization, the Hamiltonian is defined by

$$H=\sum_{\mathbf{k}\sigma}\ \epsilon_{\mathbf{k}}c^{+}_{\mathbf{k}\sigma}c_{\mathbf{k}\sigma}+V\sum_{i\sigma}\ (c^{+}_{i\sigma}f_{i\sigma}+f^{+}_{i\sigma}c_{i\sigma})+\epsilon_f\sum_{i\sigma}\ f^{+}_{i\sigma}f_{i\sigma}$$
$$+U\sum_{i}\ (n_{fi\uparrow}-\tfrac{1}{2})(n_{fi\downarrow}-\tfrac{1}{2}). \tag{276}$$

This model Hamiltonian is widely considered to be relevant for the description of a large class of strongly correlated systems, most notably the heavy fermion compounds and the so-called "Kondo insulators."

Using the fact that in the $d\to\infty$ limit the local interaction gives rise to a local (i.e., $\mathbf{k}$-independent) self-energy, the various components of the Green's functions are obtained in the form:

$$G_c(i\omega_n,\mathbf{k})^{-1}=i\omega_n-\epsilon_{\mathbf{k}}-\frac{V^2}{i\omega_n-\epsilon_f-\Sigma_f(i\omega_n)}, \tag{277}$$

$$G_f(i\omega_n,\mathbf{k})^{-1}=i\omega_n-\epsilon_f-\Sigma_f(i\omega_n)-\frac{V^2}{i\omega_n-\epsilon_{\mathbf{k}}}, \tag{278}$$

$$G_{cf}(i\omega_n,\mathbf{k})^{-1}=\frac{1}{V}\{[i\omega_n-\epsilon_{\mathbf{k}})(i\omega_n-\epsilon_f-\Sigma_f(i\omega_n)]-V^2\}. \tag{279}$$

In these expressions, $\Sigma_f(i\omega_n)$ is the self-energy of the f electrons, and the chemical potential μ has been absorbed in the definitions of $\epsilon_{\mathbf{k}}$ and ϵ_f. Using the methods of Secs. II and III, the reduction to a self-consistent single-site model is easily performed and the effective action reads

$$S_{\rm eff}=-\int_0^\beta d\tau\int_0^\beta d\tau'\sum_\sigma\ f^{+}_\sigma(\tau)\mathcal{G}_0^{-1}(\tau-\tau')f_\sigma(\tau')$$
$$+U\int_0^\beta d\tau[n_{f\uparrow}(\tau)-\tfrac{1}{2}][n_{f\downarrow}(\tau)-\tfrac{1}{2}] \tag{280}$$

with the f self-energy obtained from

$$\Sigma_f=\mathcal{G}_0^{-1}-G_f^{-1},\quad G_f\equiv-\langle Tff^{+}\rangle_{S_{\rm eff}}. \tag{281}$$

Not surprisingly, the effective action is that of a single-impurity Anderson model. The self-consistency condition requires that the local f Green's function of the lattice model coincides with the Green's function of the impurity problem, namely:

$$\int_{-\infty}^{\infty}\frac{d\epsilon\ D(\epsilon)}{i\omega_n-\epsilon_f-\Sigma_f(i\omega_n)-V^2/(i\omega_n-\epsilon)}=G_f(i\omega_n), \tag{282}$$

where $D(\epsilon)$ refers as usual to the noninteracting density of states of the conduction electrons. It is often useful to rewrite this self-consistency condition in terms of the Hilbert transform $\tilde{D}$ of the density of states [cf. Eq. (11)] as

$$G_f(i\omega_n)=\frac{1}{i\omega_n-\epsilon_f-\Sigma_f}+\frac{V^2}{i\omega_n-\epsilon_f-\Sigma_f}$$
$$\times\tilde{D}\left(i\omega_n-\frac{V^2}{i\omega_n-\epsilon_f-\Sigma_f}\right). \tag{283}$$

Note that the Hilbert transform appearing in the right-hand side of this equation coincides with the local conduction electron Green's function $G_c(i\omega_n)$.

This description of the Anderson lattice as a self-consistent single impurity Anderson model was originally introduced by Kuramoto and Watanabe (1987). Generalizations of these equations to the description of the ordered phases of this model can be easily constructed following the lines of Sec. V.

In the work of Georges, Kotliar, and Si (1992), these dynamical mean-field equations were combined with general theorems on the single-impurity Anderson model (Langreth, 1966), along similar lines to those reviewed in Sec. VII.H for the Hubbard model. This analysis shows that the metallic phase of the $d=\infty$ PAM (in the absence of long-range order and in zero magnetic field) is a Fermi liquid and has a Fermi surface which accommodates the *total number* n_c+n_f *of conduction and f electrons*.

Most quantitative studies of the $d=\infty$ PAM that have appeared in the literature have focused on the (insulating) half-filled case, which is reviewed in the next section. A notable exception is the early work of Schweitzer and Czycholl (1989, 1990a, 1991b) who make use of second-order perturbation theory in the coupling U. Both the direct weak-coupling expansion (in which the free fermions Green's function enters the second-order self-energy) and the "self-consistent" one (in which the full interacting propagator is used) were considered. One-particle spectral densities, and the temperature dependence of the resistivity $\rho(T)$ and thermopower $Q(T)$, were calculated using these approximations. The results for $\rho(T)$ and $Q(T)$ at various electron densities are reproduced in Figs. 65 and 66. Schweitzer and Czycholl make the interesting observation that $\rho(T)$ has a monotonic behavior (characteristic of a normal metal) at low electron fillings (i.e., when μ is far below the effective f level), while a plateau develops for higher electron densities, which turns into a resistivity maximum at the Kondo scale (followed by a regime with a negative slope $\partial\rho/\partial T$) as one enters the mixed valence regime (i.e., when μ is close to the effective f level). A concomitant change in behavior is observed for $Q(T)$. Both types of behavior are observed experimentally in heavy fermion compounds.

A crucial issue in the field of heavy fermions is the competition between Fermi-liquid coherence (the Kondo effect) and magnetic (Ruderman-Kittel-Kasuya-Yosida, or RKKY, and superexchange) interactions. The

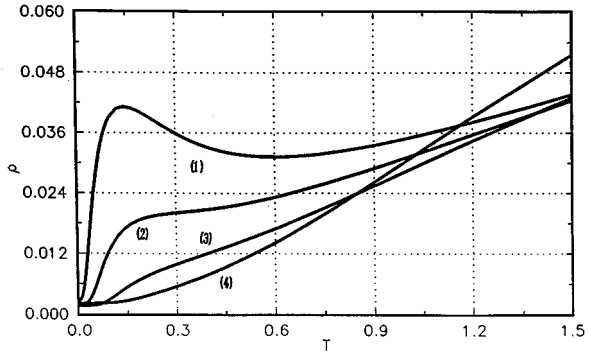

FIG. 65. Temperature dependence of the resistivity for the periodic Anderson model on the hypercubic lattice with U=1 and V=0.4 ($t_{ij} = 1/\sqrt{2d}$), as obtained from "self-consistent" second-order perturbation theory. (1) $n_{\rm tot}$=0.8, (2) $n_{\rm tot}$=0.6, (3) $n_{\rm tot}$=0.4, (4) $n_{\rm tot}$=0.2 (from Schweitzer and Czycholl, 1991b).

LISA (d=∞) approach does have a bearing on this issue, albeit a partial one (Georges, Kotliar, and Si, 1992; Jarrell, 1995). Namely, both the superexchange and the RKKY couplings are indeed present: the RKKY coupling scales as $1/d$ between nearest-neighbor sites, $1/d^2$ between next nearest neighbors, etc. which is precisely the correct scaling such that a finite contribution to the magnetic energy is obtained. [For a more detailed analysis of the RKKY coupling in large dimensions, see Jarrell (1995).] Therefore, phases with long-range order do appear. This makes the LISA approach more suitable to capture these effects than the large-N methods (in which magnetic effects only appear at order $1/N^2$, cf. Read, Newns, and Doniach, 1984). These magnetic scales also appear in two-particle response functions at a fixed value of $\mathbf{q}$ above the ordering temperature. However, they do not show up in single-particle properties such as the self-energy, so that no precursor effect of the magnetic transitions exists, e.g., for the effective mass in this approach. Also, collective excitations (e.g., spin waves) are absent. The problem was already discussed in Sec. VII in connection with the Mott transition, and is intrinsic to single-site descriptions. Extensions of the LISA method are required to capture these effects (cf. Sec. IX).

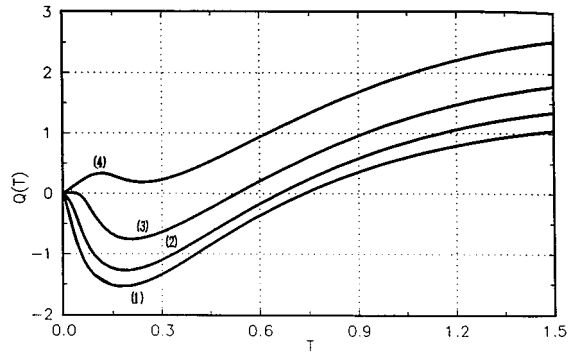

FIG. 66. Temperature dependence of the thermopower $Q(T)$ for the same parameters as in Fig. 65 (from Schweitzer and Czycholl, 1991b).

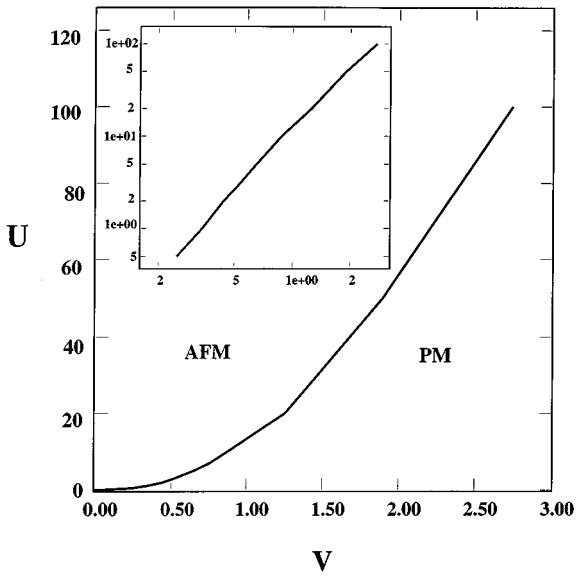

FIG. 67. Phase diagram of the periodic Anderson model on the z=∞ Bethe lattice. The inset shows, in a log-log plot, that the second-order critical line obeys $U_c \approx V_c^2$ as U becomes large. The results are from exact diagonalization with n_s=6.

2. Half-filled case: Kondo insulators

More recently, quantitative studies of the LISA equations for the periodic Anderson model going beyond perturbative approximations have appeared in the literature, focusing particularly on the half-filled case $\langle n_c\rangle + \langle n_f\rangle = 2$ (ϵ_f=0 with the notations above). This case is relevant for the so-called "Kondo insulators" such as CeNiSn, $Ce_3Bi_4Pt_3$, and SmB_6 (and perhaps also FeSi). In the work of Jarrell, Akhlaghpour, and Pruschke (1993a) and Jarrell (1995), the quantum Monte Carlo method is used to solve the associated impurity problem and calculate densities of states and various response functions. It was also found that the half-filled solution has an antiferromagnetic instability for some range of parameters.

The study of solutions with commensurate antiferromagnetic long-range order was considered by Sun, Yang, and Hong (1993) within a slave-boson approximation for the impurity problem, and in more detail by Rozenberg (1995) using the exact diagonalization method. The resulting phase diagram is depicted in Fig. 67. The paramagnetic and antiferromagnetic phases are separated by a second-order critical line that obeys $V^2/UD \approx J_c/D$, with $J_c \approx 0.075D$. Thus the large dimensional solution of the PAM realizes early ideas of Doniach (1977), who found that at the (static) mean field level $J_c/D \sim O(1)$, and argued that dynamical fluctuations should strongly reduce this ratio. It is also interesting to note that the phase diagram is in good agreement with the recent results of Vekič *et al.* (1995) for the *two-dimensional* PAM obtained from quantum Monte Carlo simulations on a finite lattice, and to those of Möller and Wölfle (1993) in the three-dimensional case.

A typical result for the spectral density of the half-filled PAM in the paramagnetic phase is depicted in Fig.

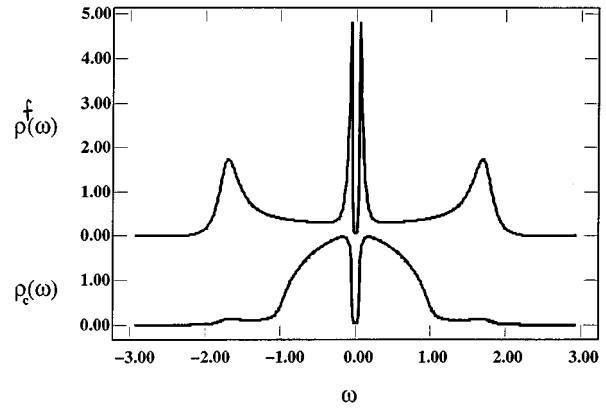

FIG. 68. Density of states for the c and f electrons (bottom and top) in the half-filled periodic Anderson model for $U/D=2.5$ and $V/D=0.4$ at $T/D=0.01$.

68. The result was obtained by the iterated perturbation theory method (Sec. VI.B.2), and compares favorably with the results of exact diagonalizations or quantum Monte Carlo [there are small differences, though, as noted in the work of Jarrell, Akhlaghpour, and Pruschke (1993a)]. It is useful to note that the iterated perturbation theory method, similarly to what happens in the case of the Hubbard model, bases its success on the property of capturing correctly the limit in which either $D\to 0$ or $V\to 0$, and also (by construction) the weak-coupling limit $U\to 0$. The spectral density displays a narrow insulating gap $\Delta_{\rm ind}$, with two sharp peaks on each side. As discussed below, this gap corresponds to an *indirect gap* of the renormalized band structure. Furthermore, satellites at $\pm U/2$ are also found, as expected from the study of the atomic limit. As already observed for the Hubbard model in Sec. VI.B.2, these high-energy satellites are not correctly captured by the "self-consistent" weak-coupling expansions mentioned above; a comparison with Figs. 3(a)–3(c) of Schweitzer and Czycholl (1990a), in which these peaks are absent, illustrates the point. We believe that the sharp peaks on the gap edges are related to the features observed by photoemission on FeSi by Park, Shen, *et al.* (1994).

These results can be understood by performing a low-frequency analysis of the dynamical mean-field equations. Let us make the assumption that the f-electron spectral density displays a gap $\Delta_{\rm ind}$. This implies that the low-frequency behavior of the f-electron Green's functions is $G_f(i\omega_n)\sim i\omega_n$. A convenient parametrization of this linear behavior is

$$V^2 G_f(i\omega_n)=-\left(1+\frac{\langle\epsilon^2\rangle}{V_*^2}\right)i\omega_n+O(\omega_n^3). \tag{284}$$

In this expression, V_* is an effective hybridization renormalized by the interaction (for $U=0$, it is easily checked that $V_*=V$) and $\langle\epsilon^2\rangle$ simply denotes $\int d\epsilon\, D(\epsilon)\epsilon^2$. Inserting this into the self-consistency condition (283), one finds that the density of states of the effective bath entering the impurity model take the form

$$\Delta(\omega)\equiv-\frac{1}{\pi}\,\mathrm{Im}\mathcal{G}_0^{-1}(\omega+i0^+)$$

$$=\frac{V_*^2}{V_*^2+\langle\epsilon^2\rangle}\,\delta(\omega)+\Delta_g(\omega), \tag{285}$$

in which $\Delta_g(\omega)$ denotes a nonsingular density of states also displaying a gap. Hence, the effective bath density of states has a single localized level at zero energy, in the middle of the insulating gap. Solving the Anderson impurity model with this bath shows that (i) the assumption of a gap is a self-consistent one and (ii) a local Kondo effect does take place (despite the insulating character of the lattice problem), involving the f orbital and this localized level. The low-energy expansion of the self-energy reads

$$\mathrm{Re}\,\Sigma_f(\omega+i0^+)=-\left(\frac{V^2}{V_*^2}-1\right)\omega+O(\omega^3) \tag{286}$$

while $\mathrm{Im}\Sigma_f(\omega+i0^+)$ vanishes inside the gap, and is actually zero within a wider interval of energies (or "direct gap"): $-\Delta_{\rm dir}/2<\omega<+\Delta_{\rm dir}/2$, as we will show. The "renormalized" (quasiparticle) bands $E_{\mathbf{k}}$ are obtained by locating the poles of the conduction electron Green's function $G_c(\mathbf{k},\omega)$; i.e., the bands are solutions of

$$[E_{\mathbf{k}}-\epsilon_{\mathbf{k}}][E_{\mathbf{k}}-\Sigma_f(E_{\mathbf{k}})]-V^2=0. \tag{287}$$

An approximation of the band structure and of $\Delta_{\rm ind}$ and $\Delta_{\rm dir}$ can be obtained by substituting the self-energy in this equation by its low-frequency linear behavior (286). This leads to

$$E_{\mathbf{k}}^{\pm}\simeq\frac{1}{2}\left[\epsilon_{\mathbf{k}}\pm\sqrt{\epsilon_{\mathbf{k}}^2+4V_*^2}\right]. \tag{288}$$

This expression is identical to the one for $U=0$, with the replacement $V\to V_*$. The indirect gap corresponds to the distance between renormalized band edges. Denoting by D the half-width of the noninteracting density of states, we obtain

$$\Delta_{\rm ind}\simeq\sqrt{D^2+4V_*^2}-D \tag{289}$$

while the smallest direct gap is for $\epsilon_{\mathbf{k}}=0$ and reads

$$\Delta_{\rm dir}\simeq 2V_*. \tag{290}$$

It is seen that $\Delta_{\rm ind}\simeq 2V_*^2/D\ll\Delta_{\rm dir}$ when $V_*\ll D$.

The indirect gap appearing in the spectral density also sets the low-energy scale appearing in the temperature dependence of the uniform spin and charge susceptibilities. Consistently with the existence of sharp peaks at the gap-edges in the spectral density, the magnetic susceptibility raises sharply as a function of temperature for $T>\Delta_{\rm ind}$, and reaches a maximum at a scale set by the gap $\Delta_{\rm ind}$ itself. This behavior is in good qualitative agreement with the experimental findings of Jaccarino *et al.* (1967) for FeSi. The QMC result of Jarrell, Akhlaghpour, and Pruschke (1993a) for $\chi(T)$ is displayed in Fig. 69. Jarrell (1995) reports a charge and spin gap comparable to each other: $\Delta_c\simeq\Delta_s\simeq 2\Delta_{\rm ind}$, but recent results of Rozenberg, Kotliar, and Kajueter (1995) in the deep

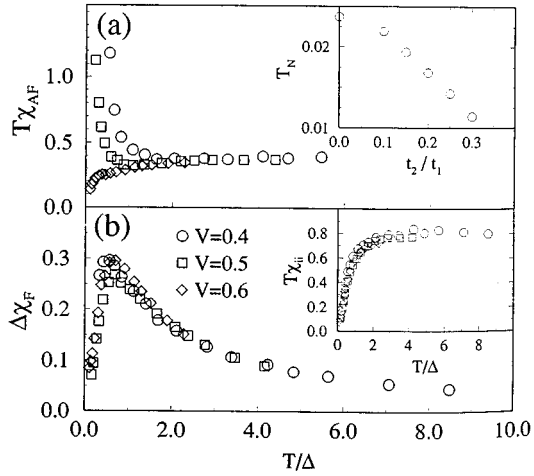

FIG. 69. Staggered (AF) and uniform (F) spin susceptibilities of the symmetric PAM with U=2 on the hypercubic lattice [$t_{ij}=1/2\sqrt{d}$, for various values of V (from Jarrell, Akhlaghpour, and Pruschke (1993a, 1993b)]. The inset of (a) shows the Néel temperature T_N when V=0.4 as a function of a frustrating hopping t_2/t_1. The inset of (b) shows the local spin susceptibility.

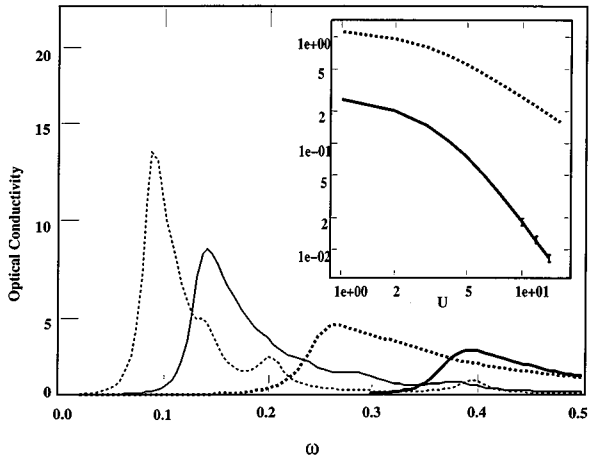

FIG. 70. The optical conductivity spectra of the periodic Anderson model, obtained by iterated perturbative theory for values of the interaction U=0.5,1,2,3 (right to left), keeping the hybridization V=0.25 fixed. The inset shows the gap from the optical spectra $\Delta_c \approx \Delta_{\rm dir}$ and the indirect gap $\Delta_{\rm ind}$ from the local density of states for V=0.6. The slopes of these curves indicate that $V^{*2}/D \propto \Delta_{\rm ind}$ and $V^* \propto \Delta_{\rm dir}$ in the strong correlation region. Similar results have been obtained by Jarrell (1995) using the QMC method.

Kondo regime may indicate deviation from this behavior, and we regard this issue as yet unresolved. Note that, in the one-dimensional case, $\Delta_c \gg \Delta_s$ (Nishino and Ueda, 1993), while the Gutzwiller approximation (Rice and Ueda, 1986) leads to $\Delta_c \simeq \Delta_s$. Jarrell (1995) has also studied the behavior of the thermodynamic properties as a function of temperature, and whether a scaling behavior applies to each of them, as a function of $T/\Delta_{\rm ind}$. Recent work by Saso and Itoh (1995) studies the effect of an applied magnetic field on Kondo insulators using the LISA.

We now briefly describe the results for the optical conductivity. This was first investigated by Jarrell (1995) using QMC, and recently by Rozenberg, Kotliar, and Kajueter (1995) using exact diagonalization and the iterated perturbation theory approximation to treat the strong coupling regime. These results can be compared to the recent experimental results of Bucher *et al.* (1994) and Schlesinger *et al.* (1993) on the optical response of $Ce_3Bi_4Pt_3$ and FeSi respectively. A plot of the optical conductivity $\sigma(\omega)$ for different values of U at T=0 is shown in Fig. 70. These results show that the optical gap is set by the *direct gap* $\Delta_{\rm dir}$ of the renormalized band structure. This is because ImΣ becomes nonzero at this scale. Thus the emerging picture is consistent with the usual interpretation of the hybridization band insulator, with a renormalized hybridization as described above. However, interesting effects are found as a function of temperature. In Fig. 71 we show the optical conductivity for different temperatures and the parameters U=3 and V=0.25 fixed. The gap is essentially temperature independent. It begins to form at $T^* \approx \Delta_{\rm dir}/5$, and is fully depleted only at temperatures of the order of $T^*/5$, that is, when T becomes comparable to the size of the gap in the density of states. It is actually interesting to compare how the process of filling of the optical gap is correlated with the filling of the gap in the coherent features of the single-particle spectra and with their subsequent disappearance at high temperature. This comparison makes more evident the different energy scales associated with the optical gap and the coherent gap in the density of states. The single-particle spectra for the c and f electrons is displayed in Fig. 72.

The behavior described above is qualitatively similar to the experimental observations in the Kondo insulator systems mentioned above, which are reproduced in Figs. 73 and 74. Note that, while they correspond to different compounds, the two spectra have many common features. A point worth mentioning is that the solution of the model within the iterated perturbation theory

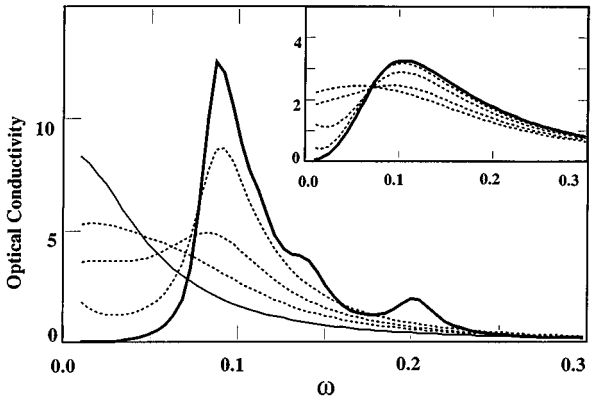

FIG. 71. The optical conductivity for the Anderson model at T=0.001 (bold), 0.005, 0.01, 0.02 (dotted), 0.03 (thin). The interaction U=3 and V=0.25. Inset: The same quantity at T=0.001 (bold); 0.005, 0.01, 0.02, 0.03 (dotted); with Lorentzian random site disorder of width Γ=0.005.

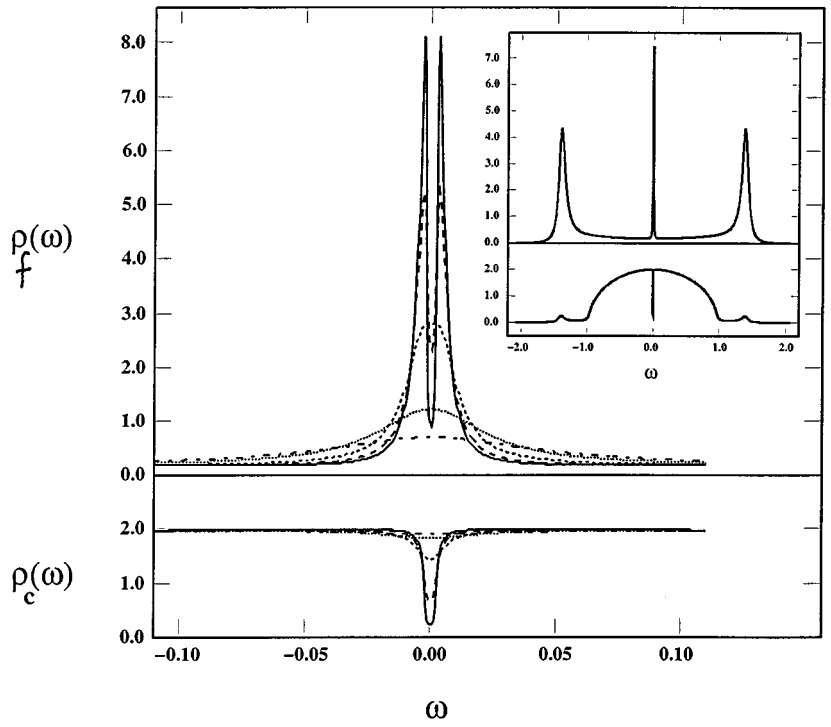

FIG. 72. Low-frequency part of the density of states for the f and c electrons (top and bottom) obtained from iterative perturbation theory at T=0.001 (full), 0.005 (long-dashed), 0.01 (short-dashed), 0.02 (dotted), 0.03 for U=3 and V=0.25. Inset: The density of states in the full frequency range at T=0.001.

method predicts an interesting nonmonotonic behavior of the total integrated optical spectral weight as a function of the temperature. It is observed that the integrated weight initially increases with temperature, up to temperatures of the order of the size of the optical gap. A further increase of T leads to a decrease of the integrated weight as the system turns metallic and correlations become unimportant. The fact that in the low-temperature range the integrated weight increases with T may be relevant for the resolution of the problem of the "missing spectral weight" experimentally observed in the Kondo insulators compounds (Schlesinger *et al.*, 1993; Bucher *et al.*, 1994).

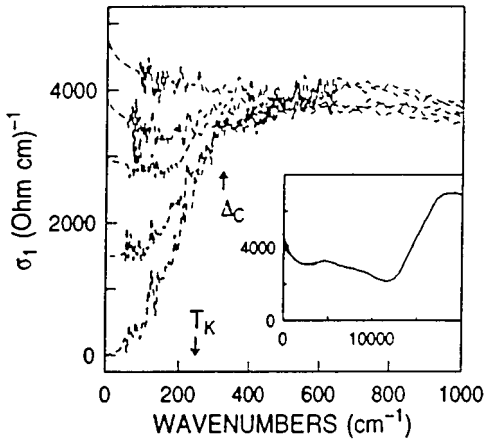

FIG. 73. Optical conductivity $\sigma(\omega)$ of $Ce_3Bi_4Pt_3$ for different temperatures (from below: 25, 50, 75, 100, and 300 K), from Bucher *et al.* (1994). A gap is opening below 100 K; the prominent feature at Δ_c seems to be independent of temperature. The inset presents the optical region of σ.

To end this section, we mention that an alternative model for FeSi has been proposed and studied in the $d\to\infty$ limit by Fu and Doniach (1994). The model is that of a strongly correlated semiconductor consisting of two bands of dominantly iron character. The proposed Hamiltonian reads

$$H=\sum_{\langle ij\rangle\sigma} -t(c^{\dagger}_{i1\sigma}c_{j1\sigma}-c^{\dagger}_{i2\sigma}c_{j2\sigma}+\text{H.c.}) + \sum_{i\sigma} V(c^{\dagger}_{i1\sigma}c_{i2\sigma}+\text{H.c.}) + \sum_{i} U(n_{c_{i1\uparrow}}n_{c_{i1\downarrow}}+n_{c_{i2\uparrow}}n_{c_{i2\downarrow}}). \quad (291)$$

The opposite sign of the two hopping terms provides a direct gap between the valence and conduction band. The self-consistent perturbation theory was used by Fu and Doniach to compute various quantities, among which are the temperature dependence of the susceptibility and the spectral functions. At this moment, we are

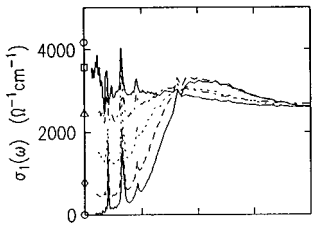

FIG. 74. Optical conductivity $\sigma(\omega)$ of cubic FeSi for different temperatures (from below: 20, 100, 150, 200, and 250 K), from Schlesinger *et al.* (1993). The symbols at ω=0 show the measured values of σ_{dc} for the same temperature sequence.

not aware of attempts to study the LISA equations for this model with more accurate methods. The model should provide an interesting starting point to study many-body effects in semiconductors within the LISA framework. The same model with the opposite relative sign of t was studied by Moeller, Dobrosavljević, and Ruckenstein (1995) using the iterated perturbation theory method.

3. The multichannel Kondo lattice

Close to half-filling and for large U, charge fluctuations can be ignored, and the periodic Anderson model can be formulated as a Kondo lattice model using the Schrieffer-Wolff canonical transformation. In this case the conduction electrons interact with localized spins only, and the Hamiltonian reads

$$\sum_{\mathbf{k}\sigma} \epsilon_{\mathbf{k}} c^{+}_{\mathbf{k}\sigma} c_{\mathbf{k}\sigma} + J_K \sum_{i\sigma\sigma'} \sum_{a=x,y,z} S^a_i \frac{1}{2} c^{+}_{i\sigma} \sigma^a_{\sigma\sigma'} c_{i\sigma'} . \quad (292)$$

The LISA equations for this model (Georges, Kotliar, and Si, 1992) are conveniently expressed in terms of the *conduction electron* self-energy, defined from the corresponding Green's function by

$$G_c(i\omega_n, \mathbf{k}) = \frac{1}{i\omega_n - \epsilon_{\mathbf{k}} - \Sigma_c(i\omega_n)} . \quad (293)$$

The single-site effective action is found to be

$$S_{\text{eff}} = -\int_0^\beta d\tau \int_0^\beta d\tau' \sum_\sigma c^{+}_\sigma(\tau) \mathscr{G}_0^{-1}(\tau - \tau') c_\sigma(\tau') + J_K \sum_a \int_0^\beta d\tau S^a \frac{1}{2} \sum_{\sigma\sigma'} c^{+}_\sigma \sigma^a_{\sigma\sigma'} c_{\sigma'} + L_s[S], \quad (294)$$

where $L_s[S]$ is a spin-1/2 Lagrangian that can be expressed in any of the standard representations used to construct a spin Lagrangian (e.g., Popov representation, slave fermion, Schwinger boson, or Abrikosov pseudofermion representation). Alternatively, if the spin is treated in the coherent path integral formulation, L_s is the spin Berry phase. S_{eff} describes a single-impurity Kondo model in an effective conduction bath $\mathscr{G}_0$.

The self-consistency condition reads

$$G_c(i\omega_n) \equiv -\langle c^{+}(i\omega_n) c(i\omega_n) \rangle_{S_{\text{eff}}} = \int_{-\infty}^{\infty} \frac{D(\epsilon) d\epsilon}{i\omega_n - \epsilon - \Sigma_c(i\omega_n)} ,$$

$$\Sigma_c \equiv \mathscr{G}_0^{-1} - G_c^{-1} . \quad (295)$$

The model can be generalized to consider M "flavors" or "channels" for the conduction electrons $c^{+}_{k\sigma} \to c^{+}_{k\sigma\alpha}$, with $\alpha = 1, \ldots, M$, yielding the multichannel Kondo lattice Hamiltonian:

$$\sum_{\mathbf{k}\sigma\alpha} \epsilon_{\mathbf{k}} c^{+}_{\mathbf{k}\sigma\alpha} c_{\mathbf{k}\sigma\alpha} + J_K \sum_{\alpha=1}^{M} \sum_{i\sigma\sigma' a} S^a_i c^{+}_{i\alpha\sigma} \frac{\sigma^a_{\sigma\sigma'}}{2} c_{i\alpha\sigma'} . \quad (296)$$

The associated impurity model is the single-impurity multichannel Kondo model. In the last few years there has been an intensive search of *lattice* models exhibiting a non-Fermi liquid fixed point at low temperatures. Model (296) with $M>1$ is a very interesting candidate for this behavior since in the absence of the self-consistency condition (295) the local action S_{eff} is known from the work of Nozieres and Blandin (1981) to be driven to a non-Fermi liquid fixed point. As pointed out by Georges, Kotliar, and Si (1992) and Cox (1994), this implies immediately that the lattice model with the Lorentzian density of states is not a Fermi liquid (since in that case the self-consistency condition becomes trivial). The same is likely to be true in $d=\infty$ for other density of states with nontrivial feedback from the lattice induced by the self-consistency condition, as long as no low-frequency singularity of the effective bath density of states is induced in the process.

The single-site ($d=\infty$) dynamical mean-field theory ignores however the important issues raised by the feedback of interimpurity interactions into single-particle quantities, which could drastically change this picture. More elaborate approaches such as the self-consistent cluster embeddings of Sec. IX are required to put the interimpurity effects and the local Kondo physics on equal footing and answer this question (except in the case where the inter-impurity coupling is a quenched random exchange, see below). Note that, with two channels of conduction electrons, the two-impurity Kondo model has been shown to display interesting non-Fermi liquid behavior in the particle-hole symmetric case, in the presence of finite RKKY interactions (Ingersent, Jones, and Wilkins, 1992; Georges and Sengupta, 1995). Even for the single-channel Kondo lattice, the question of how intersite fluctuations affect Fermi liquid behavior close to the AF phase boundaries requires an extension of the single-site LISA approach. This question is crucial for the physics of heavy fermions.

4. Metallic quantum spin glasses

There is one remarkable situation, however, in which (RKKY) intersite magnetic couplings do induce precursor effects of magnetic transitions even at the level of a single-site LISA description. This is when these couplings are modeled as a *quenched random exchange*. This description is relevant when the low-temperature phase has spin-glass order, as observed in $Y_{1-x}U_xPd_3$ and related compounds (cf. Maple *et al.*, 1994, and references therein). Recently, a Kondo lattice model taking these effects into account has been studied in the $d=\infty$ limit (Sachdev, Read, and Oppermann, 1995; Sengupta and Georges, 1995). Specializing to Ising exchange J_{ij}, with a Gaussian distribution normalized such that $\overline{J_{ij}^2} = J^2/z$, the Hamiltonian reads

$$H = -\sum_{ij\sigma} t_{ij} c^{+}_{i\sigma} c_{j\sigma} + J_K \sum_i \vec{S}_i \cdot \vec{s}(i) - \sum_{\langle ij \rangle} J_{ij} S^z_i \cdot S^z_j . \quad (297)$$

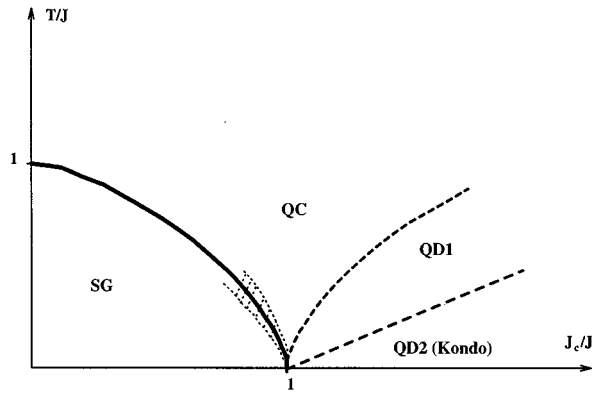

FIG. 75. Schematic phase diagram of the metallic spin-glass model described in the text, as a function of T/J and J_c/J (with $J_c \simeq \Lambda \simeq T_K$). The full line is the critical boundary with the spin-glass phase. All other lines are crossover lines between the quantum-critical (QC) and quantum-disordered regimes (QD1,QD2). The hatched region is that of classical behavior near the critical boundary. From Sachdev, Read, and Oppermann (1995) and Sengupta and Georges (1995).

Following the techniques of Sec. III, the problem is easily mapped onto a single-site effective action:

$$S_{\rm eff} = -\int_0^\beta d\tau \int_0^\beta d\tau' \Sigma_{\sigma,ab} c^+_{\sigma a}(\tau) \mathcal{G}^{-1}_{0ab}(\tau-\tau') c_{\sigma b}(\tau') + J_K \int_0^\beta d\tau \Sigma_a \vec{S}_a(\tau)\cdot\vec{s}_a(\tau) - J^2 \int_0^\beta d\tau \int_0^\beta d\tau' \Sigma_{a,b} S^z_a(\tau) D_{ab}(\tau-\tau') S^z_b(\tau') \quad (298)$$

in which $a,b = 1\cdots n$ are replica indices. A self-consistency condition relates the Weiss functions to the conduction electron Green's function and the spin-spin correlation function, which reads (on the Bethe lattice)

$$\mathcal{G}^{-1}_{0ab}(i\omega_n) = (i\omega_n+\mu)\delta_{ab} - t^2 G_{ab}(i\omega_n),$$
$$D_{ab}(\tau-\tau') = \langle T S^z_a(\tau) S^z_b(\tau')\rangle_{S_{\rm eff}}. \quad (299)$$

In the high-temperature paramagnetic phase, all these correlators are replica diagonal. Because J_{ij} scales as $1/\sqrt{d}$, the magnetic exchange does enter the single-site effective action in both phases, leading to new dynamical effects.

The schematic phase diagram resulting from the analysis of this model (Sachdev, Read, and Oppermann, 1995; Sengupta and Georges, 1995) is displayed in Fig. 75. A spin-glass phase is found for large J, with a freezing critical temperature driven to $T_c=0$ when the strength of the Kondo coupling is increased. This is reminiscent of the Doniach (1977) phase diagram. Several crossover regimes are found near this $T=0$ quantum critical point. In the "quantum critical" regime, the specific heat coefficient γ and uniform susceptibility χ display nonanalytic corrections to Fermi-liquid behavior, while the NMR relaxation rate and resistivity have a *non-Fermi liquid* temperature dependence: $\rho \sim T^{3/2}$, $1/T_1 T \sim 1/T^{3/4}$ (Sengupta and Georges, 1995). In the low-temperature part of the quantum-disordered region ("Kondo regime"), Fermi-liquid behavior is recovered, but the NMR and scattering rate are critically enhanced as the transition is reached, while γ and χ are not.

B. The Falicov-Kimball model

We now turn to the spinless Falicov-Kimball model (Falicov and Kimball, 1969). This model was originally introduced to describe the metal-insulator transition of systems containing both localized and itinerant electrons. It has also attracted interest as a model for electron-induced formation of crystalline order (Kennedy and Lieb, 1986; Lieb, 1986). Remarkably, it can be solved exactly by analytical methods in infinite dimensions, as described in the pioneering work of Brandt and Mielsch (1989, 1990, 1991).

The model involves spinless conduction electrons c_i, and localized f electrons (or ions). The Hamiltonian reads

$$H = -\sum_{ij} t_{ij} c^+_i c_j + \sum_i \epsilon_f f^+_i f_i - \mu \sum_i (c^+_i c_i + f^+_i f_i) + U \sum_i c^+_i c_i f^+_i f_i . \quad (300)$$

The chemical potential μ constrains the *total* number of electrons and ions. ϵ_f sets the energy level of the ions with respect to the middle of the electron band. U is an on-site repulsion between electrons and ions. When $\epsilon_f=0$, the model corresponds to the spin-1/2 Hubbard model with only one of the spin components allowed to hop.

Integrating out all the electrons except for those at the central site we obtain the effective action of the associated impurity model (in a phase without translational symmetry breaking):

$$S_{\rm eff} = -\int_0^\beta d\tau \int_0^\beta d\tau' c^+(\tau) \mathcal{G}_0^{-1}(\tau-\tau') c(\tau') + \int_0^\beta d\tau \{ U c^+ c f^+ f + f^+ (\partial/\partial\tau + \epsilon_f) f - \mu (c^+ c + f^+ f)\}. \quad (301)$$

In contrast to the Hubbard model, it is easy to solve for the impurity model Green's function in terms of the Weiss function $\mathcal{G}_0$. Indeed, the two sectors of the Hilbert space $f^+f=0$ and $f^+f=1$ evolve independently under the dynamics defined by (301). One thus obtains

$$G(i\omega_n) \equiv -\langle c^+ c\rangle_{S_{\rm eff}} = \frac{w_0}{\mathcal{G}_0^{-1}(i\omega_n)} + \frac{w_1}{\mathcal{G}_0^{-1}(i\omega_n) - U}, \quad (302)$$

where $w_0 = 1 - w_1$ and

$$w_1=\left\{1+\exp\left(\beta(\epsilon_f-\mu)+\sum_n \{\ln[\mathcal{G}_0^{-1}(i\omega_n)]-\ln[\mathcal{G}_0^{-1}(i\omega_n)-U]\}e^{i\omega_n 0^+}\right)\right\}^{-1}, \quad (303)$$

Differentiating the partition function with respect to ϵ_f, we see that w_1 is the f particle number per site. The local conduction electron self-energy is defined as usual through

$$G(i\omega_n)^{-1}=\mathcal{G}_0^{-1}(i\omega_n)-\Sigma(i\omega_n). \quad (304)$$

When combined with the explicit form of the Green's function Eq. (302), this leads to the functional form of the self-energy $\Sigma(i\omega_n)\equiv\Sigma_n$ in terms of the local Green's function $G(i\omega_n)\equiv G_n$:

$$\Sigma_n(G_n)=U/2-1/2G_n\pm\sqrt{(U/2-1/2G_n)^2+w_1U/G_n}, \quad (305)$$

where the sign is to be chosen (depending on frequency) in such a way that Σ has the appropriate analytic properties. Furthermore, the self-consistency equation reads, as usual,

$$G_n=\int_{-\infty}^{\infty}d\epsilon\,\frac{D(\epsilon)}{i\omega_n+\mu-\epsilon-\Sigma_n(G_n)}, \quad (306)$$

where $D(\epsilon)$ is the conduction electron bare density of states. Equations (303), (305), and (306), first derived by Brandt and Mielsch (1989), form a closed set of equations for the *conduction electron* Green's function and self-energy in phases without long-range order. An interpretation of these equations as a mean-field theory, rather different in spirit to the mapping onto an effective impurity problem, has been given by van Dongen and Vollhardt (1990) and van Dongen (1991a, 1992).

Before turning to the description of possible long-range order and of the phase diagram of the model, let us mention some results on the behavior of the Green's function in phases without order (e.g., at high temperature). van Dongen (1991a, 1992) established that the model displays a metal-insulator transition as a function of U at half-filling $n_c+n_f=1$, at $U_c=D$ when $D(\epsilon)$ is semicircular with a half-bandwidth D. Si, Kotliar, and Georges (1992) established that there are two regions, as a function of the total density $n=n_c+n_f$ and U:

(i) For U larger than $U_c(n)$, the number of f electrons per site is either $n_f=0$ or $n_f=1$. In that region, the conduction electrons obviously behave as a free Fermi gas.

(ii) For U smaller than $U_c(n)$, there is a finite occupancy $0<n_f<1$, and the chemical potential *remains pinned* at the effective f-electron level: $\mu=E_f$, with E_f defined by $w_1=\{1+\exp\beta(E_f-\mu)\}^{-1}$. In this regime, the conduction electron self-energy has a *finite imaginary part* at zero frequency, and the Fermi-liquid theory breaks down.

The f electron (ion) Green's functions is more difficult to obtain than the conduction electron one. To this aim, it is useful to realize that the Hamiltonian form of the impurity effective action (301) is the x-ray edge Hamiltonian:

$$H=\sum_{\mathbf{k}}E_{\mathbf{k}}a_{\mathbf{k}}^{+}a_{\mathbf{k}}+(\epsilon_f-\mu)f^{+}f+Uf^{+}f\sum_{\mathbf{k}\mathbf{k}'}a_{\mathbf{k}}^{+}a_{\mathbf{k}'} \quad (307)$$

with the spectral representation

$$\mathcal{G}_0^{-1}=\left\{\sum_{\mathbf{k}}\frac{1}{i\omega_n-E_{\mathbf{k}}}\right\}^{-1}-\mu. \quad (308)$$

It results from this mapping that, in the pinning region mentioned above, the f-electron spectral function has an x-ray edge singularity at low frequencies (Si, Kotliar, and Georges, 1992). A numerical study of the heavy electron Green's function of this model (Brandt and Urbanek, 1992) is consistent with a thermal smearing of the x-ray singularity. Further analytic work on this problem was carried out by Janiš (1993).

At low temperature, the $d=\infty$ Falicov-Kimball model displays ordered phases in which both the conduction electron and f-electron (ion) charge densities acquire nonzero values, at a given ordering vector $\mathbf{q}$. For the symmetric half-filled case ($\epsilon_f=0$, $n_c=n_f=1/2$), the ordering is towards a commensurate [$\mathbf{q}=(\pi,\ldots,\pi)$] ordered state, in which the particles order in a checkerboard pattern: the conduction electrons occupy one sublattice, and the ions the other one. (Viewing each electrons species as a given spin species, this state can be called a spin-density wave state, and is the direct analog of the Néel state). This is true in any dimension on a bipartite lattice, and has been established rigorously (Brandt and Schmidt 1986, 1987; Kennedy and Lieb, 1986). For $d=\infty$, Brandt and Mielsch (1989, 1990, 1991) were able to establish equations for the CDW susceptibility $\chi(\mathbf{q})$, and computed the critical temperature at half-filling as a function of U. van Dongen and Vollhardt (1990) showed analytically that $T_c\sim 1/U$ for large U, while $T_c\sim U^2\ln(1/U)$ for small U. The CDW transition is second-order (Ising-like), but can be driven first-order in the presence of a nearest-neighbor repulsion V (van Dongen, 1991a, 1992). For $V>U/2$, a charge-density wave transition is found instead, with doubly occupied sites on one sublattice, and holes on the other (van Dongen, 1991a, 1992).

These results have been extended for arbitrary electron density n_c (keeping $n_f=1/2$) by Freericks (1993a), for the $d=\infty$ hypercubic lattice. He showed that, for a given U, the ordering becomes *incommensurate* for a range of electron concentrations. For still smaller densities, a segregated phase is found (in which ions and electrons cluster in separate regions). As explained in Sec. IV, the ordering wave vector can be characterized by $X(\mathbf{q})=1/d\Sigma_{i=1}^{d}\cos q_i$. It varies continuously with U and n_c within the incommensurate phase. The phase diagram established by Freericks (1993a) is displayed in Fig. 76. Freericks (1993b) also used the LISA as a dynamical mean-field approximation to the *finite-dimensional* Falicov-Kimball model, and concluded that the approximation is inaccurate at strong coupling in $d=1$, but is a very good description of the model in $d\geq 2$. The optical conductivity of the Falicov-Kimball model on the hypercubic lattice was computed by Moeller, Ruckenstein, and Schmitt-Rink (1992).

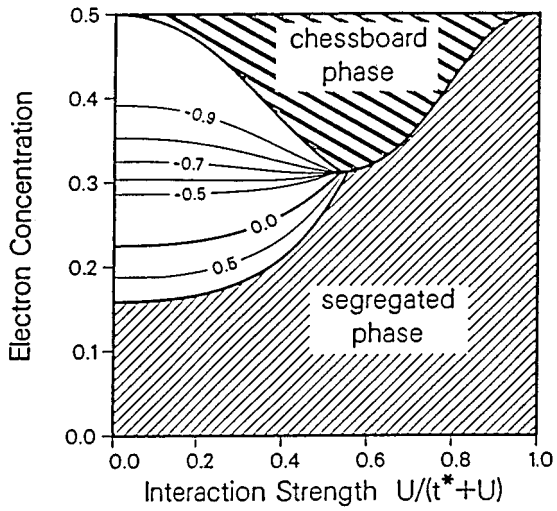

FIG. 76. Phase diagram of the Falicov-Kimball model on the hypercubic lattice for n_f=1/2, ϵ_f=0, as a function of U and electron concentration n_c. Contour lines of constant $X(\mathbf{q})$ are indicated. From Freericks (1993a).

Finally, let us mention that the Falicov-Kimball model has been used by several authors to devise *approximations* to the solution of the $d=\infty$ Hubbard model. The general idea behind these approaches is to treat one of the spin species as moving in the background of the other one, considered frozen and static (Janiš and Vollhardt, 1992a; Li and d'Ambrumenil, 1992; Edwards, 1993; Laad, 1994).

C. Multiband models: Combining LISA and LDA

The models considered up to now in this article are idealized models of strongly correlated electron systems containing a single conduction electron band. In actual materials, one is always faced with the issue of orbital degeneracy. Even in relatively simple systems such as the transition-metal monoxides (e.g., NiO, FeO, etc.), a minimal realistic description must take into account a fivefold d band splitted by crystal field effects into, for example, $d_{x^2-y^2}$, $d_{3z^2-r^2}$, d_{xy}, d_{xz}, d_{yz}, and a threefold oxygen band p_x, p_y, p_z. This also allows a classification of transition-metal oxides into Mott insulators (for $U_{dd} \ll \epsilon_p - \epsilon_d$) and charge-transfer insulators (for $U_{dd} \gg \epsilon_p - \epsilon_d$; see Zaanen, Sawatzky, and Allen, 1985). In this section, we describe how the LISA approach can be used as a dynamical mean-field *approximation* to deal with the band degeneracy and lattice structure of actual materials in a more realistic way. Quantitative calculations along these lines are only starting, but we expect it to be a fruitful direction for further research.

The starting point of any such calculation is the band structure of the material, as obtained e.g., by the LDA method (or some other technique). This zeroth-order starting point provides one with a Hamiltonian

$$H_0 = \sum_{\nu\sigma\mathbf{k}} \epsilon_\nu(\mathbf{k}) c^+_{\mathbf{k}\sigma\nu} c_{\mathbf{k}\sigma\nu} \tag{309}$$

in which ν denotes a band index. Band calculations are an excellent description of many materials, but are well-known to fail to predict correctly the insulating character of oxides such as CoO or FeO because of the neglect of electron-electron interactions. Various schemes have been proposed to include those in the LDA approach (such as the "LDA+U" method of Anisimov, Zaanen, and Andersen, 1991). These schemes do lead to significant improvement, but obviously do not include all the dynamical effects of the interaction. Capturing these effects is the main motivation of the LISA method.

Starting from H_0, the most straightforward way of implementing the LISA method is to use a *tight-binding projection* of the band structure. This consists in projecting the Bloch waves onto a set of orbitals $d_{i\sigma\alpha}$ localized at the sites $\mathbf{R}_i$ of a lattice appropriate to the material considered:

$$c^+_{\mathbf{k}\sigma\nu} = \sum_{i\alpha} e^{i\mathbf{k}\cdot\mathbf{R}_i} A_{\nu\alpha}(\mathbf{k}) d^+_{i\sigma\alpha}. \tag{310}$$

In this formula, the $A_{\nu\alpha}(\mathbf{k}) \equiv \langle \alpha | \nu, \mathbf{k} \rangle$ are the eigenvectors of the single-particle Schrödinger equation and satisfy the closure relations:

$$\sum_{\mathbf{k}\nu} A_{\nu\alpha}(\mathbf{k}) A_{\nu\beta}(\mathbf{k})^* = \delta_{\alpha\beta},$$

$$\sum_{\alpha} A_{\nu\alpha}(\mathbf{k}) A_{\nu'\alpha}(\mathbf{k})^* = \delta_{\nu\nu'}. \tag{311}$$

In terms of the tight-binding orbitals, the free Hamiltonian H_0 takes the form

$$H_0 = \sum_{ij,\sigma} t^{\alpha\beta}_{ij} d^+_{i\sigma\alpha} d_{j\sigma\beta}, \tag{312}$$

in which the hopping amplitudes $t^{\alpha\beta}_{ij}$ reads

$$t^{\alpha\beta}_{ij} = \sum_{\mathbf{k}} e^{i\mathbf{k}\cdot(\mathbf{R}_i - \mathbf{R}_j)} \sum_{\nu} A_{\nu\alpha}(\mathbf{k}) A_{\nu\beta}(\mathbf{k})^* \epsilon_\nu(\mathbf{k}), \tag{313}$$

or, in reciprocal space,

$$t^{\alpha\beta}_{\mathbf{k}} = \sum_{\nu} A_{\nu\alpha}(\mathbf{k}) \epsilon_\nu(\mathbf{k}) A_{\nu\beta}(\mathbf{k})^*. \tag{314}$$

Electron-electron interactions must now be added to H_0. A word of caution is in order here, since the LDA eigenstates $\epsilon_\nu(\mathbf{k})$ already contain some of the effects of these interactions. One of the main difficulties in this context is thus to separate the static terms, taken into account by LDA, from the additional terms, to be treated dynamically, without double counting. Without dealing further with this difficulty, we shall assume that interactions can be introduced in the tight-binding representation in the simplified form of Hubbard type local interactions, and we shall consider the Hamiltonian

$$H = H_0 + \sum_i \sum_{\alpha\beta} U_{\alpha\beta} d^+_{i\uparrow\alpha} d_{i\uparrow\alpha} d^+_{i\downarrow\beta} d_{i\downarrow\beta}. \tag{315}$$

The Hubbard parameters $U_{\alpha\beta}$ can in principle also be calculated in the framework of the LDA. Of course, a more complete description of the interactions should include nonlocal terms coupling different sites, but the treatment of the dynamical effects of such terms requires an extension of the LISA method (cf. Sec. IX).

The LISA method maps this Hamiltonian onto the solution of a self-consistent single-impurity problem. The effective single-site action associated with H reads (restricting ourselves to the paramagnetic phase)

$$S_{\rm eff}=-\int_0^\beta d\tau\int_0^\beta d\tau'\sum_\sigma d^+_{\sigma\alpha}(\tau)[\mathscr{G}_0^{-1}]_{\alpha\beta}(\tau-\tau')d_{\sigma\beta}(\tau') + \sum_{\alpha\beta} U_{\alpha\beta}\int_0^\beta d\tau d^+_{\uparrow\alpha}d_{\uparrow\alpha}d^+_{\downarrow\beta}d_{\downarrow\beta}. \tag{316}$$

In order to obtain the self-consistency equation, we consider the lattice Green's function:

$$G_{\alpha\beta}(\mathbf{k},\tau-\tau')\equiv-\langle Td_{\mathbf{k}\sigma\alpha}(\tau)d^+_{\mathbf{k}\sigma\beta}(\tau')\rangle \tag{317}$$

and postulate a momentum-independent self-energy matrix:

$$G_{\alpha\beta}(\mathbf{k},i\omega_n)^{-1}=(i\omega_n+\mu)\delta_{\alpha\beta}-t^{\alpha\beta}_{\mathbf{k}}-\Sigma_{\alpha\beta}(i\omega_n). \tag{318}$$

The self-consistency condition requires that the local (on-site) Green's function coincides with the impurity model one, with identical self-energies:

$$G_{\alpha\beta}(i\omega_n)_{\rm imp}=\sum_{\mathbf{k}} G_{\alpha\beta}(\mathbf{k},i\omega_n), \tag{319}$$

with

$$G_{\alpha\beta}(\tau-\tau')_{\rm imp}\equiv-\langle Td_{\sigma\alpha}d^+_{\sigma\beta}\rangle_{S_{\rm eff}},$$
$$G_{\alpha\beta}(i\omega_n)^{-1}_{\rm imp}=[\mathscr{G}_0^{-1}]_{\alpha\beta}-\Sigma_{\alpha\beta}. \tag{320}$$

Note that not only the knowledge of the band energies $\epsilon_\nu(\mathbf{k})$ and the associated partial density of states is required to implement this self-consistency condition, but also that of the matrix elements $A_{\nu\alpha}(\mathbf{k})$.

In this general context, the LISA, despite its local character, leads to "renormalized bands" [i.e., quasiparticle poles of $G_{\alpha\beta}(\mathbf{k},i\omega_n)$] that do not have, in general, the same $\mathbf{k}$ dependence as the LDA ones $\epsilon_\nu(\mathbf{k})$, and the self-energy does acquire $\mathbf{k}$ dependence when expressed in the basis of Bloch states:

$$\Sigma_{\nu\nu'}(\mathbf{k},i\omega_n)=\sum_{\alpha\beta} A_{\nu\alpha}(\mathbf{k})^*\Sigma_{\alpha\beta}(i\omega_n)A_{\nu'\beta}(\mathbf{k}). \tag{321}$$

Obviously, the results will depend strongly on the choice of the tight-binding basis onto which the LDA results are projected. As a result, the procedure is expected to apply better to those materials for which a set of well-defined localized orbitals is unambiguously dictated by physical considerations.

In order to illustrate this strategy on a simple concrete example, let us consider the three-band model of the CuO_2 layers in cuprate superconductors (Emery, 1987; Varma, Schmitt-Rink, and Abrahams, 1987). The Hamiltonian involves $d_{x^2-y^2}$ and p_x, p_y orbitals in the hole representation (so that the vacuum corresponds to the Cu^+ configuration). Including correlations only on copper sites as a first step, the Hamiltonian reads

$$H_{3B}=-t_{pd}\sum_{i\sigma} d^+_{i\sigma}(p_{i+x,\sigma}-p_{i-x,\sigma}+p_{i+y,\sigma}-p_{i-y,\sigma}) + 4t_{pp}\sum_{\mathbf{k}\sigma} s_x s_y p^+_{\mathbf{k}x\sigma}p_{\mathbf{k}y\sigma}+\text{H.c.} + \epsilon_p\sum_{i,\sigma}(p^+_{ix\sigma}p_{ix\sigma}+p^+_{iy\sigma}p_{iy\sigma})+\epsilon_d\sum_{i\sigma} d^+_{i\sigma}d_{i\sigma} + U_d\sum_i n^d_{i\uparrow}n^d_{i\downarrow} \tag{322}$$

with $s_{x,y}\equiv\sin(k_{x,y}/2)$. In the LISA method, this model is mapped onto a single-impurity Anderson model associated with copper sites:

$$S_{\rm eff}=U_d\int_0^\beta d\tau\, n_{d\uparrow}(\tau)n_{d\downarrow}(\tau) - \int_0^\beta d\tau\int_0^\beta d\tau'\sum_\sigma d_\sigma(\tau)\mathscr{G}_0^{-1}(\tau-\tau')d^+_\sigma(\tau') \tag{323}$$

and the self-consistency condition requests that the on-site copper Green's function $\Sigma_{\mathbf{k}}G_d(\mathbf{k},i\omega_n)$ coincides with the impurity Green's function. Introducing a momentum-independent copper self-energy $\Sigma_d(i\omega_n)$ and expressing the matrix Green's function in the (d_k, p_{kx}, p_{ky}) basis, this condition reads

$$\sum_{\mathbf{k}}\begin{pmatrix}\zeta_d & i2t_{pd}s_x & -i2t_{pd}s_y\\ -i2t_{pd}s_x & \zeta_p & 4t_{pp}s_xs_y\\ i2t_{pd}s_y & 4t_{pp}s_xs_y & \zeta_p\end{pmatrix}^{-1}_{dd} = G_d(i\omega_n)\equiv[\mathscr{G}_0^{-1}-\Sigma_d]^{-1}, \tag{324}$$

where $\zeta_p\equiv i\omega_n+\mu-\epsilon_p$ and $\zeta_d=i\omega_n+\mu-\epsilon_d-\Sigma_d(i\omega_n)$. This equation takes a much simpler form in the absence of direct oxygen-oxygen hopping $t_{pp}=0$. In this case, the copper and oxygen Green's functions read

$$G_d(\mathbf{k},i\omega_n)=\frac{\zeta_p}{\zeta_p\zeta_d-\gamma_k^2},$$
$$G_{p_x,p_y}(\mathbf{k},i\omega_n)=\frac{\zeta_d\zeta_p-4t_{pd}^2s_{y,x}}{\zeta_p(\zeta_p\zeta_d-\gamma_k^2)} \tag{325}$$

with $\gamma_k^2\equiv4t_{pd}^2(s_x^2+s_y^2)$. Hence the self-consistency condition reads, in this case,

$$G_d(i\omega_n)=\frac{\zeta_p}{2t_{pd}^2}\tilde{D}\left(\frac{\zeta_p\zeta_d}{2t_{pd}^2}-2\right), \tag{326}$$

where $\tilde{D}$ is the Hilbert transform of the square lattice density of states:

$$\tilde{D}(z)=\int\frac{d^2k}{(2\pi)^2}\frac{1}{z-\cos k_x-\cos k_y}. \tag{327}$$

These equations are easily extended to allow for symmetry breaking (e.g., antiferromagnetic or superconducting), along the lines of Sec. V. They can also be extended to include an oxygen-oxygen repulsion U_{pp}. In this case, one has to solve *two* impurity models, one associated with copper sites and the other with oxygen sites. This is because the copper and oxygen orbitals live on two different sublattices in the above Hamiltonian. For the same reason, the dynamical (excitonic) effects of the nearest-neighbor copper-oxygen repulsion (Varma, Schmitt-Rink and Abrahams, 1987) cannot be captured in the single-site LISA description. These effects, which are considered in more detail in the next section (Sec. VIII.D), can only be addressed in the LISA framework for multiband models in which the various orbitals live *on the same lattice sites*. For models such as (322), only an extension of the LISA framework to self-consistent *clusters* (Sec. IX) would be able to capture these effects.

Finally, let us mention that it is possible to construct a model very similar to Eq. (322) which has a well-defined (and nontrivial) $d=\infty$ limit such that the LISA equations become exact (Georges, Kotliar, and Krauth, 1993). The precise geometry of the CuO_2 layer is not suitable for this purpose; moreover, the CuO_d lattice with one oxygen halfway between each copper site reduces to an atomic problem as $d\to\infty$ [cf. Valenti and Gros, 1993; see, however, the recent suggestion of Schmalian *et al.* (1995) for a different scaling of the hopping in this model]. Alternatively, one may consider a simplified model, which is not quite realistic for the cuprates, but has the advantage of having a nontrivial $d=\infty$ limit. The model is simply a two-band CuO lattice involving a correlated "copper" orbital d_σ living on the A sublattice of a bipartite lattice, and an "oxygen" orbital living on the B sublattice. The copper-copper hopping is scaled as $t_{pd}/\sqrt{z}$, and the direct hopping is scaled as t_{pp}/z. In the limit $z\to\infty$, this model can be solved by considering a single-impurity Anderson model on copper sites (when only U_d is included), and the self-consistency condition reads (on the Bethe lattice)

$$\begin{aligned}&\mathcal{G}_0^{-1}(i\omega_n)=i\omega_n+\mu-\epsilon_d-t_{pd}^2G_p(i\omega_n),\\&G_p(i\omega_n)^{-1}=i\omega_n+\mu-\epsilon_p-t_{pd}^2G_d(i\omega_n)-t_{pp}^2G_p(i\omega_n).\end{aligned}\tag{328}$$

Some aspects of this model have been studied by Georges, Kotliar, and Krauth (1993) and Caffarel and Krauth (1994). It displays a metal to charge-transfer insulator transition as a function of $(\epsilon_p-\epsilon_d)/t_{pd}$ for large U_d at half-filling, and a Mott insulator to metal transition as a function of U_d/t_{pd} for large $(\epsilon_p-\epsilon_d)/t_{pd}$. The crossover diagram is very similar to the analysis of Zaanen, Sawatzky, and Allen (1985). Finally, a superconducting instability has been suggested to exist in this model for some range of parameters.

D. The extended Hubbard model and excitonic effects

In this section, we shall review some insights provided by the LISA approach into the physics of excitonic effects, that is, the dynamical effects due to the interband Coulomb interaction. There has recently been a renewed theoretical interest in these effects, with the following motivations.

(i) There is new experimental evidence in favor of Bose condensation of excitons (Lin and Wolfe, 1993; Fortin, Fafard, and Mysyrowicz, 1993) and new experimental tools for studying these effects in strongly illuminated semiconductors. There is a strong need for an approach that can describe simultaneously collective and single particle excitations, and the coherent and incoherent parts of the excitation spectra going beyond the Hartree-Fock approximation (Compte and Nozieres, 1982).

(ii) Interband Coulomb interactions may lead to important physical effects in the context of the LISA description of real materials using multiband models reviewed in the previous section (Sec. VIII.C). For cuprate superconductors for example, the copper-oxygen repulsion has been proposed as playing a crucial role by Varma, Schmitt-Rink, and Abrahams (1987; see also Varma and Giamarchi, 1994, for a review). In the limit of large connectivity z, intersite Coulomb interactions must be scaled as $1/z$, and thus produce only Hartree renormalizations of the band. Hence, excitonic effects must be studied in models where the various orbitals live on the *same* sublattice sites, as done in the present section.

(iii) It has been shown by Si and Kotliar (1993) that the Anderson impurity model, in the weak coupling limit can lead to different type of phases when the position of the impurity level is tuned to the Fermi level. In the lattice (Si, Kotliar, and Georges 1992), this tuning of the impurity level to the Fermi level occurs in a *finite range* of densities when the hybridization renormalizes to zero as in the Falicov-Kimball model (Sec. VIII.B). From this perspective, the interband interaction is a parameter that allows us to vary independently the relevant variables of the local impurity model.

Si and Kotliar (1993) considered a model in which localized ("copper") orbitals d_σ and itinerant ("oxygen") orbitals p_σ live on the *same* lattice sites. The motivation is to retain the dynamical effects of the copper-oxygen repulsion and a nontrivial off-diagonal self-energy Σ_{pd}. The Hamiltonian of the model is in the same general class as Eq. (315) and reads

$$\begin{aligned}H=&\sum_{\mathbf{k}}\sum_{\sigma=1}^{N}(\epsilon_{\mathbf{k}}-\mu)p_{\mathbf{k}\sigma}^{+}p_{\mathbf{k}\sigma}+\sum_i\sum_{\sigma=1}^{N}(\epsilon_d^0-\mu)d_{i\sigma}^{+}d_{i\sigma}\\&+\frac{U}{2}\sum_i\sum_{\sigma\neq\sigma'}^{N}d_{i\sigma}^{+}d_{i\sigma}d_{i\sigma'}^{+}d_{i\sigma'}\\&+\sum_i\sum_{\sigma=1}^{N}t(d_{i\sigma}^{+}p_{i\sigma}+\text{H.c.})\\&+\frac{V_1}{N}\sum_i\sum_{\sigma,\sigma'=1}^{N}p_{i\sigma}^{+}p_{i\sigma}d_{i\sigma'}^{+}d_{i\sigma'}\\&+\frac{V_2}{N}\sum_i\sum_{\sigma,\sigma'=1}^{N}p_{i\sigma}^{+}p_{i\sigma'}d_{i\sigma'}^{+}d_{i\sigma}.\end{aligned}\tag{329}$$

The itinerant electrons have dispersion $\epsilon_{\mathbf{k}}$, while the localized electrons electrons have an energy level ϵ_d^o, and an on-site Coulomb interaction U which is taken to be infinity. These two species of electrons are coupled, at every site, through a hybridization t, a density density interaction V_1/N, and a Kondo-exchange interaction V_2/N. For generality, an arbitrary spin degeneracy N is considered, which will also allow us to make contact with results from large-N expansion. In the spinless case (N=1) this model reduces to a generalized Falicov-Kimball model that includes, besides the usual interaction V_1, a hybridization term. In the spin-1/2 case (N=2) it is a version of the extended Hubbard model first studied in the context of the mixed valence problem (Varma, 1976; Khomskii, 1979).

The **k**-dependent lattice Green's functions are given by

$$G_d(\mathbf{k},i\omega_n)^{-1}=i\omega_n+\mu-\epsilon_d^o-\Sigma_{dd}(i\omega_n)-\frac{(t-\Sigma_{pd})^2}{i\omega_n+\mu-\epsilon_{\mathbf{k}}-\Sigma_{pp}}, \tag{330}$$

$$G_p(\mathbf{k},i\omega_n)^{-1}=i\omega_n+\mu-\epsilon_{\mathbf{k}}-\Sigma_{pp}(i\omega_n)-\frac{(t-\Sigma_{pd})^2}{i\omega_n+\mu-\epsilon_d^o-\Sigma_{dd}}. \tag{331}$$

In which the Σ's are the components of the (matrix) self-energy in the p_i, d_i basis.

The single-site effective action associated with this Hamiltonian in the LISA framework reads

$$S_{\text{eff}}=-\int_0^\beta d\tau\int_0^\beta d\tau'\,\psi^+(\tau)\mathscr{G}_0^{-1}(\tau-\tau')\psi(\tau')+\int_0^\beta d\tau\left(\frac{V_1}{N}\sum_{\sigma,\sigma'}p_\sigma^+p_\sigma d_{\sigma'}^+d_{\sigma'}+\frac{V_2}{N}\sum_{\sigma,\sigma'}p_\sigma^+p_{\sigma'}d_{\sigma'}^+d_\sigma+\frac{U}{2}\sum_{\sigma\neq\sigma'}d_\sigma^+d_\sigma d_{\sigma'}^+d_{\sigma'}\right), \tag{332}$$

where $\psi^+=(p^+,d^+)$. The Weiss function $\mathscr{G}_0^{-1}$ is a 2×2 matrix in this context. The self-consistency equation reads

$$\int_{-\infty}^{\infty}d\epsilon\;D(\epsilon)\begin{pmatrix}i\omega_n+\mu-\epsilon-\Sigma_{pp}^{\text{imp}} & t-\Sigma_{pd}^{\text{imp}}\\ t-\Sigma_{dp}^{\text{imp}} & i\omega_n+\mu-\epsilon_d^o-\Sigma_{dd}^{\text{imp}}\end{pmatrix}^{-1}=\begin{pmatrix}(\mathscr{G}_0^{-1})_{pp}-\Sigma_{pp}^{\text{imp}} & (\mathscr{G}_0^{-1})_{pd}-\Sigma_{pd}^{\text{imp}}\\ (\mathscr{G}_0^{-1})_{dp}-\Sigma_{dp}^{\text{imp}} & (\mathscr{G}_0^{-1})_{dd}-\Sigma_{dd}^{\text{imp}}\end{pmatrix}. \tag{333}$$

This set of equations has been investigated in detail by Si and Kotliar (1993) in the case of a Lorentzian density of states of the conduction electrons (for which the self-consistency condition becomes trivial, cf. Sec. II). The spinless version has also been studied on the Bethe lattice (Si *et al.*, 1994). The central result obtained by these authors is that this model has three different phases with unbroken translational symmetry corresponding to different regions of densities and coupling constants: the ordinary Fermi-liquid phase, a weak-coupling non-Fermi-liquid phase, and an "intermediate phase" exhibiting the phenomena of charge and spin separation.

Since the techniques used in the derivation of these results are most naturally formulated in the language of the generalized Anderson impurity model and since these techniques are likely to be useful in the analysis of more general models, we review the most relevant points of the analysis below.

The impurity model is first written in Hamiltonian form. The generalized Anderson impurity Hamiltonian describes *three* local states coupled to an electron bath with a smooth density of states:

$$H=\sum_{l\sigma}(\tilde{\epsilon}_l-\mu)a_{l\sigma}^+a_{l\sigma}+E_d^od_\sigma^+d_\sigma+\frac{U}{2}\sum_{\sigma\neq\sigma'}d_\sigma^+d_\sigma d_{\sigma'}^+d_{\sigma'}+\sum_\sigma t(d_\sigma^+a_{l\sigma}+\text{H.c.})+V_1\sum_{\sigma\sigma' l}d_\sigma^+d_\sigma a_{l\sigma'}^+a_{l\sigma'}+\frac{V_2}{4}\sum_{\sigma_1,\sigma_{2l},\sigma_3,\sigma_4}\vec{\tau}_{\sigma_1\sigma_2}\cdot\vec{\tau}_{\sigma_3\sigma_4}d_{\sigma_1}^+d_{\sigma_2}a_{l\sigma_3}^+a_{l\sigma_4}, \tag{334}$$

where $\vec{\tau}$ denotes the Pauli matrices. The impurity fluctuates between a singlet and a spin doublet $|\sigma\rangle=d_\sigma^+|0\rangle$ with $E_\sigma=E_d^o$. An infinite on-site interaction, $U=\infty$, is introduced to enforce the three-dimensional *restricted* configuration space. The hybridization t, the density-density interaction V_1, and the spin-exchange interaction V_2 describe the generic couplings between the local states and the electron bath. $\tilde{\epsilon}_l$ describes the dispersion of the electrons in the bath.

We envision calculating N-point correlation functions of Hubbard operators $X_{\alpha,\beta}$ at N values of imaginary time, as a Feynman sum over trajectories in local configuration space. The insertion of Hubbard operators forces the system to be at a certain configuration or to flip configurations at given values of imaginary time. The amplitude for this process is the sum over all trajectories consistent with these constraints. The weight of each trajectory depends of course on the reaction of the electrons in the neighboring sites to a given local trajectory (Haldane, 1978b; Si and Kotliar, 1993). The partition function has the form

$$\frac{Z}{Z_0}=\sum_{n=0}^{\infty}\sum_{\alpha_1,\ldots,\alpha_n}\exp(-S[\tau_1,\ldots,\tau_n]), \tag{335}$$

where

$$S[\tau_1,\ldots,\tau_n]=\sum_{i<j}[K(\alpha_i,\alpha_j)+K(\alpha_{i+1},\alpha_{j+1})-K(\alpha_i,\alpha_{j+1})-K(\alpha_{i+1},\alpha_j)]\ln\frac{\tau_j-\tau_i}{\xi_o}-\sum_i\ln(y_{\alpha_i\alpha_{i+1}})+\sum_i h_{\alpha_{i+1}}\frac{\tau_{i+1}-\tau_i}{\xi_o}. \tag{336}$$

In this expression, τ_i, for $i=1,\ldots,n$, labels the hopping events from local states $|\alpha_i\rangle$ to $|\alpha_{i+1}\rangle$, and ξ_o is the ultraviolet inverse energy cutoff. $K(\alpha,\beta)$ are stiffness constants affecting each transition between states, and the fugacities $y_{\alpha,\beta}$ are the *bare* amplitudes for quantum mechanical hopping between the configuration α and β. These quantities play an essential role in determining the long-time, low-energy behavior of this system. The charge fugacity is given by the hybridization $y_{0,\sigma}=y_t=t\xi$, and the spin fugacity corresponds to the transverse component of the Kondo exchange $y_{\sigma\neq\sigma'}=y_j=(V_2^{\perp}/2)\xi$. The fields h_α describe the energy splitting among the local configurations. They have to be introduced since generically there is no symmetry between the local many-body configurations. In our three-state problem, there exists a spin rotational symmetry but not a symmetry between spin and charge. Therefore, we introduce a field related to the d level E_d, i.e., $h_0=-\frac{2}{3}E_d\xi$ and $h_\sigma=\frac{1}{3}E_d\xi$.

The logarithmic interaction in the action (336) can be written as a spin model with long-range $1/\tau^2$ interaction:

$$\sum_{i<j} K(\alpha_i,\alpha_j)\left(\frac{\xi_0}{\tau_i-\tau_j}\right)^2.$$

This allows an extension of Cardy's renormalization-group analysis (Cardy, 1981; Chakravarty and Hirsch, 1982) to this problem (Si and Kotliar, 1993). The bare values of the stiffness constants $K(\alpha,\beta)$ provide the initial conditions of the renormalization group flow.

The renormalization group allows for a precise description of the possible low-energy behavior of this system. If the amplitude for making transitions between all states increases at long distance, the system is a Fermi liquid. If the amplitude for making transitions between states with different charge renormalizes to zero, non-Fermi liquid behavior results. Depending on the behavior of the spin degrees of freedom one can obtain a weak coupling phase where the amplitudes for making quantum mechanical transitions between different states *all* renormalize to zero, and an intermediate phase where the spin degrees of freedom are coherent but where the charge degrees of freedom cannot tunnel quantum mechanically.

The basin of attraction of the different phases can be expressed approximately in terms of the bare interactions via the combinations:

$$-K(0,\sigma)=\epsilon_t^o=\frac{1}{2}\left[\left(1-\frac{\delta_2}{\pi}-\frac{\delta_1}{\pi}\right)^2+\left(\frac{\delta_1}{\pi}-\frac{\delta_2}{\pi}\right)^2\right],$$

$$-K(\sigma\neq\sigma')=\epsilon_j^o=\left(1-2\frac{\delta_2}{\pi}\right)^2, \tag{337}$$

where the phase shifts are $\delta_1=\tan^{-1}(\pi\rho_o V_1)$ and $\delta_2=\tan^{-1}(\pi\rho_o V_2/4)$, with ρ_o the conduction electron density of states at the Fermi level. The intermediate phase occurs for $\epsilon_t>1$ and $\epsilon_j>1$. A qualitative behavior of various correlators in this phase was presented by Si and Kotliar (1993), but a quantitative computation of the exponents governing the various correlation functions has not been carried out, except for the case of an exactly solvable Toulouse point (Kotliar and Si, 1995).

Much more is known about the weak coupling (mixed valence) regime. The correlation functions at low frequencies have a *regular perturbation expansion* in the running fugacities, $t^*=t(\omega/\Gamma)^{\epsilon_t^*}$, and $(V_2^{\perp})^*=V_2^{\perp}(\omega/\Gamma)^{\epsilon_j^*}$. This allows one to calculate the one-particle local Green's functions. G_{cc} is not renormalized by the fugacities since the c electron does not create a kink. On the other hand, $G_{dc}(\omega)\sim\omega^{-1+\alpha}$ and $G_{dd}(\omega)\sim\omega^{-1+\beta}$ at low frequencies. Here the exponents are given, to leading order, by $\alpha=-(\delta_1^*+\delta_2^*)/\pi+[(\delta_1^*+\delta_2^*)/\pi]^2+(\delta_1^*/\pi)^2$ and $\beta=[(\delta_1^*+\delta_2^*)/\pi]^2+(\delta_1^*/\pi)^2$. Starred expressions indicate that the coupling constants have to be evaluated at their fixed point value. The multiparticle correlation functions show power-law behavior. For example,

$$\langle d_\sigma^+ d_{\sigma'}(\tau) d_{\sigma'}^+ d_\sigma(0)\rangle\sim(\tau)^{-\alpha_1},$$

$$\langle d_\sigma^+ c_{\sigma'}(\tau) c_{\sigma'}^+ d_\sigma(0)\rangle\sim(\tau)^{-\alpha_2},$$

$$\langle d_\sigma^+ c_{\sigma'}^+(\tau) c_{\sigma'} d_\sigma(0)\rangle\sim(\tau)^{-\alpha_3}, \tag{338}$$

where, to leading order, $\alpha_1=2\epsilon_j^*(1-\delta_{\sigma,\sigma'})$, $\alpha_2=2\epsilon_t^*\delta_{\sigma,\sigma'}+2\epsilon_{tj}^*(1-\delta_{\sigma,\sigma'})$, and $\alpha_3=2\epsilon_t^*(-\delta_1^*/\pi,-\delta_2^*/\pi)\delta_{\sigma,\sigma'}+2\epsilon_{tj}^*(-\delta_1^*/\pi,-\delta_2^*/\pi)(1-\delta_{\sigma,\sigma'})$. Here, $\epsilon_{tj}^*(\delta_1^*/\pi,\delta_2^*/\pi)=\frac{1}{2}[(1-\delta_1^*/\pi)^2+(\delta_1^*/\pi+\delta_2^*/\pi)^2]$. Therefore, the d^+c^+ superconducting correlation function is divergent, while the excitonic and d-electron correlation functions vanish.

It is interesting to point out that these results are not very different qualitatively from what is found in one dimension. There, a system at zero temperature is a Luttinger liquid (the one-dimensional version of a Fermi liquid) when the interactions are sufficiently repulsive, or a charge density wave or superconductor when the interactions are attractive.

The stability of the non-Fermi-liquid phases relies on the degree of "charge frustration" of the lattice, just as the stability of the Mott insulating phase depended on the degree of magnetic frustration.

While the non-Fermi-liquid regimes occurred for negative values of the charge-charge interactions when the density of states is Lorentzian, it has been argued (Kotliar and Si, 1993) that for realistic density of states these phases could occur for *repulsive values of the Coulomb interactions*. In this view, the generalized Anderson impurity model emerges as a result of a projective self-consistent reduction of a realistic model to low energy.

We stress that the wide variety of behaviors found even in the simplest Lorentzian case is indicative of the power and breadth of the LISA approach. More detailed investigations of this model are clearly needed.

E. Electron-phonon coupling and the Holstein model

In this section, we briefly review recent investigations of the electron-phonon problem in the LISA ($d=\infty$) framework. The attention is focused on the Holstein

model of Einstein phonons coupled to electrons through a local interaction (Holstein, 1959). The Hamiltonian reads

$$H=-\sum_{\langle ij\rangle,\sigma} t_{ij}(c_{i\sigma}^{+}c_{j\sigma}+\text{H.c.})+g\sum_i x_i(n_{i\uparrow}+n_{i\downarrow}) + \frac{1}{2}\sum_i (p_i^2+\Omega^2 x_i^2), \tag{339}$$

where x_i is the phonon coordinate and p_i the phonon momentum at site i. g is the electron-phonon coupling constant, and Ω the phonon frequency. For simplicity, the phonon mass has been normalized to $M=1$, so that the spring constant is $\kappa=\Omega^2$.

It is sometimes useful to think of the phonon bath in this problem as inducing an effective *retarded* interaction between the electrons. Integrating out the phonons, this interaction takes the form

$$\sum_i \int_0^\beta d\tau \int_0^\beta d\tau' n_i(\tau) U_{\text{eff}}(\tau-\tau') n_i(\tau'), \tag{340}$$

in which $n_i=n_{i\uparrow}+n_{i\downarrow}$ and the Fourier transform of $U_{\text{eff}}(\tau-\tau')$ reads

$$U_{\text{eff}}(i\omega)=-\frac{g^2}{2}\frac{1}{\Omega^2+\omega^2}. \tag{341}$$

The time-scale associated with the retarded character of this interaction is $1/\Omega$. It has to be compared to the characteristic time-scale for electronic motions, which is set by the conduction electron bandwidth, of order t (with a hopping scaled as $t_{ij}\propto t/\sqrt{d}$). Two regimes can be distinguished.

(i) For $\Omega\gg t$, the phonons react instantaneously and the effective interaction is no longer retarded. From (341), we see that the model maps onto an *attractive* Hubbard model, with an interaction strength:

$$U=-\frac{g^2}{\Omega^2}=2\lim_{\omega\to 0} U_{\text{eff}}(\omega). \tag{342}$$

U is the energy scale for the binding of electrons into local pairs, which occurs when U/t is large (bipolaron binding energy). For a general review of the physics of systems with local instantaneous pairing and of the negative-U Hubbard model, the reader is directed to the article of Micnas, Ranninger, and Robaszkiewicz (1990), and references therein.

(ii) In the opposite (adiabatic) limit of $\Omega\ll t$, the phonons become completely static, and the effective electron-electron interaction becomes independent of time: $U_{\text{eff}}(\tau-\tau')=U$. In that limit, the conduction electrons interact with a localized continuous degree of freedom having no dynamics and entering only through annealed averages. As a result, a mapping onto an attractive Falicov-Kimball model (generalized to many states) can be established (Freericks, Jarrell, and Scalapino, 1993).

It is convenient to use the dimensionless ratios U/t and Ω/t as the control parameters of this model, together with the total electron density n. One of the important questions is the existence of phases with long-range order at low temperature. Obvious candidates are charge density wave (CDW) ordering (commensurate or incommensurate) and superconducting order, which compete with each other. Exactly at half-filling ($n=1$) and in the instantaneous limit $\Omega\gg t$, an additional SU(2) pseudospin symmetry relates the commensurate CDW state and the superconducting state, so that they cannot be distinguished. From the extreme limits described above, one expects that superconducting order is favored for large values of Ω/t and sufficiently away from half-filling, while CDW order is favored for small Ω/t and close to half-filling. Competition of CDW and superconducting ordering is a physically relevant issue for compounds such as $Ba_{1-x}K_xBiO_3$, which has a CDW commensurate phase for $x=0$ and becomes superconducting for $x>0.35$ (Cava *et al.*, 1988; Pei *et al.*, 1990).

The LISA method maps the Holstein model onto the solution of a self-consistent single-impurity problem, supplemented by a self-consistency condition. In a phase without long-range order, the single-site effective action is easily obtained following the methods of Secs. II and III, and reads (Freericks, Jarrell, and Scalapino, 1993, 1994):

$$S_{\text{eff}}=-\int_0^\beta d\tau\int_0^\beta d\tau'\sum_\sigma c_\sigma^{+}(\tau)\mathcal{G}_0^{-1}(\tau-\tau')c_\sigma(\tau') + \frac{1}{2}\int_0^\beta d\tau[\dot{x}^2+\Omega^2x^2] + g\int_0^\beta d\tau\, x(\tau)\sum_\sigma c_\sigma^{+}(\tau)c_\sigma(\tau). \tag{343}$$

Denoting by $G(\tau-\tau')\equiv-\langle Tc(\tau)c^{+}(\tau')\rangle$ the conduction electron Green's function associated with this effective action, and defining a self-energy from $\Sigma=\mathcal{G}_0^{-1}-G^{-1}$, the self-consistency condition takes the usual form:

$$G(i\omega_n)=\tilde{D}(i\omega_n+\mu-\Sigma(i\omega_n)) \tag{344}$$

in which $\tilde{D}$ is the Hilbert transform of the noninteracting electronic density of states. Generalizations of these equations to phases with long-range order are easily derived along the lines of Sec. V and the various momentum-dependent response functions (e.g., χ^{CDW}, χ^{SC}) can be related to the impurity model response functions following the lines of Sec. IV. This impurity model is a generalization of the single-impurity Anderson model to a retarded electron-electron interaction (after integrating out the bosonic field). It coincides with the *negative U* Anderson model in the instantaneous limit $\Omega\to\infty$.

The QMC method described in Sec. VI has been adapted to the solution of the LISA equations for the Holstein model by Freericks, Jarrell, and Scalapino (1993, 1994). This numerical approach is especially useful in order to investigate the physics of this model in the difficult region of intermediate coupling. Far from this region, analytical techniques have been used to investigate the weak- and strong-coupling regimes, which will be briefly reviewed below.

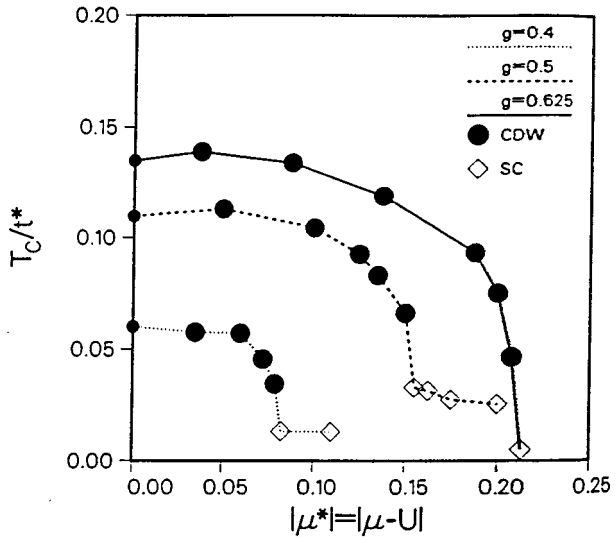

FIG. 77. Phase diagram of the Holstein model on the hypercubic lattice ($t_{ij}=t_*/2\sqrt{d}$) with $\Omega/t_*=0.5$ and three different coupling strengths (g=0.4,0.5,0.625). The solid dots are the QMC results for the commensurate CDW transition, and the open diamonds are for the superconducting transition. From Freericks, Jarrell, and Scalapino (1993).

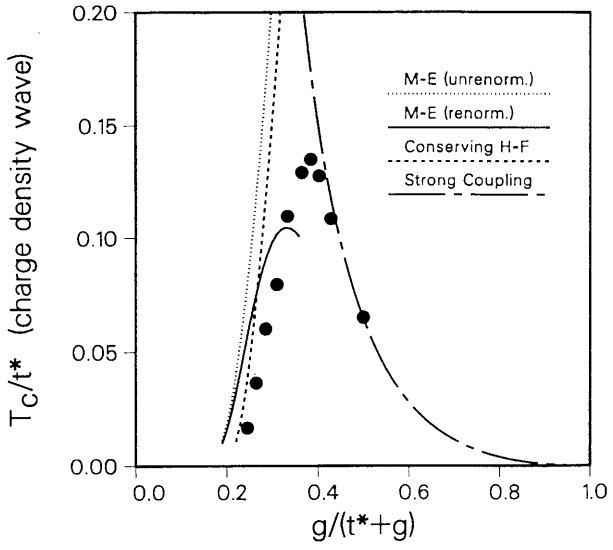

FIG. 78. The critical temperature for CDW ordering in the half-filled Hubbard model vs coupling g. The QMC results (dots) are compared to various approximations. From Freericks, Jarrell, and Scalapino (1993).

The phase diagram resulting from these studies has the form displayed in Fig. 77, as a function of temperature and electron density, for various coupling strengths. (The weak-coupling phase diagram obtained by Ciuchi *et al.* (1993) is qualitatively similar.) Note that this phase diagram has been established by looking for instabilities signalled by the divergence of two-particle response functions, and that in principle it should be supplemented by a calculation of free-energies, in order to check whether first-order transitions intervene. Close to half-filling, the system orders into a commensurate CDW phase below $T_c^{\mathrm{CDW}}(n)$. This critical temperature is maximum at half-filling (n=1), and decreases monotonically when n is decreased. In weak-coupling and for small phonon frequency, Ciuchi *et al.* (1993) demonstrated that a narrow range of densities exists at which the CDW becomes *incommensurate*. In contrast, in the QMC study of Freericks, Jarrell, and Scalapino (1993, 1994) at intermediate phonon frequency, no incommensurate order was reported. For still lower densities $n<n_c$, the ordering is into a superconducting phase. The critical density $n_c(|U|,\Omega)$ is a decreasing function of the coupling strength $|U|$, and an increasing function of the phonon frequency Ω. For a Gaussian density of states with $t_{ij}=t/2\sqrt{d}$, the maximum value of T_c^{CDW} was found to be of order $0.15t$ (independently of phonon frequency) while the maximum T_c^{SC} was found to strongly depend on frequency, and is always smaller than the maximum value of T_c^{CDW}. T_c^{CDW} ($|U|, n$=1) is small for both small and large $|U|$, with a maximum in between (Fig. 78).

Freericks, Jarrell, and Scalapino (1993, 1994) also considered the effective phonon potential $V_{\mathrm{eff}}(x)$ resulting from the average over conduction electron degrees of freedom. This is easily computed in the QMC method from the probability distribution of the phonon coordinate: $P(x)\propto e^{-\beta V_{\mathrm{eff}}(x)}$. $V_{\mathrm{eff}}(x)$ is depicted in Fig. 79 for the half-filled case and various values of the coupling strength $|U|$. Interestingly, the effective potential changes from a harmonic form in weak coupling to a strongly anharmonic double-well form in strong-coupling. In the anharmonic region, the system can be considered as a random mixture of empty sites and bi-

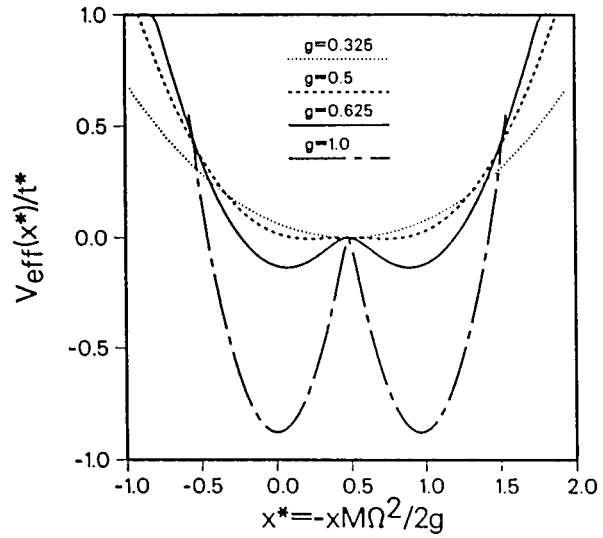

FIG. 79. Effective phonon potential for the half-filled Holstein model with $\Omega/t_*=0.5$ and $\beta t_*=7$ plotted vs the normalized coordinate $x^*=-xM\Omega^2/2g$. Four different values of g are displayed: g=0.325 (dotted line), g=0.5 (dashed line), g=0.625 (solid line), g=1.0 (dashed-dotted line). From Freericks, Jarrell, and Scalapino (1993, 1994).

polarons that fluctuates in time. Tunneling through the barrier induces correlations between these two states. The maximum value of T_c^{CDW} ($|U|$, $n=1$) is reached when the barrier height is of the order of T_c itself. These results are qualitatively similar to the findings of Yu and Anderson (1984).

These numerical results can be substantiated and compared to various analytic approximation schemes for weak and strong coupling:

(i) In the weak-coupling regime $|U| \ll t$, explicit expressions can be obtained for the various response functions, and the CDW and superconducting transition temperatures can be derived in closed form (Ciuchi *et al.*, 1993; Freericks and Scalapino, 1994; Freericks, 1994; Freericks and Jarrell, 1994a). Technically, the simplifications of perturbation theory arising in the $d \to \infty$ limit and explained in Sec. III.B allow one to perform these weak-coupling expansions without resorting to additional approximations such as the neglecting of vertex corrections. Because of the Migdal theorem, these vertex corrections are small in the adiabatic limit $\Omega/t \ll 1$, but become important in the opposite (instantaneous) limit, as studied in detail in the above references. The weak-coupling phase diagram (Ciuchi *et al.*, 1993) displays all the features of the generic case described above. Recently, various schemes attempting to extend these perturbative methods beyond the weak-coupling regime have been studied in great detail for the $d=\infty$ Holstein model, and compared to each other and to numerical results (Freericks *et al.*, 1993; Freericks, 1994). These schemes include various types of conserving approximations, the Migdal-Eliashberg approximation (valid for $\Omega/t \ll 1$), and the (nonconserving) iterated perturbation theory scheme of Sec. VI.B.2, and modified versions of it (Freericks and Jarrell, 1994a). The conclusion of these studies is that the iterated perturbation theory approximation is superior to both second-order conserving schemes and the Migdal-Eliashberg theory for estimating the self-energy and the vertex functions, but that none of these approximate methods is accurate for a wide range of values of $|U|/t$ and Ω/t. The iterated perturbation theory approximation turned out to be very accurate in predicting the CDW transition temperature at half-filling and the SC transition temperature in the doped case, because of accidental cancellations between self-energy and vertex higher-order corrections.

(ii) In the strong-coupling regime $|U| \gg t$, the electrons pair into bipolarons (see Micnas, Ranninger, and Robaszkiewicz, 1990). In this limit, degenerate perturbation theory in the hopping t can be used to map the Holstein model onto an anisotropic Heisenberg antiferromagnet in a uniform external field (Beni, Pincus, and Kanamori, 1974; Hirsch and Fradkin, 1982, 1983). This expansion was pushed to fourth order by Freericks (1993c). This introduces a four-spin coupling and frustration in the effective Hamiltonian. The method was applied in the $d=\infty$ limit (in which the effective spin model can be treated within mean-field theory) in order to find explicit formulas for T_c^{CDW}/t and T_c^{SC}/t valid to order $(t/|U|)^3$, which were successfully compared to the QMC results. In particular these formula correctly indicate the existence of a maximum in T_c vs U.

Recently, Freericks and Jarrell (1995b) considered the effect of an additional Coulomb repulsion $+U_c \Sigma_i n_{i\uparrow} n_{i\downarrow}$ in the Holstein Hamiltonian. They concentrated on the case of a small to moderate value of U_c in comparison to $|U|$, and found that both (incommensurate) CDW phases and the superconducting phase are stabilized by the Coulomb repulsion. However, surprisingly, the commensurate CDW transition temperature is more robust than the superconducting one.

In contrast to these rather detailed studies of the Holstein model phase diagram, comparatively little is known about the properties of the *paramagnetic normal state* above the superconducting and CDW ordering temperatures. Among the various physical issues is the crossover between a normal Fermi liquid at weak coupling to a normal state with a large number of preformed local pairs (bipolarons) at strong-coupling (see, e.g., Nozieres and Schmitt-Rink, 1985; Randeria, Duan, and Shieh, 1989, 1990). These local pairs form much above the superconducting transition temperature, and should substantially affect Fermi-liquid properties (see, e.g., Randeria *et al.*, 1992). The LISA framework seems very well adapted to address these issues in the future.

A recent work somewhat related to these issues is due to Ciuchi, de Pasquale, and Feinberg (1995), who considered the problem of a *single electron* coupled to Einstein phonons in the $d \to \infty$ limit. Even though the single-electron problem is not directly related to the finite-density one, it does clarify the structure of the collective entity formed by the electron dressed by the phonon bath (small polaron problem). Ciuchi, de Pasquale, and Feinberg were able to find an exact solution of the impurity effective action (343) under the assumption that a single particle is present in the conduction electron effective bath, in the form of a continuous fraction representation of the electron Green's function. Their results for the single-electron spectral density and self-energy are depicted in Fig. 80 for increasing coupling strengths. A polaron quasiparticle resonance (with infinite lifetime $\mathrm{Im}\Sigma=0$) splits out of the continuum above a critical coupling. The effective mass of the polaron state was also calculated in the work of Ciuchi, de Pasquale, and Feinberg (1995), providing an interpolation between the known weak-coupling and strong-coupling results (in the latter case, the polaron mass enhancement is of order $e^{|U|/\Omega}$).

F. Colossal magnetoresistance and doped manganates

Perovskite-type manganese oxides $La_{1-x}A_xMnO_3$, where A is in the second column of the periodic table (Ba, Sr) are being studied intensively. From the point of view of fundamental physics, this system offers another material where the strength of the electron-electron interaction and the carrier concentration can be varied continuously (Tokura *et al.*, 1994; Hwang *et al.*, 1995).

From the point of view of technological applications, the goal is to exploit the "colossal (negative) magnetore-

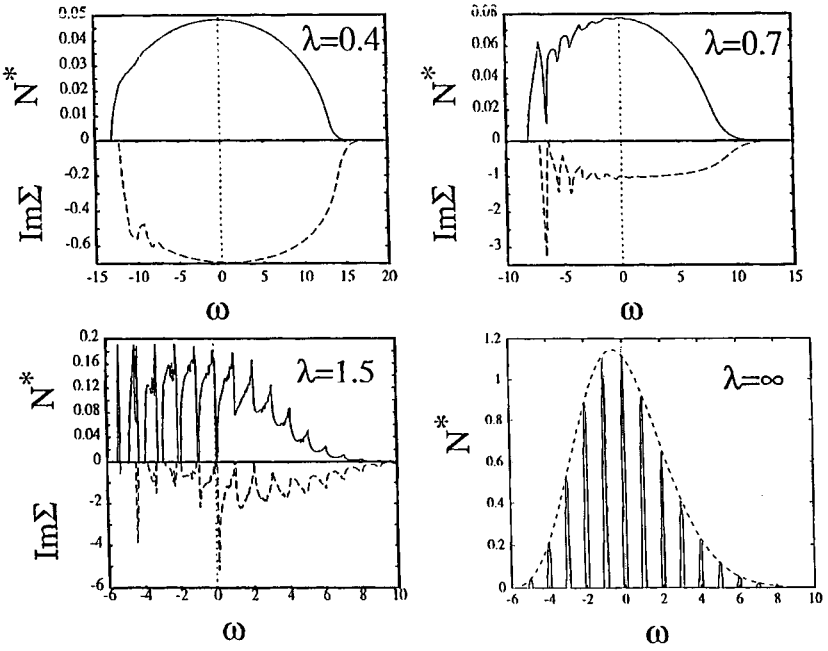

FIG. 80. Spectral density and inverse lifetime (ImΣ) for a single electron in the Holstein model, at different values of the coupling $\lambda = g^2/(M\Omega^2 t_*) = |U|/t_*$, for fixed $g^2/M\Omega^3 = 5$. From Ciuchi, de Pasquale, and Feinberg (1995).

sistance" phenomenon (von Helmholt *et al.*, 1993; Jin *et al.*, 1994): a drop in resistivity when a magnetic field is applied, which, in a certain region of temperature and concentration, is larger by orders of magnitude than in previously known systems. The goal of this section is not to provide an introduction to this rapidly developing field (for recent discussions and references on this problem, see, e.g., Millis, Littlewood, and Shraiman, 1995), but to point out several recent applications of the LISA dynamical mean-field approach to this problem, and to indicate open questions.

Several aspects of the physics of these materials are well understood. The electronically active orbitals are the Mn d orbitals, and the mean number of d electrons per Mn is $4-x$. The cubic crystal field splitting and Hund's rule coupling are sufficiently large that three electrons go into tightly bound d_{xy}, d_{yz}, d_{xz} core states and couple to form an $S=3/2$ spin. The remaining $(1-x)$ electrons go into a band of width ~ 2.5 eV made mostly of the outer-shell $d_{x^2-y^2}$ and $d_{3z^2-r^2}$ orbitals. The outer shell electrons are aligned to the core states by a Hund's Rule coupling J_H which is believed to be large. The large value of J_H means that the hopping of an outer-shell electron between two Mn sites is affected by the relative alignment of the core spins, being maximal when the core spins are parallel and minimum when they are antiparallel. This phenomenon, called "double exchange," is believed to play a significant role in this material.

It is also known (Kanamori, 1959; Goodenough, 1968; Kuggel and Khomski, 1973, 1982) that the conduction electrons in $LaMnO_3$ have a twofold orbital degeneracy. In this case, spin and orbital correlations are very important. In addition to the possibility of spontaneous orbital ordering, Kuggel and Khomski have reviewed the resulting Jahn-Teller electron phonon coupling which accompanies the orbital degeneracy. In fact the cubic-tetragonal phase transition observed for $0 \lesssim x \lesssim 0.2$ is known to be due to a frozen-in Jahn-Teller distortion with long-range order.

As a function of doping, this compound displays a rich variety of physical phenomena. Its ground-state varies from being an antiferromagnetic Mott insulator, to a ferromagnetic metal, to a charge ordered state (Urushibara *et al.*, 1995). Disorder can also play an important role in the optimization of the physical properties of this compound.

A model Hamiltonian can be written to describe this compound: $H = H_0 + H_{J-T} + H_{\rm Hub}$ with

$$H_0 = -\sum_{ij\alpha} t_{ij}^{ab} d_{ia\alpha}^+ d_{jb\alpha} - J_H \sum_{i,a,\alpha} \vec{S}_c^i \cdot d_{ia\alpha}^+ \vec{\sigma} d_{ia\alpha} + \sum_i \vec{h} \cdot \vec{S}_i , \tag{345}$$

$$H_{J-T} = g \sum_{ja\sigma} d_{ja\sigma}^+ Q^{ab}(j) d_{jb\sigma} + k \sum_j [Q^2(j) + \Pi(j)^2/2kM], \tag{346}$$

and

$$H_{\rm Hub} = (U+2J) \sum_{i,a} n_{ia\uparrow} n_{ia\downarrow} + U \sum_{i,a\neq b} n_{ia\uparrow} n_{ib\downarrow} + \frac{U-J}{2} \sum_{i,a\neq b\sigma} n_{ia\sigma} n_{ib\sigma} . \tag{347}$$

In Eq. (345) $d_{ia\sigma}$ creates an outer-shell d electron of spin σ in the a orbital on site i, and $n_{ia\sigma} = d_{ia\sigma}^+ d_{ia\sigma}$. The local lattice distortions that cause the Jahn-Teller splitting transform as a twofold degenerate representation of the cubic group, which couples to the electrons as a

traceless symmetric matrix (Millis, Shraiman, and Mueller, 1995): $Q=r[\cos(\phi)\tau_z+\sin(\phi)\tau_x]$. In Eq. (346), g is the electron-phonon coupling, k the phonon stiffness, and Π is the momentum canonically conjugate to Q. The external magnetic field is $\vec{h}$; for simplicity we have coupled it to the local spin, and a more sophisticated model should include its coupling to the orbital and spin degrees of freedom of the conduction band as well. The parent compound is an antiferromagnetically ordered Mott insulator. Equation (347) describes a minimal model of the electron-electron interactions, containing two orbitals, and neglecting spin-flip terms (Cyrot and Lyon-Caen, 1975). For further discussion of spin-rotational invariance, see, e.g., Dworin and Narath (1970).

The LISA framework is very promising for dealing with this Hamiltonian, asserting the relative importance of the various terms, and contributing to the understanding of these compounds. Several studies using this framework have already appeared, and we summarize the main results below. In a nice series of papers, Furukawa (1994, 1995a, 1995b, 1995c) investigated the double exchange model (ferromagnetic Kondo lattice)—Eq. (345)—with the local spins treated in the classical approximation ($S_c\to\infty$). In this limit, the model is very similar to the Falicov-Kimball model, and many results can be obtained analytically. Furukawa was able to account qualitatively for the strong dependence of the dc conductivity on magnetic field and temperature, for the anomalous temperature dependence of the optical conductivity, and for the doping dependence of the Curie temperature.

Millis, Littlewood, and Shraiman (1995) and Zang, Bishop, and Roder (1995) have argued that the electron-phonon (Jahn-Teller) interaction is crucial, however, in order to account for the large value of the resistivity in the paramagnetic phase and near the transition. Millis, Shraiman, and Mueller (1995) have added the Jahn-Teller Hamiltonian Eq. (346), and also applied a LISA treatment, neglecting the quantum fluctuations of the phonon field. (See also the related treatment of this problem by Zang, Bishop, and Roder using the Lang-Firstov transformation.)

The local effects of disorder can be simply incorporated in the LISA framework. A recent study of the effects of disorder has been carried out by Sarma *et al.* (1995) in connection with the doped titanate series. It would be interesting to carry out a similar study using a generalization of Hamiltonian (345)–(347) in order to understand the effects of disorder on the photoemission spectroscopy and on the conductivity of the doped manganates.

Finally, we point out that the dynamical effects of the Hubbard interactions have not yet been treated for this problem. Photoemission experiments (Saitoh *et al.*, 1995) and optical conductivity measurements (Okimoto *et al.*, 1995) on this material reveal the transfer of spectral weight over large energy scales, reminiscent of the V_2O_3 system. This phenomenon is a dynamical manifestation of the Coulomb interactions which so far can only be described using the LISA method, as described in detail in Sec. VII. Applying this method to the doubly degenerate Hubbard model appropriate for the manganates, in order to account for these effects, would shed significant light on this system.

G. Systems with quenched disorder

1. Models of disorder

An important advantage the LISA has over other techniques for treating the strong correlation problem is that the dynamical mean field equations and the techniques to solve them can be easily adapted to situations where the lattice translational invariance is broken by local imperfections, or when there is no underlying periodic lattice as in the case of amorphous systems. Randomness can affect both the hopping matrix elements (off-diagonal disorder) and the site energies (diagonal disorder). So far, most studies have focused on the disordered Hubbard model Hamiltonian:

$$H=\sum_{ij}\sum_{\sigma}[-t_{ij}+\varepsilon_i\delta_{ij}]c^{+}_{i\sigma}c_{j\sigma}+U\sum_i n_{i\uparrow}n_{i\downarrow}. \quad (348)$$

A very useful parametrization of the off-diagonal disorder is the one used by Dobrosavljević and Kotliar (1993, 1994), in which the following form is chosen for the hopping term:

$$t_{ij}=y_{ij}x_ix_j. \quad (349)$$

The y_{ij}'s are independent *bond* variables with a symmetric distribution, as in the gauge invariant model of Wegner (1976), and the x_i's are local *site* variables (which directly control the hopping randomness), with a distribution $P_H(x_i)$. The intuitive content of this idea is to associate small values of x_i to sites which are weakly coupled to the rest of the sites and large values of x_i to sites which are strongly hybridized with their neighbors. This is a suitable model for a doped semiconductor such as Si:P. One can take the y_{ij}'s to be Gaussian random variables with zero mean, and with the variance

$$\overline{y_{ij}^2}=\frac{1}{z}f_{ij}t^2. \quad (350)$$

Here, the matrix f_{ij} is the lattice connectivity matrix (f_{ij}=1 for sites connected by a bond, f_{ij}=0 for disconnected sites), and one scales the (square of the) hopping elements t_{ij}^2 by the coordination number $z=\Sigma_j f_{ij}$, in order to obtain finite result in the $z\to\infty$ limit. Diagonal disorder is also introduced through the distribution of site energies $\varepsilon_i P_S(\varepsilon_i)$.

The local version of the pure Hubbard model is an Anderson impurity model. The local version of the disordered Hubbard model is a *collection* of Anderson impurity models which describe the physics of the different local environments felt at different sites. The local action describing site i has the form

$$S_{\rm eff}^{(i)}=\sum_{\sigma}\int_0^\beta d\tau\int_0^\beta d\tau' c_{i\sigma}^{+}(\tau)[\delta(\tau-\tau')(\partial_\tau+\varepsilon_i-\mu) + W_{i\sigma}(\tau,\tau')]c_{i\sigma}(\tau') + U\int_0^\beta d\tau c_{i\uparrow}^{+}(\tau)c_{i\uparrow}(\tau)c_{i\downarrow}^{+}(\tau)c_{i\downarrow}(\tau), \quad (351)$$

with the self-consistency condition (on the Bethe lattice)

$$W_{is}(\omega_n)=\sum_j\int d\varepsilon_j P_S(\varepsilon_j)\int dt_{ij}P(t_{ij})t_{ij}^2 G_{js}(\omega_n), \quad (352)$$

where $G_{j\sigma}(\omega_n)=\langle c_{j\sigma}^{\dagger}(\omega_n)c_{j\sigma}(\omega_n)\rangle$ are the local Green's functions evaluated using the effective action in Eq. (351).

2. Interplay of disorder and SDW or CDW ordering

The properties of this model in the presence of diagonal disorder have been studied in a series of works by Vollhardt and collaborators. The dynamical mean-field equations in this case were established by Janis and Vollhardt (1992b). Using quantum Monte Carlo methods, Janis, Ulmke, and Vollhardt (1993; see also Ulmke, Janis, and Vollhardt, 1995) investigated the phase diagram at half-filling for a binary distribution of the form

$$P_S(\varepsilon_i)=\tfrac{1}{2}[\delta(\varepsilon_i-\tfrac{1}{2}\Delta)+\delta(\varepsilon_i+\tfrac{1}{2}\Delta)]. \quad (353)$$

Their phase diagram (obtained by evaluating the response functions) is reprinted in Fig. 81. They observed that a weak diagonal disorder suppresses the Néel temperature for small U but enhances it slightly for large U. For small values of U, the magnetism is due to a spin density wave formation. Magnetic ordering in this limit is strongly dependent on the existence of perfect nesting, which is suppressed by disorder, causing a strong reduction of T_N as disorder is increased for small U. It is useful to think about this model in the limit $U>D$ and $\Delta>D$, in which metallic behavior is suppressed. In this limit the model has two regimes: in one regime when $U<\Delta$ the system is a band insulator, and the *correlations* can be treated perturbatively: for $U>\Delta$ the system is a Néel-Mott insulator and the *disorder* can be treated perturbatively. The exchange constant in that limit decreases with increasing Δ.

Janis, Ulmke, and Vollhardt (1993) also computed the compressibility as a function of U for fixed temperature. It has a maximum when U is close to Δ. This can be understood by analyzing the atomic limit of the associated impurity model: for $U\simeq\Delta$, two atomic configurations are found to be degenerate, giving rise to a large charge response. The authors conjecture that the metal insulator transition at $T=0$ in this model will occur from an antiferromagnetic metallic phase to an antiferromagnetic insulating phase, as in the fully frustrated model of Sec. VII.

The interplay of disorder and charge density wave formation was analyzed in a model of spinless fermions with nearest-neighbor interactions by Vlaming, Uhrig, and Vollhardt (1992) and Uhrig and Vlaming (1993; see also Vlaming and Vollhardt, 1992 for the general formalism associated with disordered spinless fermion models in $d=\infty$). In this model the limit of large lattice coordination reduces to the Hartree approximation, and hence one is really dealing with a *static* mean-field theory. Even in this relatively crude approximation, this model displays a metal-insulator transition from a homogeneous metallic phase to an insulating charge density wave state. The behavior of the physical quantities near this transition has been studied as a function of filling, temperature, and frequency. Away from half-filling this model displays incommensurate order and phase separation (Uhrig and Vlaming, 1993).

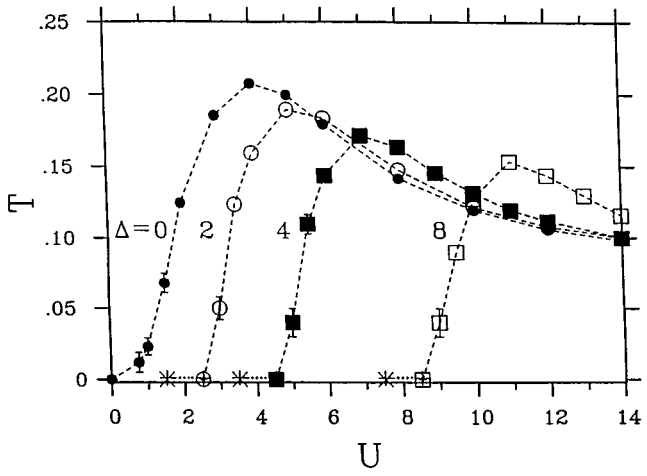

FIG. 81. T-U phase diagram for disorder strengths Δ=0,2,4,8. The paramagnetic (antiferromagnetic) phase is stable above (below) the curves. From Janis, Ulmke, and Vollhardt (1993). The results are for the Bethe lattice, and U, T, Δ are in units of $D/2$, with D the half-bandwidth.

Finally, let us mention that the dynamics of a single hole in the $d=\infty$ t-J model with local disorder has been investigated by Strack and Vollhardt (1992).

3. Formation of local moments and the Mott transition in disordered systems

Many disordered systems, such as doped semiconductors, do not order magnetically down to the lowest temperatures that have been measured. For these systems, the paramagnetic solution of the dynamical mean field equations is relevant. Dobrosavljevič and Kotliar (1993, 1994) applied the LISA method to the physics of these systems, and observed that it provides a microscopic derivation of the two-fluid model (Quirt and Marko, 1972). This simple model of a strongly disordered metal is known to be very successful in interpreting experiments on these systems. In this picture, the disordered system is viewed as a sum of a localized component and of an itinerant component. The localized component controls the susceptibility and other thermodynamic properties while the itinerant component controls the transport. The LISA method justifies this picture, and allows one to deal with the dynamical effects of the in-

teraction and the strong-coupling regime (for a Hartree treatment of the interaction in this problem, see Milovanović, Sachdev, and Bhatt, 1989).

The disorder induces a broad distribution of Kondo energies. At a given temperature the "localized" component of the two-fluid picture is identified with the sites having a Kondo energy lower than the temperature, while the "itinerant" component is identified with those sites that have a Kondo temperature larger than the temperature. Once the local Green's functions are self-consistently determined, the energy $E(T)$ and the specific heat have an additive form over the members of the ensemble having energies ε_i and hopping parameters x_i:

$$E(T)=\int d\varepsilon_i P_S(\varepsilon_i)\int dx_i P_H(x_i)\,\frac{1}{\beta}\sum_n\,[i\omega_n+\mu + W_i(\omega_n)]G_i(\omega_n). \tag{354}$$

For a continuous distribution of x_i's, the low-temperature specific heat is dominated by sites with $T_K(x_i)<T$, and has the form

$$\gamma(T)\sim\frac{1}{T}\,n_{\rm fr}(T). \tag{355}$$

Here, the fraction of "free spins" reads

$$n_{\rm fr}(T)=\int_0^{x^{\max}(T)} dx_i P_H(x_i) \tag{356}$$

with

$$x^{\max}(T)=\left(\frac{\Delta_o}{U}\ln\frac{D_o}{T}\right)^{-2}. \tag{357}$$

For any distribution $P_H(x_i)$ that extends all the way to x_i=0, and having a low x_i tail slower than exponential (e.g., power-law or lognormal), the resulting $\gamma(T)$ *diverges* as $T\to 0$. The precise form of this singularity depends on the details of $P_H(x_i)$. However, for any power-law or even lognormal form of the law x_i tail, the quantity $n_{\rm fr}(T)$ decreases to zero as $T\to 0$ *slower* than any power, giving an anomalously slow decrease of the number of "free" spins with temperature, and a large anomaly in $\gamma(T)$.

Therefore, for a large class of models with continuous distributions of hopping, the LISA equations admit non-Fermi-liquid metallic solutions. We expect the non-Fermi-liquid behavior of disordered metallic phases to be a generic feature of such model beyond mean-field theory (cf. Bhatt and Fisher, 1992). However, the detailed dependence on the probability distribution for disorder is likely to be an artifact of the $d=\infty$ mean-field theory, and is probably replaced by renormalized distributions.

The transport coefficients such as the conductivity can also be written as averages over the ensemble of Anderson impurity models, but in this case, the transport is nonlinear in the probability distribution of randomness and it weights more heavily the sites with a *large* Kondo temperature. For instance, the conductivity reads (Sec. IV)

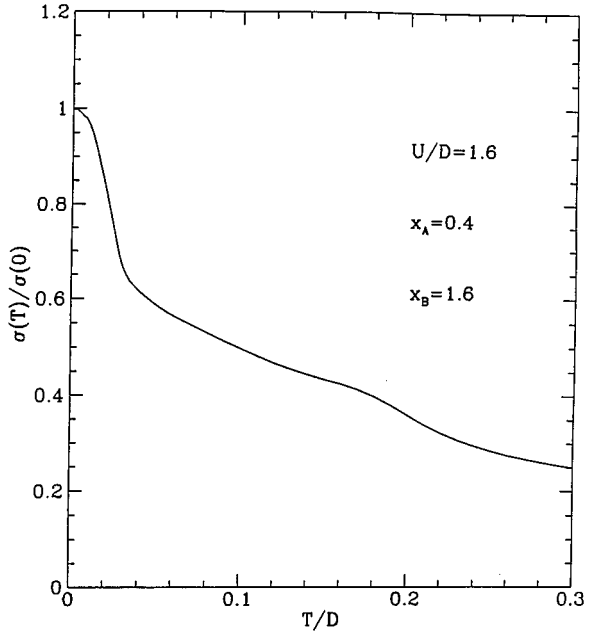

FIG. 82. DC conductivity as a function of temperature for the model described in the text. Note the sharp increase at low temperature, reflecting the onset of coherence due to Kondo screening of the local moments. From Dobrosavljevič and Kotliar (1994).

$$\mathrm{Re}\sigma(\omega)=4\pi a^2t^2\int d\omega'\rho_W(\omega')\rho_W(\omega'+\omega)\times\frac{f(\omega')-f(\omega'+\omega)}{\omega}, \tag{358}$$

where $f(\omega)$ is the Fermi function, and $\rho_W(\omega)$ is the *local* spectral function corresponding to the averaged cavity field:

$$\rho_W(\omega)=-\frac{1}{\pi}\,\mathrm{Im}\int d\varepsilon_i P_S(\varepsilon_i)\times\int dx_i P_H(x_i)x_i^2 G_i(\omega+i0^+). \tag{359}$$

At ω=0, and low temperatures, the expression reduces to

$$\sigma_{\rm dc}(T)=4\pi a^2t^2\rho_W^2\ (\omega=0,T). \tag{360}$$

The behavior of the transport and thermodynamics of a disordered system near the Mott transition was examined in the work of Dobrosavljecvič and Kotliar (1993, 1994). At zero temperature there is minimal metallic conductivity while at finite temperatures there is a rounded jump. This is shown in Fig. 82. It is amusing to notice that these results are very similar to the analysis of the experimental data by Möbius (1989, 1990). Far from the transition the presence of local moments does induce *anomalous low-temperature corrections* to $\sigma_{\rm dc}$, which could be crucial in understanding the transport properties in systems such as doped semiconductors. These anomalous contributions arise because in a disordered system different sites have different environments.

It is useful to analyze qualitatively Eqs. (359) and (360) assuming off-diagonal disorder only. Even far from the transition, the statistical distribution of hoppings results in the existence of strongly correlated sites with a spectral function $\rho_i(\omega_n)$ which develops a sharp peak near the Fermi surface. As the temperature is increased from $T=0$, inelastic scattering will destroy this coherent peak at a characteristic temperature T_K. However, in a *random* system, this process takes place *locally*, and a given *site* becomes "incoherent" at $T\sim T_K(x_i)$, when this Kondo resonance is washed out. Thus, in contrast to thermodynamic response, appreciable contributions to the conductivity come from those sites with $T_K(x_i)>T$, which remain coherent:

$$\rho_i(\omega_n\to 0)\sim\begin{cases}0, & T_K(x_i)<T,\\ \dfrac{1}{x_i^2\Delta_o}, & T_K(x_i)>T.\end{cases} \tag{361}$$

Again, to leading order we can ignore the frequency dependence of $\rho_i(\omega_n)$, and we find (at $\omega_n\to 0$)

$$\rho_W(T)\sim\int_{x_{\max}(T)}^{+\infty} dx_i P_H(x_i). \tag{362}$$

By using this result, and Eq. (360), we find that the leading low-temperature correction to the dc conductivity assumes the form

$$\delta\sigma_{\rm dc}(T)\sim n_{\rm fr}(T). \tag{363}$$

It is interesting to note that, although $n_{\rm fr}(T)$ vanishes more slowly than any power as $T\to 0$, for realistic distributions one can write:

$$n_{\rm fr}(T)=T^{\alpha(T)}, \tag{364}$$

where $\alpha(T)$ depends on temperature only very weakly, typically *logarithmically* (Dobrosavljevič, Kirkpatrick, and Kotliar, 1992). Experimentally, one expects to measure some *effective* exponent α. Since $\alpha\to 0$ at $T\to 0$, one expects these effective exponents to be small. This behavior is to be contrasted with the fact that similar, nonanalytic finite temperature corrections to the conductivity of dirty metals follow from *weak localization* and *interaction* effects. Mean-field theory then produces a very different mechanism for anomalous temperature dependence of the conductivity.

A full theory of the interplay of disorder and interactions should include both the local moments and the hydrodynamic (diffusion) corrections. As discussed in Sec. IX, the loop expansion (Dobrosavljevič and Kotliar, 1993, 1994) would incorporate these two distinct corrections to the transport coefficients in a unified framework.

Finally, we emphasize that one of the main limitations of the LISA method in dealing with disordered electronic systems is its inability to capture the effects of Anderson localization. Indeed, localization effects disappear in the $d\to\infty$ limit. Physically, this is because each site has a large number of neighbors, so that diffusive behavior is always possible. Formally, it manifests itself, e.g., in the fact that the on-site Green's function is a self-averaging quantity. It would be extremely interesting to find a way out of this difficulty, perhaps along the lines of Sec. IX.

IX. BEYOND $d=\infty$: INCLUDING SPATIAL FLUCTUATIONS

A. Motivations

An obvious limitation of the dynamical mean-field theory based on the $d\to\infty$ limit is that it fails to capture fully the dynamical effects of *intersite interactions*, in either the charge channel (e.g., nearest-neighbor repulsion) or spin channel (exchange). More precisely, we have seen that these interactions do enter two-particle response functions at specific values of $\mathbf{q}$ (such as $\mathbf{q}=\mathbf{0}$) but do not affect *local* response functions or one-particle properties. Hence the approach is able to capture the possible symmetry breakings induced by these interactions, but does not take into account the dynamical effect of the fluctuations in the high-temperature disordered phase. An example making this observation particularly clear is that of the t-J model in $d=\infty$. In the paramagnetic phase, the exchange coupling J disappears completely from the mean-field equations based on a single-site effective action. The antiferromagnetic phase transition has no precursor effect on one-particle properties in this limit. (Note that this no longer applies for random exchange couplings, as described in Sec. VIII.A.4.)

Such dynamical effects are crucial however for the physics of several strongly correlated fermion problems. A few prominent examples are quoted here.

(i) In heavy-fermion compounds, the competition of the RKKY interaction with the Kondo effect is a crucial question, which remains largely unanswered. As described in Sec. VIII.A.1, only some aspects of this competition are captured in the LISA framework.

(ii) In the cuprate superconductors, the superexchange interaction J is a fairly large scale. This interaction has to be taken into account in the description of the spin dynamics, such as the "spin-gap" phenomenon. Large-N (Castellani, Grilli, and Kotliar, 1991) and large-S (Kane, Lee, and Read, 1989) studies suggest that the divergence of the effective mass near the Mott transition found in the $d=\infty$ approach (Sec. VII) is going to be significantly modified by intersite interactions when J is large.

(iii) The dynamical effects of longer-range Coulomb repulsion (such as a nearest-neighbor term $V_{pd}n_{i\sigma}n_{j\sigma'}$) may also be important for cuprates (Varma, Schmitt-Rink, and Abrahams, 1987). Such an interaction reduces to its Hartree term in the single-site mean field theory (Müller-Hartmann, 1989a; cf. Secs. VIII.C and VIII.D).

(iv) Anderson localization, that is the possibility of an insulating state which is caused entirely by randomness, plays an important role in the physics of doped semiconductors. This phenomena is absent in the limit of infinite dimensions because spatial fluctuations caused by the randomness are completely averaged out, and the Green's function becomes self-averaging (Sec. VIII.G).

The same limitations affect the description of ordered phases. It is impossible, for example, to describe a pairing state with extended spatial symmetry (such as d-wave) in the context of the single-site approach.

All these observations call for an extension of the dynamical mean-field framework to take into account these *nonlocal physical effects*. One may hope that, whenever the relevant correlation lengths of a physical system are small, it may be sufficient to include *short-range fluctuations* and that an approach based on a quasilocal point of view is valid. This suggests extending the dynamical mean-field framework from a single-site effective theory to that of a *finite cluster embedded in a self-consistent medium*.

Such generalizations of mean-field theory based on a self-consistent cluster embedding have a long history in the statistical mechanics of classical spin models (see, e.g., Burley, 1972). The simplest example is the Bethe-Peierls approximation which reintroduces pair correlation effects. These methods have been developed systematically, following in particular the work of Kikuchi (1951), and have led to sequences of approximations based on larger and larger clusters which give an excellent quantitative description of thermodynamic properties (Suzuki, 1988). Critical properties can even be inferred from the study of the convergence of this sequence of approximations. In these sections, we shall describe various possible ways of generalizing these cluster approaches to models of strongly correlated fermions. The subject is still at a developmental stage. Very few actual calculations have been undertaken using these schemes, and it may be that these approximations suffer from various limitations or inconsistencies. These methods however are natural extensions of the LISA framework, and in one form or another this type of approach should allow progress to be made on some of the physical issues above. We view this section as an incentive for further investigation of this route. Another possible, perhaps more systematic, approach is to perform direct $1/d$ expansions for *properly chosen* quantities. This has not yet been undertaken for the Hubbard model or any other model of comparable complexity. $1/d$ expansions have been performed, however, for simpler models (Vlaming and Vollhardt, 1992; Halvorsen, Uhrig, and Czycholl, 1994) and have also been used as a simplifying tool of approximation methods (Schweitzer and Czycholl, 1990b, 1991a; van Dongen, 1994).

Apart from these attempts to include the physics of *short-range* fluctuations, an outstanding problem in the field is to include *long-wavelength* modes (such as spin waves), which are absent in the $d=\infty$ limit. This requires some kind of loop expansion around this limit. In order to set up this expansion, a functional integral formulation is needed, in which the LISA appears as a saddle point. So far, this has been accomplished only for models involving hopping randomness (Dobrosavljević and Kotliar, 1993, 1994). While this approach has not yet been extended to nonrandom models, and no loop corrections to physical quantities have been calculated yet, we believe it deserves further investigation and we describe it briefly in Sec. IX.D.

B. The Bethe-Peierls approximation

The most natural extension of the Weiss mean field approach is the Bethe-Peierls approximation. For classical systems, this coincides with the exact solution on a Bethe lattice. For quantum systems, the exact solution of a model of correlated electrons on the Bethe lattice can be reduced to an infinite number of coupled functional equations for an infinite number of functions (i.e., all the connected n-point functions). Unfortunately, given the difficulty of handling mean field equations for just a single function (as in the $z=\infty$ limit), this route looks, at this point, prohibitively difficult, so we must introduce additional approximations to obtain tractable schemes.

The first self-consistent cluster scheme that we shall introduce is a fairly straightforward adaptation of the Bethe-Peierls scheme for spin systems. It is designed for the Bethe lattice with finite connectivity z. The idea is to single-out a finite cluster of sites, made of a central site o and its nearest neighbors $i=1,\ldots,z$ (Fig. 83). Following the strategy of the cavity method (Sec. III.A), one thinks of eliminating all degrees of freedom in the lattice except on that single cluster. No small parameter (like $1/z$) is now available to control this elimination, and one has to resort to some approximations. The approximation made here is to include, in the effective action for the cluster, only the quadratic (one-particle) terms generated by the elimination procedure. With this assumption, the most general form for the cluster effective action reads

$$\begin{aligned} S_{\rm eff} = &- \int_0^\beta d\tau \int_0^\beta d\tau' \sum_\sigma \sum_{i\in\mathscr{B}} c_{i\sigma}^+(\tau)\mathscr{G}_0^{-1}(\tau-\tau')c_{i\sigma}(\tau') \\ &- \int_0^\beta d\tau \sum_\sigma c_{o\sigma}^+(\tau)(-\partial_\tau+\mu)c_{o\sigma}(\tau) \\ &- \int_0^\beta d\tau \sum_{\sigma,i\in\mathscr{B}} t_{io}(c_{i\sigma}^+ c_{o\sigma}+c_{o\sigma}^+ c_{i\sigma}) \\ &+ U\int_0^\beta d\tau \left[n_{o\uparrow}n_{o\downarrow}+\sum_{i\in\mathscr{B}} n_{i\uparrow}n_{i\downarrow}\right]. \end{aligned} \tag{365}$$

In this expression, $\mathscr{G}_0$ is the "Weiss function" resulting from the elimination of the lattice degrees of freedom.

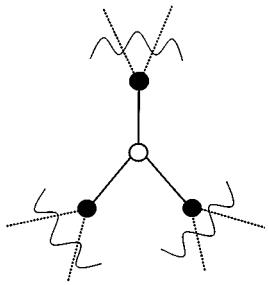

FIG. 83. Cluster used in the Bethe-Peierls method.

Note that it acts only on the z sites of the boundary $\mathscr{B}$ of the cluster, since only those are connected to the rest of the lattice. Also, note that it is purely site diagonal: this is a feature of the Bethe lattice, which splits into z disconnected sublattices once the cavity has been created (i.e., the cluster has been removed), so that two different sites on the boundary can no longer communicate. t is the nearest-neighbor hopping, which is *not* being scaled as $1/\sqrt{z}$ in this section.

From $S_{\rm eff}$, interacting Green's functions can be calculated as a function of $\mathscr{G}_0$ for both the central sites and the sites on the boundary:

$$G_{oo}(\tau-\tau')\equiv-\langle Tc_o(\tau)c_o^+(\tau')\rangle_{S_{\rm eff}},$$
$$G_{ii}=-\langle Tc_i(\tau)c_i^+(\tau')\rangle_{S_{\rm eff}}. \tag{366}$$

One needs to supplement these equations with a single self-consistency equation to obtain a closed set of equations for the single unknown function $\mathscr{G}_0$. A very natural way of achieving this is to request *translation invariance* of the lattice Green's function, i.e., to determine $\mathscr{G}_0$ from the condition

$$G_{oo}[\mathscr{G}_0]=G_{ii}[\mathscr{G}_0]. \tag{367}$$

Equations (365), (366), and (367) form a closed set of equations which are *exact* in the following limits.

(i) *Large connectivity* $z\to\infty$. Restoring the scaling $t=t_*/\sqrt{z}$, the boundary sites can be eliminated to dominant order so that an effective single-site action for the central site is obtained, with a Weiss function:

$$\mathscr{G}_0^{-1}=i\omega_n+\mu-t^2\sum_{i=1}^{z}G_{ii}(i\omega_n)$$
$$=i\omega_n+\mu-t_*^2G_{oo}(i\omega_n), \tag{368}$$

where Eq. (367) has been used. This is seen to be equivalent to the exact mean-field equations for the $z=\infty$ Bethe lattice.

(ii) *Atomic limit* $t=0$. In that case the cluster effective action splits into $z+1$ disconnected pieces. The piece corresponding to the central site is seen to be the single-site action of the Hubbard model in the atomic limit, so that $G_{oo}=G_{\rm atomic}$. In view of the form of the effective action for the boundary sites, the self-consistency condition Eq. (367) then implies $\mathscr{G}_0^{-1}=i\omega_n+\mu$, as required.

(iii) *Free system* $U=0$. The effective action becomes quadratic and can be solved in closed form. Diagonalizing the corresponding $(z+1)\times(z+1)$ matrix yields $G_{oo}^{-1}=i\omega_n+\mu-zt^2\mathscr{G}_0$ and $G_{ii}=\mathscr{G}_0-t^2\mathscr{G}_0^{-1}$. The self-consistency condition (367) then leads to the following equation for $\mathscr{G}_0$: $(z-1)t^2\mathscr{G}_0^2-(i\omega_n+\mu)\mathscr{G}_0+1=0$. Comparing with Eq. (A41) of Appendix A, one identifies $\mathscr{G}_0$ with the cavity Green's function $G_{ii}^{(o)}$, and checks that these equations yield the exact Green's function in the free case for the Bethe lattice with arbitrary connectivity, as expected.

It should be pointed out that, in contrast to classical spin systems, these equations inspired by the Bethe-Peierls method are not exact for the finite connectivity Bethe lattice except in the above limits. Indeed, higher-order cumulants have been neglected in the effective action.

Though simple in spirit, the Bethe-Peierls approximation has several limitations. It is designed for the Bethe lattice, has no clear generalization to cluster involving loops, and requires the solution of an Anderson model involving $z+1$ impurity sites. The next section describes more flexible and practical cluster approximations.

C. Self-consistent cluster approximations

We describe here a self-consistent cluster embedding approximation that has been recently proposed independently by the present authors and by Schiller and Ingersent (1995). The idea is to replace the lattice problem by that of a cluster of a specific shape, embedded self-consistently in the lattice in all possible ways. As we shall see, in order to avoid double counting, subclusters of the original cluster must also be considered. The method can in principle be adapted to any lattice and an arbitrary cluster shape. In this section however, we shall illustrate it on the simplest example, namely that of a cluster made of a pair of neighboring sites.

In order to set up the equations, it is convenient to work in terms of the Luttinger-Ward functional $\Phi[\{G_{ij}\}]$ already introduced in Sec. III.B and defined as the sum of all vacuum-to-vacuum skeleton diagrams. The free energy can be viewed as a functional of both the full Green's function G_{ij} and of the self-energy Σ_{ij}, which reads

$$\Omega[G_{ij},\Sigma_{ij}]=-\,\mathrm{Tr}\,\ln[(i\omega_n+\mu)\delta_{ij}-t_{ij}-\Sigma_{ij}]$$
$$-\,\mathrm{Tr}\Sigma\cdot G+\Phi[\{G_{ij}\}]. \tag{369}$$

Stationarity with respect to both G and Σ yields the Dyson equation relating these quantities and the expression of Σ as the derivative of the Luttinger-Ward functional:

$$G_{ij}=[i\omega_n+\mu-t_{ij}-\Sigma_{ij}]^{-1},\quad \Sigma_{ij}=\frac{\delta\Phi}{\delta G_{ij}}. \tag{370}$$

The main idea of the self-consistent cluster method is to expand the functional Φ as a sum of functionals involving the contribution of single-site clusters, two-site clusters of nearest-neighbor sites, etc. A very similar procedure is applied to the entropy term for classical statistical mechanics models (see, e.g., Sanchez, Ducastelle, and Gratias, 1984; Morita, 1990). Let us write such an expansion as

$$\Phi=\sum_i\tilde{\Phi}_1[G_{ii}]+\sum_{\langle ij\rangle}\tilde{\Phi}_2[G_{ii},G_{jj},G_{ij}]+\cdots, \tag{371}$$

where only contributions of single sites and pairs of nearest neighbors have been explicitly written. The auxiliary functionals $\tilde{\Phi}_1,\tilde{\Phi}_2$ are the "connected" contributions of single-site and pair clusters. They are determined by the observation that this expansion can also be applied to a lattice made of just a single site or a single pair, and thus

$$\Phi_1[G_{ii}]=\tilde{\Phi}_1[G_{ii}], \tag{372}$$

$$\Phi_2[G_{ii},G_{jj},G_{ij}]=\tilde{\Phi}_2[G_{ii},G_{jj},G_{ij}]+\Phi_1[G_{ii}]+\Phi_1[G_{jj}], \tag{373}$$

where Φ_1 and Φ_2 are the Luttinger-Ward functionals corresponding to a single-site and a pair cluster, respectively. Thus, one gets the expansion

$$\Phi=(1-z)\sum_i \Phi_1[G_{ii}]+\sum_{\langle ij\rangle}\Phi_2[G_{ii},G_{jj},G_{ij}]+\cdots, \tag{374}$$

where z is the connectivity of the lattice. The crucial role of the last subtracted term in (374) is to avoid overcounting of the single-site contributions, as can be checked by working out the first few orders of perturbation theory for Φ explicitly.

The self-consistent cluster approximation simply amounts to truncating this expansion at a given order. The rationale behind this approximation is that the cumulants $\tilde{\Phi}$ should become small for large cluster sizes. If only Φ_1 is included, the single-site dynamical mean-field theory (exact for $d=\infty$) is recovered, as discussed in Sec. III.B. Including both single-sites and pair clusters yields the next approximation. Using (370), the self-energy has two components within this approximation: a purely local one $\Sigma_{\rm loc}(i\omega_n)$ and a nearest-neighbor one $\Sigma_{\rm NN}(i\omega_n)$, given by

$$\Sigma_{\rm loc}=\frac{\delta\Phi}{\delta G_{ii}}=(1-z)\,\frac{\delta\Phi_1}{\delta G_{ii}}+z\,\frac{\delta\Phi_2}{\delta G_{ii}}, \tag{375}$$

$$\Sigma_{\rm NN}=\frac{\delta\Phi_2}{\delta G_{ij}}. \tag{376}$$

These equations express the self-energy as a functional of the full Green's functions. Combined with the Dyson equation in (370) relating G_{ij} to Σ_{ij}, one obtains in principle a set of closed equations for these quantities. However, in order to put these equations in a practical form, it is convenient to generate Φ_1 and Φ_2 from the action of a one-impurity and a two-impurity model, respectively. One thus introduces two sets of auxiliary Weiss fields: a local one $\mathcal{G}_{0(1)}$ for the single-impurity model, and a 2×2 matrix $[\mathcal{G}_{0(2)}]_{ij}$, where i,j can take the values 1,2 and denote the two nearest-neighbor sites in a pair. The effective actions generating Φ_1 and Φ_2 read

$$S^{(1)}_{\rm eff}=-\int_0^\beta d\tau\int_0^\beta d\tau'\sum_\sigma c^\dagger_{1\sigma}(\tau)\mathcal{G}^{-1}_{0(1)}(\tau-\tau')c_{1\sigma}(\tau')+U\int_0^\beta d\tau\, n_{1\uparrow}n_{1\downarrow}, \tag{377}$$

$$S^{(2)}_{\rm eff}=-\int_0^\beta d\tau\int_0^\beta d\tau'\sum_{i,j=1}^{2}\sum_\sigma c^\dagger_{i\sigma}(\tau)[\mathcal{G}^{-1}_{0(2)}(\tau-\tau')]_{ij}\times c_{j\sigma}(\tau')+U\sum_{i=1}^{2}\int_0^\beta d\tau\, n_{i\uparrow}n_{i\downarrow}. \tag{378}$$

Let us denote by $G_{\rm loc}\equiv G_{11}=G_{22}$ and $G_{NN}\equiv G_{12}=G_{21}$ the local (on-site) and nearest-neighbor Green's functions of the lattice model. The Weiss fields must be chosen so that the impurity Green's function coincide with $G_{\rm loc}$ and G_{NN}. This must yield three self-consistency conditions to fully determine the three Weiss fields $\mathcal{G}_{0(1)}$ and $[\mathcal{G}_{0(2)}]_{ij}$. The first condition is simply that the Green's function of the single-impurity model must coincide with the on-site component of the two-impurity model Green's function. In order to express the two other conditions, we define self-energies associated with each impurity model in the usual way:

$$\Sigma^{(1)}\equiv\mathcal{G}^{-1}_{0(1)}-G^{-1}_{\rm loc},\quad \Sigma^{(2)}_{ij}\equiv[\mathcal{G}^{-1}_{0(2)}]_{ij}-[G^{-1}]_{ij},\quad i,j\in\{1,2\}. \tag{379}$$

From which the on-site and nearest-neighbor components of the lattice self-energy can be obtained using (376) as

$$\Sigma_{\rm loc}(i\omega_n)=(1-z)\Sigma^{(1)}(i\omega_n)+z\Sigma^{(2)}_{11}(i\omega_n),\qquad \Sigma_{NN}(i\omega_n)=\Sigma^{(2)}_{12}(i\omega_n). \tag{380}$$

The two additional self-consistency conditions then read

$$G_{\rm loc}=\sum_{\mathbf{k}}\frac{1}{i\omega_n+\mu-\epsilon_{\mathbf{k}}-\Sigma_{\rm loc}(i\omega_n)-C(\mathbf{k})\Sigma_{\rm NN}(i\omega_n)}, \tag{381}$$

$$G_{\rm NN}=\sum_{\mathbf{k}}\frac{e^{i\mathbf{k}\cdot\vec{\delta}}}{i\omega_n+\mu-\epsilon_{\mathbf{k}}-\Sigma_{\rm loc}(i\omega_n)-C(\mathbf{k})\Sigma_{\rm NN}(i\omega_n)}, \tag{382}$$

where $C(\mathbf{k})$ is the Fourier transform of the lattice connectivity matrix, and $\vec{\delta}$ is the lattice vector between nearest-neighbor sites. For a model with only nearest-neighbor hopping $t_{ij}=t$, one has $\epsilon_{\mathbf{k}}=tC(\mathbf{k})$. These expressions can be further simplified:

$$G_{\rm loc}=\frac{1}{1+\Sigma_{\rm NN}/t}\,\tilde{D}\left(\frac{i\omega_n+\mu-\Sigma_{\rm loc}}{1+\Sigma_{\rm NN}/t}\right), \tag{383}$$

$$zG_{\rm NN}=\frac{1}{t+\Sigma_{\rm NN}}[-1+(i\omega_n+\mu-\Sigma_{\rm loc})G_{\rm loc}]. \tag{384}$$

The solution of the one and two-impurity effective actions submitted to the set of self-consistency equations just established provides us, in principle, with a closed approximation scheme for the determination of the Green's functions and self-energies. In practice, one will have to proceed, as usual, by iteration, for example, along the following route:

$$\Sigma^{(1)},\Sigma^{(2)}_{ij}\xrightarrow{\text{Eq. (380)}}\Sigma_{\rm loc},\Sigma_{NN}\xrightarrow{\text{Eq. (381)}}G_{\rm loc},\qquad G_{NN}\xrightarrow{\text{Eq. (379)}}\mathcal{G}_{0(1)},\ [\mathcal{G}_{0(2)}]_{ij}\to\Sigma^{(1)\rm new},\Sigma^{(2)\rm new}_{ij}, \tag{385}$$

where the last step requires the solution of both impurity models, and is of course the hard part in practice.

Some general remarks can be made on this type of approximations. First we note that, like the Bethe-Peierls approximation, it is exact in the limits $t=0$ (atomic), $U=0$ (free), and the exact single-site equations are recovered for $d=\infty$. Also, the pair scheme includes

all contributions to the free-energy up to order $1/d$. Nonetheless, it is not obvious *a priori* that these approximations are free of intrinsic difficulties, in contrast to the single-site dynamical mean-field theory which was free of internal inconsistencies because of the underlying $d=\infty$ limit. In the cluster scheme, it is not guaranteed for example that the solutions satisfy analyticity properties (i.e., have always positive spectral densities). Indeed, it is well known that attempts to generalize to clusters the CPA approximation for disordered alloys are faced with such problems (see Elliott, Krumhansl, and Leath, 1974, for a review).

Only exploratory studies of this set of equations have been made in special cases at this time. Schiller and Ingersent (1995) have applied it to the Falicov-Kimball model, and the present authors have applied the IPT scheme to these equations for the half-filled Hubbard model in a preliminary study of the effect of intersite fluctuations on the Mott transition. In both of these works, problems with the analyticity and uniqueness of the solutions have been noted in some range of parameters. It is not yet clear whether this is intrinsic to the method or connected to the approximations made. In any case, self-consistent cluster embeddings have the potential to account for the competition between local coherence and intersite effects. This is achieved by bringing in the physics of two-impurity models that are known to capture this competition (see, e.g., Jones, Varma, and Wilkins, 1988). In contrast, a perturbative expansion in $1/d$ would reintroduce these effects only as a subdominant perturbation. The authors feel that cluster-embedding schemes should be explored further before a final conclusion is reached. Simpler cluster-embedding schemes can also be devised, like naively extending the CPA approach of Sec. III.D to a single pair of sites plus an effective medium. However, such naive extensions have overcounting problems. This is the rationale for introducing the two simultaneous impurity problems, as was done in this section.

D. Functional integral formulation and loop expansion

A quite different approach, beyond the $d=\infty$ mean field solution, intended to capturing long-wavelength fluctuations, is to carry out a loop expansion, for which it is necessary to obtain the mean-field equations as a saddle point in a functional integral representation of the partition function. Expansion around the saddle point then generates the conventional loop expansion for spin systems. In the quantum case, this functional integral representation has been derived only in the case of the random models described in Sec. VIII.G (Dobrosavljevič and Kotliar, 1994). We summarize their method below. The starting point is the functional integral representation of the partition function of the random model described in Sec. VIII.G. Its Hamiltonian was given by

$$H=\sum_{ij}\sum_{\sigma}[-t_{ij}+\varepsilon_i\delta_{ij}]c^{+}_{i\sigma}c_{j\sigma}+U\sum_i c^{+}_{i\uparrow}c_{i\uparrow}c^{+}_{i\downarrow}c_{i\downarrow}. \tag{386}$$

The partition function is replicated so as to be able to carry out the disorder average:

$$\overline{Z^n}=\int D\varepsilon_i P[\varepsilon_i]Dt_{ij}P[t_{ij}]\int D\bar{c}_i Dc_i \exp\{-S\}, \tag{387}$$

with the action $S=S_{\rm loc}+S_{\rm hop}$ consisting of a local part (that includes the Hubbard interaction)

$$S_{\rm loc}=\sum_i S_{\rm loc}(i)=\sum_i\left[\sum_{\alpha,s}\int_0^\beta d\tau\,\bar{c}^{\alpha}_{si}[\partial_\tau+\varepsilon_i-\mu]c^{\alpha}_{si} + U\sum_{a,i}\int_0^\beta d\tau\,\bar{c}^{\alpha}_{\uparrow i}c^{\alpha}_{\uparrow i}\bar{c}^{\alpha}_{\downarrow i}c^{\alpha}_{\downarrow i}\right], \tag{388}$$

and a hopping part

$$S_{\rm hop}=\sum_{\langle ij\rangle}S_{\rm hop}(i,j)=\sum_{\langle ij\rangle}\left[t_{ij}\sum_{\alpha,s}\int_0^\beta d\tau[\bar{c}^{\alpha}_{si}c^{\alpha}_{sj}+\text{H.c.}]\right]. \tag{389}$$

Here, $\bar{c}^{\alpha}_{s,i}$ and $c^{\alpha}_{s,i}$ are the electronic (Grassmann) fields with spin $s=\uparrow,\downarrow$, the replica index $\alpha=1,\ldots,n$, at lattice site i, and β is the inverse temperature. The random site energies ε_i are described by their probability distribution $P_S[\varepsilon_i]$, and the random hopping elements t_{ij} by the corresponding distribution $P_H[t_{ij}]$. In the following, a specific form of the hopping $t_{ij}=x_i x_j y_{ij}$ will be chosen, the x_i's being random variables with a distribution $P_X(x)$, and y_{ij} being independent Gaussian variables such that $\overline{y_{ij}^2}=t^2 f_{ij}/z$, with f_{ij} the lattice connectivity matrix.

At this point, it is convenient to explicitly perform the averaging over the Gaussian random (bond) variables y_{ij}, after which the hopping part of the action takes the form

$$S_{\rm hop}=\frac{1}{2}t^2\sum_{ij}\frac{1}{z}f_{ij}x_i^2x_j^2\left[\sum_{\alpha s}\int_0^\beta d\tau[\bar{c}^{\alpha}_{si}(\tau)c^{\alpha}_{sj}(\tau) + \text{H.c.}]\right]^2. \tag{390}$$

As we can see from this expression, the averaging over disorder has generated a *quartic* term in the action, which is nonlocal in (imaginary) time, spin, and replica indices. We are now in a position to introduce collective Q fields of the form

$$Q^{\alpha_1\alpha_2,s_1s_2}_{\omega_1\omega_2}(i)=\frac{1}{z}\sum_j f_{ij}x_j^2\bar{c}^{\alpha_1}_{js_1}(\omega_1)c^{\alpha_2}_{js_2}(\omega_2), \tag{391}$$

by decoupling the (quartic) hopping term using a Hubbard-Stratonovich transformation.

It is now possible to formally integrate out the electron (Grassmann) fields, and the resulting action for the Q fields can be written as

$$S[Q]=S_{\rm hop}[Q]+S_{\rm loc}[Q]. \tag{392}$$

The nonlocal part of the action $S_{\rm hop}[Q]$ takes a simple quadratic form in terms of the Q fields

$$S_{\rm hop}[Q]=-\frac{1}{2}t^2\sum_{ij}\sum_{\alpha_1\alpha_2}\sum_{s_1s_2}\sum_{\omega_1\omega_2}K_{ij}Q^{\alpha_1\alpha_2,s_1s_2}_{\omega_1\omega_1}(i)\times Q^{\alpha_2\alpha_1,s_2s_1}_{\omega_2\omega_1}(j), \tag{393}$$

where $K_{ij}=1/zf^{-1}_{ij}$ is the inverse lattice matrix, scaled by coordination number z. In contrast, all the nonlinearities are contained in the *local* part of the action

$$S_{\rm loc}[Q]=-\sum_i \ln\int dx_iP_X(x_i)\int d\varepsilon_iP_S(\varepsilon_i)\times\int D\bar{c}_iDc_i\exp\{-S_{\rm eff}[\bar{c}_i,c_i,Q_i,x_i,\varepsilon_i]\}, \tag{394}$$

where the effective action for on-site electrons takes the form

$$\begin{aligned}S_{\rm eff}[\bar{c}_i,c_i,Q_i,x_i,\varepsilon_i]=&-\sum_{\alpha_1\alpha_2}\sum_{s_1s_2}\sum_{\omega_1\omega_2}\bar{c}^{\alpha_1}_{is_1}(\omega_1)\\&\times[(i\omega_1+\mu-\varepsilon_i)\delta_{\alpha_1\alpha_2}\delta_{s_1s_2}\delta_{\omega_1\omega_2}\\&-x_i^2t^2Q^{\alpha_1\alpha_2,s_1s_2}_{\omega_1\omega_2}(i)]c^{\alpha_2}_{is_2}(\omega_2)\\&+U\sum_{\alpha}\sum_{\omega_1+\omega_3=\omega_2+\omega_4}\bar{c}^{\alpha}_{i\uparrow}(\omega_1)\\&\times c^{\alpha}_{i\uparrow}(\omega_2)\bar{c}^{\alpha}_{i\downarrow}(\omega_3)c^{\alpha}_{i\downarrow}(\omega_4).\end{aligned} \tag{395}$$

The local effective action $S_{\rm eff}[\bar{c}_i,c_i,Q_i,x_i,\varepsilon_i]$ is identical to the action of a (generalized) Anderson impurity model embedded in an electronic bath characterized by a hybridization function $x_i^2t^2Q^{\alpha_1\alpha_2,s_1s_2}_{\omega_1\omega_2}(i)$. We can thus interpret our system as a *collection* of Anderson impurity models that are "connected" through the existence of collective Q fields. Here we note that, in contrast to an ordinary Anderson model, the hybridization function is now *nondiagonal* in frequency, spin, and replica indices. Physically, this reflects the fact that, for an arbitrary dimension, each site can be regarded as an Anderson impurity model in a fluctuating bath, which breaks local translational invariance in time, space, and spin.

When $z\to\infty$, the functional integral over Q fields, representing the partition function, can be evaluated exactly by a saddle-point method, and we should rederive the mean-field theory.

$$\frac{\delta S[Q]}{\delta Q^{\alpha_1\alpha_2,s_1s_2}_{\omega_1\omega_2}(i)}=0. \tag{396}$$

Assuming that the saddle-point solution $Q^{\rm SP}$ is translationally invariant in time, space, and conserves spin, and is *diagonal* in all indices

$$[Q^{\alpha_1\alpha_2,s_1s_2}_{\omega_1\omega_2}(i)]|_{\rm SP}=\delta_{\alpha_1\alpha_2}\delta_{s_1s_2}\delta_{\omega_1\omega_2}Q^{\rm SP}_s(\omega), \tag{397}$$

the saddle-point equations assume the form

$$Q^{\rm SP}_s(\omega)=\int d\varepsilon_iP_S(\varepsilon_i)\int dx_iP_X(x_i)x_i^2G_{i,s}(\omega), \tag{398}$$

where

$$G_{i,s}(\omega)=\langle\bar{c}_s(\omega)c_s(\omega)\rangle_{S_{\rm eff}[\bar{c},c,Q^{\rm SP},x_i,\varepsilon_i]}. \tag{399}$$

Hence, the Weiss function entering the effective action for site i reads $\mathcal{G}_0^{-1}=i\omega_n-x_i^2t^2Q^{\rm SP}_s(\omega)$, so that the dynamical mean-field equations of the LISA method are recovered at the saddle-point level.

In order to systematically study the fluctuation effects, one should carry out an expansion in terms of the deviations of the collective Q fields from their saddle-point value, i.e., in powers of $\delta Q(i)=Q(i)-Q^{\rm SP}$. This expansion around a nontrivial function has been used in other disordered problems, such as spin glasses, to generate systematic corrections to the mean-field theory (de Dominicis, Kondor, and Temesvari, 1987).

The method is particularly convenient when applied to long-range models, i.e., $f_{ij}=1$ for $|i-j|<L$, where L is a cutoff distance and the coordination $z\sim L^d$. In that case, the loop corrections are ordered by a small parameter $1/z$. The loop expansion can be applied also to large dimensionality models and in that case a given order in a loop expansion can be considered to be an infinite resummation of the simple $1/d$ expansion, since each term contains all powers of $1/d$. When the expansion of the effective action in terms of δQ is carried to lowest, quadratic order, we obtain a theory describing Gaussian fluctuations around the saddle point, which represent weakly interacting collective modes. Higher-order terms in the expansion then generate effective interactions of these modes, which under appropriate conditions can lead to fluctuation-driven phase transitions.

The Gaussian fluctuations of the Q fields would allow us to compute the leading corrections to mean-field theory. They have the form

$$\begin{aligned}S^{(2)}[Q]=&-\frac{1}{2}t^2\sum_{l_1\cdots l_4}\int\frac{dk}{(2\pi)^d}\delta Q_{l_1l_2}(k)[(L^2k^2+1)\\&\times\delta_{l_1l_4}\delta_{l_2l_3}-t^2W(l_1)W(l_3)\delta_{l_1l_2}\delta_{l_3l_4}\\&+t^2\Gamma(l_1\cdots l_4)]\delta Q_{l_3l_4}(-k).\end{aligned} \tag{400}$$

This expression is appropriate for a long-ranged model in which case the inverse lattice matrix in momentum space takes the form $K(k)\approx1+L^2k^2$, and the momentum integrals should be cut off at $\Lambda=2\pi/L$. Note that the coefficient of k^2, which can be interpreted as the *stiffness* of the δQ modes, is $\sim L^2$, so we see that indeed the fluctuations are suppressed for $L\to\infty$. In the above formula, the index l_m is used to represent the frequency, spin, and replica indices. The local vertex function $\Gamma(l_1\cdots l_4)$ is given by

$$\begin{aligned}\Gamma(l_1\cdots l_4)=&\int d\varepsilon_iP_S(\varepsilon_i)\int dx_iP_X(x_i)\\&\times x_i^4\langle\bar{c}_i(l_1)c_i(l_2)\bar{c}_i(l_3)c_i(l_4)\rangle_{S_{\rm eff}[Q^{\rm SP}]}.\end{aligned} \tag{401}$$

At this level, the dynamics of the collective fluctuations δQ is governed by the form of $S^{(2)}[\delta Q]$, which is expressed in terms of the *local correlation functions* of the saddle-point theory, i.e., of the $d=\infty$ disordered Hubbard

model. Accordingly, a detailed study of the $d=\infty$ limit does not provide only a mean-field description of the problem, but also determines the form of the leading corrections resulting from fluctuations. Corrections to physical quantities at the one-loop level have, however, not been calculated to date. The transverse fluctuations in these theories are the soft modes identified by Finkhelstein (1987) in his pioneering work on the interplay of localization and interactions. A detailed study of the effects of fluctuations still remains to be carried out. The methods of Sec. VI.C may prove to be very useful for the evaluation of the coefficients of the effective Lagrangian.

In the derivation presented in this section, the randomness on the hopping matrix elements greatly facilitated the formulation of a path-integral approach. Nevertheless it seems to us that it only played the role of a technical trick, and in fact one should be able to formulate a similar loop expansion for the nonrandom models. This is clearly an important problem for further research.

X. CONCLUSION

This rather long article can only end with a brief conclusion. The main message that we have tried to convey is that the local impurity self-consistent approximation (LISA) provides a powerful framework for the quantitative description of strongly correlated fermion systems. This approximation becomes exact in the limit of infinite dimensions/infinite lattice coordination, but can be viewed more generally as a *dynamical mean-field theory* for these systems. As reviewed in this article, this approach has led to significant progress on several problems in the physics of strongly correlated fermions. Some favorable comparisons of the LISA results to experimental findings on various materials have already been made.

In the hope of stimulating further work in this area, we have tried to emphasize in this article the physical content of the LISA method, and to review in detail the derivation of the dynamical mean-field equations, and the various analytical techniques and numerical algorithms available to solve them. It seems to us that there are at least three general directions in which further research is needed and progress is possible:

(i) Improvements in the efficiency and flexibility of the algorithms for the solution of the LISA dynamical mean-field equations would be technically very helpful (cf. Sec. VI).

(ii) In an attempt to push further the comparison with experiments (particularly on transition metal oxides), an effort could be made to include more realistic features of the actual materials (such as band structure aspects and orbital degeneracy) within the LISA method. It may even be possible to incorporate ideas from the LISA method into electronic structure calculations of real materials (cf. Sec. VIII.C).

(iii) The LISA method is a mean-field approximation in the sense that it freezes *spatial* fluctuations. It is clearly an outstanding theoretical problem in the field to go beyond the LISA, and treat these fluctuations in a consistent manner (both from the point of view of short-range correlations and of long wavelength collective modes, cf. Sec. IX).

In our view, the field of strongly correlated electron systems is ripe for new progress, and we expect the LISA method to play a major role in the quantitative description of these fascinating materials.

ACKNOWLEDGMENTS

We are deeply indebted to our collaborators in the field, M. Caffarel, V. Dobrosavljevič, D. S. Fisher, H. Kajueter, L. Laloux, G. Moeller, S. Sachdev, D. D. Sarma, A. Sengupta, Q. Si, G. Thomas, X. Y. Zhang, and have benefitted from very useful discussions with C. Castellani, P. van Dongen, D. Feinberg, J. Freericks, T. Giamarchi, C. Gros, M. Imada, K. Ingersent, I. Inoue, V. Janiš, M. Jarrell, Y. Kuramoto, A. Millis, E. Müller-Hartmann, W. Metzner, P. Nozières, A. Ruckenstein, A. Schofield, Z. X. Shen, and D. Vollhardt. We acknowledge expert help with computers from T. Besancon. We would like to thank G. Toulouse and D. Pines for their encouragement in writing this article. During the course of this work, we have benefitted from the hospitality of the International Center for Theoretical Physics (Trieste), the Institute for Scientific Interchange (Torino), and the Aspen Center for Physics. Laboratoire de Physique Théorique de l'Ecole Normale Supérieure is Unité propre du CNRS (UP 701) associée à l'ENS et à l'Université Paris-Sud. Laboratoire de Physique Statistique de l'Ecole Normale Supérieure is Laboratoire associé au CNRS (URA 1306) et aux Universités Paris VI et Paris VII. G.K. was supported by the NSF under Grant DMR-92-2400. We acknowledge support from a joint CNRS-NSF grant (NSF-INT-93-14273COOP) which has been instrumental for carrying out this work.

APPENDIX A: FERMIOLOGY IN $d=\infty$

In this appendix, we collect various useful results on the fermiology of tight-binding electrons on infinite-dimensional lattices. A large part of this section follows the paper of Müller-Hartmann (1989a).

1. Density of states of some $d=\infty$ lattices

We start with the simplest case of free electrons on a d-dimensional cubic lattice with nearest-neighbor hopping. The lattice spacing a is set to $a=1$. The hopping is normalized to

$$t_{ij}=\frac{t}{\sqrt{2d}} \tag{A1}$$

so that the Fourier transform of the kinetic energy per spin reads

$$\epsilon_{\mathbf{k}}=-\frac{2t}{\sqrt{2d}}\sum_{i=1}^{d}\cos k_i\,. \tag{A2}$$

The density of states

$$D(\epsilon)=\int \frac{d^dk}{(2\pi)^d}\,\delta(\epsilon-\epsilon_{\mathbf{k}})\equiv\langle\delta(\epsilon-\epsilon_{\mathbf{k}})\rangle \tag{A3}$$

can be obtained in the limit $d=\infty$ by applying the central limit theorem to the sum in Eq. (A2). Indeed, in this limit, $\cos k_i$ can be considered (for a generic $\mathbf{k}$) as a random number between –1 and 1, and the mean and variance of $\epsilon_{\mathbf{k}}$ read (denoting by $\langle\cdots\rangle$ averages over the Brillouin zone)

$$\langle\epsilon_{\mathbf{k}}\rangle=0,\quad \langle\epsilon_{\mathbf{k}}^2\rangle=\frac{4t^2}{2d}\,d\langle\cos^2k_1\rangle=t^2. \tag{A4}$$

The density of states is thus a Gaussian for $d=\infty$:

$$D(\epsilon)=\frac{1}{\sqrt{2\pi t^2}}\,e^{-\epsilon^2/2t^2}. \tag{A5}$$

The tails of $D(\epsilon)$ extending to infinity are due to the "exceptional" values of the momentum (such that $\mathbf{k}=0$) which contribute "coherently" to the sum in Eq. (A2), so that the sum becomes of order d rather than $\sqrt{d}$. Equation (A5) can be established more explicitly, and finite-dimensional corrections estimated, by introducing the Fourier transform

$$\Phi_d(s)\equiv\int_{-\infty}^{+\infty}d\epsilon\;e^{is\epsilon}D(\epsilon). \tag{A6}$$

This reads

$$\Phi_d(s)=\left[\int_{-\pi}^{+\pi}\frac{dk}{2\pi}\exp\left(-i\,\frac{2ts}{\sqrt{2d}}\cos k\right)\right]^d. \tag{A7}$$

This integral is easily expanded in powers of $1/d$:

$$\Phi_d(s)=\exp\left[-\frac{t^2}{2}\,s^2-\frac{t^4}{16d}\,s^4+O\left(\frac{1}{d^2}\right)\right]. \tag{A8}$$

For $d=\infty$, all terms but the first one can be ignored in the argument of the exponent, and the inverse transform yields Eq. (A5). Retaining higher terms yields finite-dimensional corrections to the Gaussian limiting form. $\Phi_d(s)$ can actually be obtained in explicit form:

$$\Phi_d(s)=\left[J_0\left(\frac{2t}{\sqrt{2d}}\,s\right)\right]^d, \tag{A9}$$

where J_0 is the Bessel function. The asymptotic expansion above is controlled to all orders in $1/d$ by the maximum of J_0 at $s=0$. The density of states for a finite-dimensional lattice differs from the Gaussian mostly because of Van Hove singularities [of the form $(\epsilon-\epsilon_{VH})^{d/2-1}$], which are due to the opposite region of integration $s\geqslant\sqrt{d}$, and contribute exponentially small contributions (of order e^{-d}) to the expansion above. These singularities are thus "nonperturbative" effects from the viewpoint of a $1/d$ expansion. Quantitative comparison between the density of states in finite dimensions and the Gaussian form is displayed in Fig. 84 (from Vollhardt, 1993). It is seen that the $d=\infty$ limit becomes a rather good approximation very quickly, and

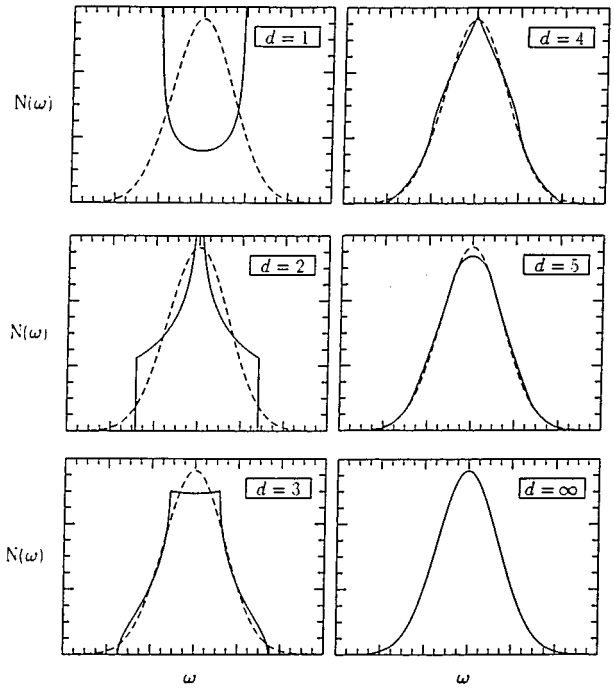

FIG. 84. Density of state $D(\epsilon)$ for tight-binding electrons with nearest neighbor hopping on a hypercubic lattice of various dimensionalities. From Vollhardt (1994).

that already for $d=3$, the density of states differs appreciably from the Gaussian only in the vicinity of the Van Hove singularities.

We also derive the expression (11) for the Hilbert transform of the Gaussian density of states:

$$\tilde{D}(z)\equiv\int_{-\infty}^{+\infty}d\epsilon\,\frac{D(\epsilon)}{z-\epsilon}. \tag{A10}$$

It is convenient to introduce the integral representation (valid for $\mathrm{Im}z>0$):

$$\frac{1}{z-\epsilon}=-i\int_0^{+\infty}d\lambda e^{i\lambda(z-\epsilon)}. \tag{A11}$$

Performing the Gaussian integration over ϵ, one obtains

$$\tilde{D}(z)=-i\int_0^{+\infty}d\lambda\;e^{iz\lambda-\lambda^2/4}. \tag{A12}$$

Shifting the integration variable finally yields

$$\tilde{D}(z)=-i\sqrt{\pi}e^{-z^2}\mathrm{erfc}(-iz)\quad(\mathrm{Im}z>0), \tag{A13}$$

where the complementary complex error function is defined by

$$\mathrm{erfc}(z)\equiv\frac{2}{\sqrt{\pi}}\int_z^{+\infty}e^{-t^2}dt. \tag{A14}$$

The function $\tilde{D}(z)$ is directly proportional to the function $w(z)$ discussed in Chapter 7 of Abramowitz and Stegun (1972), in which many useful properties are listed. An efficient numerical algorithm for the evalua-

tion of this function in the complex plane is implemented in the program LISAQMC.F (cf. Appendix D).

We now discuss longer-range hopping on the $d=\infty$ cubic lattice (Müller-Hartmann, 1989a). A first possibility is to consider only hopping to those neighbors of a given site that can be reached in m jumps *along a given coordinate axis*. The number of such distant neighbors is always $2d$, independently of m, so the kinetic energy is scaled as

$$\epsilon_{\mathbf{k}}=\sum_{m=1}^{\infty} t_m \epsilon_m(\mathbf{k}), \quad \epsilon_m(\mathbf{k})\equiv -\frac{2}{\sqrt{2d}}\sum_{i=1}^{d}\cos(mk_i), \tag{A15}$$

where the t_m's are hopping parameters. Extending the asymptotic expansion above to this case, it is easy to see that the density of states *remains Gaussian*, with the parameter t in (A5) given by

$$t^2=\sum_{m=1}^{\infty} t_m^2. \tag{A16}$$

The reason for this is that the hopping energies $\epsilon_m(\mathbf{k})$ become statistically independent in the limit of high dimensions. Since the dynamical mean-field equations for the one-particle Green's function in a paramagnetic phase only involve the density of states $D(\epsilon)$, we see that these extra hoppings leave unchanged all one-particle properties. However, it is expected that *two-particle response functions* are affected, and that the possible symmetry breaking towards a magnetic phase at low temperature are different for different choices of t_m's corresponding to the same value of t. In particular, note that the perfect nesting condition $\epsilon_{\mathbf{k}+\mathbf{Q}}=-\epsilon_{\mathbf{k}}$ [with $\mathbf{Q}=(\pi,...,\pi)$] is no longer satisfied if hopping is allowed to neighbors with an *even* value of m. As we shall see below, the momentum dependence of response functions is affected by the t_m's.

More general forms of longer-range hoppings do modify the density of states, however. We consider the simple model which has hopping to any of the $2d$ nearest neighbors, and to the $2d(d-1)$ next nearest neighbors (along the diagonals of an elementary cell). The kinetic energy is written as

$$\epsilon_{\mathbf{k}}=t_1\epsilon_{nn}(\mathbf{k})+t_{11}\epsilon_{nnn}(\mathbf{k}), \tag{A17}$$

$$\epsilon_{nn}(\mathbf{k})=-\frac{2}{\sqrt{2d}}\sum_{i=1}^{d}\cos k_i, \tag{A18}$$

$$\epsilon_{nnn}(\mathbf{k})=-\frac{4}{\sqrt{2d(d-1)}}\sum_{i=2}^{d}\sum_{j=1}^{i-1}\cos k_i\cos k_j. \tag{A19}$$

The mean-square energy is now given by

$$\langle\epsilon_{\mathbf{k}}^2\rangle=t_1^2+t_{11}^2. \tag{A20}$$

The density of states is no longer Gaussian, however, because $\epsilon_{nn}(\mathbf{k})$ and $\epsilon_{nnn}(\mathbf{k})$ are not independent variables. Indeed, a simple calculation shows that

$$\lim_{d\to\infty}\epsilon_{nn}(\mathbf{k})^2=1-\sqrt{2}\epsilon_{nnn}(\mathbf{k}), \tag{A21}$$

so that the kinetic energy can be rewritten, as $d\to\infty$:

$$\epsilon_{\mathbf{k}}\to t_1\epsilon_{nn}(\mathbf{k})+\frac{t_{11}}{\sqrt{2}}[1-\epsilon_{nn}(\mathbf{k})^2]. \tag{A22}$$

The density of states is then easily found from the known Gaussian distribution of the variable $\epsilon_{nn}(\mathbf{k})$, and reads (Müller-Hartmann, 1989a)

$$D(\epsilon)=\sqrt{(2/\pi)}\,\frac{1}{E}\cosh(Et_1/2t_{11}^2)e^{(t_1^2-E^2)/4t_{11}^2},$$
$$E(\epsilon)\equiv[t_1^2+2t_{11}^2-2\sqrt{2}t_{11}\epsilon]^{1/2}, \tag{A23}$$

where it is understood that $D(\epsilon)=0$ whenever $E(\epsilon)$ is not real. $D(\epsilon)$ has a finite band edge, with a square-root divergence. The ratio t_{11}/t_1 is a parameter controlling the degree of magnetic frustration of the model.

We finally mention a last example, which has been studied by Santoro *et al.* (1993) and consists in the $d=\infty$ generalization of the honeycomb ($d=2$) or diamond ($d=3$) lattices. A generalization of these lattices to arbitrary dimensions can be defined as a *bipartite* lattice such that (i) each lattice site has $d+1$ nearest neighbors at a distance $a=1$, belonging to the opposite sublattice, and (ii) denoting by $\mathbf{e}_i$, $i=1,\ldots,d+1$, the set of $d+1$ unit vectors connecting lattice sites to its neighbors, any pair of these vectors make a constant angle:

$$\mathbf{e}_i\cdot\mathbf{e}_j=-1/d, \quad i\neq j. \tag{A24}$$

The common feature of this class of lattices in arbitrary dimensions is that the density of state is symmetric $D(\epsilon)=D(-\epsilon)$ but vanishes linearly at the Fermi energy for the half-filled case $D(\epsilon)\propto|\epsilon|$, so that one has a "semimetal." For $d\to\infty$, the density of states takes the limiting form:

$$D(\epsilon)=\frac{|\epsilon|}{t^2}e^{-\epsilon^2/2t^2}. \tag{A25}$$

In Fig. 85, a comparison is made between this limiting form and the density of states of the honeycomb ($d=2$) and diamond ($d=3$) lattices. These lattices are bipartite, but not nested, so that the critical value of U for antiferromagnetic long-range order at half-filling is nonzero [and found by Santoro *et al.* (1993) to be $U_c/t\simeq 2.3$ for $d\to\infty$].

2. Momentum dependence of response functions

We shall now discuss the momentum dependence of two-particle response functions on $d=\infty$ lattices, concentrating for simplicity on the hypercubic lattice with nearest-neighbor hopping. As shown in Sec. IV, the momentum dependence is entirely contained in the particle-hole bubble:

$$\tilde{\chi}_{\mathbf{q}}^0(i\nu,;i\omega)\equiv-\sum_{\mathbf{k}}G(\mathbf{k},i\nu)G(\mathbf{k}+\mathbf{q},i\nu+i\omega)$$
$$=-\sum_{\mathbf{k}}\frac{1}{\zeta_\nu-\epsilon_{\mathbf{k}}}\frac{1}{\zeta_{\nu+\omega}-\epsilon_{\mathbf{k}+\mathbf{q}}}, \tag{A26}$$

where $\zeta_\nu\equiv i\nu+\mu-\Sigma(i\nu)$. This can be rewritten:

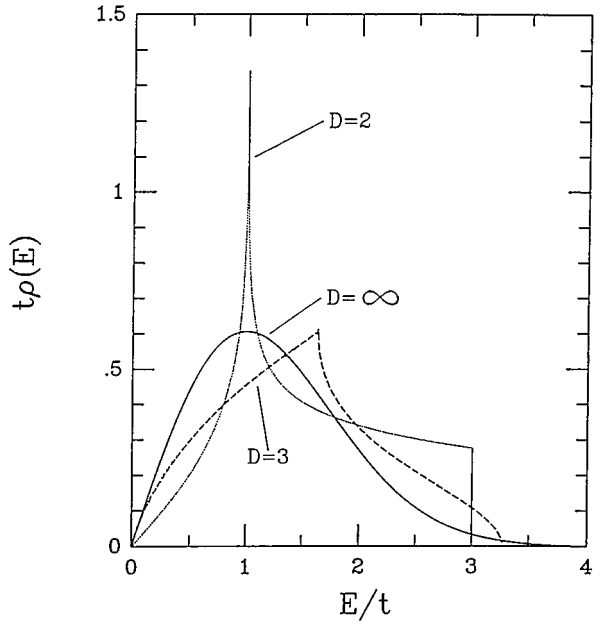

FIG. 85. Density of states of the generalized diamond lattice for various dimensionalities. From Santoro *et al.* (1993).

$$\tilde{\chi}^0_{\mathbf{q}}(i\nu;i\omega) = -\int_{-\infty}^{+\infty} d\epsilon_1 D(\epsilon_1) \int_{-\infty}^{+\infty} d\epsilon_2 D(\epsilon_2) \times \frac{\Delta_{\mathbf{q}}(\epsilon_1,\epsilon_2)}{(\zeta_\nu - \epsilon_1)(\zeta_{\nu+\omega} - \epsilon_2)}, \tag{A27}$$

where

$$\Delta_{\mathbf{q}}(\epsilon_1,\epsilon_2) \equiv \sum_{\mathbf{k}} \delta(\epsilon_{\mathbf{k}} - \epsilon_1)\,\delta(\epsilon_{\mathbf{k}+\mathbf{q}} - \epsilon_2) \tag{A28}$$

The function $\Delta_{\mathbf{q}}(\epsilon_1,\epsilon_2)$ measures the distribution of energies of a particle-hole pair of momentum $\mathbf{q}$. It is convenient to consider the Fourier transform:

$$\Delta_{\mathbf{q}}(s_1,s_2) \equiv \int_{-\infty}^{+\infty} d\epsilon_1 \int_{-\infty}^{+\infty} d\epsilon_2 e^{i(s_1\epsilon_1 + s_2\epsilon_2)} \Delta_{\mathbf{q}}(\epsilon_1,\epsilon_2), \tag{A29}$$

which reads

$$\Delta_{\mathbf{q}}(s_1,s_2) = \int \frac{d^d k}{(2\pi)^d} \exp\left\{ \frac{2it}{\sqrt{2d}} \left[s_1 \sum_{i=1}^{d} \cos k_i + s_2 \sum_{i=1}^{d} \cos(k_i + q_i) \right] \right\}. \tag{A30}$$

As above, the exponential can be expanded in powers of $1/\sqrt{d}$, and the averages over the Brillouin zone are easily performed, with

$$\langle \cos k_i \cos(k_i + q_i) \rangle = \langle \cos^2 k_i \rangle \cos q_i - \langle \cos k_i \sin k_i \rangle \sin q_i = \frac{1}{2} \cos q_i \tag{A31}$$

So that, for $d=\infty$,

$$\Delta_{\mathbf{q}}(s_1,s_2) = \exp\left(-\frac{t^2}{2} [s_1^2 + s_2^2 + 2X(\mathbf{q}) s_1 s_2] \right). \tag{A32}$$

As discussed in Sec. IV, the $\mathbf{q}$ dependence is entirely contained in the parameter

$$X(\mathbf{q}) = \frac{1}{d} \sum_{i=1}^{d} \cos q_i . \tag{A33}$$

The Fourier transform of Eq. (A32) yields the final expression:

$$\Delta_{\mathbf{q}}(\epsilon_1,\epsilon_2) = \frac{1}{2\pi t^2 \sqrt{1-X^2}} \exp - \frac{1}{2t^2(1-X^2)} \times (\epsilon_1^2 + \epsilon_2^2 - 2X\epsilon_1\epsilon_2), \tag{A34}$$

which can be used into (A27) for the computation of $\tilde{\chi}^0_{\mathbf{q}}(i\nu;i\omega)$. Note that $\Delta_{\mathbf{q}}(\epsilon_1,\epsilon_2)$ takes a simpler form for the uniform wave vector $\mathbf{q}=\mathbf{0}$ ($X=+1$), the nesting wave vector $\mathbf{q}=\mathbf{Q}$ ($X=-1$), and a generic wave vector corresponding to $X=0$:

$$\text{Generic } \mathbf{q} \ (X=0): \quad \Delta_{\mathbf{q}}(\epsilon_1,\epsilon_2) = D(\epsilon_1) D(\epsilon_2), \tag{A35}$$

$$\mathbf{q}=\mathbf{0} \ (X=+1): \quad \Delta_{\mathbf{q}}(\epsilon_1,\epsilon_2) = \delta(\epsilon_1 - \epsilon_2) D(\epsilon_1), \tag{A36}$$

$$\mathbf{q}=\mathbf{Q} \ (X=-1): \quad \Delta_{\mathbf{q}}(\epsilon_1,\epsilon_2) = \delta(\epsilon_1 + \epsilon_2) D(\epsilon_1), \tag{A37}$$

leading to the expressions (72) given in Sec. IV.

We note finally that the $\mathbf{q}$ dependence of two-particle response functions depends crucially on the specific lattice. Two lattices having the same density of states (and hence the same one-particle Green's functions in the absence of long-range order) may well have different response functions. An example is provided by the model with longer-range hopping along the coordinate axis, Eq. (A15), which always has a Gaussian density of states. The above expression (A34) of $\Delta_{\mathbf{q}}(\epsilon_1,\epsilon_2)$ in terms of X still holds for this model, but the $\mathbf{q}$ dependence of $X(\mathbf{q})$ is modified, namely,

$$X(\mathbf{q}) = \frac{1}{d} \sum_{m=1}^{\infty} \frac{t_m^2}{t^2} \sum_{i=1}^{d} \cos(m q_i). \tag{A38}$$

Note in particular that $X(\pi,\ldots,\pi)=-1$ only if there is no hoppings to neighbors with an even value of m. If such hoppings are present, no wave vector satisfies $X=-1$, reflecting the absence of nesting.

3. Fermions on the Bethe lattice

We conclude this appendix by summarizing some useful properties of the Bethe lattice and its large connectivity limit. The Bethe lattice of connectivity z is the tree-like structure displayed in Fig. 86. It is bipartite for all values of z. The special case $z=2$ yields a one-dimensional lattice. Except in this case, there is no simple Fourier transform on these lattices, and it is very convenient to use the cavity method of Sec. III.A. Let us derive the density of states of tight binding electrons

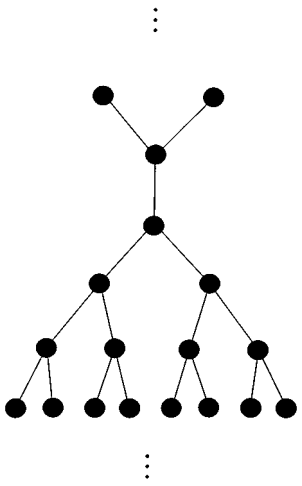

FIG. 86. Bethe lattice (depicted here with connectivity $z=3$).

with nearest-neighbor hopping $t_{ij}=t/\sqrt{z}$, for arbitrary connectivity z. We concentrate on site o and perform the Gaussian integration over all other sites (Fig. 86). Setting $\zeta \equiv i\omega_n+\mu$, this yields

$$G_{oo}^{-1}(\zeta)=\zeta-\frac{t^2}{z}\sum_{\langle i,o\rangle} G_{ii}^{(o)}=\zeta-t^2 G_{ii}^{(o)}. \tag{A39}$$

In this equation i denotes a neighbor of o and $G_{ii}^{(o)}$ is the Green's function of site i *once o has been removed*. Translation invariance has been used, all sites i being identical. For finite connectivity however, $G_{ii}^{(o)}$ does not coincide with G_{oo} even in the limit of an infinite lattice. This is because the local topology has been changed when removing site o: each neighbor i now has only $z-1$ nearest neighbors. For large connectivity, this is of course a $1/z$ effect, and $G_{ii}^{(o)}$ can be identified to G_{oo} in the equation above, yielding a closed formula. Even for finite connectivity however, the elimination process can be taken one step further, performing the Gaussian integration over the $z-1$ neighbors of each site i. This yields

$$[G_{ii}^{(o)}]^{-1}=\zeta-(z-1)\,\frac{t^2}{z}\,G_{jj}^{(o,i)}. \tag{A40}$$

In this equation, $G_{jj}^{(o,i)}$ denotes the Green's function of a neighbor j of i, in the truncated tree where both sites o and i have been removed. For an infinite lattice, j is entirely similar to i, so that $G_{ii}^{(o)}=G_{jj}^{(o,i)}$. This yields a closed equation for this quantity:

$$\frac{z-1}{z}\,t^2[G_{ii}^{(o)}]^2-\zeta G_{ii}^{(o)}+1=0, \tag{A41}$$

from which the local Green's function $G\equiv G_{oo}$ [which is also the Hilbert transform $\tilde{D}(\zeta)$ of the density of states] is finally obtained as [for $\mathrm{Im}(\zeta)>0$]

$$G\equiv\tilde{D}(\zeta)=\frac{(z-2)\zeta-z\sqrt{\zeta^2-4(z-1)t^2/z}}{2(zt^2-\zeta^2)}. \tag{A42}$$

The density of states $D(\epsilon)=-\mathrm{Im}G(\epsilon+i0^+)/\pi$ thus reads

$$D(\epsilon)=\frac{\sqrt{\epsilon^2-4(z-1)t^2/z}}{2\pi(t^2-\epsilon^2/z)}. \tag{A43}$$

(One can check that the familiar $d=1$ expression can be recovered for $z=2$.) Taking the $z\to\infty$ limit yields the expressions often used in this article:

$$G\equiv\tilde{D}(\zeta)=\frac{\zeta-\sqrt{\zeta^2-4t^2}}{2t^2},\quad D(\epsilon)=\frac{\sqrt{\epsilon^2-4t^2}}{2\pi t^2}. \tag{A44}$$

It may also be useful to quote the expression of the reciprocal function $R(G)$ of the Hilbert transform $\tilde{D}(\zeta)$, i.e., such that $R(\tilde{D}(\zeta))=\zeta$. For arbitrary connectivity, it is the solution of the quadratic equation:

$$(z-1)R^2+\frac{(z-1)(z-2)}{G}R-(z-1)^2\left(\frac{z}{z-1}\,t^2+\frac{1}{G^2}\right)=0. \tag{A45}$$

For $z\to\infty$, one recovers (Sec. II)

$$R(G)=t^2G+\frac{1}{G}. \tag{A46}$$

APPENDIX B: DETAILS OF THE MONTE CARLO ALGORITHM

In this Appendix, we first sketch the derivation of some of the formulas in Sec. VI.A.1, and show the equivalence of the Hirsch-Fye approach with the Blanckenbeckler, Scalapino, and Sugar algorithm. We also provide some guidance for the QMC programs provided with this article. Finally, details are given on the numerical implementation of the self-consistency condition.

1. Some derivations

Equation (139) for the discretized partition function can be established by making use of the following identity:

$$Tr_{c_i^+,c_i}\{e^{-\Sigma_{ij}c_i^+A_{ij}c_j}e^{-\Sigma_{ij}c_i^+B_{ij}c_j}e^{-\Sigma_{ij}c_i^+C_{ij}c_j}\}\equiv\det[1+e^{-A}e^{-B}e^{-C}], \tag{B1}$$

and of its generalization to more than three matrices. Equation (B1) is easily derived using the rules of Gaussian integration for Grassmann variables, and a very instructive elementary derivation can be found in (Hirsch, 1985). The equivalence of $\det \mathscr{O}_{s_1,\ldots,s_L}$ with the Blanckenbeckler, Scalapino, and Sugar formula Eq. (139) can then be shown by Gaussian elimination (replacing successively the first row of $\mathscr{O}$ by multiples of rows $L,L-1,\ldots,1$, $\{\mathscr{O}_{1i}\}_{i=1,\ldots,L}\to\{\mathscr{O}_{1i}-B_LB_{L-1}\cdots B_{L-k+1}\times\mathscr{O}_{L-k+1,i}\}_{i=1,\ldots,L}$ for $k=0,1,\ldots,L-1$).

The identity $g^{\Delta\tau}_{s_1,\ldots,s_L} = \mathscr{O}^{-1}_{s_1,\ldots,s_L}$ is easily established in a similar way. It is quite useful to consider the simple example of a 3×3 matrix (of *matrices* B_i), for which we explicitly write down the inverse.

$$\mathscr{O}=\begin{pmatrix} 1 & 0 & B_3 \\ -B_1 & 1 & 0 \\ 0 & -B_2 & 1 \end{pmatrix}, \tag{B2}$$

$$\mathscr{O}^{-1}=\begin{pmatrix} \{1+B_3B_2B_1\}^{-1} & -B_3B_2\{1+B_1B_3B_2\}^{-1} & -B_3\{1+B_2B_1B_3\}^{-1} \\ B_1\{1+B_3B_2B_1\}^{-1} & \{1+B_1B_3B_2\}^{-1} & -B_1B_3\{1+B_2B_1B_3\}^{-1} \\ B_2B_1\{1+B_3B_2B_1\}^{-1} & B_2\{1+B_1B_3B_2\}^{-1} & \{1+B_2B_1B_3\}^{-1} \end{pmatrix}. \tag{B3}$$

The reader will easily be able to verify Eq. (B3) and to generalize it for arbitrary L. Manifestly, Eq. (B3) reproduces Eq. (140).

To derive the Dyson equation it is useful to consider the matrix $\mathscr{O}\exp(-V)$ with the $Ln_s\times Ln_s$ matrix

$$e^{-\tilde{V}}_{s_1,\ldots,s_L}=\begin{pmatrix} e^{-V(s_1)} & \cdot & \cdot & 0 \\ \cdot & e^{-V(s_2)} & \cdot & \cdot \\ \cdot & \cdot & \cdot & \cdot \\ 0 & \cdot & \cdot & e^{-V(s_L)} \end{pmatrix}; \tag{B4}$$

$\mathscr{O}\exp(-\tilde{V})$ is therefore a matrix which depends on $(s_1,\ldots,s_L)$ only in the space- and time-diagonal elements

$$\mathscr{O}_{s_1,\ldots,s_L}e^{-\tilde{V}}_{s_1,\ldots,s_L}-\mathscr{O}_{s'_1,\ldots,s'_L}e^{-\tilde{V}}_{s'_1,\ldots,s'_L}=e^{-\tilde{V}}_{s_1,\ldots,s_L}-e^{-\tilde{V}}_{s'_1,\ldots,s'_L}. \tag{B5}$$

Abbreviating $g\equiv g_{s_1,\ldots,s_L}$ and $g'\equiv g_{s'_1,\ldots,s'_L}$, etc., and using $\mathscr{O}=g^{-1}$, it is very easy to see that Eq. (B5) leads to $\exp(V'-V)g'-g=g[\exp(V'-V)-1]g'$, which is equivalent to Eq. (125).

2. Numerical implementation of the QMC and Gray code enumeration

As described in the main body of the paper, the Monte Carlo procedure consists of two independent parts (single impurity problem, self-consistency). This structure is mirrored in the setup of our numerical program, which consists of two parts: LISAQMC.F and LISASELF.F. The programs communicate with each other via files that contain the current values of $G(\tau_i)$ and $\mathscr{G}_0(\tau_i)$.

In the program LISAQMC.F, the different parts of the algorithm are distributed over a few subroutines, in a way explained in the following table:

function	purpose	Equation
DETRAT	calculate determinant ratio	Eq. (131)
INITIAL	initialize ($\mathscr{G}^{\Delta\tau}_0(\tau)\rightarrow\mathscr{O}^{-1}_{0,\ldots,0}(\tau,\tau')$)	−
RECORD	perform fast update	Eq. (130)
UPDATE	compute $G^{\Delta\tau}_{s_1,\ldots,s_L}$ from $\mathscr{G}^{\Delta\tau}_0$	Eq. (128)

Besides the Monte Carlo update, the program LISAQMC.F also allows one to compute physical Green's functions by *complete enumeration* using the Gray code. In this method, *all* possible configurations of Ising spins are visited in an order in which every configuration of spins $(s_1,\ldots,s_L)$ differs from the following one $(s'_1,\ldots,s'_L)$ in a single index only ($s_i = s'_i$, except for a single value of i). More precisely, the configurations are enumerated by flipping the spin s_i with the largest possible value of i, provided that this flip does not yield a previously visited configuration. As an example, let us give the first steps of a Gray code enumeration for L=5:

$$\begin{array}{cc} \begin{bmatrix} + & + & + & + & + \\ + & + & + & + & - \\ + & + & + & - & - \\ + & + & + & - & + \\ + & + & - & - & + \\ + & + & - & - & - \\ + & + & - & + & - \\ + & + & - & + & + \\ & & \vdots & & \end{bmatrix} & \begin{bmatrix} + & + & + & + & + \\ + & + & + & + & - \\ + & + & + & - & + \\ + & + & + & - & - \\ + & + & - & + & + \\ + & + & - & + & - \\ + & + & - & - & + \\ + & + & - & - & - \\ & & \vdots & & \end{bmatrix} \\ \text{Gray code} & \text{standard} \end{array} \tag{B6}$$

This algorithm can be simply programmed (cf. Press *et al.*, 1991). By doing this, we can again compute the Green's function $G^{\Delta\tau}_{s_1,\ldots,s'_k,\ldots,s_L}$ from $G^{\Delta\tau}_{s_1,\ldots,s_k,\ldots,s_L}$ by the fast update RECORD [in $O(L^2)$ steps], rather than having to compute it from $\mathscr{G}^{\Delta\tau}_0$ in $O(L^3)$ steps (using UPDATE). Naturally, the averages must now be computed by including the determinant in the statistical weight. Furthermore, the normalization needs also be calculated. Further details can be found in the program LISAQMC.F.

Both the Monte Carlo and the exact enumeration include checks to avoid loss of precision. In the Monte Carlo algorithm, this is done from time to time by confronting the result of subroutine UPDATE with the single spin-flip updates. In the exact enumeration calculation, the precision can be evaluated simply by restarting the Gray code with an initial spin configuration $(s_1,\ldots,s_L)$ different from (1,...,1).

Finally, we briefly discuss the discretization error in $\Delta\tau$ which is introduced by the Trotter breakup. Let us first

note the remarkable fact that besides this error—i.e., the passage from Z [Eq. (116)] to $Z^{\Delta\tau}$ [Eq. (120)]—*no* other systematic error is introduced. Due to the cyclic nature of the fermion trace

$$\mathrm{Tr}\ \exp(-\tau\mathscr{H}_0)\exp(-\tau\mathscr{H}_1)$$
$$=\mathrm{Tr}\ \exp(-\tau\mathscr{H}_0/2)\exp(-\tau\mathscr{H}_1)\exp(-\tau\mathscr{H}_0/2), \quad \text{(B7)}$$

Eq. (120) can be obtained from Eq. (116) using the third-order approximation in $\Delta\tau$:

$$e^{-\Delta\tau(\mathscr{H}_0+\mathscr{H}_1)}=e^{-\Delta\tau\mathscr{H}_0/2}e^{-\Delta\tau\mathscr{H}_1}e^{-\Delta\tau\mathscr{H}_0/2}+O(\Delta\tau^3), \quad \text{(B8)}$$

which results in an $O(\Delta\tau^2)$ discretization error for $Z^{\Delta\tau}=Z+O(\Delta\tau^2)$. An important point is that in order to keep the systematic errors introduced by the Trotter breakup under control, one should not use a value of the argument that is too large for the exponential in Eq. (119). As a working rule one may use $\Delta\tau U/2<1$, but this depends of course on the quantity considered.

Regarding the Green's function, it has been established that the error committed when solving the Anderson impurity model with the Hirsch-Fye algorithm is also of order $\Delta\tau^2$ (Fye, 1986). In the LISA context (i.e., with the additional complication of the self-consistency condition), this observation still appears to hold empirically (see, e.g., the inset of Fig. 14).

3. Numerical implementation of the self-consistency condition

As indicated in the main text, the Fourier transform of the discretized $G^{\Delta\tau}(\tau)$ is not calculated by a straightforward fast Fourier transform. Rather, it is an interpolation of $G(\tau)$ which is Fourier transformed. In the program FOURIER, a (natural) spline interpolation

$$G^{\mathrm{interpol}}(\tau)=\alpha_i+\beta_i(\tau-\tau_i)+\gamma_i(\tau-\tau_i)^2+\delta_i(\tau-\tau_i)^3,$$
$$\tau_i<\tau<\tau_{i+1}, \quad \text{(B9)}$$

is computed. The coefficients $\alpha_i,\beta_i,\gamma_i,\delta_i$ are analytically calculated from the $G^{\Delta\tau}(\tau_i)$ such that $G^{\mathrm{interpol}}(\tau)$ is a twice continuously differentiable function (cf. Stoer and Bulirsch, 1980). From $G^{\mathrm{interpol}}(\tau)$ it is a simple matter to calculate the piecewise integral $\int_{-\beta}^{\beta}d\tau G^{\mathrm{interpol}}(\tau)\ \exp(i\tau\omega_n)$, which yields $G(i\omega_n)$. Explicit formulas can be found in the subroutine FOURIER.

APPENDIX C: DETAILS OF THE EXACT DIAGONALIZATION ALGORITHM

In this appendix, we assemble a few details on the exact diagonalization algorithms and make contact with the programs LISADIAG.F and LISALANC.F. Both programs split up into three main parts, of which the first and the third are identical.

(i) The construction of $\mathscr{H}$ (or of the nonzero elements of the matrix) is achieved by the subroutine BUILDBASIS, which constructs the vectors $|i\rangle$ defined in Eq. (143), for each of the sectors $(n^{\uparrow},n^{\downarrow})$ at a time. After construction of the Hilbert space, the Hamiltonian is built with the subroutines ADAG and A, which allow the computing of the vectors $a_j^{+}|i\rangle$ and $a_j|i\rangle$. In the exact diagonalization program, the matrix $\mathscr{H}$ is then diagonalized exactly (subroutine DIAG), using the QL algorithm (Stoer and Bulirsch, 1980). For reasons of simplicity, the eigenvectors (which are later needed for the calculation of Green's functions) are then dumped onto file storage.

In the Lanczos procedure, the ground-state eigenvalues for *all* sectors are calculated by diagonalizing $\mathscr{H}$ in an (approximately) invariant subspace spanned by vectors $\mathscr{H}^n|p_0\rangle$, $n=0,\ldots,n_L$. The power of the Lanczos algorithm stems from the fact that usually a small number of vectors ($n_L\sim 100$, largely independent of the dimension of $\mathscr{H}$) allows an extremely precise computation of the ground-state eigenvalue and eigenvector—cf. Lin and Gubernatis (1993) for a practical introduction to the Lanczos method, and Golub and Van Loan (1983) for a thorough discussion. The diagonalization of $\mathscr{H}$, restricted to the indicated subspace, is again performed using the QL algorithm. This first Lanczos procedure is coded in the subroutine FINDGROUNDSTATE1. A simple iterative scheme (vector iteration) then verifies (in the routine FINDGROUNDSTATE), that the ground state has indeed been found to machine precision.

(ii) The calculation of the Green's function is done in a straightforward manner in the case of the exact diagonalization algorithm: to calculate $\langle i|d^{+}|j\rangle$, the corresponding vectors are fetched from disk storage and computed. In the case of the Lanczos procedure, the vector $d^{+}|\mathrm{g.s.}\rangle$ is initially formed, where $|\mathrm{g.s.}\rangle$ is the overall ground state of the Hamiltonian (the lowest of the sector-wise ground states computed being FINDGROUNDSTATE1). The procedure has to be generalized in the case of a ground-state degeneracy (several sectors with the same ground-state eigenvalue). The Green's function can then be calculated from a *second* Lanczos procedure, with initial vector $|p_0\rangle=d^{+}|gs\rangle$ (cf. Haydock *et al.*, 1975). It is straightforward to determine the parameters of the continuous fractions Eq. (146):

$$a_i^{\alpha}=\langle p_i^{\alpha}|H|p_i^{\alpha}\rangle, \quad b_i^{\alpha 2}=\frac{\langle p_i^{\alpha}|p_i^{\alpha}\rangle}{\langle p_{i-1}^{\alpha}|p_{i-1}^{\alpha}\rangle}, \quad \text{(C1)}$$

where $\alpha=\rangle,\langle$ and $|p_0^{>}\rangle=d^{\dagger}|\mathrm{g.s.}\rangle$, $|p_0^{<}\rangle=d|\mathrm{g.s.}\rangle$ and

$$|p_{i+1}^{\alpha}\rangle=H|p_i^{\alpha}\rangle-a_i^{\alpha}|p_i^{\alpha}\rangle-b_i^{\alpha 2}|f_{i-1}^{\alpha}\rangle \quad \text{(C2)}$$

and $b_0^{\alpha}=0$. The construction of the $|p_i^{\alpha}\rangle$ is done in the subroutine LANCZOS. The evaluation of the continued fractions is programmed in the subroutine COMPUTEGREEN. Again, care has to be taken in the case of a degenerate ground state.

(iii) After computing the Green's function, we are able to iterate once through the self-consistency loop. The projection of the "new" bath Green's function $\mathscr{G}_0\rightarrow\mathscr{G}_0^{n_s}$ can be easily assembled from a routine, CALCG0, which evaluates $\mathscr{G}_0^{n_s}$ for a given set of parameters $V,\tilde{\epsilon}$, another one, ENERGY, which calculates the mismatch between $\mathscr{G}_0^{n_s}$ and $\mathscr{G}_0$, and a minimization rou-

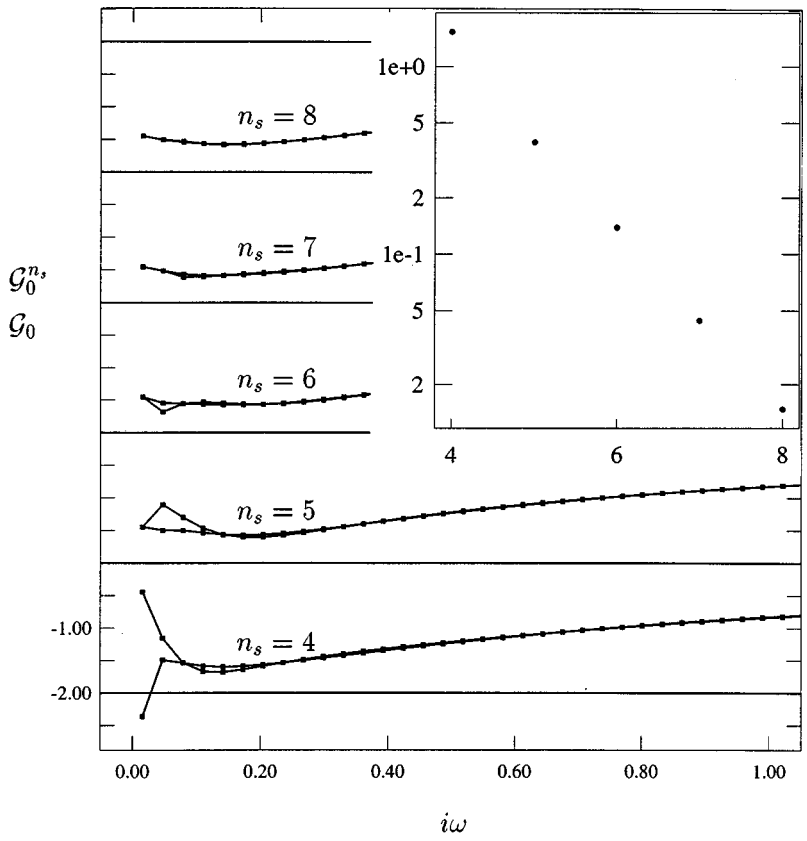

FIG. 87. Effective bath Green's functions $\mathcal{G}_0$ and $\mathcal{G}_0^{n_s}$ at self-consistency for the half-filled Hubbard model at $U=3D/\sqrt{2}$, $\beta D/\sqrt{2}=200$ for $n_s=4,\ldots,8$. Curves labeled $n_s=4,\ldots,6$ are for the exact diagonalization algorithm at finite temperature β. The curves at $n_s=7$ and 8 were obtained by the Lanczos algorithm, in which β only serves as a discretization parameter defining the grid of imaginary frequencies. The inset shows the maximum difference between $\mathcal{G}_0$ and $\mathcal{G}_0^{n_s}$ as a function of n_s (note the semilogarithmic scale).

tine, (conjugate-gradient routine MINIMIZE), which determines the optimal function $\mathcal{G}_0^{n_s}$.

In Fig. 87, we give an example of the comparison between $\mathcal{G}_0^{n_s}(i\omega)$ and $\mathcal{G}_0(i\omega)$, again for the half-filled Hubbard model at $U/t=3$ for $n_s=3,\ldots,8$ and at $\beta D\sqrt{2}=200$. Naturally, the agreement between the two quantities is the least acceptable at *small* frequencies, closest to the real axis. However, at larger frequencies, $\mathcal{G}_0^{n_s}$ and $\mathcal{G}_0$ agree for all intents and purposes. For example, at $\omega=0.1$, the two solutions differ by less than 10^{-5}, and there is virtually *no* detectable dependence on n_s. The precision obtained is thus quite spectacular. The mismatch between $\mathcal{G}_0$ and $\mathcal{G}_0^{n_s}$ decreases nicely by a constant factor as n_s is incremented by one, as shown in the inset of the figure. This scaling of the "discretization" error with the number of sites is an empirical fact, but a highly plausible one: In increasing the number of sites, the Hilbert space of the Hamiltonian increases exponentially, and there is a much larger number of basis vectors, of which the function $\mathcal{G}_0^{n_s}$ can be constructed. This scaling would not be observed if the positions of the conduction electrons were taken fixed.

It is very interesting to compare the full diagonalization algorithm with the Lanczos procedure, and the interesting reader is invited to perform such a comparison. The full diagonalization program contains an option which allows computing zero-temperature Green's functions (and other response functions), which (should) agree to machine precision with the ones of the Lanczos algorithm. The zero-temperature Green's functions, and other response functions may however appreciably differ from the (self-consistent) results at very small finite temperatures. This is as it should be, and translates the importance of low-temperature scales, for example, in the vicinity of the Mott transition. Notice that most of the low-temperature variability is brought in through the self-consistency condition: at a *given* $\mathcal{G}_0^{n_s}$, the calculated Green's functions almost coincide, but are driven apart under repeated iterations. As was mentioned in several places throughout the article, the impurity model is usually uncritical, and the critical effects are brought in by the lattice, i.e., by the self-consistency condition.

APPENDIX D: ACCESS TO FORTRAN PROGRAMS

The programs described in this section may be obtained by ANONYMOUS FTP, or in the WWW.

To access the programs by ftp, you should log on to ftp.lps.ens.fr. Register as "anonymous," and give your complete electronic address as the password. You should first retrieve a file called HOW-TO-GET-SOFTWARE, which will inform you about the availability of codes. This file also points you to the necessary auxiliary files and provides further information. Suppose your username is username@usernode.univ.edu. To retrieve the above file (and any other), you should proceed as follows:

ftp ftp.lps.ens.fr
Username: anonymous
Password: username@usernode.univ.edu
cd pub/users/lisa
ls
get HOW-TO-GET-SOFTWARE

The WWW access is via http://www.lps.ens.fr/~krauth

A short synopsis of the available programs is given in the following table:

Program	Purpose	Section
QMCEXAMPLE.F	small example by Blanckenbecler, Scalapino, and $\mathcal{O}^{-1}$, Hirsch-Fye algorithm	VI.A.1.e
LISAQMC.F	Hirsch-Fye algorithm	VI.A.1.c
LISASELF.F	Fourier transforms $\tau \rightarrow i\omega$, self-consistency	VI.A.1.d
LISADIAG.F	exact diagonalization, finite temperature	VI.A.2. C
LISALANC.F	Lanczos algorithm (zero temperature)	VI.A.2. C
LISAIPT0.F	iterated perturbation theory approximation (zero temperature)	VI.B.2
LISAIPT.F	iterated perturbation theory approximation (finite temperature)	VI.B.2

REFERENCES

[Preprint numbers refer to the archives cond-mat@babbage.sissa.it]

Abramowitz, M., and I. A. Stegun, 1972, *Handbook of Mathematical Functions* (Dover, New York).

Abrikosov, A. A., L. P. Gorkov, and I. E. Dzialoshinski, 1965, *Methods of Quantum Field Theory in Statistical Physics* (Pergamon, Elmsford, New York).

Affleck, I., and A. W. W. Ludwig, 1991, Nucl. Phys. B **352**, 849; **360**, 641.

Anders, F. B., 1995, Preprint No. cond-mat/9502020 (unpublished).

Anderson, P. W., 1961, Phys. Rev. **124**, 41.

Anderson, P. W., 1970, J. Phys. C **3**, 2439.

Anderson, P. W., G. Yuval, and D. R. Hamann, 1970, Phys. Rev. B **1**, 4464.

Andrei, N., K. Furuya, and J. H. Lowenstein, 1983, Rev. Mod. Phys. **55**, 331.

Anisimov, V. I., J. Zaanen, and O. K. Andersen, 1991, Phys. Rev. B **44**, 943.

Appelbaum, J. A., and D. R. Penn, 1969, Phys. Rev. **188**, 874.

Balatsky, A. V., and E. Abrahams, 1992, Phys. Rev. B **45**, 13125.

Bang, Y., C. Castellani, M. Grilli, G. Kotliar, R. Raimondi, and Z. Wang, 1992, Int. J. Mod. Phys. **6**, 531.

Beni, G., P. Pincus, and J. Kanamori, 1974, Phys. Rev. B **10**, 1896.

Berezinskii, V. L., 1974, JETP Lett. **20**, 287.

Bhatt, R. N., and D. S. Fisher, 1992, Phys. Rev. Lett. **68**, 3072.

Bickers, N. E., 1987, Rev. Mod. Phys. **59**, 845.

Blankenbecler, R., D. J. Scalapino, and R. L. Sugar, 1981, Phys. Rev D **24**, 2278.

Brandt, U., and C. Mielsch, 1989, Z. Phys. **75**, 365.

Brandt, U., and C. Mielsch, 1990, Z. Phys. **79**, 295.

Brandt, U., and C. Mielsch, 1991, Z. Phys. **82**, 37.

Brandt, U., and R. Schmidt, 1986, Z. Phys. **63**, 45.

Brandt, U., and R. Schmidt, 1987, Z. Phys. **67**, 43.

Brandt, U., and M. P. Urbanek, 1992, Z. Phys. **89**, 297.

Brinkman, W. F., and T. M. Rice, 1970, Phys. Rev. B **2**, 4302.

Bucher, B., Z. Schlesinger, P. C. Canfield, and Z. Fisk, 1994, Phys. Rev. Lett. **72**, 522.

Burley, D. M., 1972, in *Phase Transitions and Critical Phenomena*, edited by C. Domb and M. Green (Academic, New York), Vol. II.

Caffarel, M., and W. Krauth, 1994, Phys. Rev. Lett. **72**, 1545, and unpublished.

Cardy, J. L., 1981, J. Phys. A **14**, 1407.

Carter, S. A., T. F. Rosenbaum, J. M. Honig, and J. Spalek, 1992, Phys. Rev. Lett. **67**, 3440.

Carter, S. A., T. F. Rosenbaum, P. Metcalf, J. M. Honig, and J. Spalek, 1993, Phys. Rev. B **48**, 16841.

Castellani, C., C. DiCastro, D. Feinberg, and J. Ranninger, 1979, Phys. Rev. Lett. **43**, 1957.

Castellani, C., M. Grilli, and G. Kotliar, 1991, Phys. Rev. B **43**, 8000.

Castellani, C., G. Kotliar, R. Raimondi, M. Grilli, Z. Wang, and M. Rozenberg, 1992, Phys. Rev. Lett. **69**, 2009.

Castellani, C., C. R. Natoli, and J. Ranninger, 1978, Phys. Rev. B **18**, 4945.

Cava, R. J., B. Batlogg, J. J. Krajewski, R. Farrow, L. W. Rupp, A. E. White, K. Short, W. F. Peck, and T. Kometani, 1988, Nature **332**, 814.

Chakravarty, S., and J. Hirsch, 1982, Phys. Rev. B **25**, 3273.

Chen, 1994, Phys. Rev. Lett. **73**, 1982.

Ciuchi, S., F. de Pasquale, and D. Feinberg, 1995, Europhys. Lett. **30**, 151.

Ciuchi, S., F. de Pasquale, C. Masciovecchio, and D. Feinberg, 1993, Europhys. Lett. **24**, 575.

Clarke D. G., T. Giamarchi, and B. Shraiman, 1993, Phys. Rev. B **48**, 7070.

Coleman, P., 1987, Phys. Rev. B **35**, 5072.

Compte, C., and P. Nozieres, 1982, J. Phys. (Paris) **43**, 1069.

Costi, T. A. and A. C. Hewson, 1990, Physica B **163**, 179.

Cox, D. L., 1994, Physica B (to be published).

Cox, D. L., and A. E. Ruckenstein, 1993, Phys. Rev. Lett. **71**, 1613.
Cyrot, M., 1972, J. Phys. (Paris) **33**, 125.
Cyrot, M., and C. Lyon-Caen, 1975, J. Phys. (Paris) **36**, 253.
Dagotto, E., 1994, Rev. Mod. Phys. **66**, 763.
de Dominicis, C., I. Kondor, and T. Temesvari, 1991, J. Phys. A **24**, L301.
Dobrosavljevič, V., T. R. Kirkpatrick, and G. Kotliar, 1992, Phys. Rev. Lett. **69**, 1113.
Dobrosavljevič, V., and G. Kotliar, 1993, Phys. Rev. Lett. **71**, 3218.
Dobrosavljevič, V., and G. Kotliar, 1994, Phys. Rev. B **50**, 1430, and Acta Physica Polonica **85**, 21.
Doniach, S., 1977, Physica B **91**, 231.
Dworin, L., and A. Narath, 1970, Phys. Rev. Lett. **25**, 1287.
Economou, E. N., 1983, *Green's Functions in Quantum Physics* (Springer-Verlag, Berlin).
Edwards, D. M., 1993, J. Phys. Cond. Mat. **5**, 161.
Elliott, R. J., J. A. Krumhansl, and P. L. Leath, 1974, Rev. Mod. Phys. **46**, 465.
Emery, V., 1987, Phys. Rev. Lett. **58**, 2794.
Emery, V., and S. Kivelson, 1992, Phys. Rev. B **46**, 10812.
Emery, V., and S. Kivelson, 1993a, Physica C **209**, 597.
Emery, V., and S. Kivelson, 1993b, in *Strongly Correlated Electronic Materials*, edited by K. Bedell, Z. Wang, A. Balatzky and E. Abrahams (Addison-Wesley, Reading, MA).
Emery V., and S. Kivelson, 1995, unpublished.
Emery, V., S. Kivelson, and Q. Lin, 1990, Phys. Rev. Lett. **64**, 475.
Falicov, L. M., and J. C. Kimball, 1969, Phys. Rev. Lett. **22**, 997.
Fetter, A. L., and J. D. Walecka, 1971, *Quantum Theory of Many-Particle Systems* (McGraw-Hill, New York).
Finkelshtein, A. M., 1987, Sov. Phys. JETP **46**, 407.
Fisher, D. S., G. Kotliar, and G. Moeller, 1995, Phys. Rev. B **52**, 17112.
Fortin E., S. Fafard, and A. Mysyrowicz, 1993, Phys. Rev. Lett **70**, 3951.
Freericks, J. K., 1993a, Phys. Rev. B **47**, 9263.
Freericks, J. K., 1993b, Phys. Rev. B **48**, 14797.
Freericks, J. K., 1993c, Phys. Rev. B **48**, 3881.
Freericks, J. K., 1994, Phys. Rev. B **50**, 403.
Freericks, J. K., and M. Jarrell, 1994a, Phys. Rev. B **50**, 6939.
Freericks, J. K., and M. Jarrell, 1994b, in *Computer Simulations in Condensed Matter Physics*, edited by D. P. Landau, K. K. Mon, and H.-B. Schüttler (Springer, Berlin).
Freericks, J. K., and M. Jarrell, 1995a, Phys. Rev. Lett. **74**, 186.
Freericks, J. K., and M. Jarrell, 1995b, Phys. Rev. Lett. **75**, 2570.
Freericks, J. K., M. Jarrell, and D. J. Scalapino, 1993, Phys. Rev. B **48**, 6302.
Freericks, J. K., M. Jarrell, and D. J. Scalapino, 1994, Europhys. Lett. **25**, 37.
Freericks, J. K., and D. J. Scalapino, 1994, Phys. Rev. B **49**, 6368.
Fresard, R., and P. Wölfle, 1992, Int. J. Mod. Phys. B **6**, 685; **6**, 3087(E).
Frota, H. O., and L. N. Oliveira, 1986, Phys. Rev. B **33**, 7871.
Fu, C., and S. Doniach, 1994, Phys. Rev. B **49**, 2219.
Fu, C., and S. Doniach, 1995, Phys. Rev. B **51**, 17 439.
Fujimori, A., I. Hase, H. Namatame, Y. Fujishima, Y. Tokura, H. Eisaki, S. Uchida, K. Takegahara, and F. M. F. de Groot, 1992, Phys. Rev. Lett. **69**, 1796.
Fujimori, A., F. Minami, and S. Sugano, 1984, Phys. Rev. B **29**, 5225.
Fujimori, A., *et al.*, 1992, Phys. Rev. B **46**, 9841.
Furukawa, N., 1994, J. Phys. Soc. Jpn. **63**, 3214.
Furukawa, N., 1995, unpublished.
Furukawa, N., 1995a, J. Phys. Soc. Jpn. **64**, 2754.
Furukawa, N., 1995b, in *Proceedings of the 17th Taniguchi International Conference*, edited by (Springer Verlag, Berlin).
Furukawa, N., 1995c, J. Phys. Soc. Jpn. **64**, 2734.
Furukawa, N., 1995d, J. Phys. Soc. Jpn. **64**, 3164.
Furukawa, N. and M. Imada, 1993, Physica B **186-188**, 931.
Fye, R. M., 1986, Phys. Rev. B **33**, 6271.
Gagliano, E. R., E. Dagotto, A. Mereo, and F. C. Alcaraz, 1986, Phys. Rev. B **34**, 1677.
Georges, A., and G. Kotliar, 1992, Phys. Rev. B **45**, 6479.
Georges, A., G. Kotliar, and W. Krauth, 1993, Z. Phys. B **92**, 313.
Georges, A., G. Kotliar, and Q. Si, 1992, Int. J. Mod. Phys. B **6**, 705.
Georges, A., and W. Krauth, 1992, Phys. Rev. Lett. **69**, 1240.
Georges, A., and W. Krauth, 1993, Phys. Rev. B **48**, 7167.
Georges, A. and A. Sengupta, 1995, Phys. Rev. Lett. **74**, 2808.
Georges, A., and J. S. Yedidia, 1991, Phys. Rev. B 43, 3475.
Golub, G. H., and C. F. Van Loan, 1983, *Matrix Computations* (Baltimore University Press, Baltimore, MD).
Goodenough, J. B., 1968, Phys. Rev. **171**, 466.
Grilli, M., and G. Kotliar, 1990, Phys. Rev. Lett. **64**, 1170.
Gros, C., 1994, Phys. Rev. B **50**, 7295.
Gros, C., W. Wenzel, R. Valenti, G. Hülsenbeck, and J. Stolze, 1994, Europhys. Lett. **27**, 299.
Gubernatis, J. E., M. Jarrell, R. N. Silver, D. S. Sivia, 1991, Phys. Rev. B **44**, 6011.
Gubernatis, J. E., T. C. Olson, D. J. Scalapino, and R. L. Sugar, 1986, J. Stat. Phys. **43**, 831.
Gunnarson, O., and K. Schönhammer, 1983a, Phys. Rev. Lett. **50**, 604.
Gunnarson, O., and K. Schönhammer, 1983b, Phys. Rev. B **28**, 4315.
Gutzwiller, M. C., 1965, Phys. Rev. **137**, A1726.
Haldane, F. D. M., 1978a, Phys. Rev. Lett. **40**, 416 (Ph.D thesis, Univ. of Cambridge).
Haldane, F. D. M., 1978b, J Phys. C **11**, 5015.
Halvorsen, E., G. S. Uhrig, and G. Czycholl, 1994, Z. Phys. B **94**, 291.
Haydock, R., 1985, *The Recursion Method and Its Applications* (Springer-Verlag, Heidelberg).
Haydock, R., V. Heine, and M. J. Kelly, 1975, J. Phys. C **8**, 2591.
Held, K., M. Ulmke, and D. Volhardt, 1995, Preprint No. cond-mat/9505147.
Hewson, A. C., 1993, *The Kondo Problem to Heavy Fermions*, Cambridge Studies in Magnetism Vol. 2 (Cambridge University Press, Cambridge, England).
Hirsch, J. E., 1983, Phys. Rev. B **28**, 4059.
Hirsch, J. E., 1985, Phys. Rev. B **31**, 4403.
Hirsch, J. E., 1988, Phys. Rev. B **38**, 12 023.
Hirsch, J. E., and E. Fradkin, 1982, Phys. Rev. Lett. **49**, 402.
Hirsch, J. E., and E. Fradkin, 1983, Phys. Rev. B **27**, 4302.
Hirsch, J. E., and R. M. Fye, 1986, Phys. Rev. Lett. **56**, 2521.
Holstein, T., 1959, Ann. Phys. (N.Y.) **8**, 325.
Hong, J., and H. Y. Kee, 1995a, Phys. Rev. B **52**, 2415.
Hong, J., and H. Y. Kee, 1995b, Europhys. Lett. (to be published).

Hubbard, J., 1964, Proc. Roy. Soc. (London) A **281**, 401.
Hubbard, J., 1979, Phys. Rev. B **19**, 2626.
Hüfner, S., 1994, Adv. Phys. **43**, 183.
Hülsenbeck, G., and F. Stephan, 1994, Z. Phys. B **94**, 281.
Hwang, H. Y., S. W. Cheong, P. G. Radaelli, M. Morezio, and B. Batlogg, 1995, Phys. Rev. Lett. **75**, 914.
Iga, F., T. Nishiguchi, N. Shirakawa, K. Murata, Y. Nishihara, T. Ishii, Y. Uwatoko, and G. Oomi, 1995, Bull. Electrotechn. Lab. **59**, 459.
Imada, M., 1994, J. Phys. Soc. Jpn. **63**, 3059.
Ingersent, K., B. A. Jones, and J. W. Wilkins, 1992, Phys. Rev. Lett. **69**, 2594.
Inoue, I. H., I. Hase, Y. Aiura, A. Fujimori, Y. Haruyama, T. Maruyama, and Y. Nishihara, 1995, Phys. Rev. Lett. **74**, 2539, and private communication.
Jaccarino, V. G., K. Wertheim, J. H. Wernick, L. R. Walker, and S. Arajs, 1967, Phys. Rev. **160**, 476.
Janiš, V., 1986, Czech. J. Phys. B **36**, 1107.
Janiš, V., 1989, Phys. Rev. B **40**, 11331.
Janiš, V., 1991, Z. Phys. B **83**, 227.
Janiš, V., 1993, J. Phys Cond. Matter **5**, L425.
Janiš, V., 1994, Phys. Rev. B **49**, 1612.
Janiš, V., M. Ulmke, and D. Vollhardt, 1993, Europhys. Lett. **24**, 287.
Janiš, V., and D. Vollhardt, 1992a, Int. J. Mod. Phys. B **6**, 731.
Janiš, V., and D. Vollhardt, 1992b, Phys. Rev. B **46**, 15712.
Jarrell, M., 1992, Phys. Rev. Lett. **69**, 168.
Jarrell, M., 1995, Phys. Rev. B **51**, 7429.
Jarrell, M., H. Akhlaghpour, and Th. Pruschke, 1993a, Phys. Rev. Lett. **70**, 1670.
Jarrell, M., H. Akhlaghpour, and Th. Pruschke, 1993b, in *Quantum Monte Carlo Methods in Condensed Matter Physics*, edited by M. Suzuki (World Scientific, Singapore).
Jarrell, M., J. K. Freericks, and Th. Pruschke, 1995, Phys. Rev. B **51**, 11704.
Jarrell, M., and J. Gubernatis, 1996, Phys. Rep. (in press).
Jarrell, M., and T. Pruschke, 1993a, Z. Phys. B **90**, 187.
Jarrell, M., and T. Pruschke, 1993b, Phys. Rev. B **49**, 1458.
Jin, S., T. H. Tiefel, M. McCormack, R. A. Fastnacht, R. Ramesh, and L. H. Chen, 1994, Science **264**, 413.
Jones, B., C. M. Varma, and J. W. Wilkins, 1988, Phys. Rev. Lett. **61**, 125.
Kajueter, H., and G. Kotliar, 1995, Preprint No. cond-mat/9509152.
Kajueter, H., G. Kotliar, and G. Moeller, 1995, unpublished.
Kakehashi, Y., 1992, Phys. Rev. B **45**, 7196.
Kanamori, J., 1959, J. Phys. Chem. Solids **10**, 87.
Kane, C. L., P. A. Lee, and N. Read, 1989, Phys. Rev. B **39**, 6880.
Kee, H. Y., and J. Hong, 1995, Preprint No. cond-mat/9508096.
Kennedy, T., and E. H. Lieb, 1986, Physica **138A**, 320.
Khomskii, D., 1979, Sov. Phys. Usp. **22**, 879.
Khurana, A., 1990, Phys. Rev. Lett. **64**, 1990.
Kikuchi, R., 1951, Phys. Rev. **81**, 988.
Kim, C. I., Y. Kuramoto, and T. Kasoya, 1990, J. Phys. Soc. Jpn. **59**, 2414.
Kohn, W., 1964, Phys. Rev. **133**, A171.
Kohno, H., and K. Yamada, 1988, Prog. Theor. Fiz. **80**, 623.
Kopietz, P., 1994, J. Phys. Cond. Matter **6**, 4885; Physica B **194-196**, 271.
Kotliar, G., 1993a, in *Correlated Electron Systems*, edited by V. J. Emery (World Scientific, Singapore).
Kotliar, G., 1993b, in *Strongly Correlated Electronic Materials*, edited by K. Bedell, Z. Wang, D. Meltzer, A. Balatzky, and E. Abrahams (Adison-Wesley, Reading, MA).
Kotliar, G., 1994, in *Strongly Interacting Fermions and High T_c Superconductivity*, edited by B. Doucot and J. Zinn-Justin (Elsevier Science, New York).
Kotliar, G., and J. Liu, 1988, Phys. Rev. Lett. **61**, 1784.
Kotliar, G., and M. Rozenberg, 1995, in *The Hubbard Model*, Proceedings of the Conference on the Mathematics and Physics of the Hubbard model (San Sebastian), edited by D. Bareswyl, D. Campbell, J. Carmelo, and F. Guinea (Plenum, New York).
Kotliar, G., and A. Ruckenstein, 1986, Phys. Rev. Lett. **57**, 1362.
Kotliar, G., and Q. Si, 1993, Physica Scripta **49**, 165.
Kotliar, G., and Q. Si, 1995, Preprint No. cond-mat/9508112.
Krishnamurthy, H. R., J. W. Wilkins, and K. G. Wilson, 1980, Phys. Rev. B **21**, 1003, 1044.
Kugel, K., and D. Khomskii, 1973, Sov. Phys. JETP **37**, 725.
Kugel, K., and D. Khomskii, 1982, Sov. Phys. Usp. **25**, 231.
Kuramoto, Y., 1985, Springer Series in Sol. State. Science Vol. 62, pp. 152–162.
Kuramoto, Y. and T. Watanabe, 1987, Physica B **148**, 80.
Kuwamoto, H., J. M. Honig, and J. Appel, 1980, Phys. Rev. B **22**, 2626.
Kutzelnigg, W., 1982, J. Chem. Phys. **77**, 3081.
Kutzelnigg, W., and S. Koch, 1983, J. Chem. Phys. **79**, 4315.
Laad, M., 1994, Phys. Rev. B **49**, 2327.
Lacroix, C., 1981, J. Phys. F **11**, 2389.
Laloux, L., 1995, private communication.
Laloux, L., A. Georges, and W. Krauth, 1994, Phys. Rev. B **50**, 3092.
Langer, W., M. Plischke, and D. Mattis, 1969, Phys. Rev. Lett. **23**, 1448.
Langreth, D., 1966, Phys. Rev. **150**, 516.
Lelievre, F., G. Misguich, and A. Georges, 1995, unpublished.
Li, Y. M., and d'Ambrumenil, 1992, Mod. Phys. Lett. B **6**, 1827.
Lieb, E. H., 1986, Physica **140A**, 240.
Lin, J. L., and J. P. Wolfe, 1993, Phys. Rev. Lett. **71**, 1222.
Lin, H. Q., and J. E. Gubernatis 1993, Comput. Phys. **7**, 400.
Luttinger, J. M., and J. C. Ward, 1960, Phys. Rev. **118**, 1417.
Majumdar, P., and H. R. Krishnamurthy, 1994, Phys. Rev. Lett. **73**, 1525.
Majumdar, P., and H. R. Krishnamurthy, 1995a, Phys. Rev. B **52**, R5479.
Majumdar, P., and H. R. Krishnamurthy, 1995b, Preprint No. cond-mat/9512151.
Maple, M. B., C. L. Seaman, D. A. Gajewski, Y. Dalichaouch, V. B. Barbetta, M. C. de Andrade, H. A. Mook, H. G. Lukefahr, O. O. Bernal, and D. E. MacLaughlin, 1994, J. Low Temp. Phys. **95**, 225.
Matsuura, A., Z. X. Shen, D. S. Dessau, C. H. Park, T. Thio, J. W. Bennett, and O. Jepsen, 1994, unpublished.
Mattheiss, L., F., 1994, J. Phys. Condens. Matter **6**, 6477.
McWhan, D. B., J. P. Remeika, T. M. Rice, W. F. Brinkman, J. P. Maita, and A. Menth, 1971, Phys. Rev. Lett. **27**, 941.
McWhan, D. B., A. Menth, J. P. Remeika, W. F. Brinkman, and T. M. Rice, 1973, Phys. Rev. B **7**, 1920.
Menge, B., and E. Müller-Hartmann, 1991, Z. Phys. B **82**, 237.
Metzner, W., 1989, Z. Phys. B **77**, 253.
Metzner, W., 1991, Phys. Rev. B **43**, 8549.
Metzner, W., and D. Vollhardt, 1989, Phys. Rev. Lett. **62**, 324.

Mezard, M., G. Parisi, and M. A. Virasoro, 1987, *Spin Glass Theory and Beyond* (World Scientific, Singapore).
Micnas, R., J. Ranninger, and S. Robaszkiewicz, 1990, Rev. Mod. Phys. **62**, 113.
Millis, A., P. B. Littlewood, and B. I. Shraiman, 1995, Phys. Rev. Lett. **74**, 5144.
Millis, A., B. I. Shraiman, and R. Mueller, 1995, Preprint No. cond-mat/9507084.
Milovanović, M., S. Sachdev, and R. N. Bhatt, 1989, Phys. Rev. Lett. **63**, 82.
Möbius A., 1989, Phys. Rev. B **40**, 4194.
Möbius A., 1990, Z. Phys. B **80**, 213.
Moeller, G., V. Dobrosavljevič, and A. Ruckenstein, 1995, unpublished.
Moeller, G., A. Ruckenstein, and S. Schmitt-Rink, 1992, Phys. Rev. B **46**, 7427.
Moeller, G., Q. Si, G. Kotliar, M. J. Rozenberg, and D. S. Fisher, 1995, Phys. Rev. Lett., **74**, 2082.
Möller, B., and Wölfle, P., 1993, Phys. Rev. B **48**, 10320.
Morita, T., 1990, J. Stat. Phys. **59**, 819.
Mott, N. F., 1949, Proc. Phys. Soc. A **62**, 416.
Mott, N. F., 1956, Can. J. Phys. **34**, 1356.
Mott, N. F., 1961, Philos. Mag. **6**, 287.
Mott, N. F., 1990, *Metal Insulator Transitions* (Taylor and Francis, London).
Müller-Hartmann, E., 1984, Z Phys. B **57**, 281.
Müller-Hartmann, E., 1989a, Z Phys. B **74**, 507.
Müller-Hartmann, E., 1989b, Z. Phys. B **76**, 211.
Müller-Hartmann, E., 1989c, Int. J. Mod. Phys. B **3**, 2169.
Newns, D. M., and N. Read, 1987, Adv. Phys. **36**, 799.
Nishino, T., and K. Ueda, 1993, Phys. Rev. B **47**, 12451.
Nozieres P., and A. Blandin, 1980, J. Phys. (Paris) **41**, 193.
Nozieres P., and S. Schmitt-Rink, 1985, J. Low. Temp. Phys. **59**, 195.
Ohkawa, F. J., 1991a, J. Phys. Soc. Jpn. **60**, 3218.
Ohkawa, F. J., 1991b, Prog. Theor. Phys. (Suppl.) **106**, 95.
Okimoto, Y., T. Katsufuji, T. Ishikawa, A. Urushibara, T. Arima, and Y. Tokura, 1995, Phys. Rev. Lett. **75**, 109.
Onsager, L., 1936, J. Am. Chem. Soc. **58**, 1486.
Park, C. H., Z. X. Shen, A. G. Loeser, D. S. Dessau, D. G. Mandrus, A. Migliori, J. Sarrao, and Z. K. Fisk, 1994, unpublished.
Park, J. H., L. H. Tjeng, J. W. Allen, P. Metcalf, and C. T. Chen, 1994, AT&T Bell Labs Report.
Pei, S., J. D. Jorgensen, B. Dabrowski, D. G. Hinks, D. R. Richards, A. W. Mitchell, J. M. Newsam, S. K. Sinha, D. Vaknin, and A. J. Jacobson, 1990, Phys. Rev. B **41**, 4126.
Penn, D. R., 1966, Phys. Rev. **142**, 350.
Press, W. H., S. A. Teukolsky, W. T. Vetterling, and B. P. Flannery, 1991, *Numerical Recipes*, 2nd ed. (Cambridge University Press), Cambridge, England.
Pruschke, T., D. L. Cox, and M. Jarrell, 1993a, Europhys. Lett. **21**, 593.
Pruschke, T., D. L. Cox, and M. Jarrell, 1993b, Phys. Rev. B **47**, 3553.
Pruschke, T., and N. Grewe, 1989, Z. Phys. B **74**, 439.
Pruschke, T., and M. Jarrell, 1994, Physica B **199**, 217.
Pruschke, T., M. Jarrell, and J. K. Freericks, 1995, Adv. Phys. **44**, 187.
Qin, Q., and G. Czycholl, 1994, Physica B **199-200**, 219.
Quirt, J. D., and J. R. Marko, 1972, Phys. Rev. Lett. **26**, 318.
Raimondi, R., and C. Castellani, 1993, Phys. Rev. B **48**, 11453.
Randeria, M., J. Duan, and L. Shieh, 1989, Phys. Rev. Lett. **62**, 981.
Randeria, M., J. Duan, and L. Shieh, 1990, Phys. Rev. B **41**, 327.
Randeria, M., N. Trivedi, A. Moreo, and R. T. Scalettar, 1992, Phys. Rev. Lett. **69**, 2001.
Read, N., D. M. Newns, and S. Doniach, 1984, Phys. Rev. B **30**, 3841.
Rice, T. M., and K. Ueda, Phys. Rev. B **34**, 6420.
Rozenberg, M. J., 1995, Phys. Rev. B **52**, 7369.
Rozenberg, M. J., I. H. Inoue, H. Makino, F. Iga, and Y. Nishihara, 1996, Preprint No. cond-mat/9603051.
Rozenberg, M. J., G. Kotliar, and H. Kajueter, 1995, Preprint No. cond-mat/9509182.
Rozenberg, M. J., G. Kotliar, H. Kajueter, G. A. Thomas, D. H. Rapkine, J. M. Honig, and P. Metcalf, 1995, Phys. Rev. Lett. **75**, 105.
Rozenberg, M. J., G. Kotliar, and X. Y. Zhang, 1994, Phys. Rev. B **49**, 10181.
Rozenberg, M. J., G. Moeller, and G. Kotliar, 1994, Mod. Phys. Lett. B **8**, 535.
Rozenberg, M., X. Y. Zhang, and G. Kotliar, 1992, Phys. Rev. Lett. **69**, 1236.
Sachdev, S., and A. Georges, 1995, Phys. Rev. B **52**, 9520.
Sachdev, S., N. Read, and R. Oppermann, 1995, Phys. Rev. B **52**, 10 286.
Saitoh, T., A. E. Bocquet, T. Mizokawa, H. Namatame, A. Fujimori, M. Abbate, Y. Takeda, and M. Takano, 1995, Phys. Rev. B **51**, 13942.
Sakai, O. and Y. Kuramoto, 1994, Solid State Commun. **89**, 307.
Sakai, O., Y. Shimizu, and T. Kasuya, 1989, J. Phys. Soc. Jpn. **58**, 162.
Salomaa, M., 1981, Solid State Commun. **38**, 815.
Sanchez, J. M., F. Ducastelle, and D. Gratias, 1984, Physica **128A**, 334.
Santoro, G., M. Airoldi, S. Sorella, and E. Tosatti, 1993, Phys. Rev. B **47**, 16216.
Sarma, D. D., S. Barman, H. Kajueter, and G. Kotliar, 1995, unpublished.
Saso, T., and M. Itoh, 1995, Preprint No. cond-mat/9512094.
Schiller, A., and Ingersent, K., 1995, unpublished.
Schlesinger, Z., Z. Fisk, H. T. Zhang, M. B. Maple, J. F. DiTusa, and G. Aeppli, 1993, Phys. Rev. Lett. **71**, 1748.
Schmalian, J., P. Lombardo, M. Avignon, and K. H. Bennemann, 1995, Physica B (to be published).
Schotte, K. D., and U. Schotte, 1969, Phys. Rev. **182**, 479; Phys. Rev. **185**, 509.
Schrieffer, J. R., and P. A. Wolf, 1966, Phys. Rev. **149**, 491.
Schwartz, L., and E. Siggia, 1972, Phys. Rev. B **5**, 383.
Schweitzer, H., and G. Czycholl, 1989, Solid State Commun. **69**, 171.
Schweitzer, H., and G. Czycholl, 1990a, Z. Phys B **79**, 377.
Schweitzer, H., and G. Czycholl, 1990b, Solid State Commun. **74**, 735.
Schweitzer, H., and G. Czycholl, 1991a, Z. Phys B **83**, 93.
Schweitzer, H., and G. Czycholl, 1991b, Phys. Rev. Lett. **67**, 3724.
Sengupta, A. M., and A. Georges, 1995, Phys. Rev. B **52**, 10 295.
Shimizu, Y., and O. Sakai, 1995, J. Phys. Soc. Jpn. (to be published).

Si, Q., and G. Kotliar, 1993, Phys. Rev. Lett. **70**, 3143; Phys. Rev. B **48**, 13 881.
Si, Q., K. Kotliar, and A. Georges, 1992, Phys. Rev. B **46**, 1261.
Si, Q., M. J. Rozenberg, K. Kotliar, and A. E. Ruckenstein, 1994, Phys. Rev. Lett. **72**, 2761.
Sire, C., C. M. Varma, and H. R. Krishnamurthy, 1993, Phys. Rev. B **48**, 13833.
Slater, J. C., 1951, Phys. Rev. **82**, 538.
Spalek, J., A. Datta, and J. M. Honig, 1987, Phys. Rev. Lett. **59**, 728.
Spalek, J., 1990, J. Sol. St. Chem. **88**, 70.
Strack, R., and D. Vollhardt, 1992, Phys. Rev. B **46**, 13852.
Stoer, J., and Bulirsch, R., 1980, *Introduction to Numerical Analysis* (Springer-Verlag, New York).
Sugiyama, G., S. E. Koonin, 1986, Ann. Phys. **168**, 1.
Sun, S. J., M. F. Yang, and T. M. Hong, 1993, Phys. Rev. B **48**, 16127.
Suzuki, M., 1988, J. Stat. Phys. **53**, 483, and references therein.
Theumann, A., 1969, Phys. Rev. **178**, 978.
Thomas, G. A., D. H. Rapkine, S. A. Carter, A. J. Millis, T. F. Rosenbaum, P. Metcalf, and D. F. Honig, 1994, Phys. Rev. Lett. **73**, 1529.
Thomas, G. A., D. H. Rapkine, S. A. Carter, T. F. Rosenbaum, P. Metcalf, and D. F. Honig, 1994, J. Low Temp. Phys. **95**, 33.
Thouless, D. J., P. W. Anderson, and R. G. Palmer, 1977, Philos. Mag. **35**, 593.
Tokura, Y., Y. Taguchi, Y. Okada, Y. Fujishima, T. Arima, K. Kumagai, and Y. Iye, 1993, Phys. Rev. Lett. **70**, 2126.
Tokura, Y., A. Urushibara, Y. Morimoto, T. Arima, A. Asamitsu, G. Kido, and N. Furukawa, 1994, J. Phys. Soc. Jpn. **63**, 3931.
Torrance, J. B., P. Lacorre, and A. I. Nazzal, 1992, Phys. Rev. B **45**, 8209.
Toulouse, G., 1970, Phys. Rev. B **2**, 270.
Treglia, G., F. Ducastelle, and D. Spanjaard, 1980, Phys. Rev. B **21**, 3729.
Tsuda, N., K. Nasu, A. Yanase, and K. Siratori, 1991, *Electronic Conduction in Oxides*, Springer Series in Solid State Sciences Vol. 94 (Springer-Verlag, Berlin).
Tsvelick, A. M., and P. B. Wiegmann, 1983, Adv. Phys. **32**, 453.
Turov, E., and V. Grebenikov, 1988, Physica B **149**, 150.
Uhrig, R. S., and R. Vlaming, 1993, Phys. Rev. Lett. **71**, 271.
Ulmke, M., 1995, Preprint No. cond-mat/9512044.
Ulmke M., V. Janiš, and D. Vollhardt, 1995, Phys. Rev. B **51**, 10 411.
Urushibara, A., Y. Moritome, T. Arima, A. Asamitso, G. Kido, and Y. Tokura, 1995, Phys. Rev. B **51**, 14103.
Valenti, R., and C. Gros, 1993, Z. Phys. B **90**, 161.
van Dongen, P. G. J., 1991a, Mod. Phys. Lett. B **5**, 861.
van Dongen, P. G. J., 1991b, Phys. Rev. Lett. **67**, 757.
van Dongen, P. G. J., 1992, Phys. Rev. B **45**, 2267.
van Dongen, P. G. J., 1994, Phys. Rev. B **49**, 7904.
van Dongen, P. G. J., 1995, Phys. Rev. Lett. **74**, 182.
van Dongen, P. G. J., and D. Vollhardt, 1990, Phys. Rev. Lett. **65**, 1663.
Varma, C. M., 1976, Rev. Mod. Phys. **48**, 219.
Varma, C. M., and T. Giamarchi, 1994, in "Strongly Interacting Fermions and High-T_c Superconductivity," edited by B. Doucot and J. Zinn-Justin (Elsevier, New York).
Varma, C. M., S. Schmitt-Rink, and E. Abrahams, 1987, Solid State Commun. **62**, 681.
Vekič M., J. W. Cannon, D. J. Scalapino, R. T. Scalettar, and R. L. Sugar, 1995, Phys. Rev. Lett. **74**, 2367.
Vidberg, H. J., and J. W. Serene, 1977, J. Low Temp. Phys. **29**, 179.
Visscher, P. B., 1974, Phys. Rev. B **10**, 943.
Vlaming, R., G. S. Uhrig, and D. Vollhardt, 1992, J. Phys. C **4**, 7773.
Vlaming, R., and D. Vollhardt, 1992, Phys. Rev. B **45**, 4637.
Vollhardt, D., 1984, Rev. Mod. Phys. **56**, 99.
Vollhardt, D., 1991, Physica B **169**, 277.
Vollhardt, D., 1993, in *Correlated Electron Systems*, edited by V. J. Emery (World Scientific, Singapore).
Vollhardt, D., 1994, in Proceedings of the Enrico Fermi School, Course CXXI, edited by Broglia and Schrieffer (North-Holland, Amsterdam).
von Helmolt, R., J. Wecker, B. Holzapfel, L. Schultz, and K. Samwer, 1993, Phys. Rev. Lett. **71**, 2331.
Wang, S. Q., W. E. Evenson, and J. R. Schrieffer, 1969, Phys. Rev. Lett **23**, 92.
Wegner, F., 1976, Z. Phys. B **25**, 327.
White, J. A., 1992, Phys. Rev. B **45**, 1100.
White, S. R., D. J. Scalapino, R. L. Sugar, E. Y. Loh, J. E. Gubernatis, R. T. Scalettar, 1989, Phys. Rev. B **40**, 506.
White, S. R., R. L. Sugar, and R. T. Scalettar, 1988, Phys. Rev. B **38**, 11665.
Wilson, K. G., 1975, Rev. Mod. Phys. **47**, 773.
Withoff, D., and E. Fradkin, 1990, Phys. Rev. Lett. **64**, 1835.
Wolff, P. A., 1961, Phys. Rev. **124**, 1030.
Wortis, M., 1974, in *Phase Transitions and Critical Phenomena*, edited by C. Domb and M. Green (Academic, London), Vol. 3.
Yamada, K., 1975, Prog. Theor. Phys. **53**, 970.
Yokoyama, H., and H. Shiba, 1987, J. Phys. Soc. Jpn. **56**, 3582.
Yosida, K., and K. Yamada, 1970, Prog. Theor. Phys. **46**, 244.
Yosida, K., and K. Yamada, 1975, Prog. Theor. Phys. **53**, 1286.
Yu, C. C., and P. W. Anderson, 1984, Phys. Rev. B **29**, 6165.
Zaanen, J., and G. A. Sawatzky, 1987, Can. J. Phys. **65**, 1262.
Zaanen, J., and G. A. Sawatzky, 1990, Prog. Theor. Phys. (Suppl.) **101**, 231.
Zaanen, J., G. A. Sawatzky, and J. W. Allen, 1985, Phys. Rev. Lett. **55**, 418.
Zang, J., A. Bishop, and H. Roder, 1995, Preprint No. cond-mat/9507097.
Zhang, X. Y., M. J. Rozenberg, and G. Kotliar, 1993, Phys. Rev. Lett. **70**, 1666.
Zlatić, V., B. Horvatić, and D. Sokcević, 1985, Z. Phys. B **59**, 151.
Zlatić, V., and B. Horvatić, 1990, Solid State Commun. **75**, 263.